

THE CURRENTS, WINDS AND TIDES OF NORTHERN HOWE SOUND

by

JOSEPH ROY BUCKLEY

B. Sc. McMaster University, 1971

A THESIS SUBMITTED IN PARTIAL FULFILMENT OF

THE REQUIREMENTS FOR THE DEGREE OF

DOCTOR OF PHILOSOPHY

in the

Department of Physics

and the

Institute of Oceanography

We accept this thesis as conforming to the
required standard

THE UNIVERSITY OF BRITISH COLUMBIA

March, 1977

copyright J. R. Buckley, 1977

In presenting this thesis in partial fulfilment of the requirements for an advanced degree at the University of British Columbia, I agree that the Library shall make it freely available for reference and study.

I further agree that permission for extensive copying of this thesis for scholarly purposes may be granted by the Head of my Department or by his representatives. It is understood that copying or publication of this thesis for financial gain shall not be allowed without my written permission.

Department of PHYSICS

The University of British Columbia
2075 Wesbrook Place
Vancouver, Canada
V6T 1W5

Date 4 March 1977



frontispiece - Northern Howe Sound from 9.6km altitude,
August 7, 1972. (National Air Photo Library photograph)

ABSTRACT

Studies were carried out to determine the circulation of water in the northern basin of Howe Sound, a small fjord on the mainland coast of British Columbia, and to determine the extent of the influence of the winds, the tide and river runoff on the circulation. In one experiment, surface-layer drogues were tracked by radar for four periods each of approximately three days duration. Data were recorded photographically, then digitized for computer processing. Cubic spline interpolation was used to produce positions, velocities and accelerations at one minute intervals along every drogue track. The interpolated data were averaged in a suitable manner to produce pseudo-Eulerian estimates of velocity.

Near the head of the fjord, both wind and tide appeared to cause temporal fluctuations in the surface current of magnitude similar to the expected mean flow due to the river. The river was the cause of spatial inhomogeneity in the flow, but did not appear to be a significant source of temporal variations. Farther down the inlet, wind forcing was the dominant cause of temporal variations in the surface-layer flow of about five times the magnitude of the expected mean river-driven flow. At no distance along the fjord was the velocity observed to be laterally uniform. Lateral gradients of long-channel velocity were strong at

the inlet head and decreased away from it, indicating that the fresh water from the river was slowly mixing across the inlet. Another experiment using drogues at three depths in the upper 6m of the water indicated that the velocity structure was not uniform, either laterally or with depth.

Analysis was done on data from six current meters moored in the northern basin of Howe Sound. The mean currents from these meters showed a surface-layer outflow and a return inflow in the waters just below. A mean down-inlet current was seen at 150m, 80m below sill depth. Spectra of the currents showed dominant peaks at diurnal and semi-diurnal periods. The wind was coherent with the currents at 3m for periods longer than 10 hours. Below this depth, no consistent relationship was seen. In the diurnal band, the currents were strongest at the surface, indicative of forcing from the surface by the wind. In the semi-diurnal band, the currents were strongest at 10m depth. Both bands also showed a phase variation with depth indicative of a baroclinic structure.

These results were compared with some models for surface-layer behaviour. The first model assumed that the wind momentum input was distributed uniformly throughout the surface layer and that the layer was not frictionally coupled to the deeper waters. Drag coefficients calculated from the wind stress and drogue acceleration gave values of 1 to 2×10^{-3} , similar to values measured in other ways. This model was only valid for the first few hours after the onset of the wind. Another model, developed by Farmer (1972),

analysed the behaviour of the surface layer of a semi-infinite canal under the influence of a steady wind stress. It predicted correctly the length of time of wind dominance of the flow, the magnitude of the velocity change and the magnitude of the acceleration of the water. A baroclinic tidal model in a two-layer fjord, adapted from Rattray (1960), correctly predicted the phase of the surface-layer currents near the head of a fjord with respect to the height of the tide.

TABLE OF CONTENTS

page

Abstract	iii
List of Tables	x
List of Figures	xii
Acknowledgements	xv
Chapter I - Introduction	1
I.1 - Howe Sound - The Fjord Under Investigation ..	3
I.2 - Silt, Circulation and Forcing Functions	9
I.3 - A Brief Background of Estuarine Theory and Forced Circulation Dynamics	12
Chapter II - Surface Layer Flow - Experiment and Data Analysis	15
II.1 - A Preliminary Experiment	15
II.2 - Main Experiment	20
II.2.1 - Introduction	20
II.2.2 - The Drogues	21
II.2.3 - The Base Station - Radar and Cameras ..	25

II.2.4 - Vessels, Communications and Logistics .	29
II.3 - Analysis of the Droque Data	31
II.4 - Data Averaging - a Problem of Lagrangian Measurements	42
Chapter III - Measurements of Wind, Tide, River Flow and Surface Layer Structure	48
III.1 - Wind Measurements	48
III.2 - River Discharge	54
III.3 - The Tide	57
III.4 - Density Measurements	61
III.5 - Comparison of the Droque Velocities with the 3m Current Meter	66
Chapter IV - Results of the Surface Layer Experiment .	70
IV.1 - Introduction	70
IV.2 - A General Surface Circulation Pattern	72
IV.3 - A Synopsis of the Data Sets	76
IV.3.1 - Techniques of Presentation	76
IV.3.2 - Week 1 - May 8-11, 1973	81
IV.3.3 - Week 2 - May 15-18, 1973	85
IV.3.4 - Week 3 - June 26-29, 1973	90
IV.3.5 - Week 4 - July 3-6, 1973	96
IV.3.6 - Summary of the Observations	101
IV.4 - Temporal and Cross-channel Variations in Surface Layer Flow	102
IV.5 - Lateral Homogeneity of the Velocity and Acceleration Fields	111
IV.6 - Temporal Variations in Laterally Averaged Velocities and Accelerations	114

IV.7 - Cross-channel Structure of the Velocity Field	118
IV.8 - Ensemble Averaged Velocity Gradients	121
Chapter V - Interlude - The Three Level Droque Experiment	125
Chapter VI - Subsurface Currents	133
VI.1 - A Description of the Subsurface Current Monitoring Programme	133
VI.2 - Time Series Records from the Current Meters	135
VI.3 - Spectral Analysis of the Currents	139
VI.4 - Techniques and Problems of Analysis	140
VI.5 - Reliability and Stability of Coherence Estimates	148
VI.6 - Mean Currents	153
VI.7 - Spectra of the Wind and Currents	157
VI.8 - Coherence of the Wind and Currents	163
VI.9 - Tidal Influence on the Currents	169
VI.10 - Changes in Hydrographic Properties as Indicators of Currents	174
Chapter VII - Summary of Results and Comparison with Theory	180
VII.1 - Summary of the Experimental Results	180
VII.1.1 - The Surface Layer Experiment	180
VII.1.2 - The Subsurface Current Experiment	182
VII.2 - Drag Coefficient Calculations	184
VII.3 - Farmer's Model of a Wind-Driven Surface Layer	189
VII.4 - Tides and a Normal-Mode Fjord Model	198

VII.5 - Summary of the Model Results	207
Bibliography	209
Appendix I - Behaviour Of A Droque In A Vertical Shear	213
Appendix II - Computer Movie Generation	226
Appendix III	on tape in Special Collections

LIST OF TABLES

Table	page
I: Average Float Velocities And Directions In the First Experiment	18
II: Comparison Of Squamish And Radar Site Winds	49
III: River Discharge And Resultant Surface-layer Velocity	56
IV: Equivalent Fresh Water Depth For Several Cross-inlet Sections	63
V: A Summary Of Drogue Observation Statistics	70
VI: Ensemble Averaged Acceleration Ratio And Velocity Shears	121
VII: Coherence And Phase Estimates Between Wind And 5m Current With Different Degrees Of Freedom	149
VIII: Ratios Of Mean Square Currents In The Diurnal Band To Those In The Semi-diurnal Band For All Depths	161
IX: Coherence And Phase Between Wind And Currents at 24h	168
X: Tidal Constituents At Squamish	169
XI: Coherence And Phase Between The Currents in the Diurnal And Semi-diurnal Bands	170
XII: Amplitude And Phase Of The Surface Layer Currents Calculated From The Normal-mode Model ..	203

XIII: The Forces And Torques On A Drogue	216
XIV: Droque Speed And Tilt Angle In A Homogeneous Current	219
XV: Droque Speed And Tilt In A Linear Shear	220
XVI: Comparison Of Droque, Mean And R.m.s. Velocities For Three Analytic Shears	223

LIST OF FIGURES

Figure	page
1: The Bathymetry Of Howe Sound	4
2: A Typical Sigma-t Section Of Howe Sound	7
3: Squamish Harbour Showing Location Of The Photographic Site And The Float Tracks From The First Experiment	18
4: The Basic Design Of The Surface Drogues Used.	22
5: Details In Drogue Construction	25
6: Howe Sound Showing The Four Radar Sites And A Three Mile Range About Each One	27
7: A Sample Radar Image, The Antenna Response Pattern And The Echo Of A Drogue	32
8: A Flow Chart Of The Drogue Track Creating And Checking Programmes	41
9: Wind Rose For The Experiment Superimposed On A Chart Of Howe Sound	52
10: A Comparison Of The Long-channel Wind Component From Squamish And The Radar Site	53
11: Discharge Of The Squamish River Throughout The Experiment	56
12: Tidal Height For The Experiment As Predicted For Pt. Atkinson	59
13: Salinity Profiles From Two Cross-inlet Sections	62

14:	A Comparison Between Water Velocity As Measured By Drogue And By Current Meter	67
15:	Pattern Of The Circulation Of The Surface Layer ..	73
16:	Correspondence Between The Actual And "Squared" Coastlines	77
17:	A Typical Diagram From The Averaged Data Set	78
18:	Typical Three Hour Average Velocities Plotted With Standard Deviation Error Bars	80
19:	The Week 1 Data Set	82
20:	The Week 2 Data Set	86
21:	The Week 3 Data Set	91
22:	The Week 4 Data Set	97
23:	Location Of The Averaging Regions	103
24:	Contours Of Long-channel Velocity As A Function Of Cross-channel Position And Time	104
25:	Total Velocity As A Function Of Cross-channel Position And Time	110
26:	Velocity And Acceleration Vs. Time For Three Cross-inlet Positions In Week 1	113
27:	Laterally Averaged Velocity And Acceleration Vs Time	116
28:	Cross-channel Structure Of The Velocity Field	119
29:	Three Layer Experiment - Shallow Drogue Tracks ...	128
30:	Three Layer Experiment - Intermediate Drogue Tracks	129
31:	Three Layer Experiment - Deep Drogue Tracks	130
32:	Velocity Contoured Cross-inlet Section From The Three Level Experiment	131

33:	Fifteen Days Of Current Meter Records	136
34:	Unsmoothed And Smoothed Current Meter Records	145
35:	Smoothed And Unsmoothed 5m Current Spectra	147
36:	The Mean Current Profile In Howe Sound, April- August 1973	154
37:	Spectra Of The Wind And Currents	158
38:	Coherence And Phase Between The Wind And Currents	164
39:	Phasor Diagrams For The Semi-diurnal And Diurnal Currents At Different Depths	173
40:	Time Series Plot Of Temperature Vs Depth At How 4	176
41:	Temperature Sections in Howe Sound on 20 September and 13 November, 1973	177
42:	Calculated "drag Coefficients" For All Four Weeks	187
43:	Velocity And Acceleration From Farmer's Model	194
44:	Geometry Of The Basin For A Normal-mode Fjord Model	200
45:	Amplitude And Phase Of The Surface Layer Currents As Calculated From Rattray's Model	205
46:	The Forces On A Drogue	216

ACKNOWLEDGEMENTS

The type of drogue study described in this thesis requires a large amount of manpower to be performed successfully. During the course of the experiment, virtually all of the Physical Oceanography graduate students and many of the staff members of the Institute of Oceanography, University of British Columbia volunteered their services. Much assistance came from Mr. David English, who helped to design the drogues and to keep the fleet of vessels operating during the experiment, and provided technical expertise in the project. Assistance in this experiment also came from the Pacific Environment Institute, West Vancouver, B.C., which provided the R/V Active Lass, her skipper Mr. A. Matheson and the Sangstercraft; from the Pacific Biological Station, Nanaimo, B.C., which provided the R/V Caligus with Mr. Ron Page, Dr. John Sibert and Dr. Robert Parker; from Construction Aggregates Ltd., which allowed us to use its property for the radar sites at Britannia Beach and at Furry Creek and to Rayonier of Canada Ltd., Woodfibre Division, which allowed us to use its property for the radar site at Woodfibre. To all these people and organizations, thank you. Without your help, it would have been impossible to perform this experiment.

My thanks are also extended to the Coastal Zone Oceanography group at the Institute of Ocean Sciences,

Patricia Bay, B.C., who maintained the current meter strings in Howe Sound and to Mr. W.H. Bell of that group who did all the preliminary analysis of the current meter data and kindly provided me with his results, and to Dr. P.B. Crean of the Numerical Modelling group of I.O.S. for providing me with tidal data in Howe Sound and results from his tidal model of the area.

I would also like to express my thanks to my committee and to those other members of the Institute who discussed the many aspects of this work with me.

The work was supported mainly by contracts from the Institute of Ocean Sciences, Patricia Bay, with some additional support from the National Research Council of Canada, grant A 8301. During my years at the University of British Columbia, I have been personally supported by a Postgraduate Scholarship and a Postgraduate Bursary from the National Research Council of Canada, by a MacMillan Family Fellowship from the University of British Columbia, by a research assistantship provided in the contracts and by several teaching assistantships from the Department of Physics, University of British Columbia.

I have also been helped through this thesis by my wife Eve, who, as well as typing the document and drafting many of the figures, constantly provided the moral support necessary to enable me to see this project to completion.

Finally, I would like to thank my research supervisor, Dr. Stephen Pond, for the expert guidance, sage advice, enthusiasm, dedication and support he has given me

throughout the five and one half years of research work
presented in this thesis.

CHAPTER I

INTRODUCTION

This thesis describes an investigation into fluctuations in water movement in a fjord and the several possible causes of these fluctuations. The investigation, conducted in Howe Sound, British Columbia, consisted of two main parts. The first part was a surface layer experiment performed in four periods, each of four days duration, in May, June and July, 1973. A number of surface drogues were tracked by radar to obtain a picture of the surface layer flow field. The subsequent analysis attempted to relate the velocity and acceleration of the water to wind stress, to tidal forcing and to variations in river flow. The second part of the investigation consisted of the analysis of data from a current meter string moored in the same fjord throughout 1973. This current meter string was maintained by the Coastal Zone Oceanography group of the Institute of Ocean Sciences, Patricia Bay, B.C. This analysis attempted to relate the currents to wind and tidal forcing.

This thesis starts with a survey of the basic oceanography of Howe Sound and a brief history of previous studies on the dynamics of water circulation in fjords. Chapter II contains a description of the surface layer experiment and of the analysis techniques used to process

the data. Chapter III is a description of the forcing functions of wind, river flow and their behaviour during the experiment. That chapter also contains a description of the measurements made to ascertain the validity of the concept of a "surface layer" in Howe Sound, and to determine the depth of this layer. In chapter IV, the results of the surface-layer experiment, both qualitative and quantitative, are described. Chapter V is the description of a short but interesting experiment performed with the drag elements of the drogues suspended at different depths in the near surface layer of Howe Sound. The results provide a bridge between the surface layer experiment described in the previous chapters and the current meter experiment described in chapter VI which contains the results obtained by spectral analysis of the current meter data. In the final chapter, the results of both experiments are examined in the light of existing theories and some conclusions are drawn about the validity of these theories.

Due to the calibration of the radar set, one unit of horizontal distance measurement used throughout this thesis is the British Nautical mile (about 1.85km). Any reference to miles in this thesis refers to this unit. With the exception of the baroclinic tidal model in chapter VII, a local right-handed co-ordinate system is used throughout this thesis, with the x axis directed up-inlet (nominally north), the y axis directed cross-inlet (nominally east) and the z axis directed vertically downward. u , v and w are the velocities in the x, y and z direction respectively.

I.1 Howe Sound - The Fiord Under Investigation

From Pt. Atkinson on the northern side of the entrance to Vancouver harbour to Squamish, 43 km north, lies a body of water that has been known for almost 200 years as Howe Sound. From a 20km wide opening onto the Strait of Georgia between Pt Atkinson and Gower Pt, Howe Sound narrows to about 3.5km at the Defence Islands 26km north. This triangular southern basin is full of islands. Its average depth is about 200m. In the Pleistocene era there was a sill made of glacial till near the south end of the basin separating the deep waters of the sound from those of the Strait of Georgia. According to K.Ricker (unpublished manuscript), this sill has since been breached by a fault and subsequently eroded in the eastern channel between Passage Island and Bowen Island allowing free mixing of the waters of this basin with those of the Strait. Between the Defence Islands and Porteau Cove there is a sill of glacial material that rises to within no greater than 70m of the surface. Just north of this sill, the channel achieves its maximum depth of 300m. The channel width from Porteau Cove to Squamish is a roughly constant 2.5km. The bathymetry and major features of Howe Sound are shown in figure 1.

The Squamish River flows into Howe Sound at the head of the inlet. It has an average annual discharge of $242 \text{ m}^3/\text{s}$ (Water Survey of Canada, 1974), one of the larger outflows in the province. Its drainage basin of 2341 km^2 is in the mountains and snowfields to the north of Squamish. This

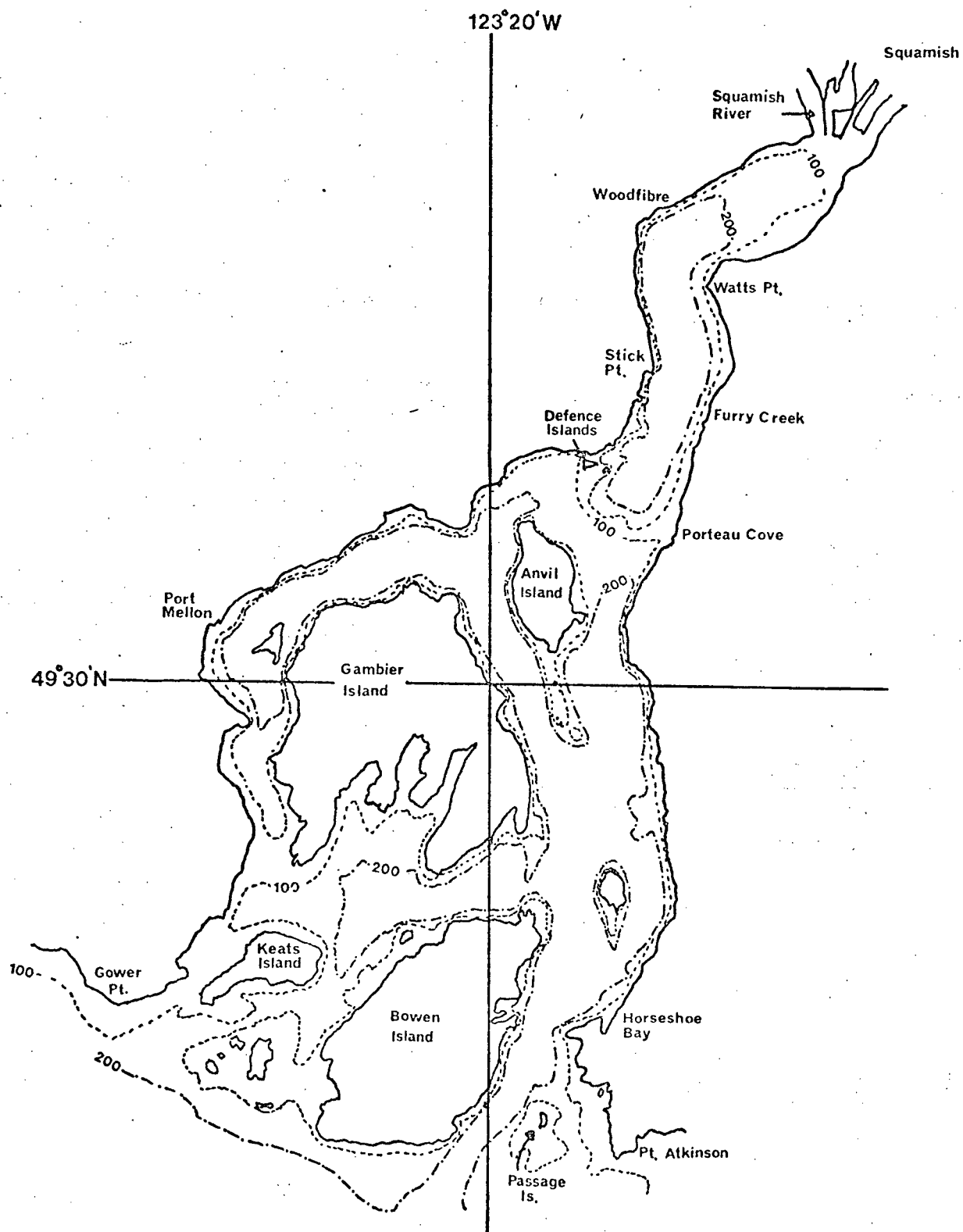


Figure 1 - Bathymetry and major features of Howe Sound.

river provides almost all of the fresh water input into the sound.

In June 1792, during his explorations of the west coast of North America, Captain George Vancouver visited Howe Sound and had these words to say about it:

Quitting point Atkinson and proceeding up the sound...we made a rapid progress, by the assistance of a fresh southerly gale, attended with dark gloomy weather that greatly added to the dreary prospect of the surrounding country. The low fertile shores we had been accustomed to see, though lately with some interruption, here no longer existed: their place was now occupied by the base of the stupendous snowy barrier, thinly wooded and rising from the sea abruptly to the clouds; from whose frigid summit, the dissolving snow in foaming torrents rushed down the sides and chasms of its rugged surface, exhibiting altogether a sublime, though gloomy spectacle, which animated nature seemed to have deserted. ...

(We) find it to terminate in a round bason encompassed on every side by the dreary country already described... The water of the sound was here nearly fresh, and in colour a few shades darker than milk; this I attributed to the melting snow and its water passing over some chalky substance.

...We had scarcely finished our examinations when the wind became excessively boisterous from the southward attended with heavy squalls and torrents of rain.

...At a distance of an hundred yards from shore, the bottom could not be reached with 60 fathoms of line, nor had we been able to gain soundings in many places since we had quitted point Atkinson with 80 and 100 fathoms, though it was frequently attempted... Westward from Anvil island ...the colour of the water changed from being nearly milk white and almost fresh to that of oceanic and perfectly salt. ...About nine o'clock (we) landed for the night near the west point of entrance into the sound, which I distinguished by the name of Howe's Sound in honor of Admiral Earl Howe.

During his short rainy visit, Vancouver observed many of the basic fjord-like characteristics of Howe Sound, the depth, the steep side walls, the silty fresh water input (although he mistakenly identified its source as a "chalky substance" instead of glacial "flour"), and the strong winds.

In the more recent past, Howe Sound was the subject of observation by Hutchinson and Lucas (1931) who examined the summer hydrographic properties of the surface 50yd (46m) at three locations in the sound as part of a larger Strait of Georgia surface layer study. Carter (1934) studied the hydrographic and chemical properties of the upper 50m several times throughout the year at the mouth and head of Howe Sound.

In more recent years, Howe Sound has been visited on occasion by personnel from the Institute of Oceanography, University of British Columbia (IOUBC) as part of ongoing British Columbia inlets studies. From 1957 to 1971 a total of 13 cruises were made. Temperature, salinity and dissolved oxygen content were recorded at discrete depths from the surface to the bottom at several stations within the Sound on each of these cruises. As a result of some of these cruises, the basic oceanographic features of Howe Sound have been described by Pickard (1961). Further sources of hydrographic data and description may be found in Marles et al. (1973).

A typical sigma-t section of the northern basin of Howe Sound is shown in figure 2. An obvious feature of this

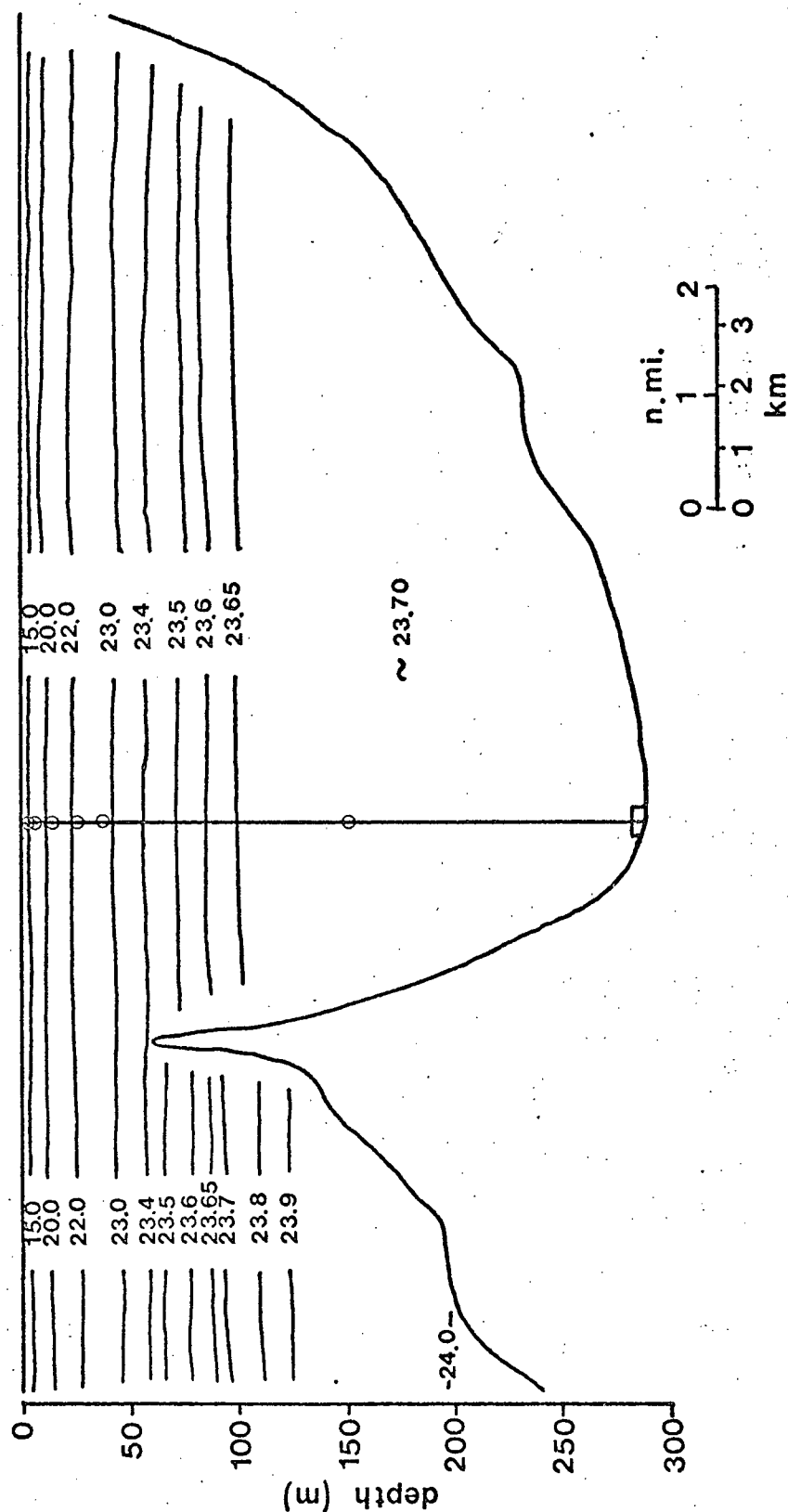


Figure 2 - Sigma-t contours in upper Howe Sound 23 July 1973. Circles on the vertical line indicate locations of current meters discussed in chapter VI.

figure is the effect of the sill on the continuity of the water masses. Inside the sill, below 150m, σ_t is a constant 23.70 within the precision of measurement, while outside the sill it increases to values greater than 24.00. The upper layers both inside and outside the sill show the expected strong stratification.

A survey of the annual variation in hydrographic properties was done as a baseline for this thesis work. A series of 19 cruises were made from July 1972 to March 1974 measuring temperature, salinity and dissolved oxygen content from bottle samples and making STD casts at seven stations from Anvil Island to Squamish. This survey showed that, although the density structure of the upper waters throughout the inlet and the deeper waters outside the sill changed continuously on an annual basis, the deep waters behind the sill did not change measurably in density. Analysis of temperature, salinity and dissolved oxygen showed an occasional deep water replacement in this inner basin. The data from these cruises have been used by Pickard(1975) to show this last result.

Scientific interest in the currents of Howe Sound is recent. Strings of current meters were installed and maintained by the Coastal Zone Oceanography section of the Institute of Ocean Sciences, Patricia Bay B.C. from November 1971 to November 1972 just north of Anvil Island; from February 1972 to November 1972 south of Anvil Island and from November 1972 to February 1974 in the centre of the channel opposite Furry Creek. The basic data from these

meters have been published by Bell (1975). These data show that the expected estuarine circulation is indeed present in Howe Sound. There was a seaward flow in the surface layer and a return flow in the deeper layers. There were, however, large variations about the mean.

The final location, shown in figure 6, was chosen to complement the hydrographic study and the surface current study described in this thesis. It is the data from these meters that will be discussed in detail in chapter VI.

Thus the background of physical data already collected in Howe Sound is quite considerable as might be expected for an inlet so close to Vancouver. It was against this background that the present investigation was set.

I.2 Silt, Circulation And Forcing Functions

The feature of the water flow in Howe Sound most noticeable to the casual observer is the silt pattern in the surface layer. It obviously comes from the river and appears to reveal a "river" of fresh water that meanders and eddies through the saltier water of the inlet until it finally diffuses throughout the surface layer. A fine example of such a silt pattern is shown in the frontispiece.

A more careful observation of these silt patterns will show that the general shape of these patterns is not fixed, but varies with a period of approximately one day. It seems most probable that these variations in silt patterns reflect variations in the total surface layer circulation. One main

objective of this thesis was to discover the cause of these variations.

Tugboat and fishboat operators on the B.C. coast refer to any current as a "tide". Certainly the tide is a likely candidate for the cause of the variations in surface currents in Howe Sound. The tides in Howe Sound are mixed semi-diurnal with a range of about 5m. The sum of the amplitudes of the diurnal constituents is about the same as the sum of the semi-diurnal constituents and so some diurnal forcing by the tide must be expected. There are, however, other possible sources of the variations in the currents.

The Squamish River depends on the snow and ice fields in the mountains north of Squamish for its water supply. Maximum runoff is in the late spring and early summer when snow melting is at its peak. Since this melting is dependant on the warmth of the sun, runoff is higher in the daytime than at night. The daily runoff peak will of course be delayed by the length of time it takes to travel from the snow fields to the inlet. These daily variations in river runoff can be seen in the gauge records, shown in figure 11, taken at Brackendale, just north of Squamish. Since the river runoff is the major driving force in the gravitational circulation in the inlet, it is possible that variations in this force cause the variations in the surface flow.

Many coastal areas are subject to the phenomenon of land and sea breezes. These winds, caused by the temperature difference between adjacent land and water areas, have basically the same periodicity as the fluctuations in land

temperature, which in turn are governed by the daily cycle of insolation. In an area like Howe Sound, during summer days the land is quite a bit hotter than the water surface, so rising air over the land causes strong up-inlet winds. At night the land cools so the temperature difference between land and sea becomes very much smaller and the winds are weak and variable in direction. The narrowing of the main channel of Howe Sound north of Porteau Cove tends to funnel the winds in from the wider areas both in the north and in the south, so that in the region of interest in this study, the winds may be expected to be stronger than a simple temperature difference model might indicate. The observations of Pickard and Rodgers (1959) have shown that the wind can have a large effect on the surface currents in a fjord. Therefore an investigation of the effects of the wind must be included in a search for the cause of apparent current fluctuations.

Tide, wind and river runoff all appear to be possible causes of the observed fluctuations in the position of the silt patterns on the surface of Howe Sound. The studies described in this thesis attempt to relate these three factors to variations not just in the silt patterns, but also in the water currents, both in the surface layer and deeper.

I.3 A Brief Background Of Estuarine Theory And Forced Circulation Dynamics

The history of the theory of water movement in fjords is almost as long as the history of oceanographic observations in the fjords. The intense stratification in many of the Scandanavian fjords led to some work around the turn of the century on internal waves (for example Ekman (1904)). Theories were advanced to predict the periods of both surface and internal seiches in fjords. Zeilon (1913) used measurments made at Bornö on the Gullmar fjord on the west coast of Sweden to verify his seiche theories.

Studies of circulation dynamics in fjords have developed along roughly the same lines as have studies of ocean dynamics. Traditionally, theories of estuarine circulation based on analytical models have tended to be steady-state and laterally homogeneous. The first such model came from Cameron (1951), whose model had constant eddy viscosity and an imposed velocity profile. Stommel and Farmer (1952) developed a two-layer model primarily to look at steady-state upper-layer dynamics. Rattray and Hansen (1962) described a similarity solution for estuarine circulation that included a steady wind stress in the surface boundary conditions. Rattray (1966) modified this solution to fit the specific case of fjord circulation. This latter model allowed the eddy viscosity to vary as a function of depth and distance along the fjord. More recently, Pearson and Winter (1975) have used the method of

weighted residuals to solve for modally decomposed velocity and density distributions in a fjord. A comprehensive description of the basics of estuarine circulation is given by Dyer (1973).

Other dynamical descriptions based on detailed observations have indicated, as have many recent oceanic experiments (for example MODE, the Mid-Ocean Dynamics Experiment), that variations about the mean are much larger than the mean itself. Some of these observers have looked at changes in the circulation caused mainly by the wind. Tully (1949) noticed that in Alberni Inlet, the surface layer depth could be increased by more than a factor of two during a period of up-inlet winds. He also remarked on the lack of lateral homogeneity of the surface flow field near the head of the inlet. Johannessen (1968) performed a regression analysis between current meter data from Drøbak Sound in the Oslo fjord and the square of the wind speed there. Although his results showed that the winds were responsible for about 67% of the variations in the current at one meter, they also showed that the correlation between the current and the wind 10 hours previously was about twice as good as that between the current and the wind with zero time lag.

Farmer (1972) was able to reproduce variations in surface layer depth in Alberni Inlet with a linear model using the square of the measured windspeed with a constant drag coefficient to model the surface wind stress. His results also showed large variations in surface layer depth as a function of time.

It has been said that, in the deep ocean, the variations in mean flow contain about one hundred times the kinetic energy of the mean flow (W.H.Munk,1975). Experiments over the last few years have provided a wealth of data to back up this statement, and now general models of oceanic circulation are being developed based on this idea (e.g. Stern(1975)). Circulation dynamics in fjords may have a similar relationship between mean and variations although the details of both parts of the circulation are quite different from the oceanic case. However, studies in fjords have not progressed as far as those in the deep ocean.

In this thesis I shall examine current data for temporal and spatial variations and attempt to relate these to various factors. While it would be premature to attempt to build a complete, consistent model of fjord circulation based on the available data, I will try to justify several existing models of fjord dynamics and attempt to coalesce them into a more consistent picture of the circulation dynamics of a fjord.

CHAPTER II

SURFACE LAYER FLOW - EXPERIMENT AND DATA ANALYSIS

II.1 A Preliminary Experiment

A small scale experiment was performed May 25 - 26, 1972 to determine the feasibility of tracking surface floats photographically. The site chosen to take the photographs from was Stawamus Chief, a flat-topped mountain near the head of Howe Sound (shown in figure 3). From the top of this mountain, 610 m above Squamish harbour, there is a clear view of the entire head of Howe Sound from the Squamish river to Woodfibre. The floats used were of a standard design used for aerial photography of water movement. They were as large and as brightly coloured as was practical, being made from coloured polyethylene sheets stretched over 4ft X 16ft frames of cedar. These floats proved to be extremely awkward to handle from a small boat and were almost impossible to launch or recover if the wind was blowing with much strength. This design was deemed unsatisfactory for future experiments without substantial modification.

The attempt to track these floats photographically was an almost total failure. Several 35mm cameras were used with several types of colour film including Infrared Ektachrome,

in order to discover which film, if any, was the best. It was necessary to use wide angle lenses in order to get at least one shore feature in each picture for absolute positioning of each float. The floats proved to be too small. At a range of 2km, they only subtended an angle of 8 min. In the most successful film, using the wide angle lens, 1.2 km of actual distance was represented by 1 cm on the negative. On this scale, each 5 m float was only 40 micrometers long. This length is not much different from the grain size of the film, so there was not much hope of reliably finding floats on the negatives under less than ideal circumstances. Use of a much larger negative size such as the size used in aerial photography would of course have helped cure this problem, but was not attempted because of other problems outlined below.

The observing conditions were often less than ideal. Sun reflections obscured the water surface most of the afternoon. The rest of the afternoon and most of the evening the surface was hidden underneath a thick blanket of "Woodfibre fog", i. e. smoke from the pulp mill. Only partially greater success was had at night, when each float carried a flashing light. In one 10 minute time exposure a faint streak that showed the position of one float could be found.

The experiment was not a total loss however. Somewhat greater success was had in tracking the floats with a transit. In the period from 1553 to 2314 on May 25, a total of 5 floats were tracked. A plot of the five float tracks is

shown in figure 3 . Their average speeds and directions are shown in table I. floats Y1, P1 and Y2 appeared to be caught

Table I

Average speed (cm/s) and direction (degrees true) of floats launched May 25, 1972 in Squamish harbour. The float positions were measured with a transit. The tracks of these floats are shown in figure 3.

float	time		average	
	start	finish	speed	direction
Y1	1556	1605	36	50
P1	1726	1913	9	20
Y2	1836	1938	5	105
G	1945	1947	24	175
N	2234	2315	17	210

in a back eddy of the river going into Squamish harbour. Floats G and N were carried along in the main flow of the river. These data are too sparse to interpret the flow field in the harbour from them alone. However, they are consistent with the field suggested by the silt patterns in the water and with the subsequent measurements made in the fourth week of the main experiment.

Even though tracking by transit proved to be marginally successful, it did not fulfill the basic criterion of

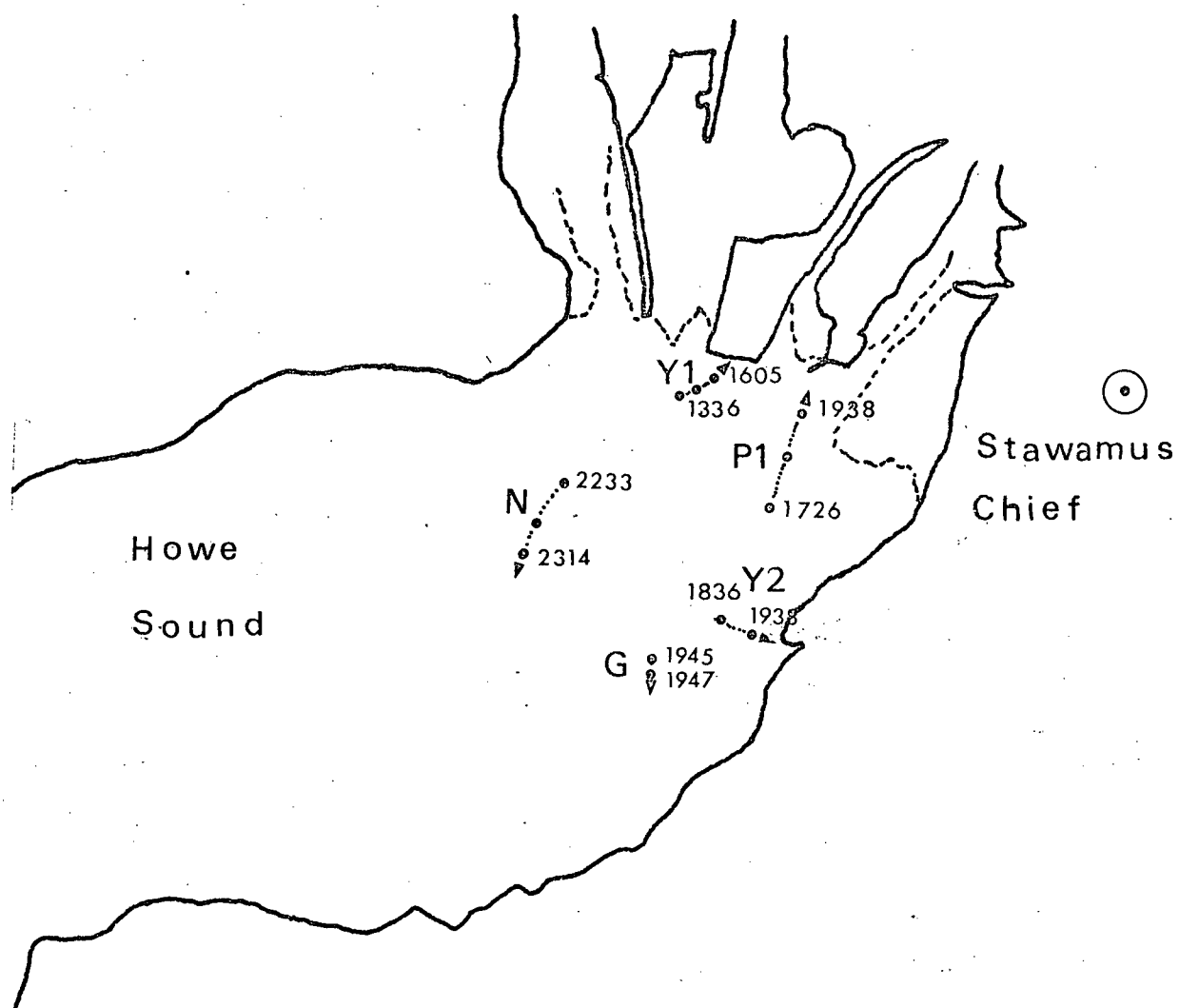


Figure 3 - Float tracks from the preliminary experiment. The letter in each float designation refers to float colour i.e. G-green, Y-yellow P-pink N(night tracked). Stawamus Chief (el. 610m) was the observation site.

tracking up to 50 floats continuously for a few days. Although the results from this experiment were largely negative, they were useful in designing the major surface layer experiment that is described in the rest of this chapter.

II.2 Main Experiment

II.2.1 Introduction

The major experimental effort took place in the spring and summer of 1973. The experience of the previous spring led to a complete redesign of the drogues to a form much more easily manageable from a small boat, much less affected by wind and more visible. Since optical tracking of the drogues had proven to be unreliable, they were tracked by a radar set mounted on the shore. Each drogue carried a radar reflector and was therefore visible to the radar set through most obscuring atmospheric conditions. These drogues were also more optically visible than the previous design: depending on conditions they could be seen up to one mile away in either daylight or darkness. As many drogues as possible were deployed as simultaneously as possible in the area of observation. A number of small vessels were used to deploy the drogues and to retrieve those that had left the area of observation. Data were recorded by photographing the Plan Position Indicator (PPI) screen of the radar set both with still and with movie cameras. The resulting still photographs were later digitized for further processing. Radar tracking of drogues has been done before with some success, for example by Kenney (1972), but the problems associated with attempting the experiment in a large, open

area with swift currents like Howe Sound, for such an extended length of time, make this experiment somewhat different from previous ones. A more complete description of the experiment follows.

II.2.2 The Droques

The drogues that were used in this experiment were designed and built at IOUBC specifically to fit the needs of this project. The basic design is shown in figure 4 .

The drag element of the drogue was of the window blind style as described in Terhune (1968). His tests of its performance showed that this type of drag element aligns itself at right angles to the flow after travelling two or three times its own length and from then on maintains the same orientation (within about 10°) to the flow. This window blind, also referred to as a sail, was 10ft wide by 6ft deep (about 3m by 2m), constructed of Polyweave, a flexible fabric woven of polyethylene fibres laminated between thin sheets of polyethylene. This fabric is quite tear resistant and durable. It was stapled to a fir 2 X 2 (5cm by 5cm) on the top edge and had a 1in diameter steel reinforcing rod sewn into the bottom edge for ballast. The sail was attached to the float pole by snap hooks that clipped into nylon rings in the centre of the top and bottom bars. Short lengths of braided nylon cord tied onto the reinforcing rod were used as ties to secure the sail into a roll for storage.

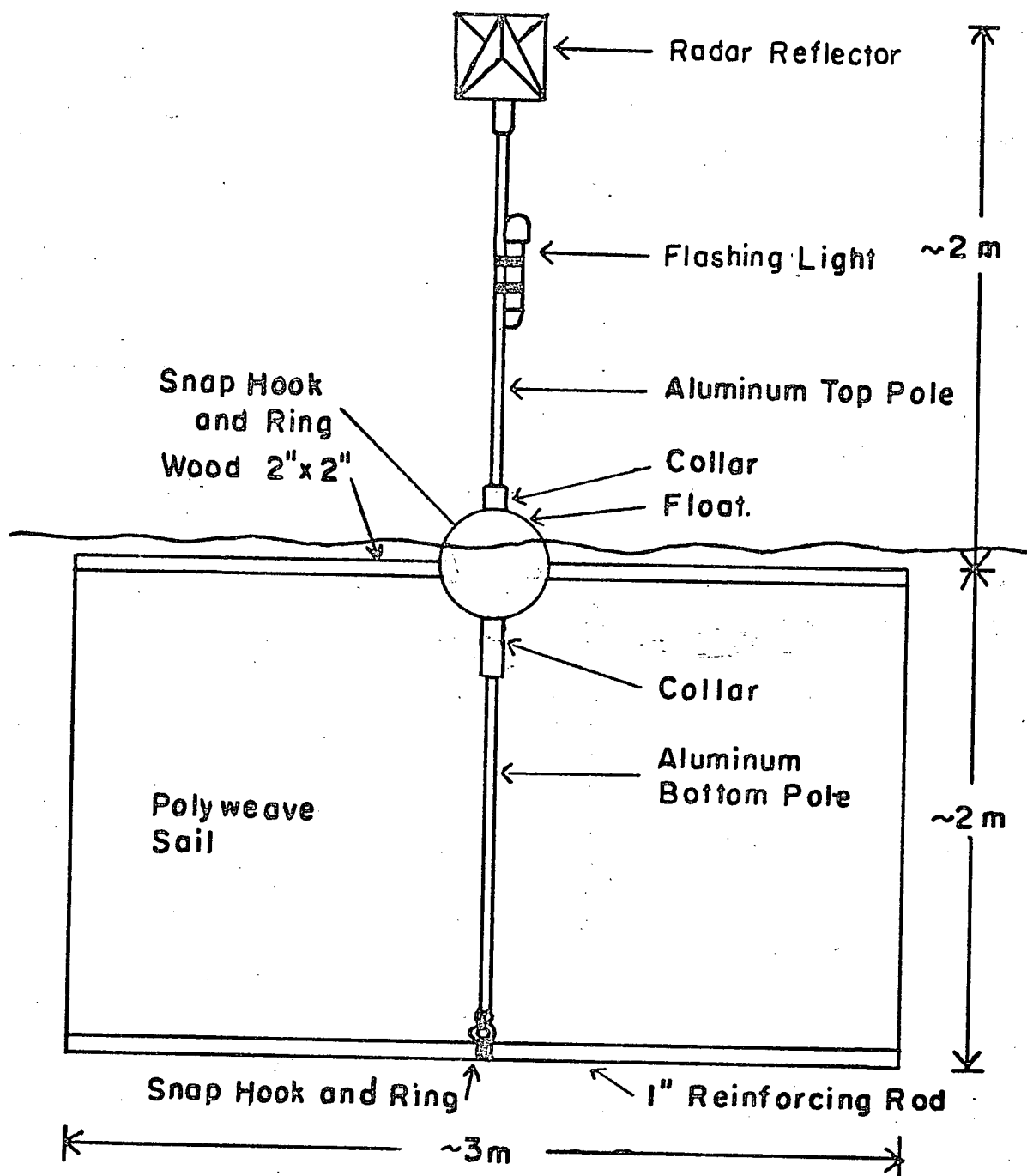


Figure 4 - Basic design of the drogues.

The vertical support element, the float pole, was an aluminum pole 1.050in OD, 12ft long, split into two parts near the centre. A 1ft long piece of 1.350in OD aluminum tube was used as a collar to hold the two pieces together. A swivel snap hook was bolted to the bottom of the bottom pole to connect with the bottom bar of the sail. The collar was pop riveted to the top of the bottom pole. The top pole was held in the collar by a 0.125in X 2.5in cotter pin. Approximately 14in up the top pole from the highest position of the collar was a machined aluminum collar placed to prevent the float from riding up the pole. At the top of the top pole, another collar of 1.350in OD tube held a 9in radar reflector. The reflector was mounted with one corner reflector pointing vertically. This arrangement was suggested in Wylie (1968) as being the way of mounting an octahedral cluster that gives the optimal response. There is a large variation in the strength of radar echo as a function of angle with the reflector mounted in this manner, as is shown later in figure 7, but the average response is greater than for any other orientation of the reflector.

The float used was a 14in OD hollow vinyl sphere with a hole through the middle, (brand name Viny, type 12B3). The bottom end of the top pole passed through this hole before being pinned into the collar. Thus the sphere was firmly attached between the two sections of pole. A loop of braided nylon cord was placed around the float, held in place by the pole top and bottom, with a snap hook tied to its centre. This hook engaged the ring on the top of the sail. A 12ft

piece of 1/4 inch diameter single braided polypropylene rope with a loop in each end was attached by one loop to the top snap hook. This rope floated on the water's surface and provided a means to recover the drogue without having to bring the vessel too close. Details of the construction of the drogues are shown in figure 5 .

For ease of transportation, the drogues were carried in four sections; the float, the top pole and reflector, the bottom pole and the rolled sail. They were deployed by assembling the sections of pole, clipping the bottom snaphook to the ring on the reinforcing rod of the still rolled sail, then lowering the drogue into the water while unrolling the sail and finally clipping the top snap hook into the ring on the 2 X 2 just before releasing the drogue into the water. In this way the large surface area of the drogue was never exposed to the wind and hence was not too difficult to handle. Recovery was the reverse procedure of installation.

II.2.3 The Base Station - Radar And Cameras

The base of operations for this experiment consisted of the radar transceiver and antenna, a shelter containing the radar display, the cameras and a two-way radio, and the necessary generators and living quarters.

The radar set that was used was a standard marine unit, a Decca RM916. The antenna was a vertically polarized 6ft long, end-fed, slotted waveguide. It was mounted together

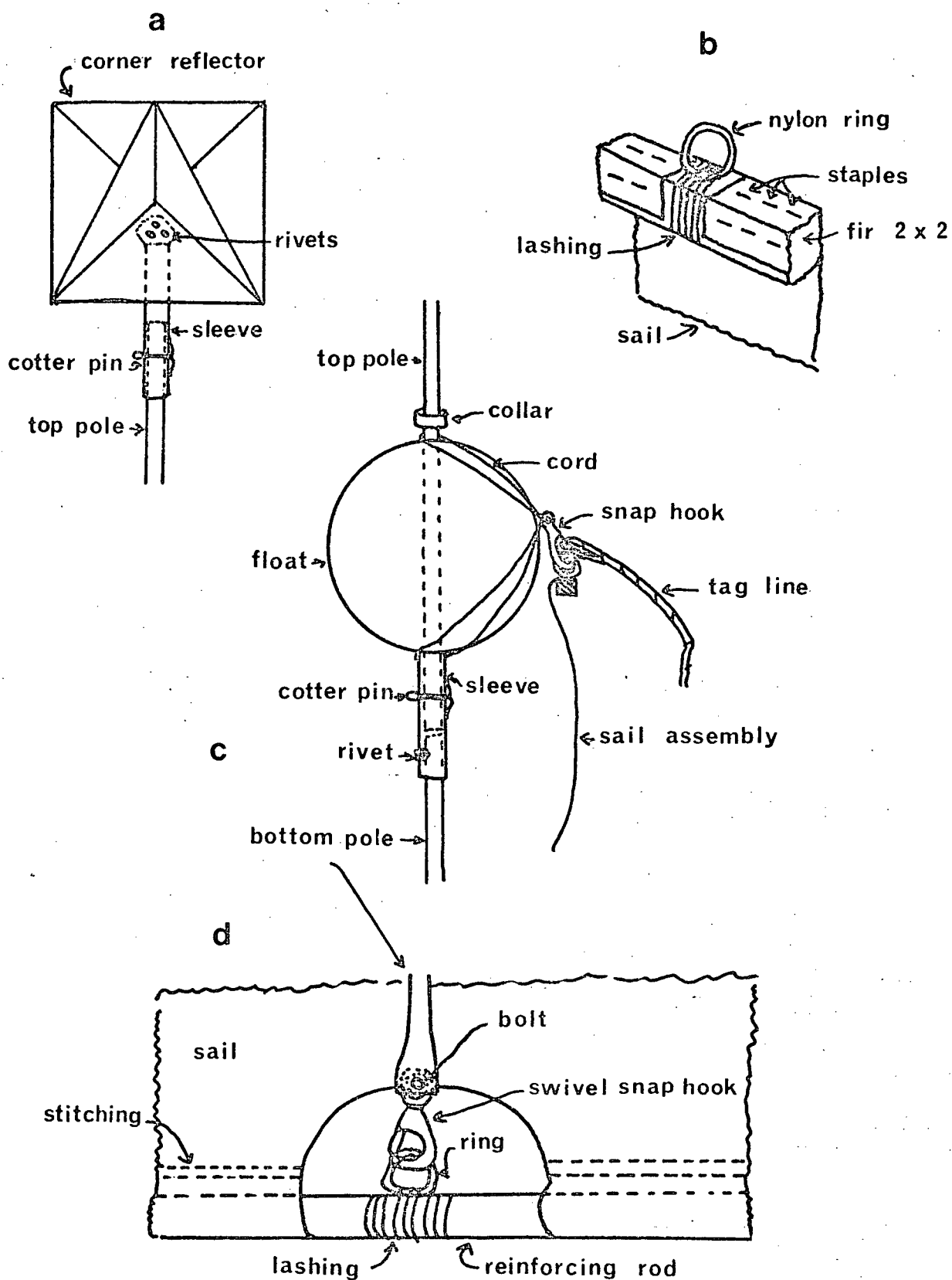


Figure 5 - Details of drogue construction. a. Attachment of the radar reflector. b. Top of the sail assembly. c. Float assembly. d. Bottom of the sail assembly.

with the transceiver on an aluminum quadropod with legs of adjustable length that kept the scanner 6 to 15 feet above the ground. The display unit was a 9in PPI cathode-ray tube whose image was refreshed every 2.14 seconds, in synchronization with the rotation of the scanner. The transmitter sent out 850 pulses per second at 10 GHz. The receiver was able to detect the drogues reliably to a range of about 2.5 nautical miles and usually out to 3 miles. This short range forced the experiment to be split into four sections, each one covering an area in Howe Sound six miles long. The four sections are identified throughout the thesis as: week 1, based at Britannia Beach from May 8-11, 1973; week 2, at Woodfibre, May 15-18; week 3, at Furry Creek June 26-29 and week 4 north of Watts Pt. July 3-6. These sections are shown in figure 6. The antenna had a horizontal beam width of 1.2° to the half power points yielding a minimum spot width on the PPI screen of 120m at three miles. The 0.75 microsecond pulse length yielded a spot length of 225m. The resultant absolute accuracy of the drogue positions will be discussed in the data analysis section.

Based on preliminary tests it was expected that each drogue would not necessarily paint a spot on the screen on each rotation of the scanner. This expectation was borne out, especially at long range. To reduce the chance of missing a drogue when photographing the screen, approximately six sweeps of the radar scanner were included in each frame by leaving the camera shutters open for 12 seconds. The lens apertures were set by trial and error; the

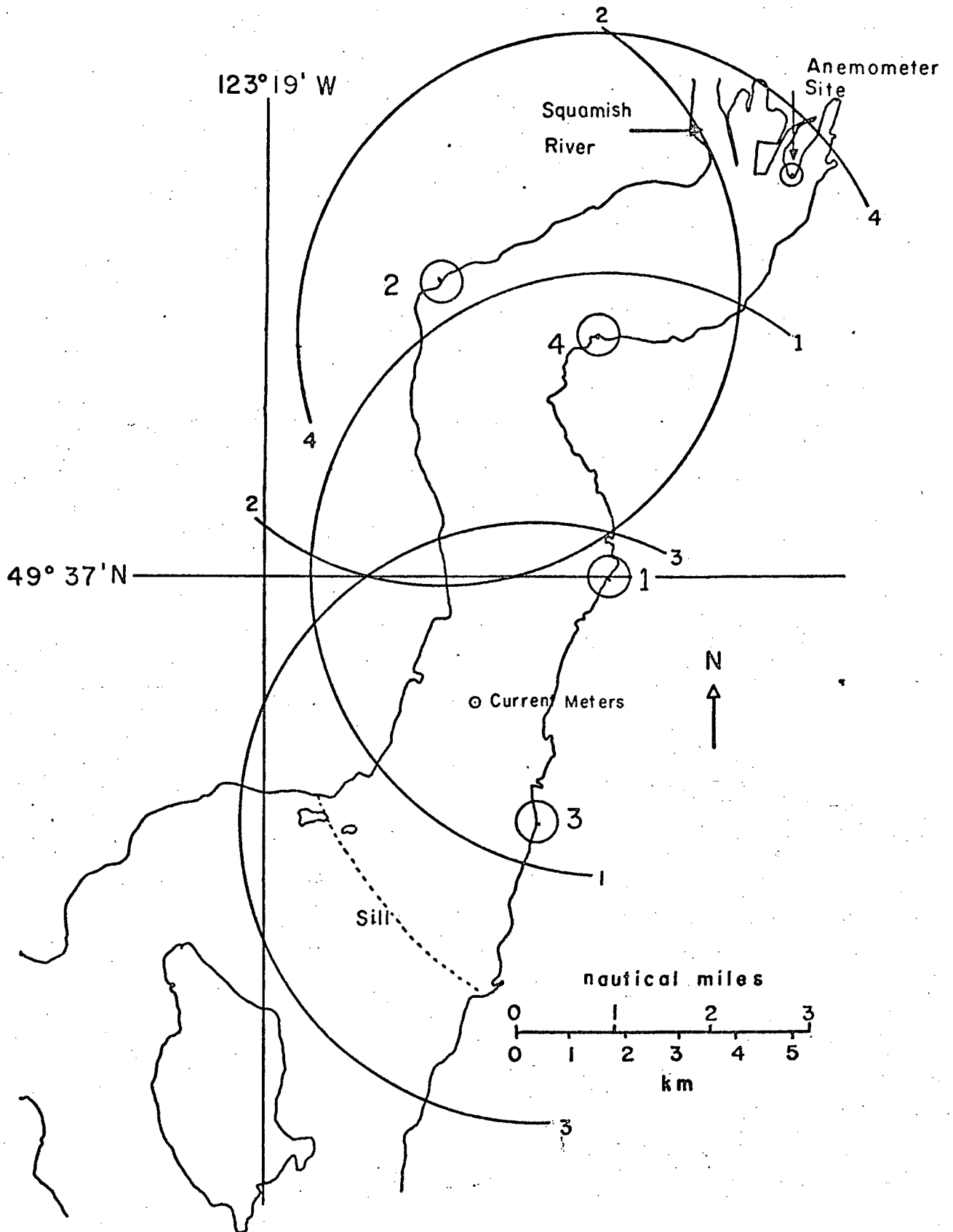


Figure 6 - The location of the four weeks of radar sites, the current meters and the anemometer in Squamish. The small circles with numbers are the radar sites, the large circular sections are 3 mile ranges about each one.

still camera usually to f11 and the movie camera usually to f16.

The still photographs were taken with a Hasselblad 500C 70mm camera with a 100mm lens and a closeup ring. Kodak Plus-X Pan film was used in 12 exposure rolls. Pictures were taken manually by holding the shutter open for about six sweeps approximately every 20 minutes whenever the radar screen was as unobscured as possible by rain or other interference. When the movie camera failed late in the experiment, still pictures were taken every five minutes.

Movies were taken with a Bolex H16 Reflex 16 mm camera using Kodak Tri-X Reversal film. One 12 second exposure was made every 30 seconds in the first two weeks and every 15 seconds in the last two weeks of the experiment. This sequence was controlled by a mechanical timer and a solenoid driving the remote cable release of the camera.

There was a watch taped to the radar screen to record on each negative the time of the photograph. Exposure quality was controlled by shooting at least one test roll of film a day on the still camera using various aperture settings, developing it at the radar site and then setting the aperture to the setting that produced the best contrast on the test roll. The movie camera aperture was determined from this test roll also. It was set to the still camera value plus some offset that was determined by shooting a movie test strip once or twice a week.

II.2.4 Vessels, Communications And Logistics

Due to the small experimental area and the sometimes large water velocities, it was necessary to keep at least one vessel at work at all times. In all, four different vessels were used in the experiment. The main vessel used was the "Active Lass", a 42 foot long converted fishing boat provided to us with her skipper, Mr. Sandy Matheson, for all four weeks of the experiment by the Pacific Environment Institute, West Vancouver, B.C. They also provided us with a 23ft stern drive Sangstercraft for the entire experiment. IOUBC provided a 21ft outboard-powered skiff. The Pacific Biological Station of the Fisheries Research Board, Nanaimo, B.C. provided the "Caligus" with her skipper, Mr. Ron Page, for the final week of the experiment. Dr. John Sibert and Dr. Robert Parker of PBS took part during this week on Caligus. An extra skipper was hired for the Active Lass to enable her to be run for two shifts a day.

The vessels operated in staggered 8 hour shifts, the Active Lass on both night shifts since she was equipped with radar to track drogues and avoid floating logs, and the Sangstercraft, Skiff and Caligus at various times during daylight. With the exception of the three skippers and the PBS scientists noted, the vessels were manned entirely with IOUBC personnel. In the four weeks of the experiment, virtually all the Physical Oceanography graduate students and technicians saw service either on the vessels or at the radar site.

Each section of the experiment was scheduled to take place in a five day week. The first day was spent moving equipment to the radar site, assembling the radar station and loading the vessels with drogues. The actual operation began in the morning of the second day. The radar operator instructed each vessel to place drogues spaced about $1/4$ mile apart across the inlet. These cross-inlet lines were spaced about $1/2$ mile apart along the inlet. About 20 drogues were initially deployed in this manner. As the drogues moved with the flow, the vessels were dispatched by the radar operator to retrieve the drogues whose images were about to leave the radar screen and to install more drogues in gaps in the array as seen on the radar screen. The operator attempted to keep as many drogues in the water as possible. This process continued until the morning of the last day when a final cleanup of drogues commenced. Thus a total of 72 hours of continuous measurements per week were possible. Of course, in practice the operation did not go nearly this smoothly, as is mentioned briefly in chapter IV, but this description is the basic plan by which each week of the experiment was run.

II.3 Analysis Of The Droque Data

The computer analysis of the still photographs of the radar screen was a complex procedure that can be broken down into two major parts; the calculation of the droque tracks and the subsequent Lagrangian and Eulerian analysis of the data. In the following paragraphs, the problems of analysis in each part will be discussed as well as the computer programmes used to solve them.

The Hasselblad photographs formed a record of 829 pictures each of which contained the radar images of boats, barges, floating logs and trees, gulls, aeroplanes, waves and rain as well as drogues. A sample picture from the radar screen is shown in figure 7 . It was necessary to differentiate between the images wanted and those not wanted. There was, of course, no way to tell one drogue from another in each picture except by pattern similarity from one picture to the next. Repeated viewing of the movies of the radar screen, although they were often underexposed and slightly out of focus, gave a good sense of the general pattern of the circulation and was of great help in following the drogues from one picture to the next. The installed position of each drogue as recorded in the log sheets usually identified it in the first picture in which it appeared. This was often sufficient information to allow a drogue to be followed along its complete track once its positions were digitized and in a form compatible to the PDP-12 computer at IOUBC.

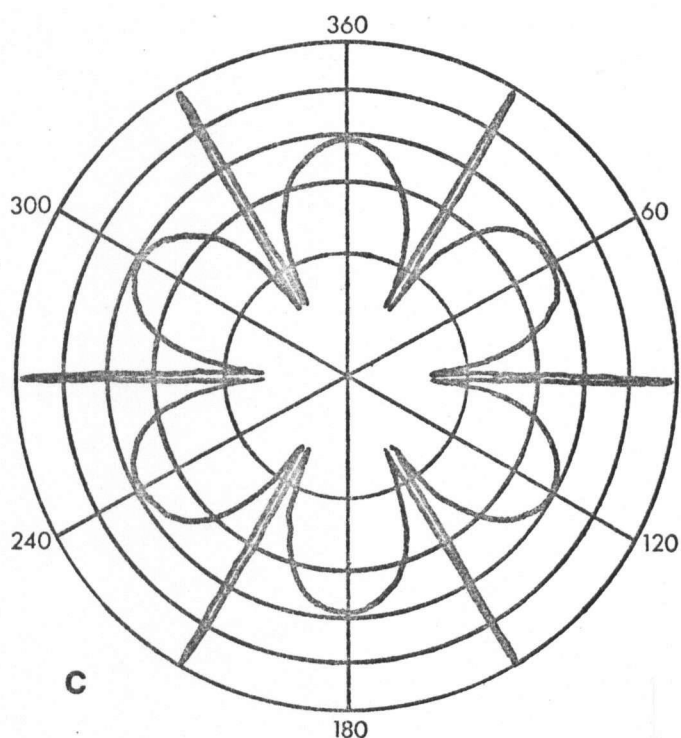
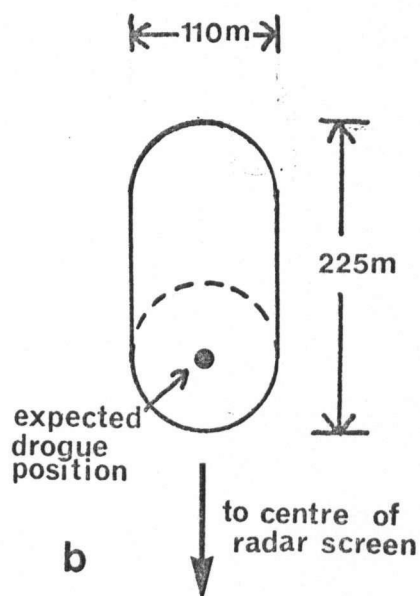
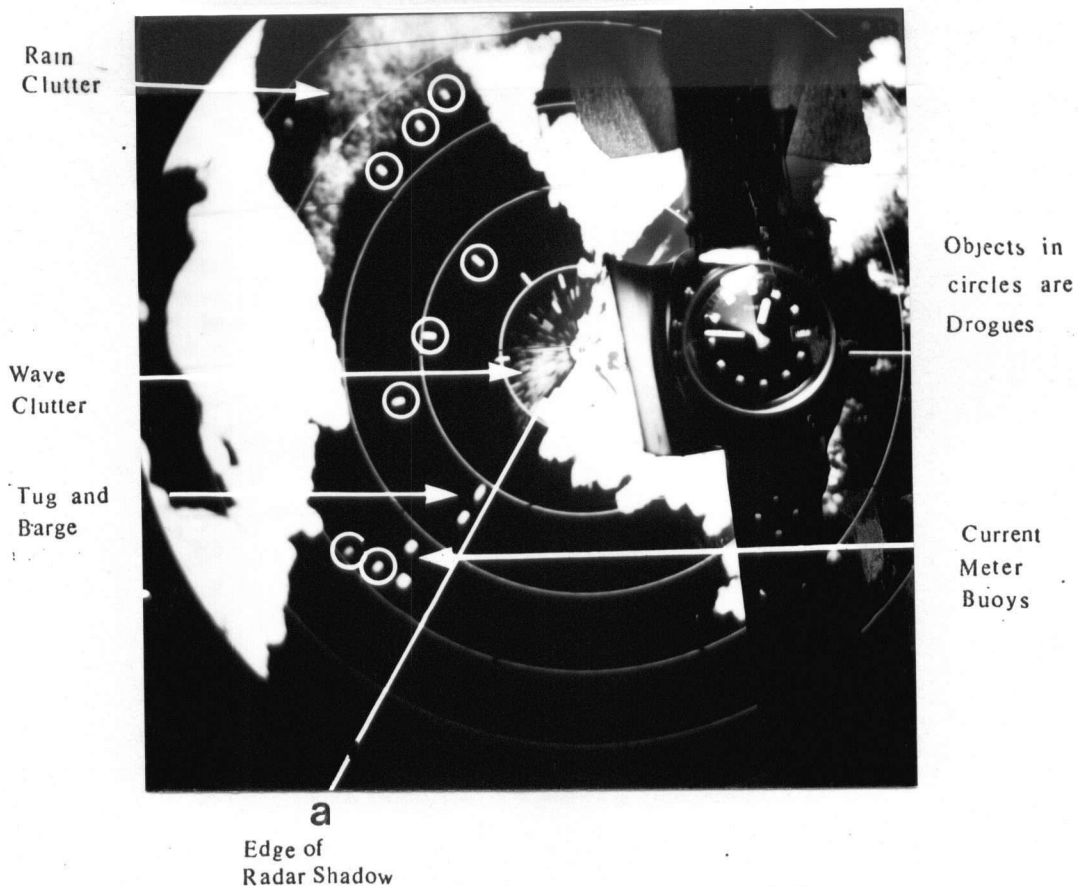


Figure 7 - a. Typical photograph of the radar screen from the week 1 data set at 1246 May 10, 1973. b. Shape of a drogue echo on the radar PPI screen indicating expected location of the drogue in the echo. c. Relative response of an octahedral cluster radar reflector as a function of angle in the horizontal plane (from Wylie (1968)).

The pictures were digitized by projecting each Hasselblad negative onto a 25in square sheet of graph paper and recording, on a keypunch coding form, the position of each object that might have been a drogue. The positions of the radar site and one other fixed point on the shore were also digitized. The true positions of these last two points were used in subsequent programmes to scale and orient each picture.

The accuracy of the graph paper was checked by plotting a 25.00in square on it using a Calcomp incremental plotter. The plotter was reputed to be accurate to 0.01in. The eye could detect no difference between the 25in square ruled on the graph paper and that plotted on it by the Calcomp. Distortion in the optical system was checked by photographing the digitization grid with the Hasselblad and projecting the resulting negative back onto the grid. No differences between the grids were found, hence there was no detectable optical distortion in the system. The projected image of the radar screen approximately filled the 25in square making the scale of digitization $1.0\text{in} = 0.24\text{mi}$. Thus a typical drogue echo of dimension 120m by 225m as discussed previously actually covered an area of $0.27\text{in} \times 0.51\text{in}$. The assumed position of the drogue in this echo was at the centre of a circle of the same diameter as the spot width centred at the radar set end of the echo. This position is shown in figure 7b. The expected accuracy of such a determination is about $\pm 30\text{m}$. This was the point that was digitized as the drogue. Accuracy of the digitization

operation was about ± 0.02 in or $1/5$ of the smallest division on the graph paper. This corresponds to ± 9 m at the scale mentioned above. Thus the major source of error in locating a drogue is in the location of the drogue within its echo, not in the actual digitization of the chosen spot.

Programme PRE12 on the IBM 370/168 took the digitized data set from each week and produced a file of object positions arranged picture by picture on a magnetic tape in a form suitable for input to the PDP-12 at IOUBC. This output tape contained a digitized outline of the shore in the appropriate area of Howe Sound, followed by a number of records each describing one digitized photograph. The shore was scaled so that the six mile radar image diameter just filled the 512 by 512 unit CRT screen of the PDP-12. This programme accepted as input for each week the true distance and direction of the vector from the radar site to the calibration point. For each picture a vector was calculated from the radar site to the calibration point on that picture. The difference between these two vectors was used to determine the rotation, translation and scaling necessary to convert the digitized image positions to true positions. The total error in each object position was therefore the sum of the errors in determining the positions of three different points, the radar set, the calibration point and the object point. This error amounts to at most $3 \times 30 \text{ m} = 90 \text{ m}$. These true positions in nautical miles were then scaled again by a factor of $512/6$ to place them in screen coordinates. A record was written on magnetic tape

containing the roll and negative number of the picture, the time and date, the positions of the radar site and of the calibration point (for transform verification purposes), the number of objects digitized and that number of four element sets each containing the X and Y coordinates of the object and two identification words (now blank because the objects were not yet identified on the computer).

This tape, called IN, was transported to the PDP-12 where it was copied onto a data disk. This data disk was the input/output file for programme MAP5 which allowed all of the digitized objects to be identified. It continuously displayed the shoreline on the CRT screen and also displayed, one at a time, each digitized picture.

Each digitized object had two identification words associated with it. The first was used to identify the general type of the object as either a drogue that could be positively identified, a drogue that could be identified only as part of a discontinuous track, or something that was not a drogue. This word also contained the drogue track status: if this was the first point on the track, the last point or some intermediate point. The second identification word contained the drogue number. In the case of a positively identified drogue, it was the drogue number recorded in the log book. In the case of a tentative identification, it was a number chosen to be unique to that track during the time it could be followed. These words were accessed by the value of an externally controlled potentiometer on the PDP-12 that was used to construct the

address in the computer memory of these words. Changing the potentiometer setting allowed all identification locations to be examined, one at a time. When a digitized object location was selected by the potentiometer for examination, that object was intensified on the screen and the contents of its identification words were displayed. Both of these identification words were set by commands from the computer console keyboard when the pointer indicated that object. In such a fashion, information was transcribed from the log sheets and the tracks already identified on the prints to the computer. When it seemed as if all possible tracks were identified, a magnetic tape called OUT was written from the disk file and taken back to the IBM 370/168, the main computer at the University of British Columbia.

The next programme in sequence, called POST, took the identified photographs, discarded the non-drogues, sorted the drogue positions into a sequence of individual tracks and scaled the positions back to miles from screen units.

This output file of drogue tracks was the input to a programme called SPLN1 that took each track and fitted it by means of a cubic spline interpolation and smoothing routine.

This routine, supplied by the UBC Computing Centre was modelled after the one described in Reinsch (1967). In this routine the calculus of variations is used to construct a function $g(t)$ that minimizes $\int_{t_0}^{t_m} g''(t)^2 dt$ subject to the condition that

$$\sum_{i=1}^n ((g(t_i) - f(t_i)) / \delta f(t_i))^2 \leq S \quad (2.1)$$

where $\delta f(t_i)$ is the expected error of the i 'th input point $(t_i, f(t_i))$ and S is a positive definite quantity chosen from the range $n - \sqrt{2n} \leq S \leq n + \sqrt{2n}$. The solution $g(t)$ is then the smoothest function that satisfies the total least square error criterion. The value chosen for S controls the total amount of deviation allowed from the input values. The value of $\delta f(t_i)$ controls the effect of a single deviation. Since in this experiment all the $\delta f(t_i)$'s were chosen to be the same size, they have a similar effect on the smoothness of the fit as does S and hence the two criteria interact strongly, i. e. a small $\delta f(t_i)$ requires a large S for smoothness of the fit and vice versa. The solution is of the form

$$g(t) = a_i + b_i(t - t_i) + c_i(t - t_i)^2 + d_i(t - t_i)^3 \quad (2.2)$$

$$t_i \leq t \leq t_{i+1}$$

Conditions on this solution are that g , g' , and g'' are continuous at $t = t_i$ but that g''' need not be. Using the values for a_i , b_i , c_i and d_i calculated in this manner, values for $g(t)$, $g'(t)$ and $g''(t)$ may be calculated for $t_i \leq t \leq t_{i+1}$.

This routine was used twice on each drogue track, once to fit the x co-ordinate of drogue position as a function of time and once to fit the y co-ordinate. Thus, in the x co-ordinate fit, $x(\text{digitized position}) = f(t)$, $x(\text{interpolated}) = g(t)$, $u = g'(t)$ and $a_x = g''(t)$. Similarly, when $y(\text{digitized}) = f(t)$, $y(\text{interpolated}) = g(t)$, $v = g'(t)$ and $a_y = g''(t)$. The interpolated results were recombined to

provide the smoothed drogue tracks. The errors δx and δy (equal to $\delta f(t_i)$ in their respective fits) necessary for the routines were chosen by trial and error to be as small as possible and still produce smoothly varying accelerations. The resulting value for these errors of $\pm 0.05\text{mi}$ ($\pm 90\text{m}$) was somewhat larger than the expected uncertainty of the data due to the resolution limits of the radar set and to digitization errors. The value of S was chosen to be quite small ($n - \sqrt{2n}$) and so the error had to be larger than expected to allow a smooth fit. The error amounted to about 1% of the total radar range. The spline fit produced the positions, velocities and accelerations for each drogue for each minute along its track.

These data were written in different forms on two different magnetic tapes. The first, called the DATA1 tape, contained records of drogue position in miles from the radar site, velocities in m/s, accelerations in m/s^2 and time as they were generated in programme SPLN1. The second tape, the BRUSHPLOT tape, contained the same data but with the values of position, velocity and acceleration in both co-ordinates for each track scaled to exactly fit the range of the digital to analogue converters on the PDP-12. The UBC Computing Centre programme *SORT was used to sort the data set on DATA1 into temporal order and write it onto a tape called DATA2. The programme MOVIE took this sorted data set and sectioned it into one minute intervals. All the positions in each section were scaled to PDP-12 screen coordinates. Another magnetic tape, called MOVIE1, was then

written from these records in a format similar to that used for the original input to MAP5 . Thus this tape contained one "picture" per minute throughout the whole experiment.

The two magnetic tapes, MOVJET and BRUSHPLOT , were both brought back to the PDP-12 . The scaled drogue tracks were played with programme D-A onto a six channel Brush chart recorder. Each of the six channels on the recorder displayed one of x or y position, velocity or acceleration. Here any abnormally large accelerations or velocities or rapid changes in either could be seen easily. The MOVJET tape was played back on the screen by means of a special display mode of programme MAP5 that displayed several pictures simultaneously on the CRT screen. After holding the frame steady for a short time, the oldest picture was dropped from the screen and replaced with the picture one minute later than the latest one already on the screen. This procedure was carried out many times in rapid succession until the input tape was completely read. This created the effect of a moving "worm" on the screen whose length and orientation indicated the speed and direction of drogue motions. Any large anomalies in the flow field could be detected by watching this movie. Any errors detected by either of these techniques were then corrected by looking for mistakes in drogue identification in the data set manipulated by MAP5 . When these errors were corrected, more acceleration plots and another movie were generated and again checked for errors.

A few times through the loop of error checking produced

for each week a consistent and smoothly varying flow field as determined by the drogue tracks. It is of course possible that this sort of subjective error finding technique might smooth over some true details of the flow field. Small details such as these could only have been determined accurately if pictures had been taken more frequently.

A flow chart of this data processing and verification procedure is shown in figure 8 .

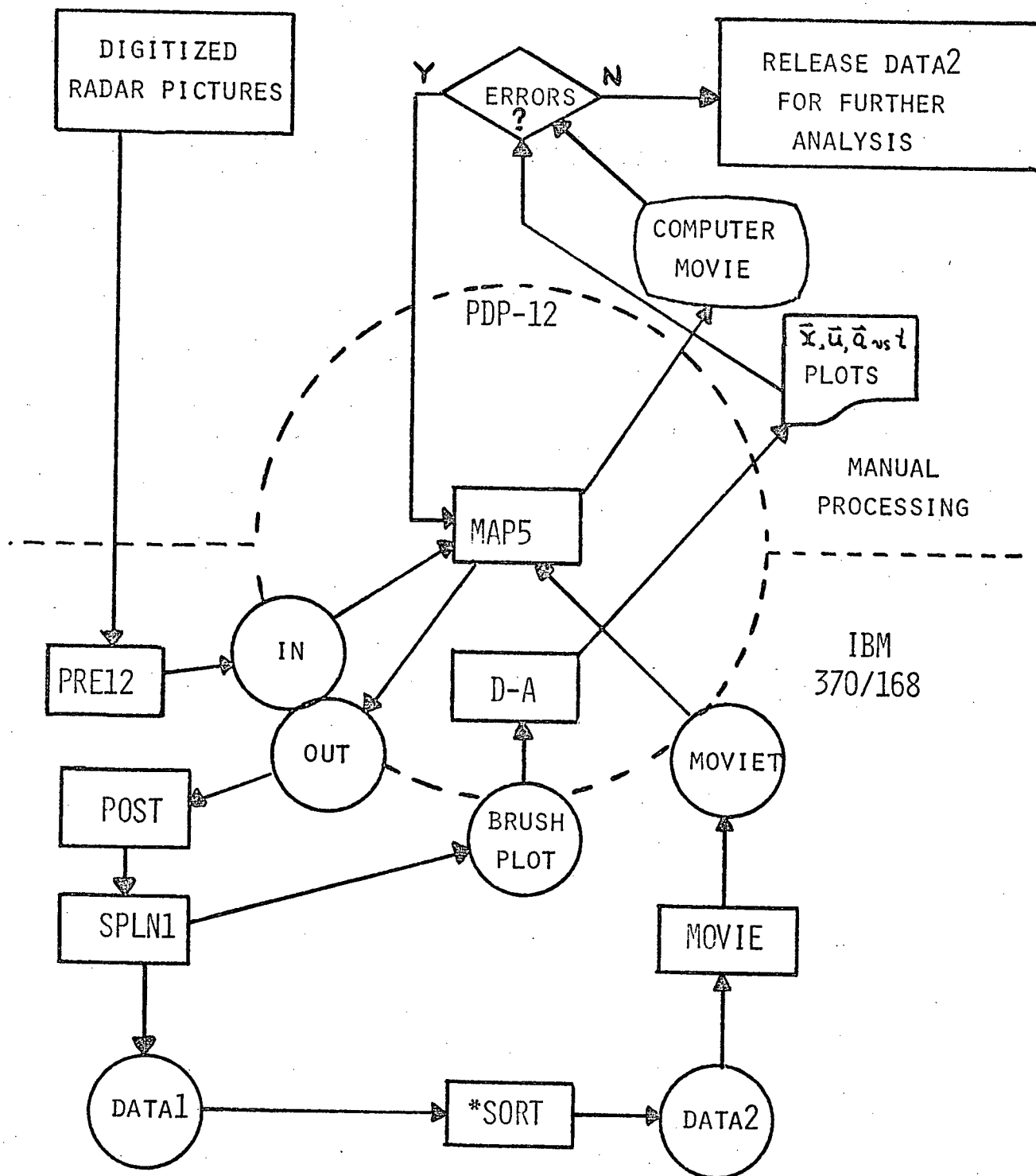


Figure 8 - Flow chart of the data analysis and verification procedures. Boxes represent computer programmes or manual procedures. Circles represent magnetic tapes used to transfer data between the different environments.

II.4 Data Averaging - A Problem Of Lagrangian Measurements

The drogue tracks that resulted from the previously mentioned series of computer programmes provide a data base far too large to look at on an individual track by track basis. It was necessary to average the data in some meaningful way to reduce the 250,000 interpolated data points to a consistent picture of the flow field of the Sound.

A problem arises in determining what sort of averaging procedure should be used to best deduce the mean Eulerian velocity field from a Lagrangian data set. Analytic averaging techniques that could be used are: temporal averaging, as defined by:

$$\overline{u_L} = (1/T) \int_0^T u_L dt \quad (2.3)$$

and spatial averaging as defined by:

$$[u_L] = (1/X) \int_0^X u_L dx \quad (2.4)$$

where u_L is the observed Lagrangian velocity. Under most circumstances, neither of these averages will correspond to the true Eulerian mean field as may be seen by considering the two following examples.

In the first case, the velocity field is homogeneous in space but varying in time. Because of the spatial homogeneity, the drogue velocity shows the same time variation as the Eulerian velocity and hence

$$u_L = U + u'(t) \quad (2.5)$$

where U is the Eulerian mean velocity of the field and $u'(t)$ is the time varying part. For example,

$$u_L = 2 + \sin t \quad (2.6)$$

$$\begin{aligned} \bar{u}_L &= (1/2\pi) \int_0^{2\pi} (2 + \sin t) dt \\ &= 2 \end{aligned}$$

but

$$[u_L] = (1/X) \int_0^X (2 + \sin t) dx \quad (2.7)$$

Since $u_L = dx/dt$, then $dx = u_L dt$ or $x = \int_0^T u_L dt + c$ so $x=4\pi$ at $T=2\pi$. Thus,

$$\begin{aligned} [u_L] &= (1/4\pi) \int_0^{2\pi} (2 + \sin t)^2 dt \\ &= 2.25 \end{aligned} \quad (2.8)$$

In the second case, considering an Eulerian velocity field dependent only on position, the drogue velocity will

have the same spatial variation as the Eulerian velocity and

$$u_L = U + u'(x) \quad (2.9)$$

For example

$$u_L = 2 + \sin x \quad (2.10)$$

$$\begin{aligned} [u_L] &= (1/2\pi) \int_0^{2\pi} (2 + \sin x) dx \\ &= 2 \end{aligned}$$

Since $u_L = dx/dt$, then $t = \int_0^x \frac{dx}{u_L}$

$$t = \int_0^x (dx / (2 + \sin x)) \quad (2.11)$$

$$= \frac{2}{\sqrt{3}} \left\{ \tan^{-1} \left(\frac{\tan(x/2) + 1}{\sqrt{3}} \right) - \tan^{-1} \frac{1}{\sqrt{3}} + n\pi \right\}$$

where n is a number such that

$$(n-1)\pi < x < (n+1)\pi$$

thus when $x=2\pi$, $t = 2\pi/\sqrt{3}$ and

$$\begin{aligned} \bar{u}_L &= \frac{\sqrt{3}}{2\pi} \int_0^{2\pi} u dx / u \\ &= \sqrt{3} \end{aligned}$$

So in the first case

$$\bar{u}_L = U, [u_L] > U \quad (2.12)$$

and in the second

$$\bar{u}_L < U, [u_L] = U \quad (2.13)$$

Of course a geophysical flow will be neither totally time dependent nor space dependent, but, in general, \bar{u}_L will usually underestimate the true Eulerian mean velocity U , and $[u_L]$ will overestimate it. Data collected in the style of the experiment performed in Howe Sound are recorded at constant intervals in time. Therefore any averaging that is done will be a form of time average and the results will approximate \bar{u}_L . Thus mean velocities calculated from the data set without regard for its Lagrangian character will probably underestimate the true mean velocity.

A.J.Dyer (1973) attempted to find a general analytic form of transformation of Lagrangian averages into Eulerian averages, but in examining analytic descriptions of various Lagrangian fields, was only able to find analytic transformations in a few cases. He concluded that if a general analytic transformation exists, it is far from trivial.

Webster and Curtin (1974), in the process of analysing a large Lagrangian data set similar in character to the Howe Sound data describe a form of approximate transform that tends to minimize the difference between Lagrangian space and time means and hence produce a mean velocity closer to the Eulerian mean. They divided their experimental area into a number of small "boxes" and averaged the data separately in each box. The final average of the data was then

calculated as the average of the box averages without regard for the number of observations in each box. This process has some of the character of a time average and some of a space average and may be therefore be expected to yield a value that overestimates \bar{u}_L and underestimates $[u_L]$. Since it is expected that

$$\bar{u}_L \leq U \leq [u_L] \quad (2.14)$$

the box average \bar{u}_g should be a reasonable estimate of U .

The problem remains of choosing the "correct" box size to obtain a best estimate of U . The maximum size the box can be is the total experimental area. This would yield $\bar{u}_g = \bar{u}_L$. As the box size is made smaller and the number of boxes increased, \bar{u}_g should increase up to the point where each box contains only drogues of the same approximate velocity. At this point, further subdivision should not affect the value of \bar{u}_g greatly. If the box size is made too small however, there will be, on average, very few drogues in each box, so that statistically, each average will not be very reliable. Thus the occasional anomalous value could affect the mean of the box averages more greatly. Therefore the optimum box size is governed by the scale of variability in the flow and the number of observations available.

In order to keep all the measurements in each box relatively the same size, the box size must be small enough so there will be reasonably small velocity differences due to gradients in the box. The measurements that will be discussed in later sections show the downstream component of

velocity to change at a rate of between 11 and 18 cm/sec/km across channel and about 2.4 cm/sec/km down-channel. The approximate rate of change of velocity with time is 3 cm/sec/hr. The maximum r.m.s. velocities in this experiment are about 30cm/s, so if a change of 10% of this or 3cm/s is allowed across each dimension of each box, then a consistent size for each box is then 0.17 to 0.25 km across by 1.2 km down channel by 1 hour long.

In practice what was used for all quantitative results was 1/10 channel width (this varied between 0.2 and 0.3 km per box depending on week), by 1.8 km along channel by 1 hour (since the wind information was available only in one hour averages). This size is close to a consistent box as just defined.

For some of the more qualitative results to follow, a larger box size is used, up to 0.9 km by 0.9 km by 3 hours. In these cases, the velocities shown may be expected to be smaller than the true Eulerian velocities in the area, but still may be considered to be a useful indicator of the relative speed and direction of the drogues in the area at that time.

CHAPTER III

MEASUREMENTS OF WIND, TIDE, RIVER FLOW AND SURFACE LAYER
STRUCTURE

To form any conclusions from the results of this experiment, knowledge of the basic forcing functions was as essential as the knowledge of the flow field itself. In this chapter the techniques of measurement of the wind, the tidal height and the river discharge are discussed. The results of these measurements in the four weeks of the experiment are also presented. Another essential set of measurements was of the density structure of the near surface waters in the inlet. These measurements and results are also discussed in this chapter.

III.1 Wind Measurements

Measurements of wind speed and direction were made at two locations each week of the experiment. A Lambrecht recording anemometer was located at the radar site each week and recorded the winds there for the duration of the experiment. It had the disadvantage of being on shore and therefore of being more or less sheltered from the winds in the centre of the channel. The second source of wind measurements was the anemometer maintained by the Atmospheric Environment Service at FMC Chemicals, located

mid-channel at the head of the inlet in Squamish. The disadvantage of this location was its distance from some of the radar sites. An anemometer was also mounted on the current meter buoy located in the centre of the week 3 working area and would have been most useful if it had worked.

The data from Squamish were reported by AES in hourly total wind run in statute miles and average direction in compass octant. For purposes of comparison with this data set, the data from the Lambrecht anemometer at the radar site were converted to this format. A comparison of these data sets is shown in table II.

The shores of the northern basin of Howe Sound are quite steep, effectively constraining the wind to blow only along the axis of the channel. This constraining implies that the long-channel component of the wind is relatively uniform along the channel for periods of fluctuation of greater than one hour. The anemometer site in Squamish is located approximately mid-channel and therefore should be a good indicator of the of the wind velocity throughout the channel. The radar site anemometer locations, being on the shore close to the side walls of the fjord, are more sheltered. This sheltering effect is substantiated by the last row in table II which shows the percentage of the Squamish wind run that is seen at the radar site. Even in the best location (week 1) the radar site anemometer saw only 75% of the wind at Squamish. Weeks 2 and 4 indicated only a very small response to the wind at the radar site,

Table II - The total number of miles of wind from each compass octant that passed the anemometers at Squamish (SQ) and at the radar site (RS) for each of the four weeks. The totals are the total wind run for each week at each anemometer. The percentage is the fraction of the wind run at Squamish that was sensed at the radar site.

	week 1		week 2		week 3		week 4	
	SQ	RS	SQ	RS	SQ	RS	SQ	RS
N	46	24	48	6	21	78	0	0
NE	7	5	3	0	0	1	0	0
E	0	0	0	1	0	2	0	0
SE	3	31	0	30	0	65	0	1
S	171	13	155	8	107	301	134	6
SW	95	167	214	1	624	0	589	227
W	0	1	0	59	0	0	0	2
NW	6	6	7	7	10	0	0	0
total	328	247	427	112	762	447	723	235
%	75		26		59		33	

showing that they were particularly well sheltered. Thus it seems as if the wind as measured at Squamish may be a better indicator of the wind strength in mid-channel than that measured much closer to the area of experiment but on the shore. Since the winds are predominantly of a land-sea breeze nature, the winds at the head of the inlet should be expected to be somewhat stronger than they are farther downchannel. Thus some of the apparent reduction in wind strength from Squamish to the radar sites may be real.

Table II also shows that the wind is predominantly bi-directional as expected. The winds measured in Squamish never blow from the east or west. With the exception of week

2, the same is mainly true of the radar site winds. A rose of the percent of the total wind run in each octant throughout the entire experiment is shown in figure 9. It shows that over 93% of the total wind comes from either south or southwest and the remainder from the north, northeast or northwest. In an area of channel-like geometry, it can be assumed that the predominant winds are either up or down channel, i. e. cross-channel winds are very much weaker than long-channel winds. Therefore, the cross-channel component of the wind will be considered to be zero and hence all winds coming from the south or southwest will be considered to be the up-channel component of the wind. Similarly, since the land area north of Squamish funnels the wind into the fjord, all winds coming from the northwest, north, or northeast will be considered to be the down channel component of the wind. The same sort of division into components will be applied to the winds at the radar sites. The same angular criteria will be used for weeks 1, 3 and 4 except that winds from the southeast will also be considered to be up-inlet. In week 2 the problem is somewhat more difficult due to the location of the radar site on a sharp bend in the fjord at the base of a valley that contributed some winds from the west and northwest. For purposes of the present analysis, the winds from the west will be considered to be up-inlet.

A comparison of the wind data broken up into components as just described is shown in figure 10. The origin of the time axis for each week in this figure and in all subsequent

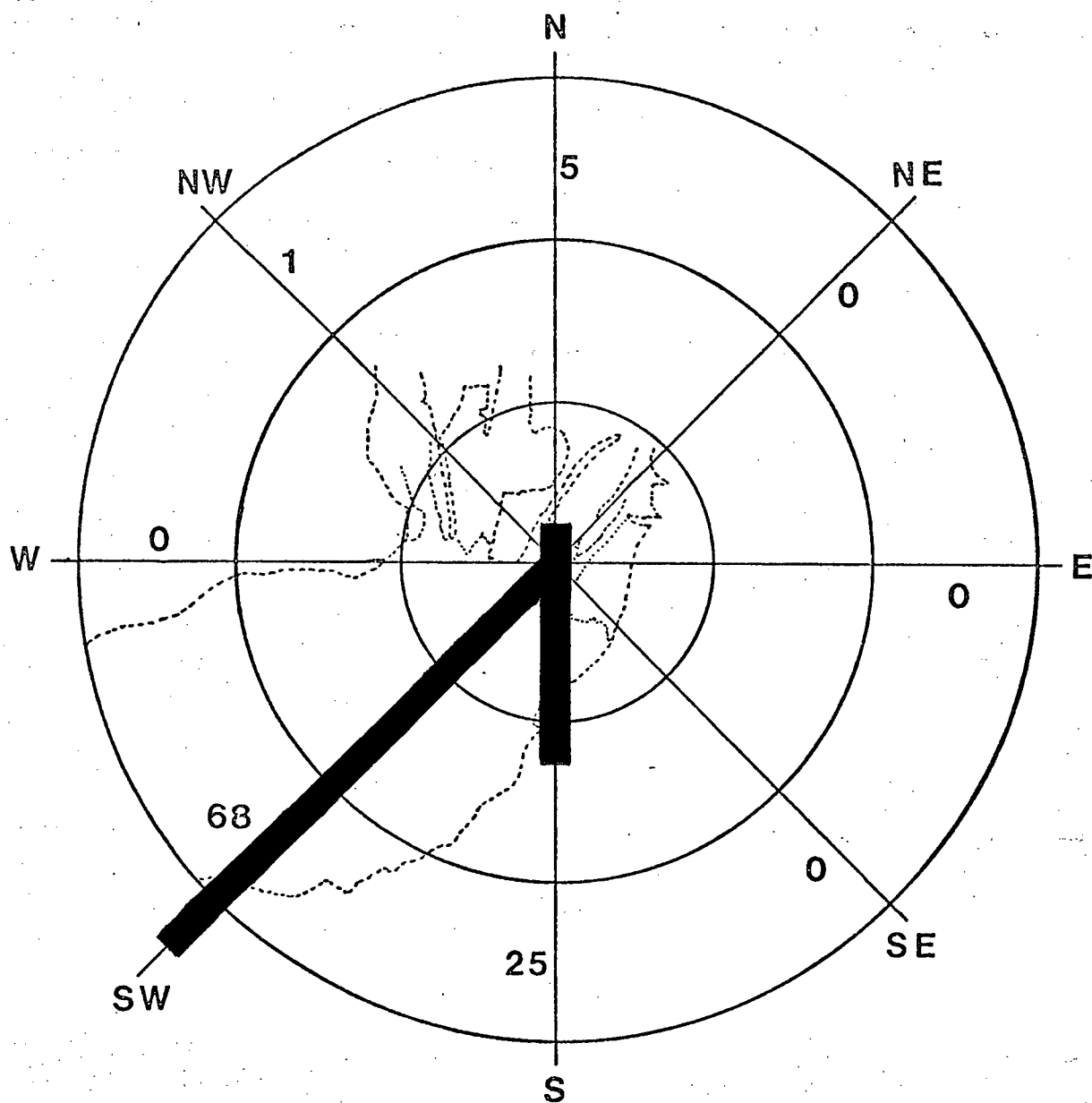


Figure 9 - A wind rose of the total wind run past the Squamish anemometer for the four weeks of the experiment. Direction is defined as the direction the wind came from.

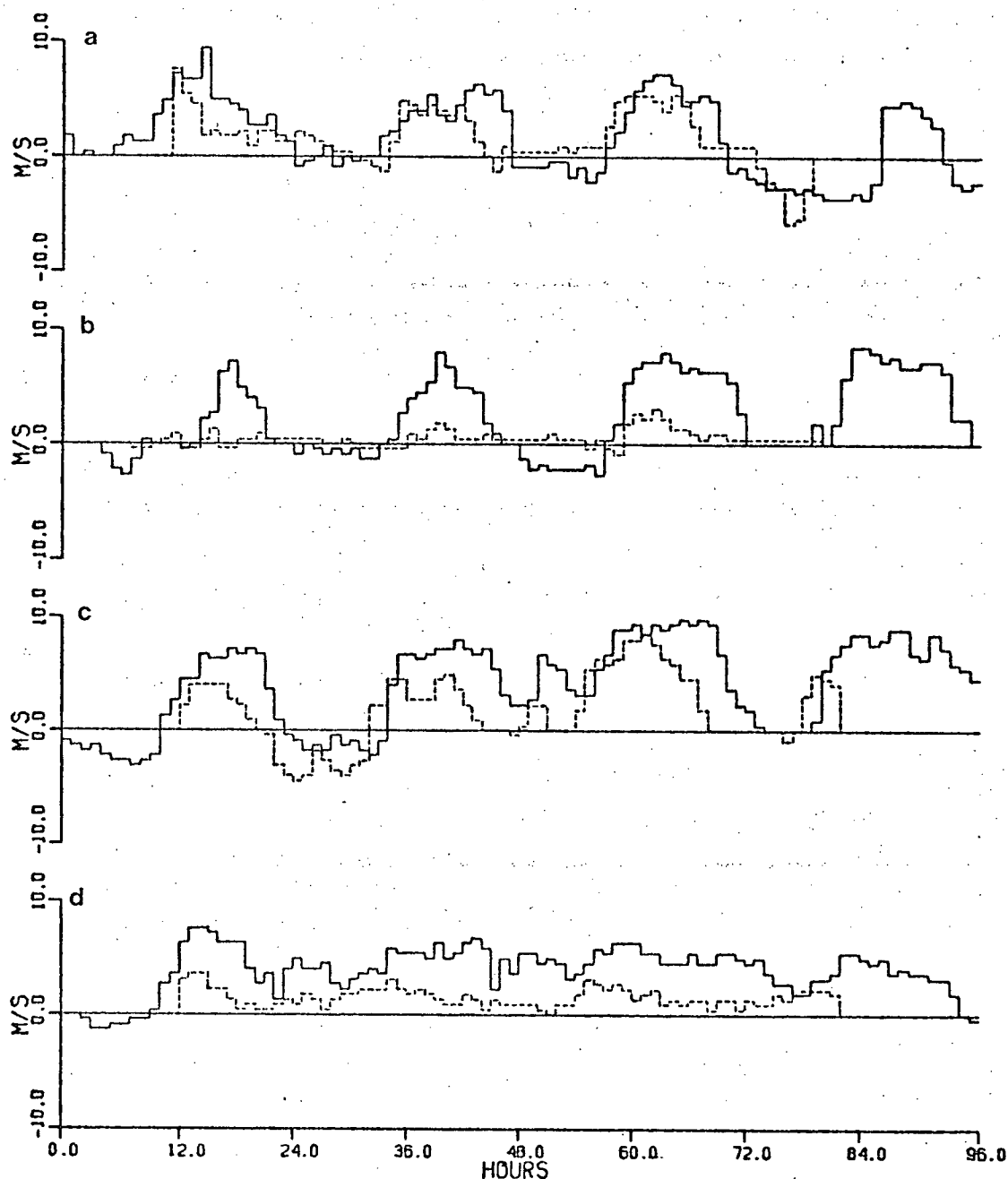


Figure 10 - Comparison between long-channel component of wind velocity as measured at Squamish (solid line) and the radar sites (dotted line) for the four weeks of measurement. a. week 1. b. week 2. c. week 3. d. week 4. Origin of the time axis is 0000h on the first day of expected observation each week. The same time origins will be used in all subsequent figures.

ones is at 0000h on the first planned day of observation in that week. Thus the time axes go from 0 to 96 hours. The radar site winds from weeks 2 and 4 can be seen to be much smaller than the corresponding Squamish winds as previously mentioned and so will be disregarded. Although the amplitudes of the winds in weeks 1 and 3 are somewhat less than those measured at Squamish, there is a general agreement between the radar site and Squamish in the phase and shape of the wind component vs time curves. For the sake of consistency in analysis of the four weeks of data, and because the data collected by AES in Squamish is, in spite of its limitations, the most generally representative that is available, the Squamish winds curves will be the ones used in the subsequent analysis.

III.2 River Discharge

Discharge of the Squamish River is measured at a gauging station at Brackendale, 17 miles north of Squamish. This gauge continuously recorded water level which was subsequently converted to rate of discharge on an hourly basis from tables provided by the Water Survey of Canada. The discharge of the Squamish River represents almost all of the fresh water input into Howe Sound and therefore the gauge records were taken as being indicative of the total fresh water input.

There were large variations in the discharge of the Squamish River from week to week but the daily variations

within each week were quite small. Figure 11 shows the discharge curve for each week. The average discharge each week is shown in table 3.

The large difference between the week 1 discharge and the week 2 discharge was caused by two intervening days of almost 30°C maximum temperature that seemed to signal the beginning of the major spring runoff peak. It can be seen in figure 11 that the period of variability in the river flow is approximately 24 hours, indicating that the variations are due to sun melting of snow in the Squamish watershed. This hypothesis is further borne out by the delay in time of maximum daily discharge from week 1 to the other weeks, indicating that, as the season progressed, the level of snow melting went from the lowlands to higher country that was farther away from the mouth of the river.

Based on an assumed surface layer depth of 4m and a channel width of 2.8km, the approximate mean surface layer velocity due to the river discharge may be calculated. The results of such calculations are shown in table III. In this table, the mean velocity is the discharge averaged over the total width of the channel. The mean core velocity is the discharge averaged only over the width of the river core, that part of the flow that moved down-inlet on average over the whole week. This core will be discussed later in chapter IV. The core velocity is more representative of the expected magnitude of the river flow in the inlet. In no case is the expected river velocity greater than 9cm/s, and therefore variations like those in week 4 of $65\text{m}^3/\text{s}$ could

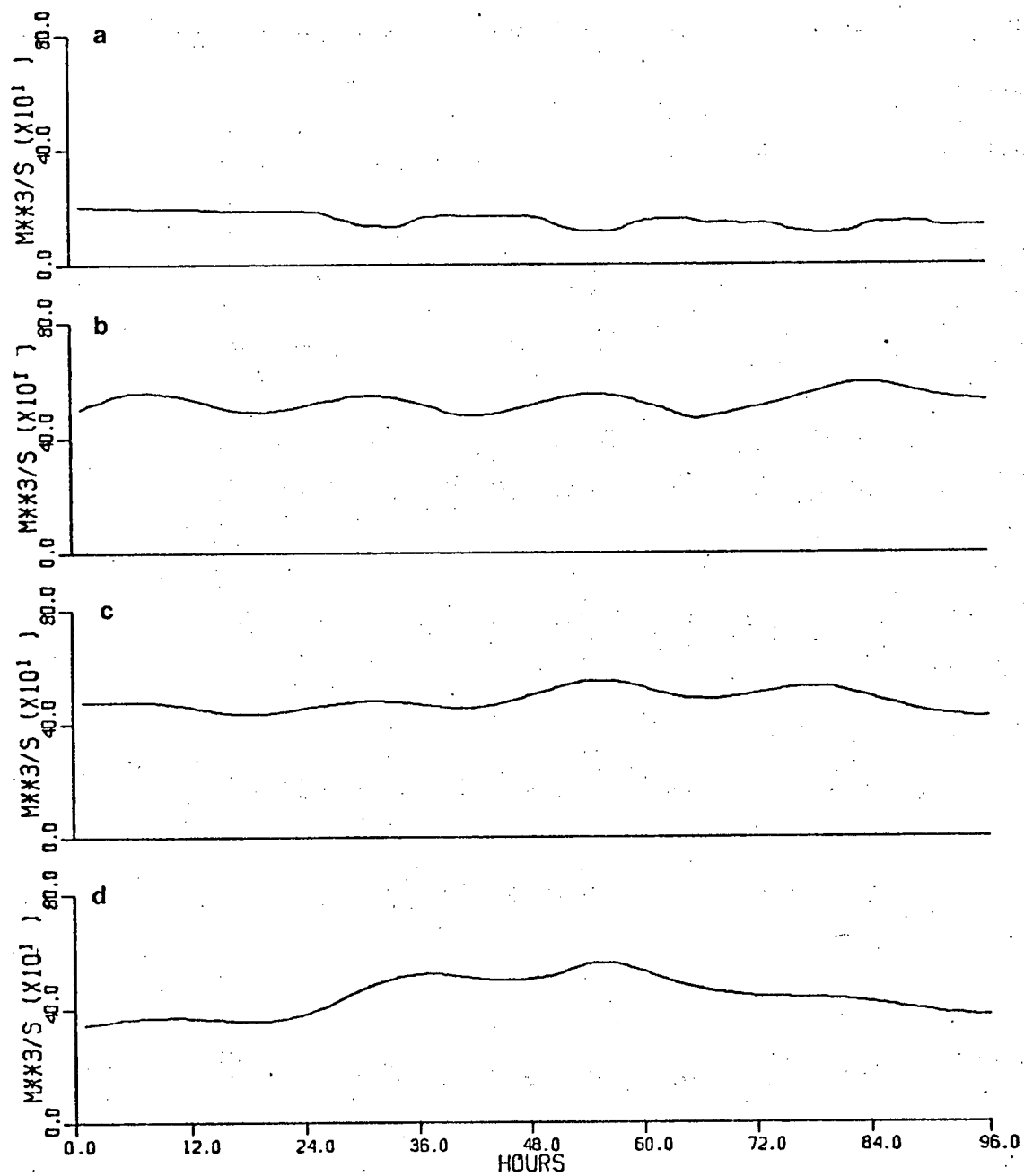


Figure 11 - River discharge for the four weeks of the experiment. a. week 1. b. week 2. c. week 3. d. week 4.

Table III - Mean river discharge and the resultant surface layer velocity taking entrainment into account. The mean discharge for each week is shown with its standard deviation. Percent entrainment means the amount of the saline deeper water necessary to give the river water the salinity observed on hydrographic cruises made before and after the experiment, expressed as a percentage of the volume of river water.

Week	discharge (m ³ /s)	entrainment %	mean velocity (cm/s)	mean core velocity (cm/s)
1	158±27	12	2	2
2	527±31	6	5	9
3	485±34	17	5	5
4	444±65	0	4	7

cause current fluctuations of no greater than about 1 cm/s. In light of the diurnal periodicity of the wind and the strong diurnal component in the tide, it seems unlikely that these daily variations in river discharge will have an observable effect on the surface circulation.

III.3 The Tide

It was not feasible to make recordings of tidal height during this experiment. Predictions of tidal height are made by the Canadian Hydrographic Service and published annually in their Tide Tables. Pt. Atkinson is a major reference port in their prediction scheme and therefore the predicted tidal heights there should be accurate to a few centimetres. Squamish is a secondary port in the predictions meaning that it varies in the same general manner as some reference port,

in this case Pt. Atkinson. Examination of the amplitudes of the tidal constituents at Squamish and Pt. Atkinson as provided by Dr. P. Crean of Institute of Ocean Sciences show differences of only a few centimetres and a few degrees in phase between the stations in all constituents. In agreement with this finding, the tide tables show only a four minute delay of high water at Squamish from Pt. Atkinson and a height difference of only a few centimetres. Such small differences indicate the absence of any barotropic tidal resonance in the main channel of Howe Sound joining these two tidal stations. Therefore the tidal height as predicted for Pt. Atkinson may be taken as being valid for the entire area of interest in the sound. A record of the tidal height at Pt. Atkinson was provided by Dr. P. Crean of Institute of Ocean Sciences containing four values per hour for the duration of the experiment. This record is shown in figure 12. The maximum range can be seen to be about 4 metres. Height changes of this magnitude occurred in about 6 hours once or twice each week. Since the experimental area is close to the head of the inlet, these large tidal height variations should not create large tidal velocities.

A simple barotropic tidal prism model predicts for a sinusoidally varying height change of 1.5m amplitude and 12h period a current amplitude across the sill (depth 70m) of 5.3 cm/s and of 1.5 cm/s just inside (depth 250m).

A slightly more complex model, discussed in more detail in chapter VII, taken from Rattray's (1960) work on generation of internal tides on the continental shelf, can

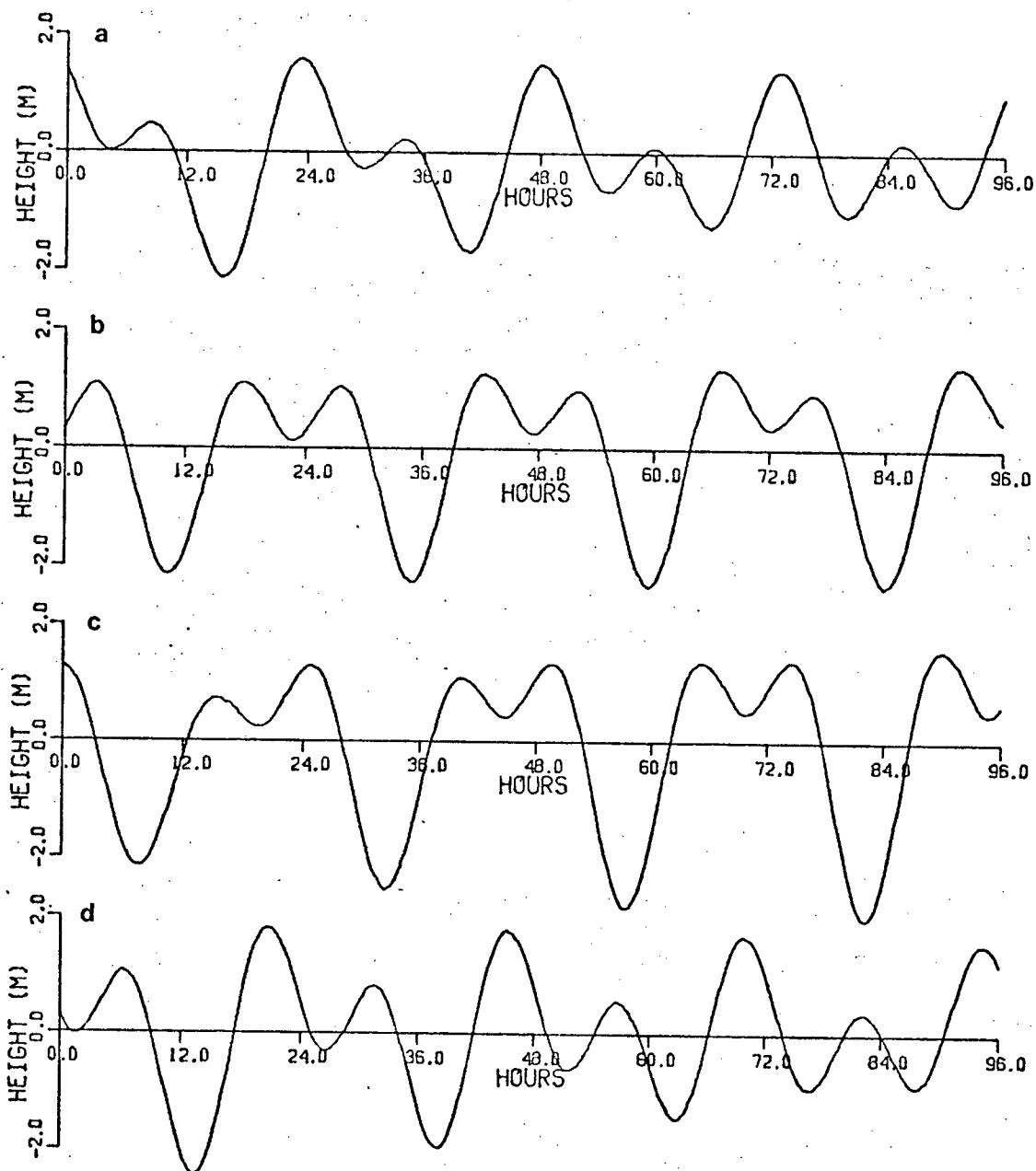


Figure 12 - Tidal height for Point Atkinson as predicted by the Canadian Hydrographic Service. a. week 1. b. week 2. c. week 3. d. week 4.

be used to calculate barotropic and baroclinic components of sinusoidally varying tidal velocity in a two layer system. Considering Howe Sound to be such a system with top layer thickness 5 metres, total depth 250m, sill depth 70m, and density difference of 2% between the layers. This model predicts just inside the sill a barotropic current amplitude of 1.7 cm/s and a baroclinic current amplitude in the surface layer of .8 cm/s. Halfway up the inlet, the same current amplitudes are .8 cm/s and 2.8 cm/s respectively. Thus the baroclinic component of the tidal current may be responsible for more than a negligible part of the observed current fluctuations at some points in the inlet.

Although both of these models are oversimplified, they indicate that the magnitude of the expected barotropic tidally induced currents is small in comparison with the speeds observed in this experiment. But the baroclinic tidal effects may be larger, so events having some steady phase relationship with the tide were looked for in the data analysis.

III.4 Density Measurements

The water in a fjord is often typified as being a discrete two-layered system with a small thickness of fresher water overlaying more saline deep water. There is often a very sharp interface between the two water types. Density profiles were made, in the latter two weeks of the experiment, of the upper 20m of the water column to ascertain the validity of this assumption in Howe Sound and to measure the depth of this "surface layer". Sets of five profiles were made from the Skiff or the Sangstercraft at equidistant points along several lines across the inlet. In week 3, two sets were taken along a line from the radar site across the inlet to the opposite shore. An Autolab 602 portable salinometer was used to make the temperature and salinity measurements. On the third set of profiles it broke, curtailing measurements for that week. In the fourth week, a Beckman RS-4 was used to make eight successful sets of measurements on lines crossing the inlet near the week 4 radar site. In each profile, measurements were made at one metre intervals from 0 to 5m, at 2.5m intervals from 5 to 15m and at 20m. At each location a bathythermograph cast was also made but the temperature structure alone gave little estimate of the density structure. Figure 13 shows salinity profiles taken in these cross inlet sections, one set for week 3 and one for week 4.

The upper set of profiles, taken near the sill, shows the stratification at its weakest: the lower set, taken near

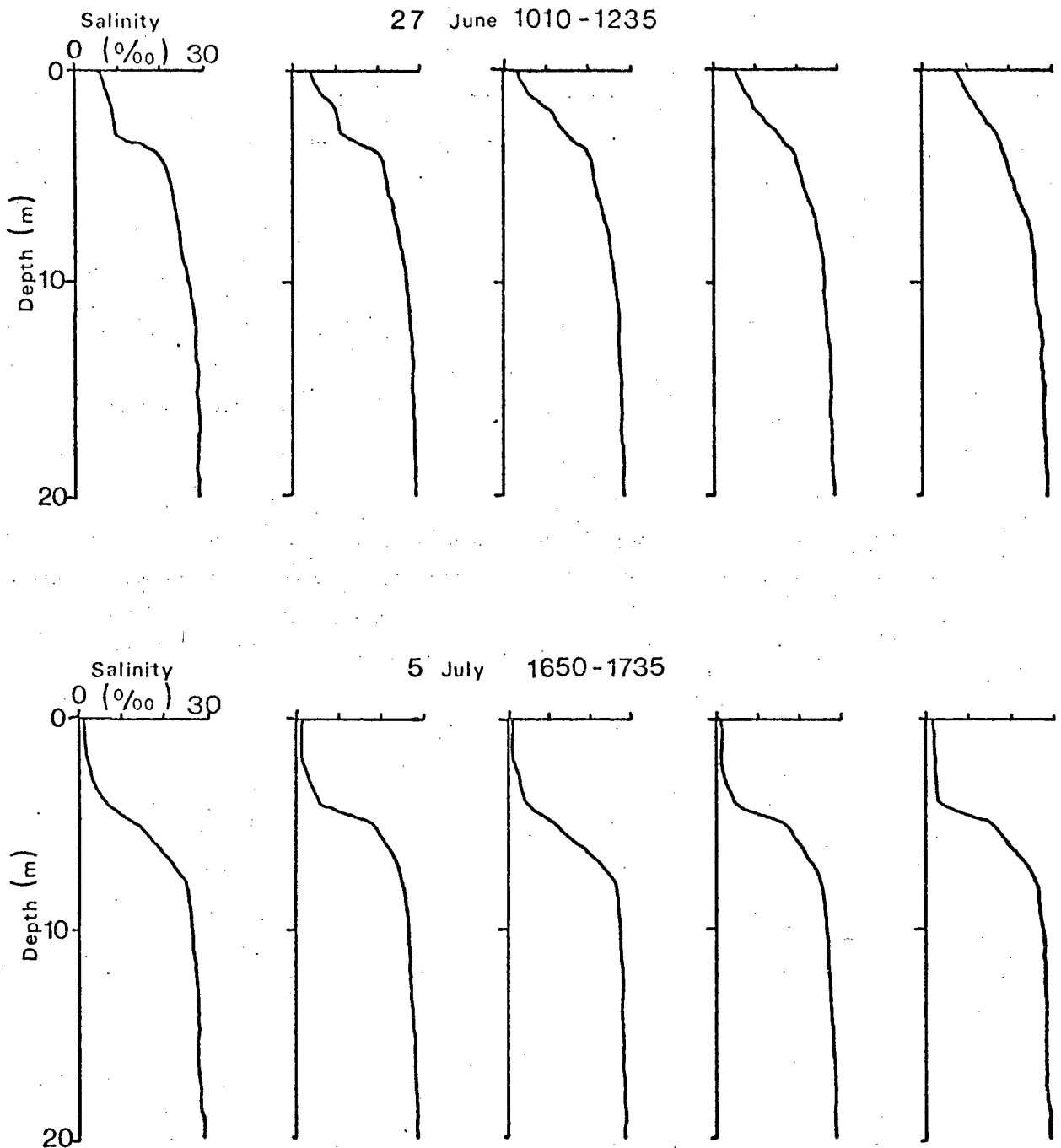


Figure 13 - Salinity profiles taken in two sections across the inlet. Progression from left to right is west to east. The section at the top was taken near the sill, the one at the bottom, near the head of the inlet.

the river mouth, shows it at its strongest.

In the case of the stronger stratification, the water column is fairly homogeneous to a depth of about 4m. Then the salinity increases rapidly with depth to about 8m, where the increase becomes more gradual. In the weaker case, on the west side, the salinity is relatively uniform down to 3m, then increases rapidly below that. However, on the east side, the halocline is right at the surface. In this location it is difficult to see any distinct surface layer.

In an attempt to quantify the surface layer of a fjord, Farmer (1972) defined an equivalent fresh water depth, F , for a water column as:

$$F = D - (1/S(D)) \int_0^D S(z) dz \quad (3.1)$$

where D is the depth of the water column under consideration and $S(D)$ is the salinity at that depth. This quantity represents the thickness that the fresh water layer would be if the water column were decomposed into two fractions, one completely fresh and the other as salty as the most saline in the water column. Table IV shows how this parameter varied for several cross inlet sections.

In this table, the stations are arranged with station 1 on the west and 5 on the east as in figure 13. The most striking feature of this table is the variation in the fresh water depth from one section to the next.

Farmer examined variations in this quantity in relation

Table IV - Equivalent fresh water depth (in metres) for several cross inlet sections. The 27 June sections were made along the same cross-inlet line. The July sections were all made along a different line much closer to the inlet head.

Date	time	stn 1	stn 2	stn 3	stn 4	stn 5
27 June	1100	4.0	3.9	3.9	3.6	3.5
27 June	1800	3.6	4.3	4.5	4.5	4.7
4 July	1030	4.6	4.8	4.9	5.1	4.9
5 July	1700	5.6	5.3	5.7	5.6	5.5
6 July	0930	4.4	4.8	4.8	4.5	4.8

to the wind. His measurements in Alberni Inlet showed that large variations in this parameter could be related to changes in the wind stress over the inlet and to the baroclinic response of the inlet to the tide. Thus, variations of this magnitude are not unexpected.

Another notable feature of this table is the definite gradient of fresh water thickness across the inlet that occurs in the first two sections. The deeper part of the layer is probably indicative of the presence of river water not yet mixed across the inlet. This river core appears to be on the west side of the channel in the first set of measurements and on the east in the second. River core movements of this type are not unusual and occur often on shifts in wind direction. A wind shift did occur between these two sets of measurements.

The most important conclusion, however, is that the layer depth is everywhere deeper than 2m, the drogue depth,

so that the drogues were, at the time of these measurements and, by extrapolation, throughout the experiment, in the surface layer as defined by the fresh water depth. It is, of course, quite possible that the velocity profile of the upper 20m of the water column would show a different structure from that suggested by the salinity profile. The depth of maximum velocity gradient need not be the same as the depth of maximum density gradient, or as the depth of the equivalent fresh water layer. Determination of the relationship between these parameters is beyond the scope of these experiments. It is likely however that the depth of maximum velocity gradient is below the bottom of the drogues. Observations of drogue tilt, as discussed in appendix I, and a comparison of drogue velocities with the velocity record from a 3 metre deep current meter, as discussed in the next section, validate this assumption.

For some later calculations it is necessary to provide some actual measure of the layer depth. Since measurements of the density profile were not made in the first two weeks and were sparse in the last two weeks, it is impossible to describe accurately the variations in the layer depth. The average depth as calculated from all the measurements taken was about 4.5m. Because of the large variations that were found around this mean, the accuracy of it must be taken to be about ± 1 m.

III.5 Comparison Of The Droque Velocities With The 3m Current Meter

A comparison between the water velocity as recorded by the drogues and by the current meter located at 3m depth at the location shown in figure 6 provides an interesting test both of the different methods of measuring current and of the conclusion that the effective surface layer depth is about 4.5m.

Only during week 3 of the experiment were there sufficient drogues in the vicinity of the current meter to allow a comparison with the current meter results. This comparison is shown in figure 14. In this figure, the current meter curves are drawn through component values calculated every 15 minutes, the instrument's sampling interval. The drogue curves were drawn through values calculated as the box average components of drogue velocities taken every 15 minutes from the spline fitted records in a box one mile square centred on the current meter location. The 15 minute interval was chosen to correspond to the current meter sample interval, the one mile box to contain enough drogues for adequate coverage. However, these dimensions are not consistent as defined in section II.4. Thus the average is more like a spatial average than a temporal average and might slightly overestimate the Eulerian average velocity in the box. This overestimation should be small enough to be negligible in the light of some of the uncertainties in the current meter

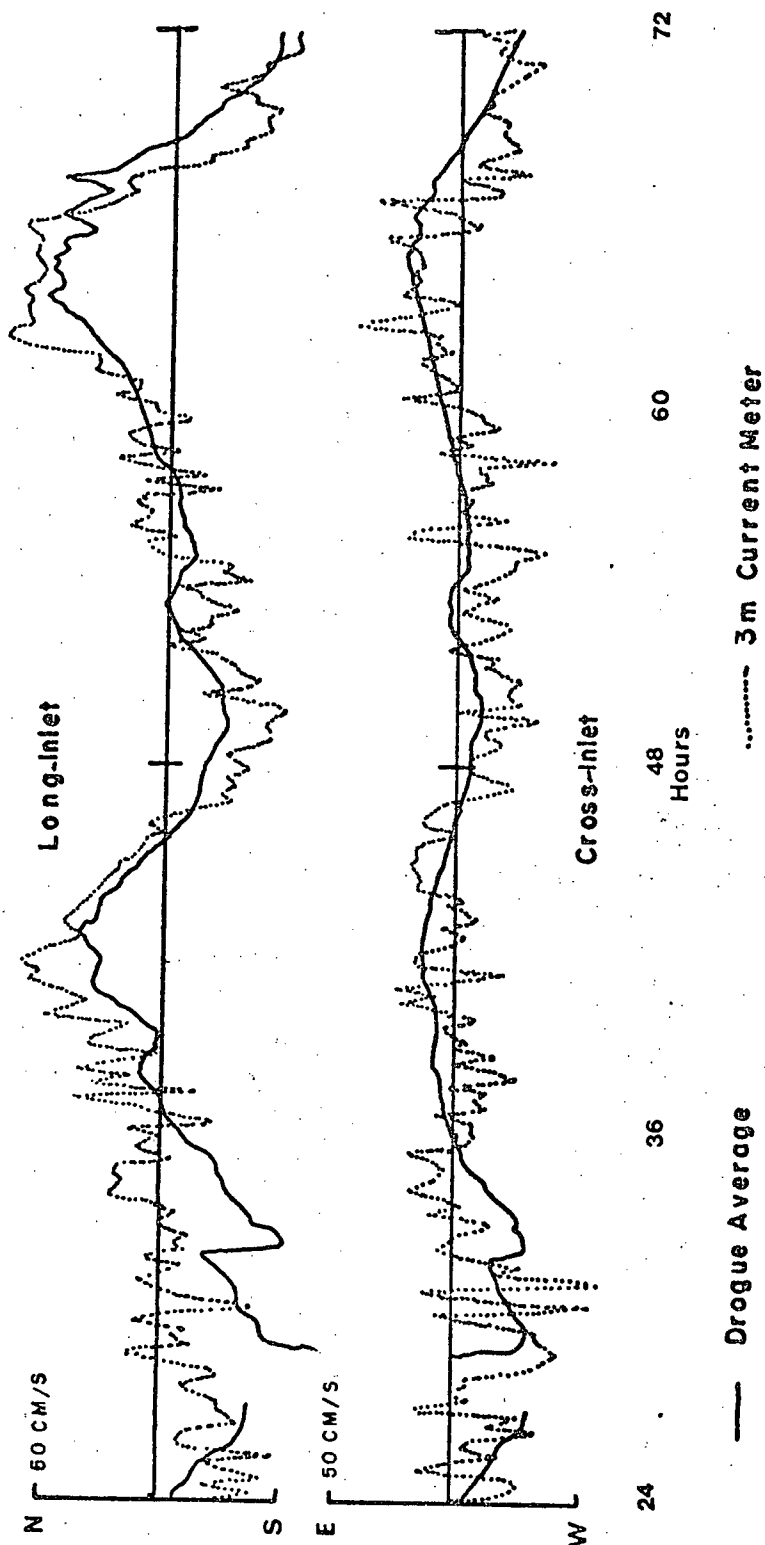


Figure 14 - A comparison of surface layer velocity in week 3 as measured by the current meter at 3m depth and by the average of the drogues in a 1 mi² box around the current meter site.

results.

The current meter velocity is often greater in magnitude than the drogue velocity. An exception occurred at about 32 hours when the prominent velocity core of the river passed through the drogue averaging square but not in the immediate vicinity of the current meter.

The velocity as recorded by the drogues was much smoother than that recorded by the current meter. The measurement area for the drogue velocities was much larger than that for the current meter. Thus the effects of small scale ($<1\text{Km}$) turbulence in the flow are averaged out in the drogue average but not in the current meter. Secondly, the current meter, being suspended from a surface mooring, is susceptible to mooring noise. In this particular meter, burst sampling lessens but does not remove the problem, as will be discussed in more detail in chapter VI. This noise would be expected to manifest itself as larger speeds and scattered directions. The differences between the current meter and drogue velocities could be accounted for by either or both of these effects.

The larger scale features of these two velocity records are quite similar. When the differences between the two techniques are taken into account, the surface layer appears to move reasonably uniformly with depth down to at least 3 metres.

The results of the previous section showed a surface layer between 3.5m and 5.5m deep based on density information and assumed that the depth of maximum current

shear, i.e. the interface between the surface and deeper layers based on velocity, was somewhere in that range. The results of this section do not conflict with that assumption and indicate that the surface layer is reasonably homogeneous in velocity at least to 3 metres.

CHAPTER IV

RESULTS OF THE SURFACE LAYER EXPERIMENT

IV.1 Introduction

The surface layer circulation experiment was quite successful. Observations were made for a total of 255 hours. Over 800 photographs were taken, yielding 12,553 observations of drogue positions and ultimately 241,115 interpolated position, velocity and acceleration estimates. A summary of these statistics on a weekly basis is given in table V.

Table V - A summary of the observation statistics for all four weeks of the drogue experiment. The numbers given are: week number, number of observation hours in that week, number of pictures taken, number of drogue tracks followed, number of drogue position observations and number of points interpolated at one minute intervals.

Week	obs hours	# pics	# tracks	# obs	# interp
1	48.4	191	180	2398	45740
2	70.3	204	295	3009	59140
3	69.8	198	271	3076	61416
4	67.0	236	325	4070	75089

The time base for each week of the experiment was set at 0000h Pacific Daylight Time on the first planned day of observation. For example, the week 1 time line started at

0000h May 8. On that day the skiff lost a propellor and the weather was miserable so actual operations did not start until 0600 May 9. Thus the records from that week start at 30h. The observations in week 1 were cut short by strong down-inlet winds early in the last day that drove all the drogues south of the observation area. By the time they were recovered it was time to pack up the equipment for the week. In the other three weeks we had greater success in achieving the goal of 3 days continuous observation.

There are only a few gaps in the data record. These usually occurred at night when the surface layer currents made a quick change in direction. The one operating vessel was not fast enough both to search for drogues leaving the area and to deploy new drogues in the area to allow the observations to continue.

This chapter contains first a general picture of the surface circulation pattern. This general picture is then substantiated with a semi-quantitative description of the flow field, a description of the observed drogue movements in each of the four weeks. The rest of the chapter gives more quantitative analyses of some of the averaged properties of the drogue observations.

IV.2 A General Surface Circulation Pattern

A basic aim of these experiments was to determine the general pattern of surface layer flow in the north end of Howe Sound. This description is based on an examination of drogue motions in all four weeks and an attempt to extrapolate from them the underlying flow field in the absence of forcing by either wind or tide.

The principal technique used to obtain this description was repeated observation of a set of movies computer generated from the spline-fitted data set described in chapter II. It was necessary to construct these movies because the time lapse movies taken of the radar screen during the experiment were intermittent due to camera malfunctions and contained all of the extraneous, distracting objects described previously. These computer generated movies were similar to those discussed in chapter II but contained more information and were transcribed onto 16mm movie film using the Bolex H16 Reflex camera interfaced to the PDP-12. A description of the movie generation techniques is given in Appendix II. And a sample of these movies is included as Appendix III.

The average circulation pattern of the surface layer in Howe Sound as qualitatively deduced from these experiments is shown in figure 15. Each individual arrow in this figure represents the direction and relative speed of the current at that location. This circulation pattern and the standard silt pattern as seen in the frontispiece are, not

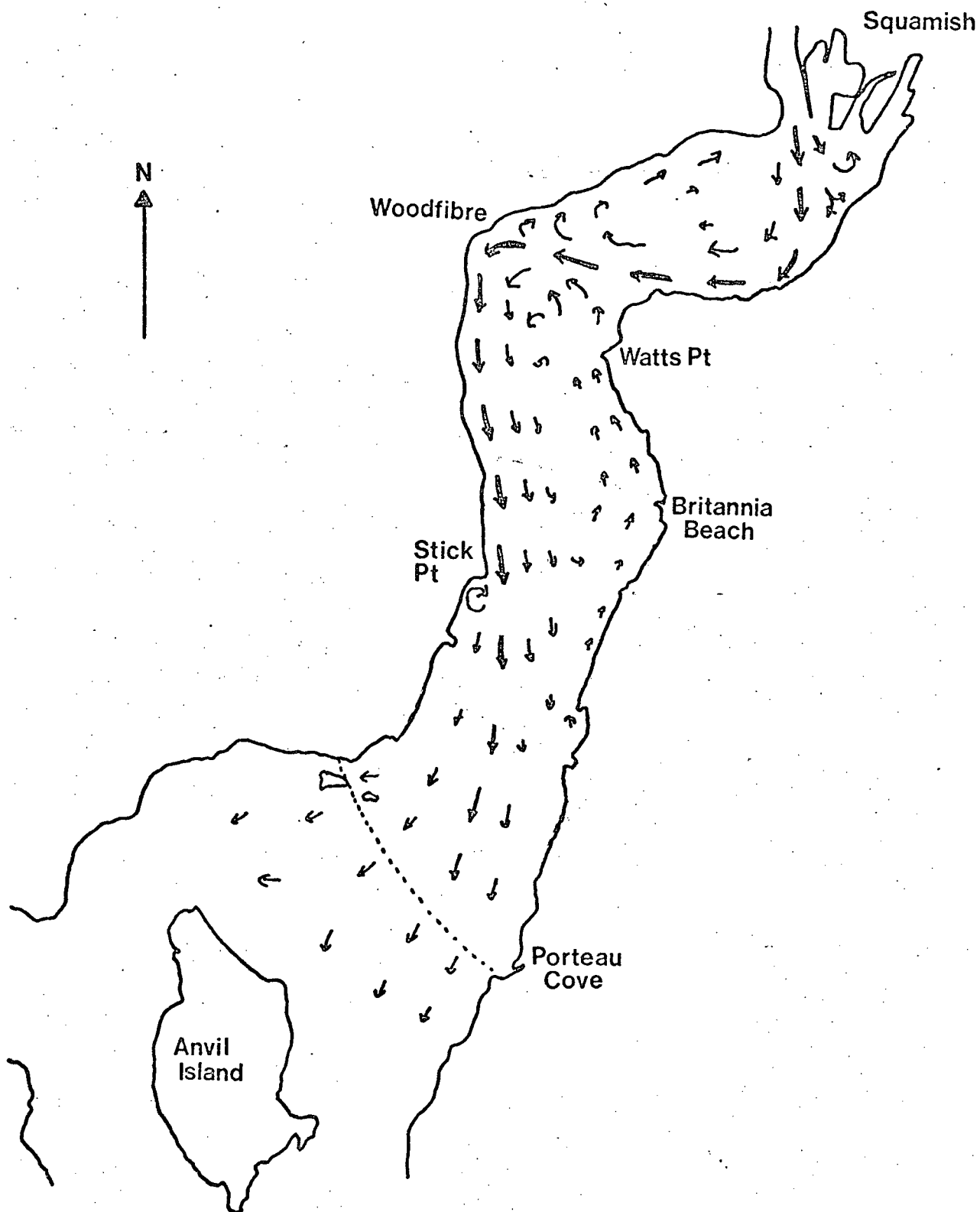


Figure 15 - A general, qualitative surface circulation pattern for upper Howe Sound as deduced from the surface drogue study. Length of the arrows indicates the relative speed of the current; the breadth of each arrow, the persistence of the current at that point.

surprisingly, quite similar. However, the sharp boundaries between the silty and non-silty water that appear in the frontispiece do not indicate the presence of sharp velocity gradients as might be expected. It was observed many times in the experiment that drogues on opposite sides of silt boundaries moved at about the same speed.

The dominant feature of this circulation pattern is the "jet" formed by Squamish River water. The core of this jet, as indicated by the heaviest arrows, proceeds down-inlet in a path constrained by the shape of the inlet. After the core leaves the mouth of the river, it proceeds across the inlet and then moves west along the southeast shore. There is often a counterclockwise back eddy on the east side of this jet that brings silty river water into Squamish harbour. Where the east shore of Howe Sound turns sharply south just north of Watts Point, the river core traverses the inlet to the vicinity of Woodfibre, whence it follows the west shore southward for several miles. When it passes Stick Point¹ it moves away from the shore to the centre of the channel due to a sharp bend in the shoreline and a slight change in the orientation of the channel. There are two large slow, persistent eddies probably driven by entrainment into this river flow in the north part of the basin. The first, a

¹ This point is nameless on the Hydrographic chart of Howe Sound, but is known locally as Stick Point for the following reason. Tug boat operators bringing booms and barges up Howe Sound usually proceed up the western shore taking advantage of the slower currents and back eddies south of this point. They found that as soon as they rounded this point they got "stuck", i. e. had trouble getting farther up the inlet. Results in this thesis should make the reason obvious.

clockwise gyre, occurs between Woodfibre and the mouth of the Squamish River, and the second, a counterclockwise gyre, between Britannia Beach and Watts Point. This second gyre is not so prominent and may be just a wind effect. It is possible but less likely that the first gyre is also wind-driven.

During its passage down-inlet, the river jet diverges slowly. This divergence will be described quantitatively in a later section. South of Stick Point, the jet is wide enough to cause all the surface layer to move downstream. In the vicinity of Porteau Cove, at the southern limit of observation in these experiments, there is still evidence of horizontal shear in the surface layer. Even at this point, 18 km from the river mouth, the classical estuarine assumption of laterally homogeneous flow has not been achieved.

It was not clear from the experiments whether the average surface flow usually goes to the west of Anvil Island or to the east of it. The experiments showed both results although flow to the western side seems to be slightly favoured. There was no obvious correlation between the wind speed or direction and the side of Anvil Island that the current flowed past.

IV.3 A Synopsis Of The Data Sets

IV.3.1 Techniques Of Presentation

The data sets collected in the four weeks of the experiment will be presented in a series of diagrams, each one containing a number of averages of the drogue velocities in 0.5 nautical mile squares covering the experimental areas. The reasons for this box averaging technique and the limitations of it when using such a large box size were discussed in chapter II. The use of longer times and larger boxes than suggested in that chapter probably decreases the measured velocities slightly, but for the purposes of a semi-quantitative description of these data sets, the possible discrepancy should be small enough to neglect. To be consistent with the 0.5 mile averaging grid, the coastline in each diagram has been drawn along the boundaries of all those squares containing appreciable water area or which have some water area and an appreciable number of drogue observations in them. The correspondence between this "squared" coastline and the actual one is shown in figure 16 .

A typical diagram from one of the sequences is shown in figure 17 . This particular one is for the period beginning at 69 hours and ending at 72 hours of the first week. Eighteen arrows representing three hour averages of drogue

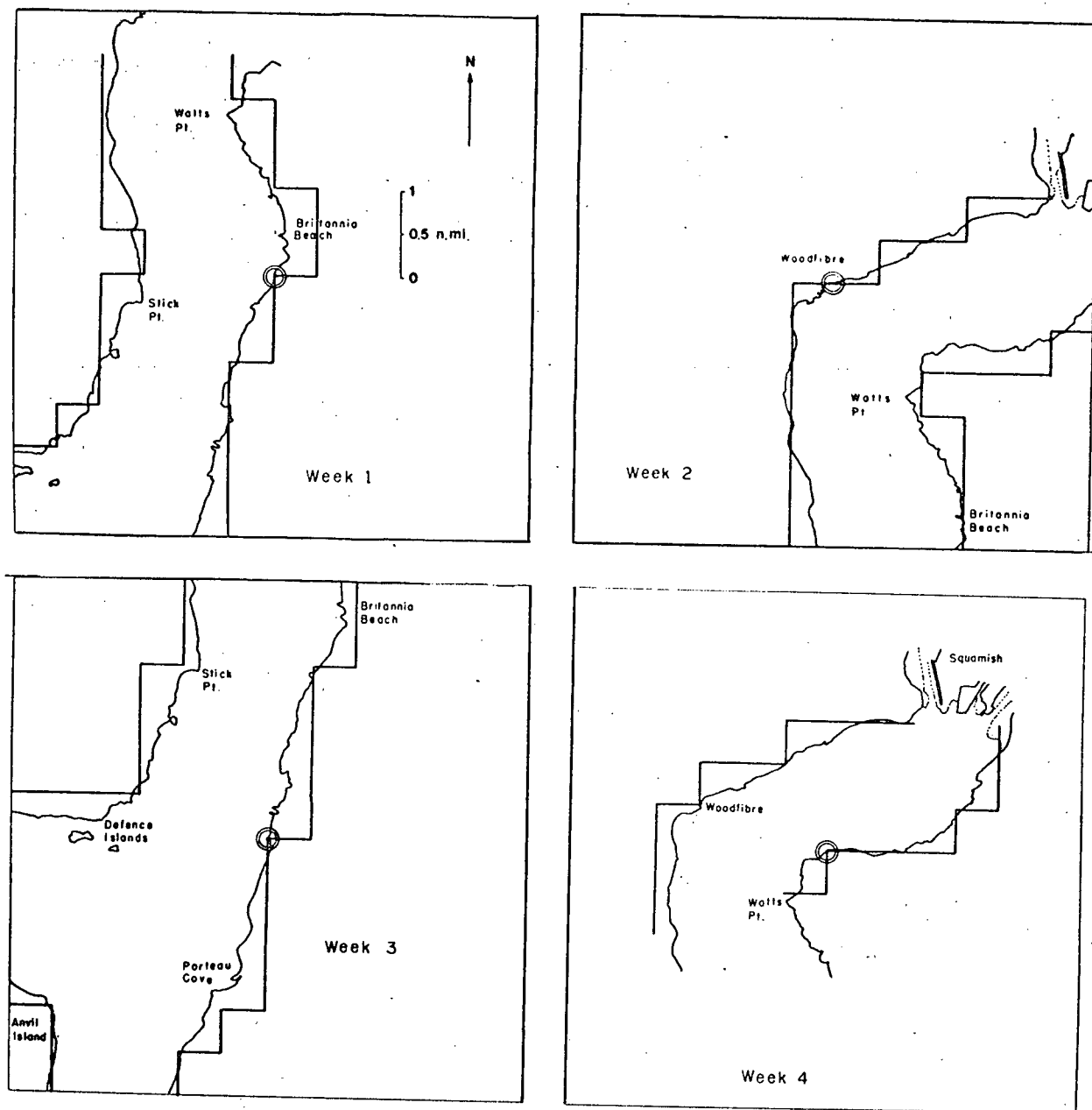


Figure 16 - Actual vs. "squared" coastlines for the four weeks. The double circle indicates the radar site in each week.

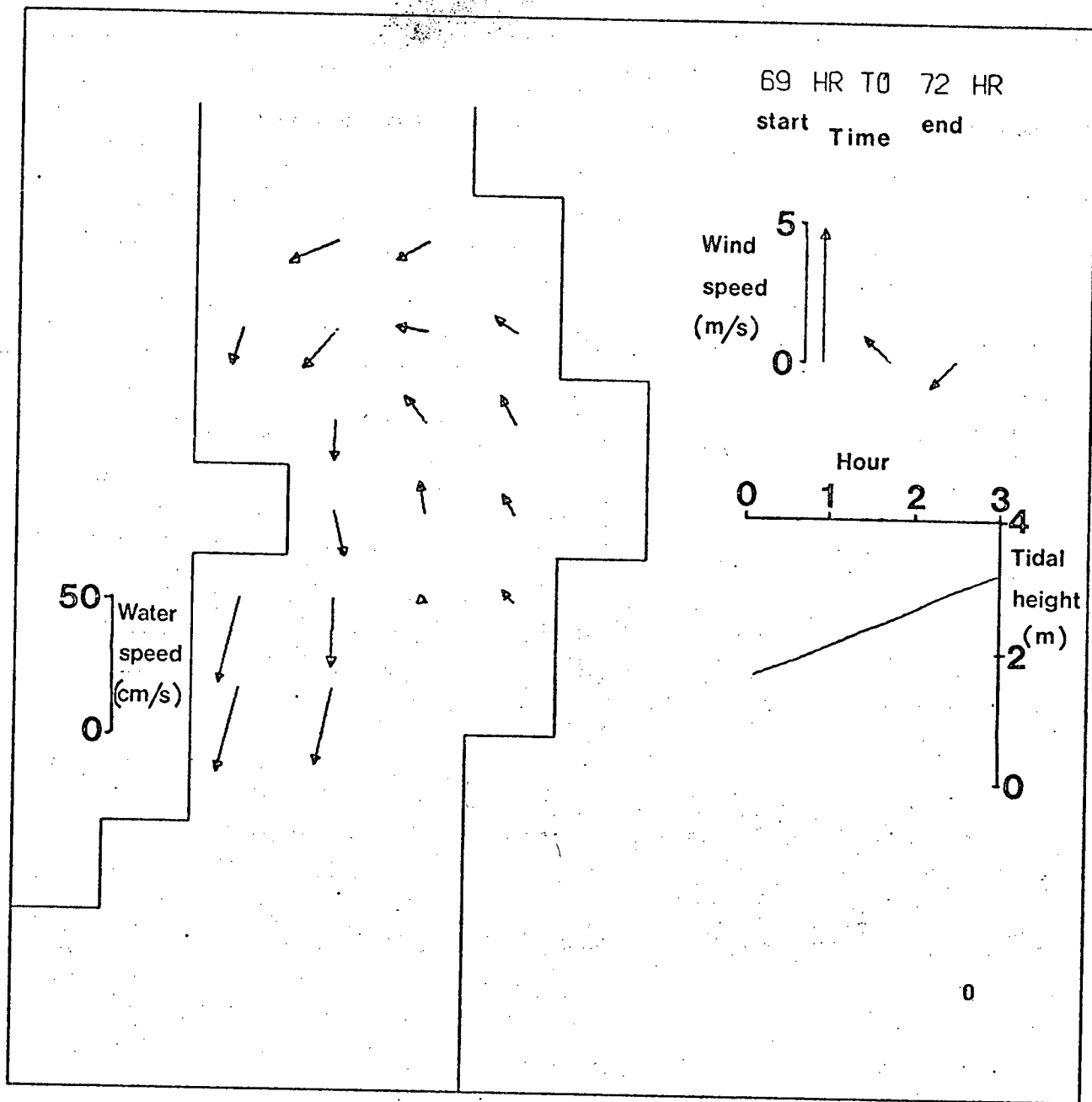


Figure 17 - A typical diagram from the 3 hour averaged data sets that are presented in figures 19-22. Shown on the figure are the current vectors, wind vectors, tidal height and the relevant scales as are described in the text.

velocities in 0.5 mile squares can be seen within the confines of the squared coastline. The scale relating the length of these arrows to the average calculated drogue speed is shown on the left of the figure. Absence of an arrow in a square indicates that there were no drogues in that square at any time in the averaging period. The tail of each arrow is at the centre of its averaging square.

This figure also contains three vectors representing the wind velocity from the AES anemometer in Squamish, one for each hour of the averaging period. The speed scale for these vectors is also shown. A section of the Pt. Atkinson tidal curve is shown, representing the height of the tide during the averaging period. All of the diagrams to follow in this chapter contain these component parts, except the scales, which are shown on one frame per page.

There is no indication in these figures of the error in the averages, or of the spread of individual values about the means. In figure 18 another typical diagram is shown, but with the observed standard deviation of each component plotted at the head of each vector. Only in the case of the smallest vectors is the standard deviation larger than the vector itself. On average, 15 values were used to form each vector, so that the standard error of each average should be about $1/4$ the size of the error bars shown. Thus for the most part, the vectors shown in the next sections are statistically reliable.

What follows now is a brief description of each data set accompanied by 17 to 24 diagrams of the sort just

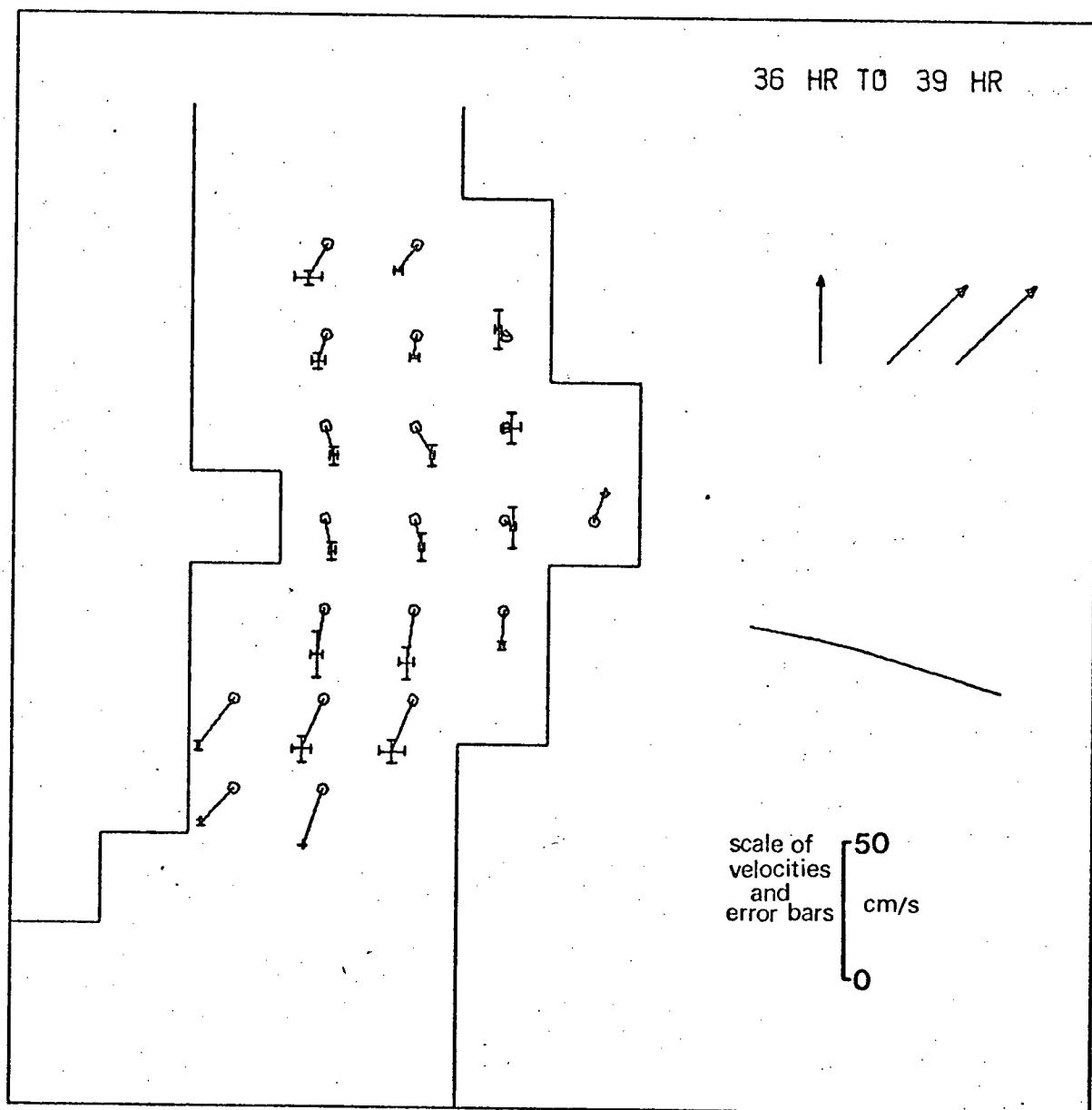


Figure 18 - Typical square-averaged plot showing error bars of ± 1 standard deviation at the head of each arrow.

described.

IV.3.2 Week 1 - May 8-11, 1973

The data collected in week 1 of these experiments are shown in figure 19 a-g.

The week started with almost no wind and an ebbing tide. The flow was down-inlet and stronger on the west than on the east. At 34 hours, (fig. 19c) the wind started to blow up-inlet and in frames d through f the flow can be seen to be slowed down and then reversed on the east side and stopped on the west. The tide was ebbing throughout most of this period. Frame g shows that, although the wind was still blowing up-inlet and the tide was flooding, the current on the west side started to flow down-inlet. Flow on the east side was still up-inlet. In frames h to k, the wind blew down-inlet weakly and the tide ebbed. Flow was strongly down-inlet on the west and moved down-inlet more weakly over the rest of the area. At 58 hours, the wind started to blow up-inlet again and frames l and m show a developing up-inlet flow field. By frame n the flow on the west had stopped and flow in the north had stopped moving up-inlet although it was still moving across the inlet. In the final frames the wind reversed direction and the flow reversed to be strongly down-inlet. In frames o and p the tide was flooding.

In summary of this week of data, there were two reversals of flow from down-inlet to up-inlet that were both apparently correlated to shifts in the wind. The two shifts

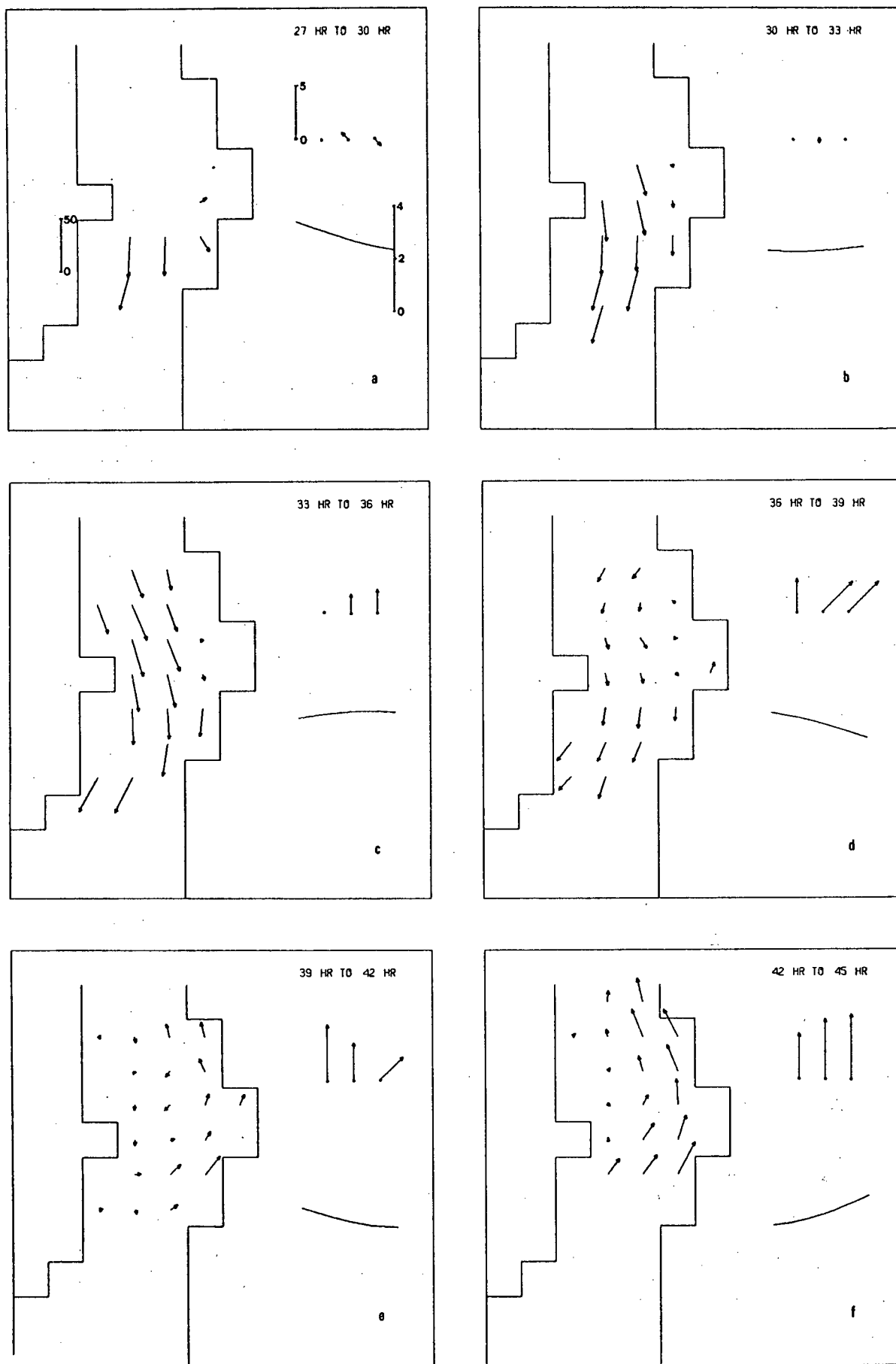


Figure 19 - The week 1 data set.

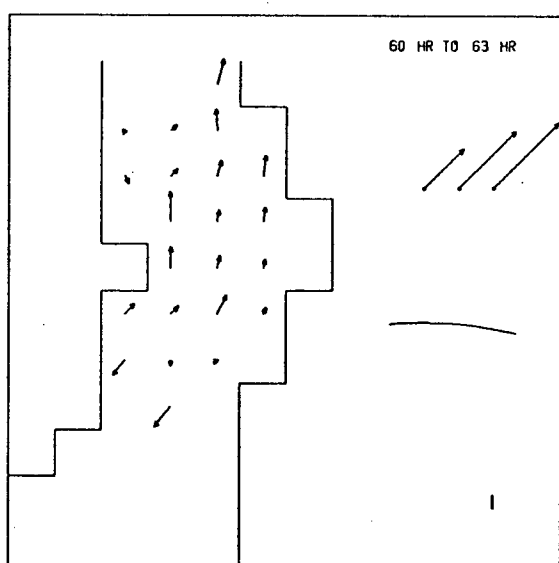
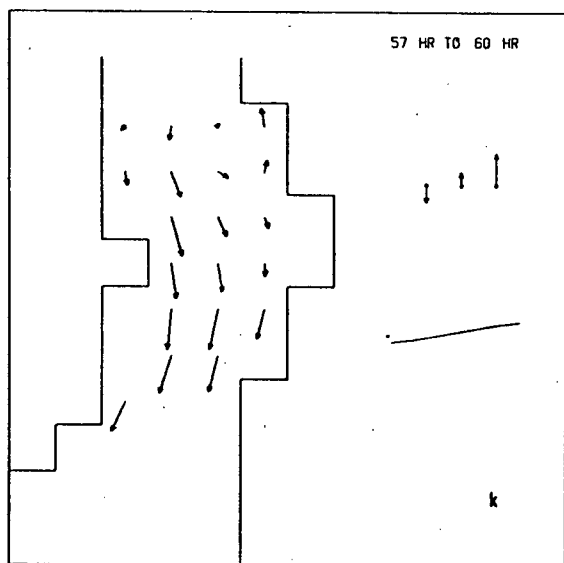
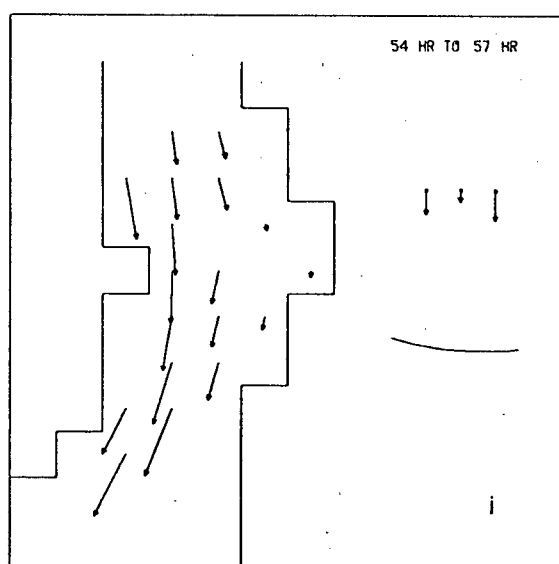
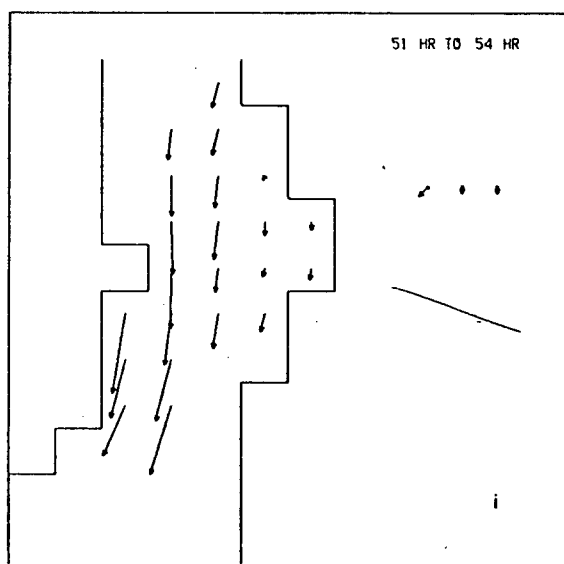
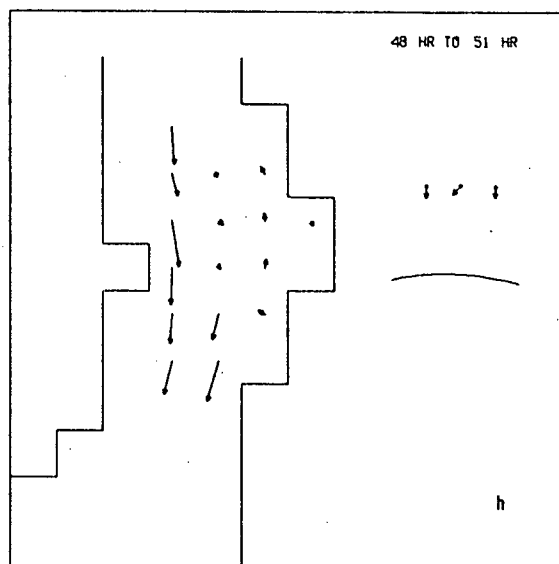
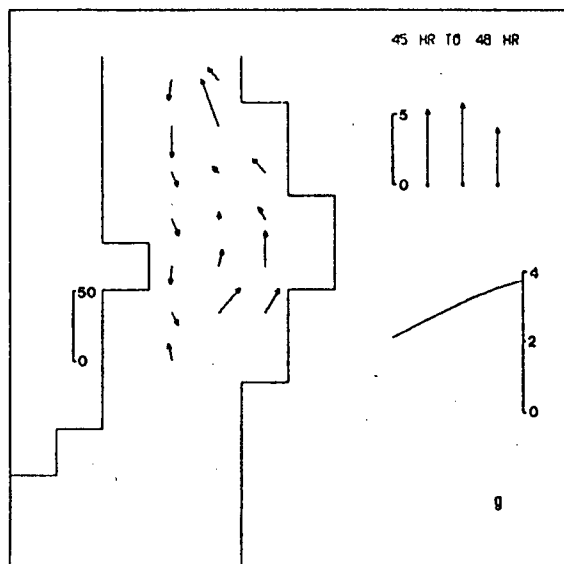


Figure 19 continued.

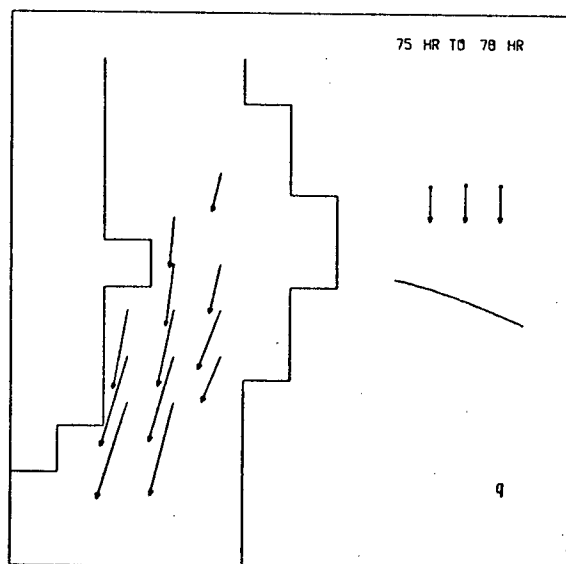
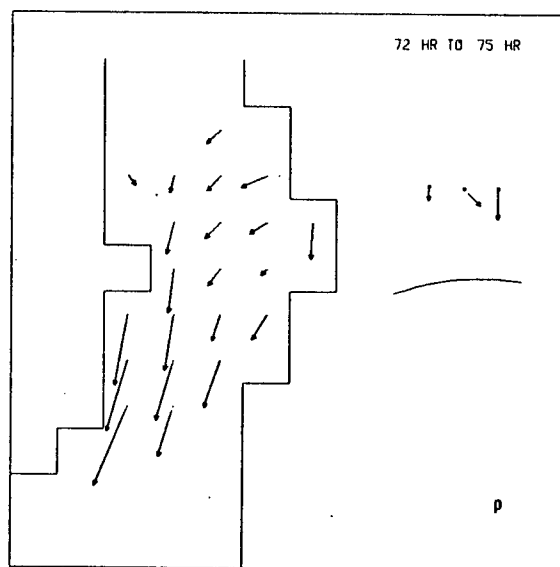
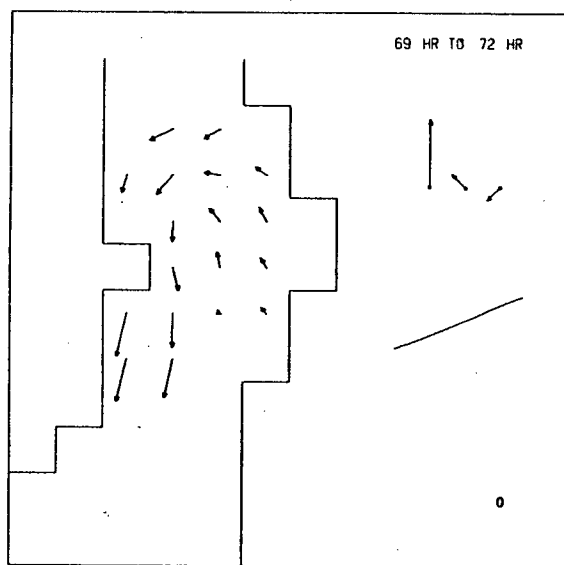
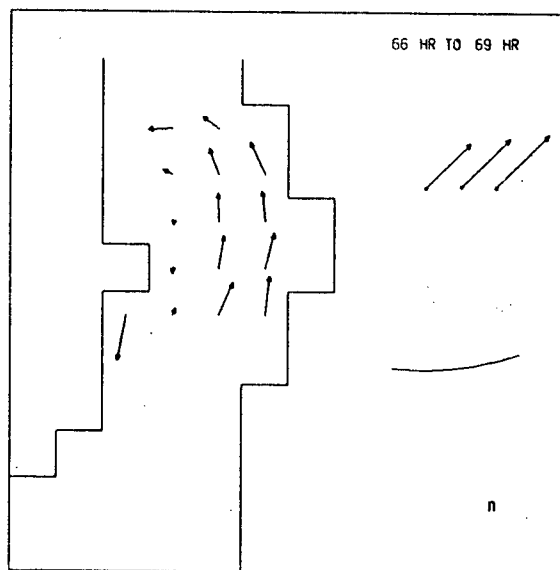
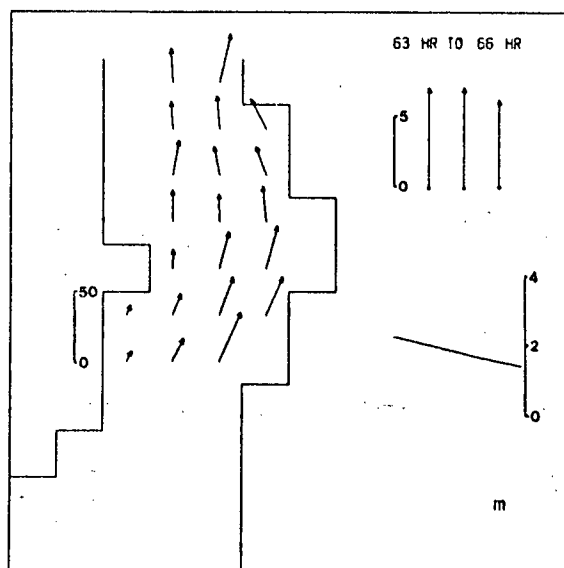


Figure 19 continued.

in current direction from up-inlet to down-inlet seemed to be correlated mainly to either ceasing of the wind or a shift in it to down-inlet. There seemed to be some tendency for the up-inlet flow to slow down despite the continuing up-inlet winds. The phase of the tide did not seem to correlate with any change in the current.

IV.3.3 Week 2 -- May 15-18, 1973

The data collected in week 2 of the experiment are shown in figure 20 a-x.

The initial current field was strong and down-inlet except in the vicinity of Watts Point where it was almost stationary. Winds were negligible. Eight hours of moderate up-inlet winds and a rising tide, as shown in frames c and d, did very little to change this pattern except to reduce the strength of the outflow. When the winds ceased at 22 hours, the down-inlet current strength appeared to increase. There was little change in the current pattern as the period of calm continued through to 36 hours. A strongly ebbing tide seemed to have little effect. For the next 9 hours, as shown in fig.20 j - l there was a moderate up-inlet wind and a rising tide. The down-inlet flow seemed to reverse to up-inlet flow in the vicinity of Watts Point for a while. Outflow speeds dropped and the region of maximum down-inlet current moved westward. The down-inlet currents became stronger and more uniform in the period from 51 to 59 hours as the tide ebbed and the wind blew weakly down-inlet. At 60

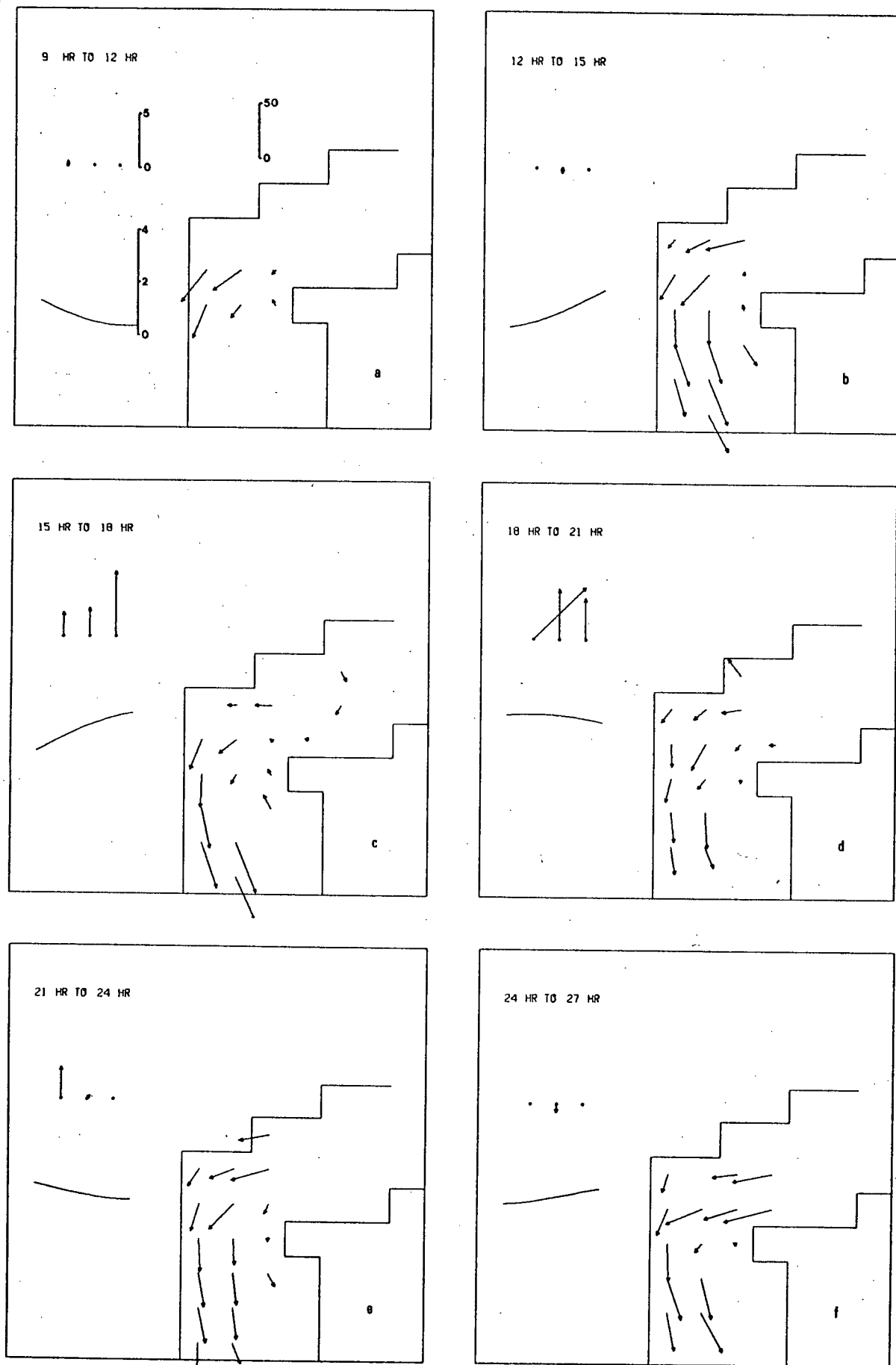


Figure 20 - The week 2 data set.

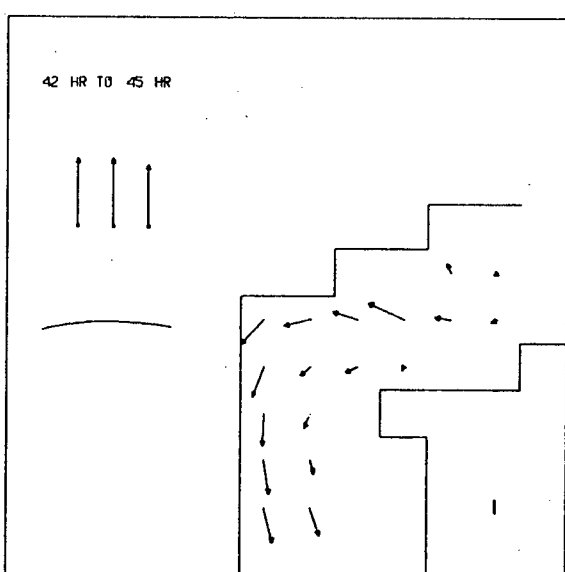
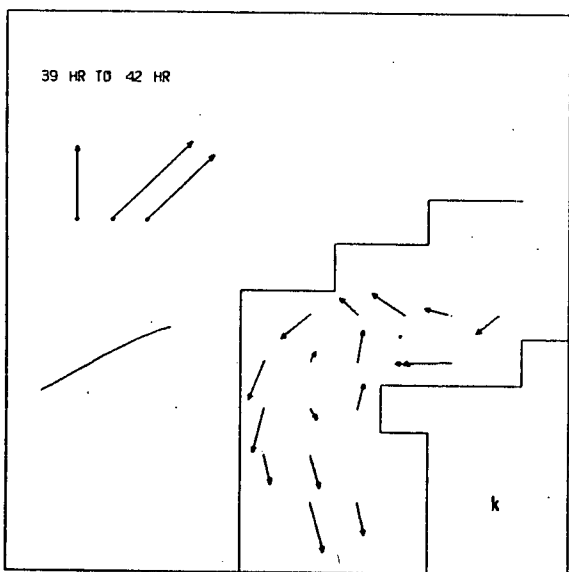
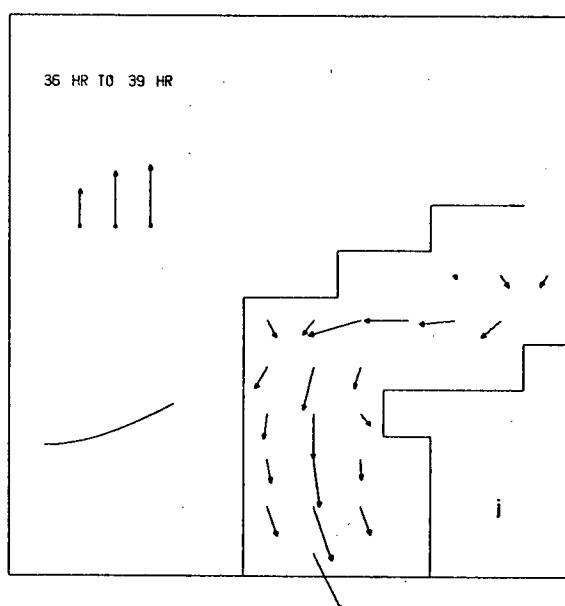
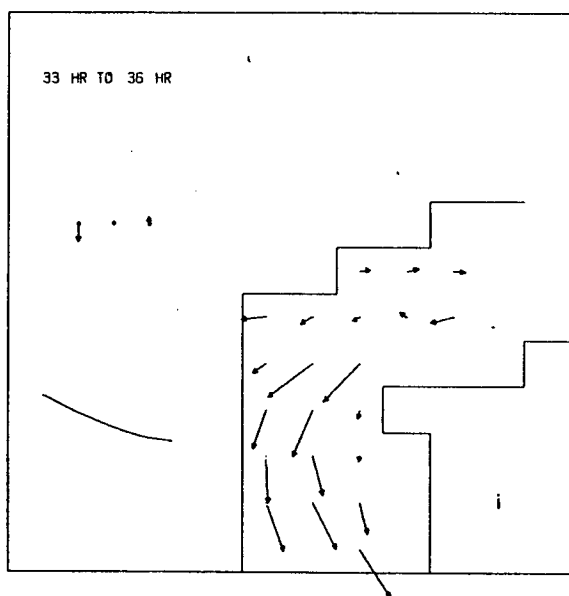
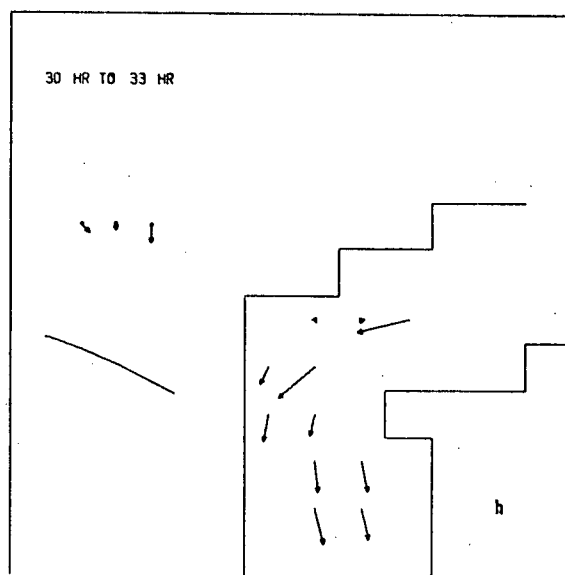
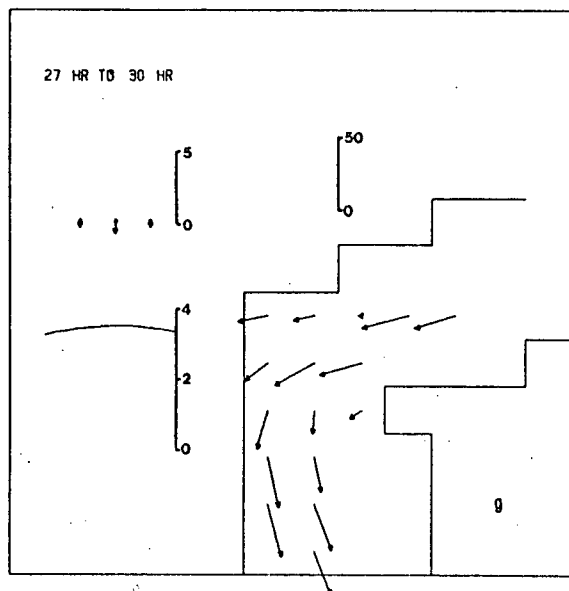


Figure 20 continued.

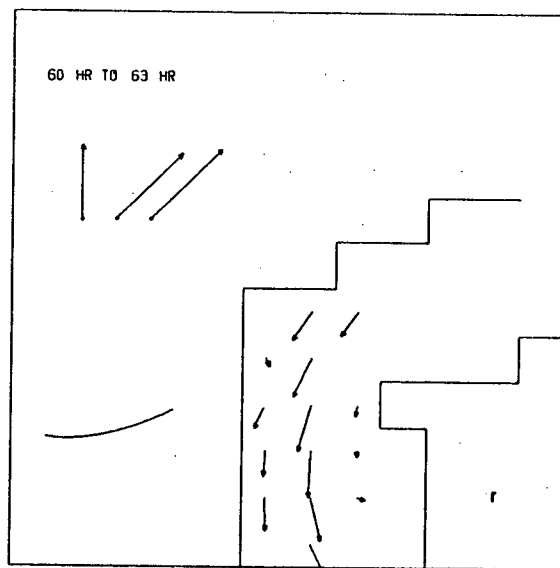
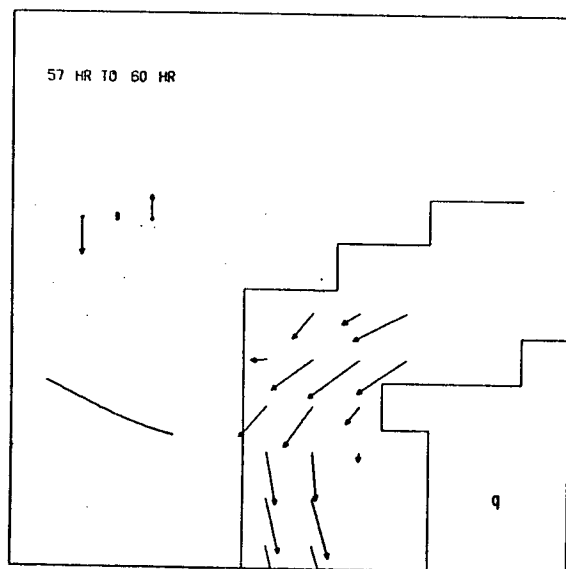
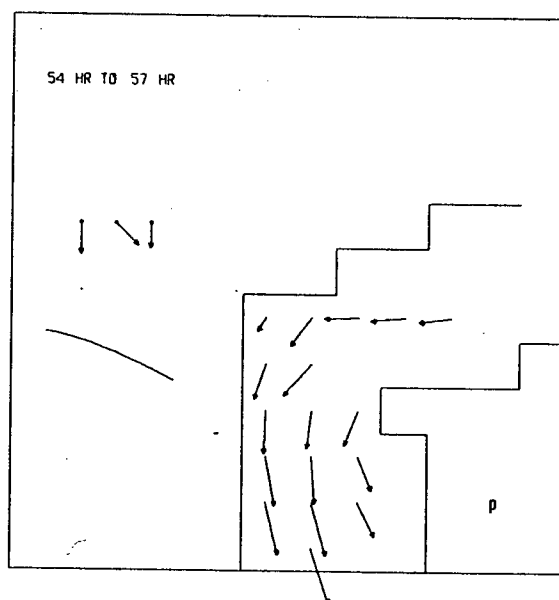
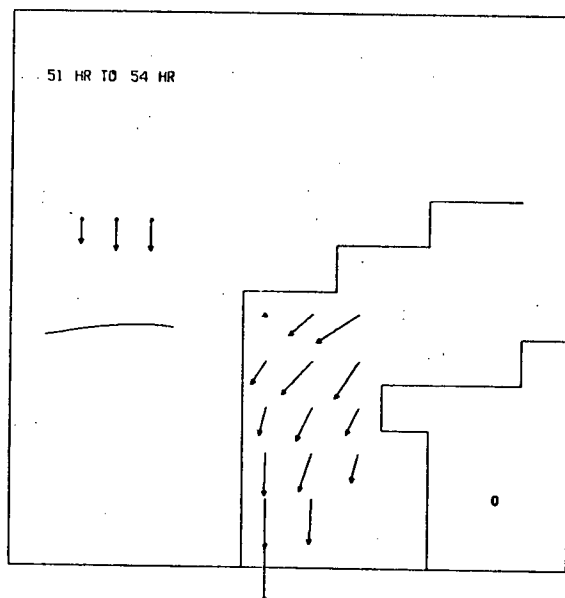
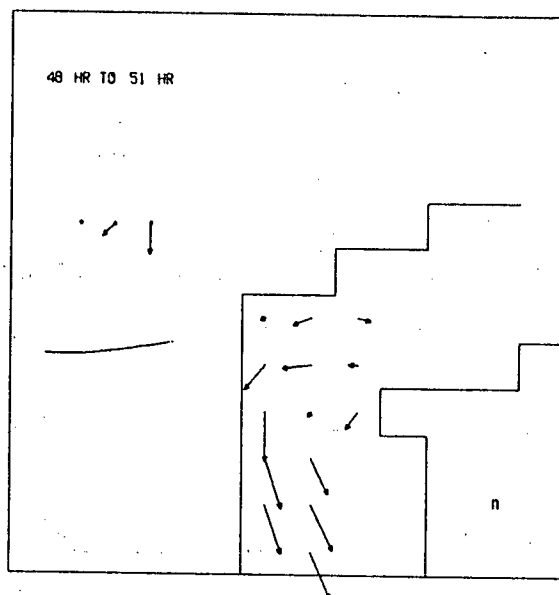
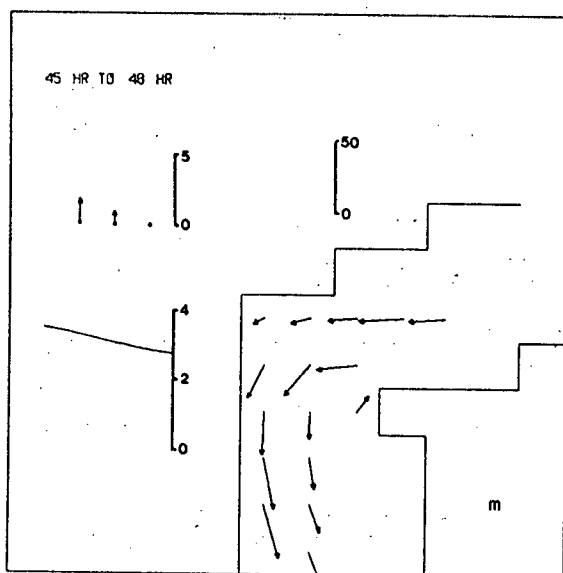


Figure 20 continued.

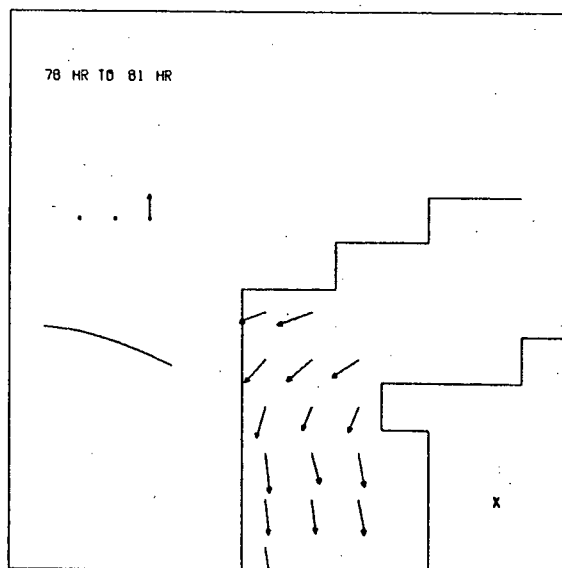
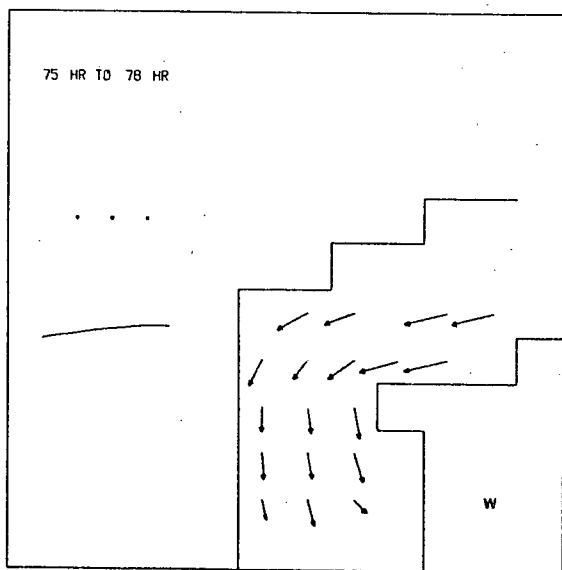
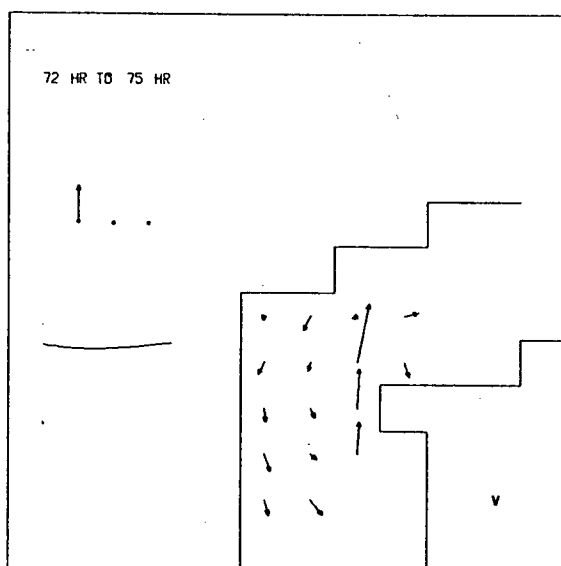
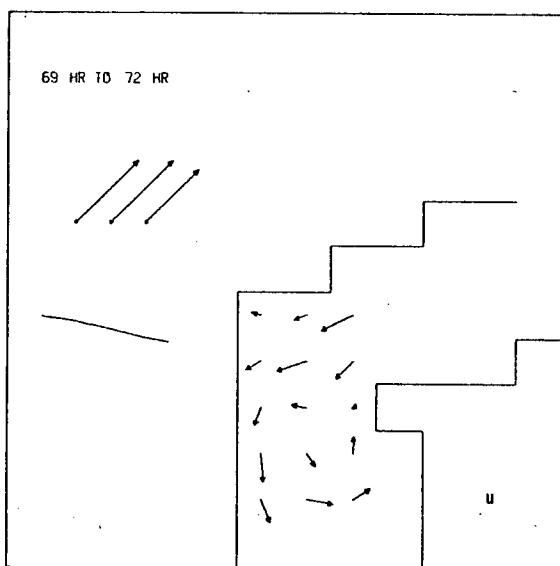
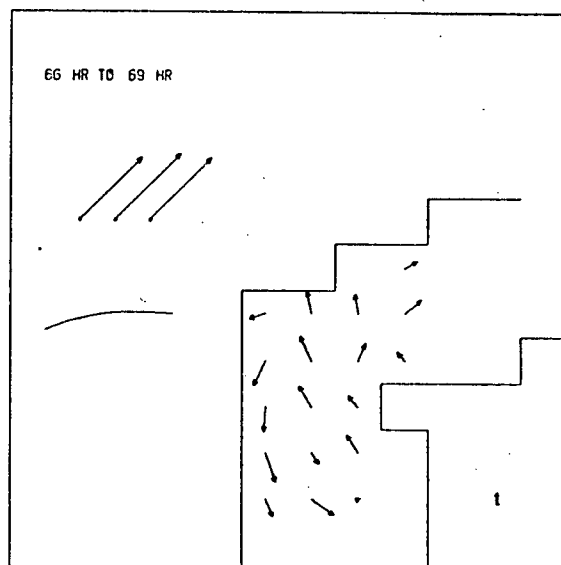
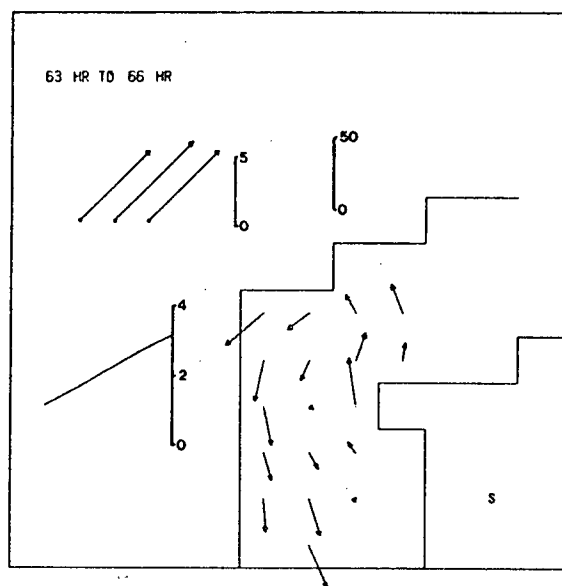


Figure 20 continued.

hours, the wind started to blow fairly strongly up-inlet and the down-inlet current velocities decreased. For the next 12 hours (63h to 75h), the wind continued to blow in the same direction, the tide flooded then remained constant and the surface water moved generally in the up-inlet direction. On the western shore however, the down-inlet flow continued. When the wind died, the current became once again uniform and down-inlet.

In summary, this week's data showed a flow field less influenced by the wind than the previous week's. No significant tidal influence was seen. Only the event from 60 to 72 hours bore much resemblance to the wind-water correlation of the week 1 data.

IV.3.4 Week 3 -- June 26-29, 1973

The data collected in week 3 of these experiments are shown in figure 21 a-w.

In the first few hours, the current was uniformly up-inlet. The wind was up-inlet and the tide was relatively slack. At 23 hours, the wind died. The period from 24 to 36 hours saw strong down-inlet currents with little wind and an ebbing tide. At 36 hours the wind again became strong and up-inlet. It stayed that way until 46 hours. The tide was flooding in frame h then remained relatively slack for 12 hours. The current in h was small on average indicating a change in direction from down to up-inlet. The current remained strong and up-inlet until k when the wind slackened

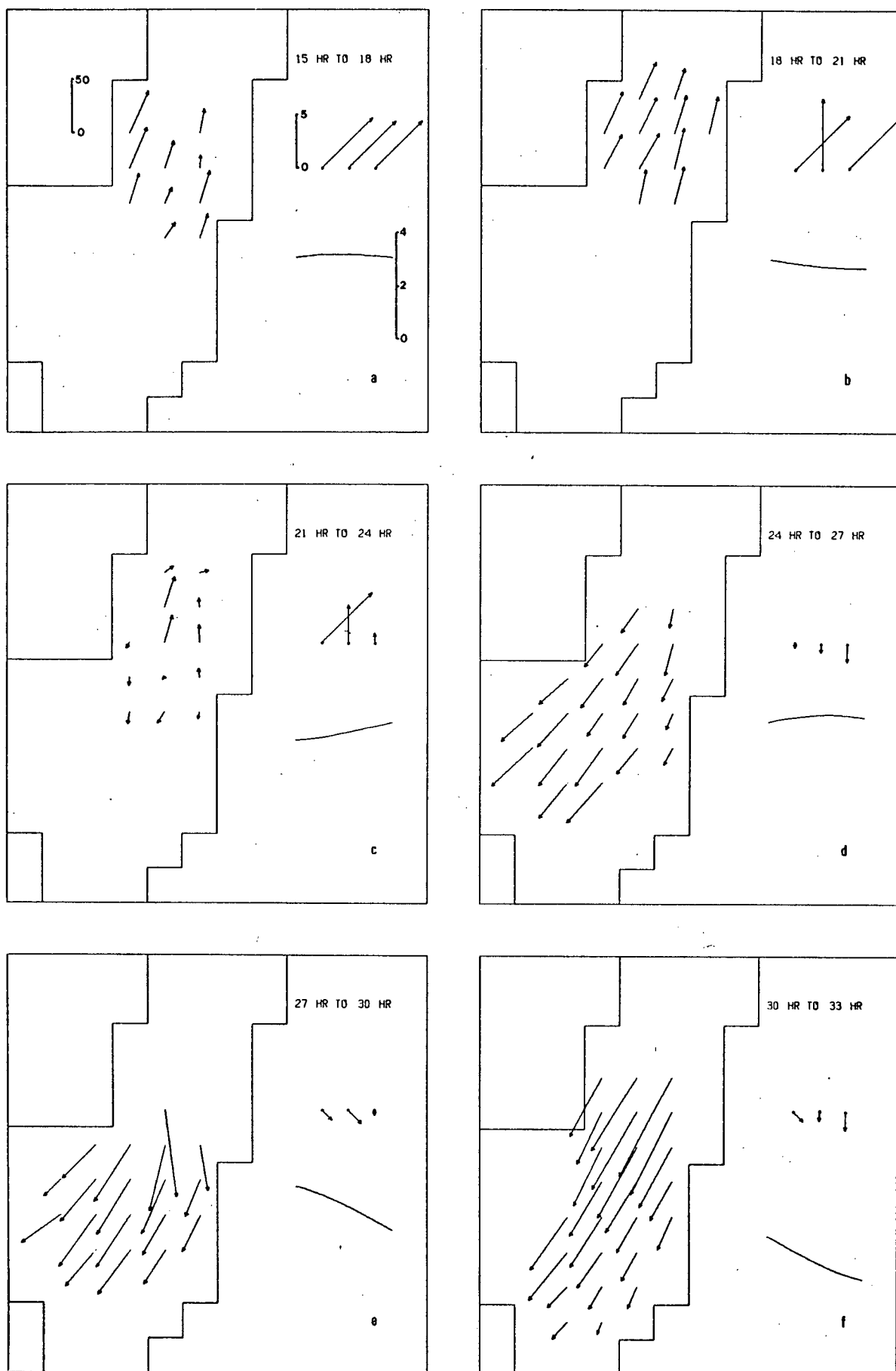


Figure 21 - The week 3 data set.

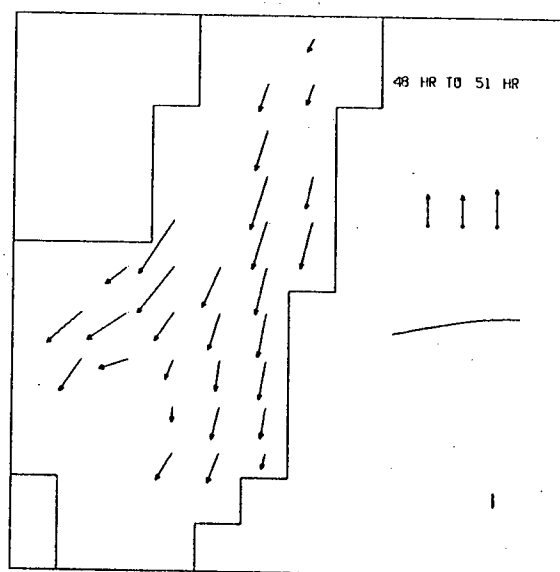
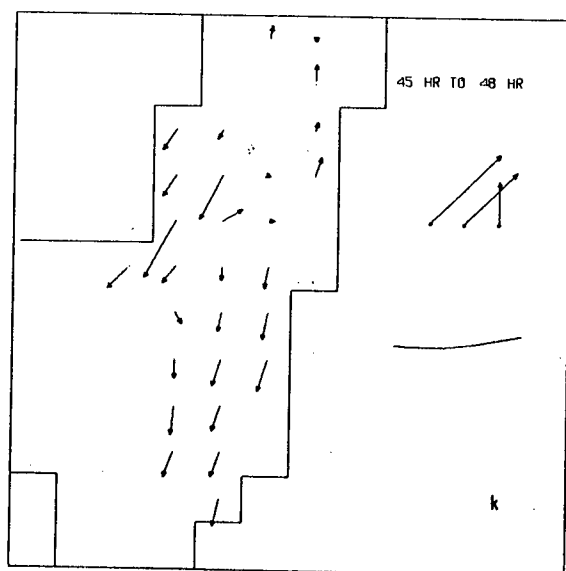
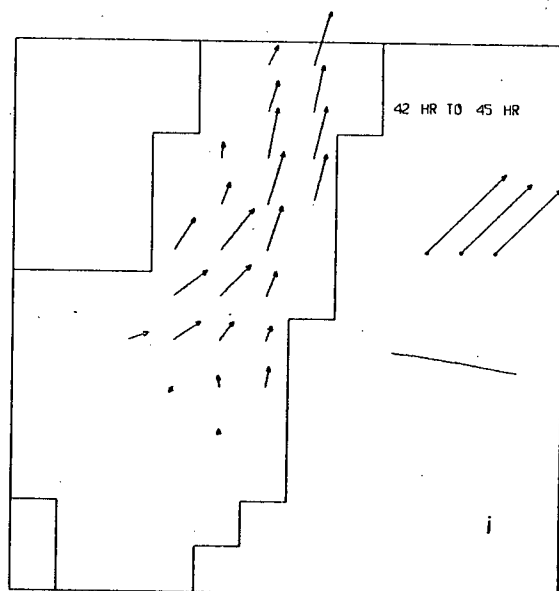
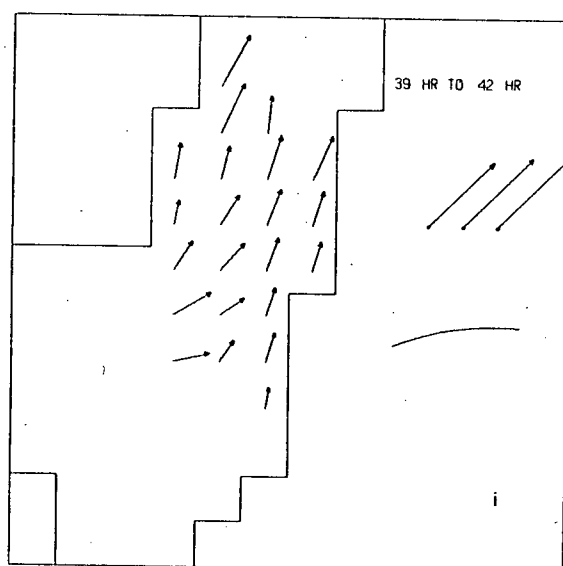
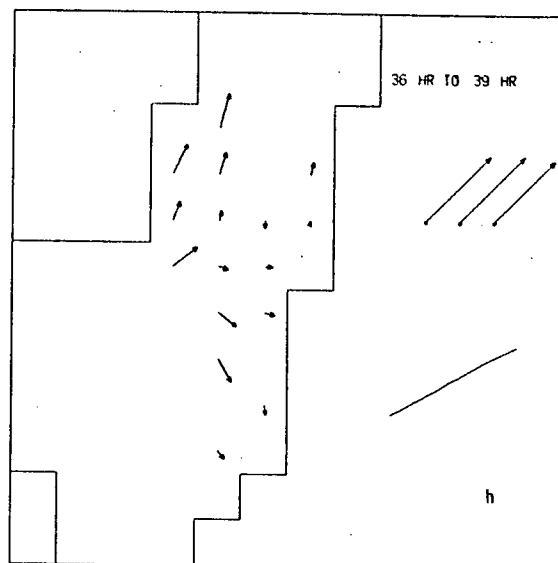
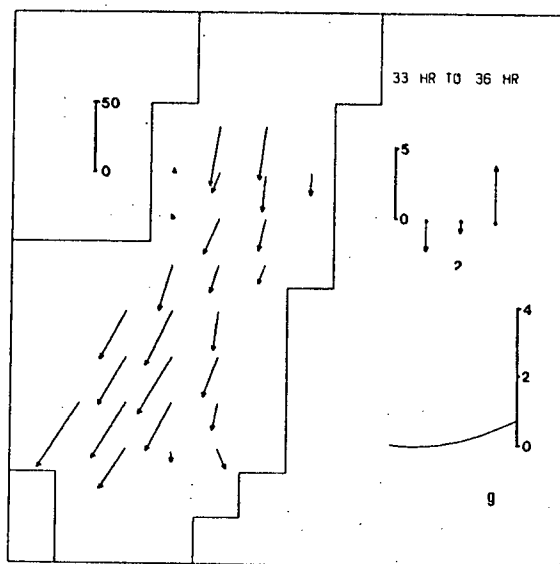


Figure 21 continued.

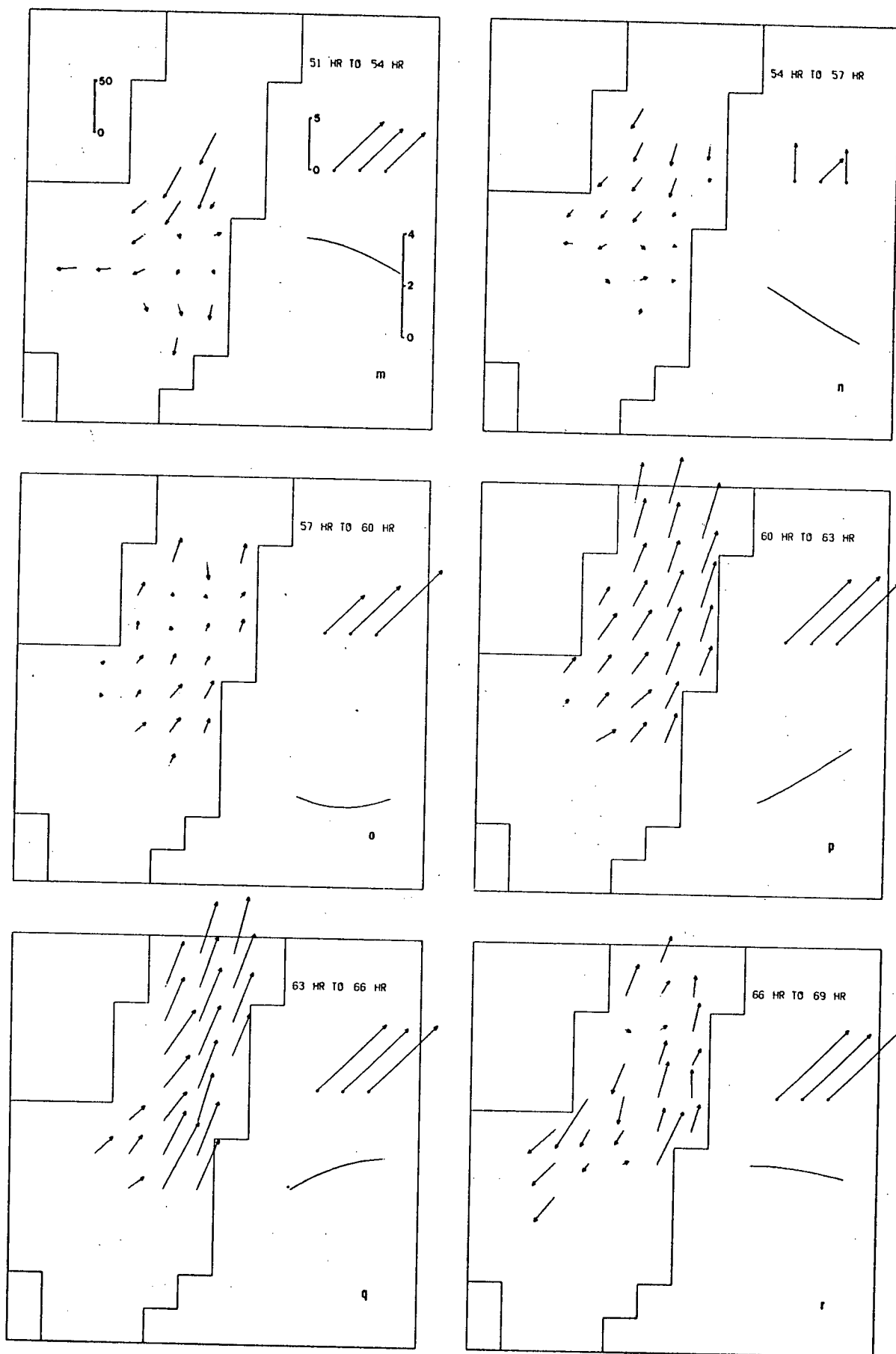


Figure 21 continued.

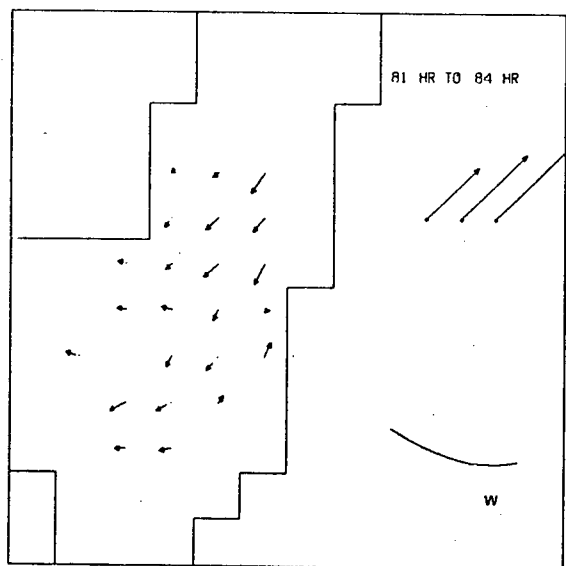
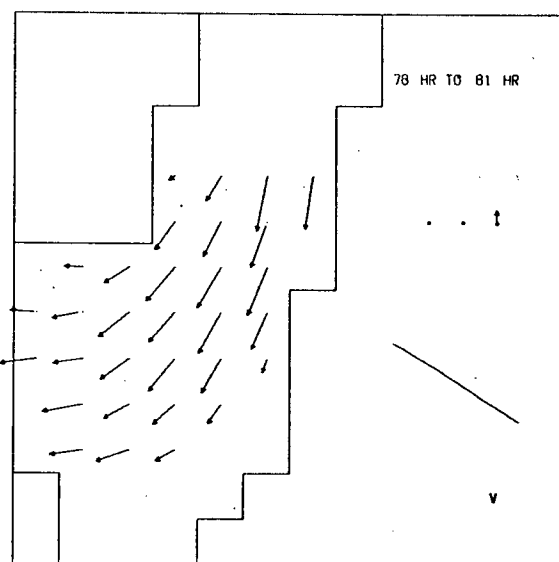
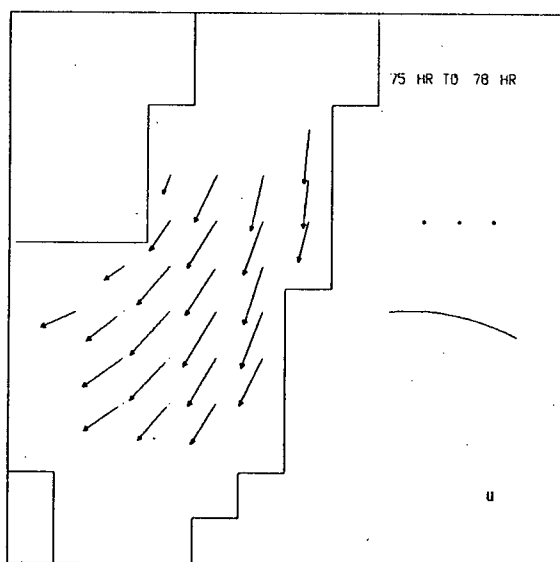
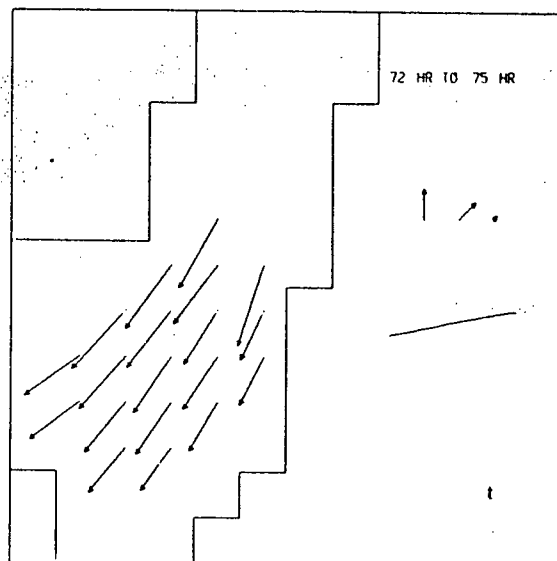
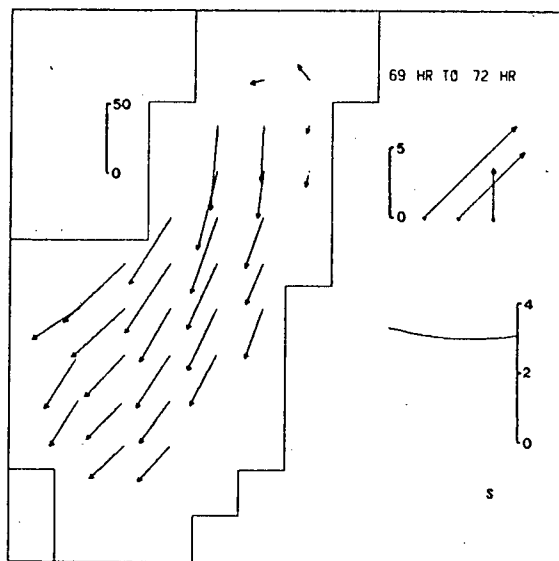


Figure 21 continued.

somewhat and the water started to move down-inlet. This continued in frame l in spite of the up-inlet winds. From 51 to 60 hours, the current field was somewhat confused, with the water near the western shore moving basically down-inlet, and the water near the southeast moving very slowly at first but increasing in speed later up-inlet. The wind in this period was blowing up-inlet with increasing magnitude and the tide was ebbing. Frames p and q show a strong uniform up-inlet current field, a moderate up-inlet wind and a rising tide. After 66 hours, although the wind was still blowing up-inlet, the current field became much less homogeneous. Water in the southwest was flowing out while water in the east was still flowing in. In frame s, the wind almost ceased and a uniform down-inlet current field was formed that persisted through frame v. The final frame, w, shows that the down-inlet current had almost stopped. The winds had started to blow up-inlet and the tide was finishing a period of ebb.

In summary, there were two reversals of flow from down-inlet to up-inlet. Both occurred with up-inlet winds and flooding tide. It seemed as if a third reversal of this type was beginning in synchronization with an up-inlet wind shift at the end of the experiment. Of the three reversals of flow from up- to down-inlet, one occurred as the wind died, one as the wind decreased in up-inlet intensity and one preceded the ceasing of the wind. The tide was relatively slack for two of these reversals and was ebbing for the third.

IV.3.5 Week 4 - July 3-6, 1973

The data collected in week 4 of the experiments are shown in figure 22 a-w.

This week of data was significantly different from the other three. The wind blew up-inlet the entire week and the average current velocities were reasonably uniform for the whole week. All the frames show a down-inlet current on the south shore and an up-inlet current on the north shore. There appeared to be little change in the clockwise gyre of this flow caused either by tide or by changes in wind speed.

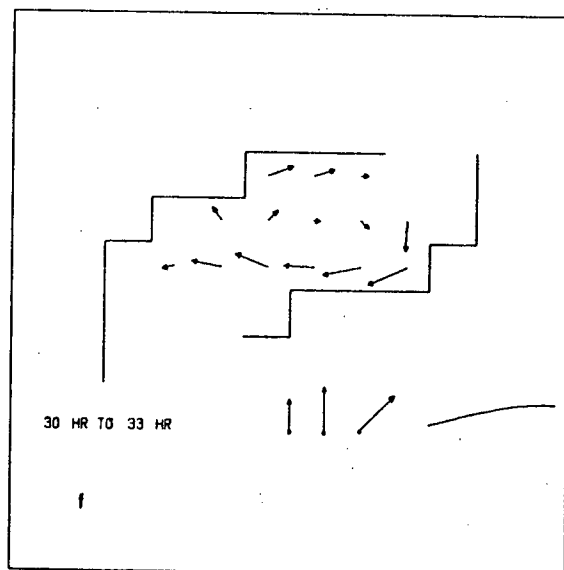
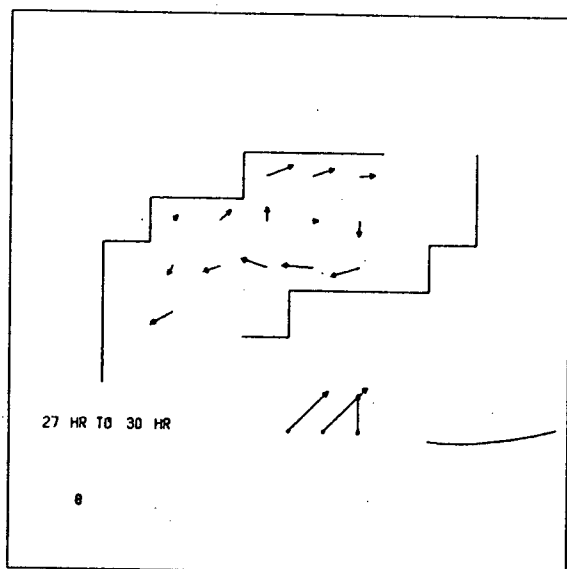
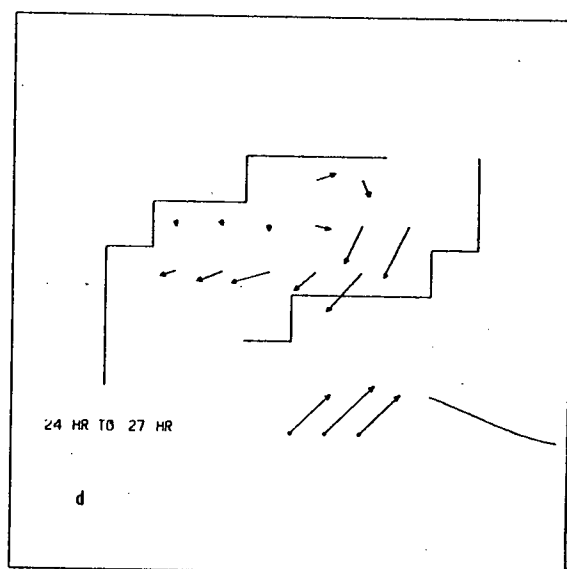
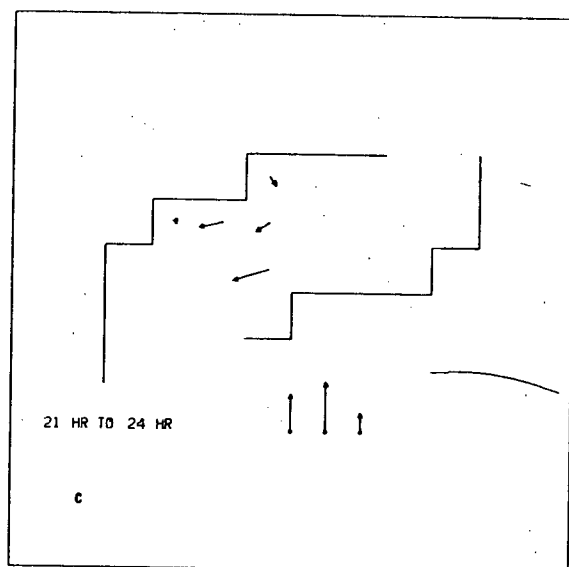
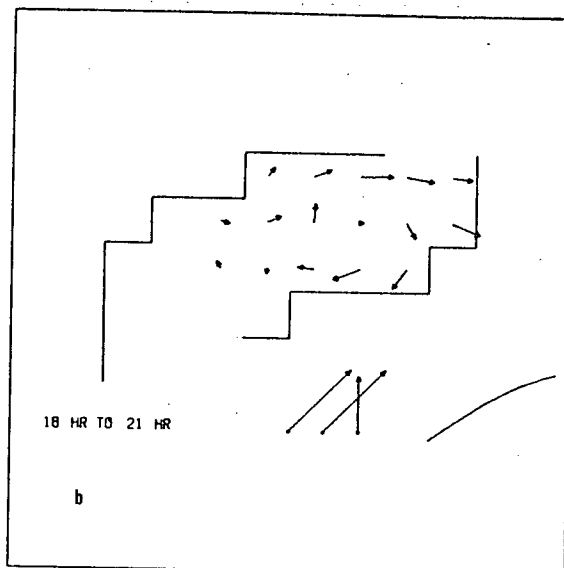
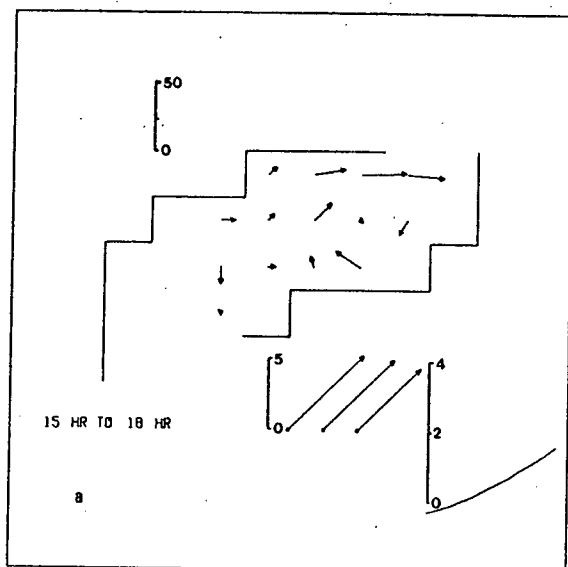


Figure 22 - The week 4 data det.

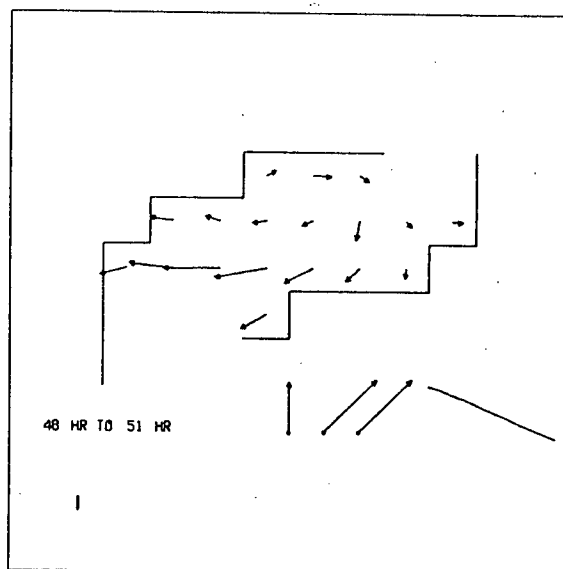
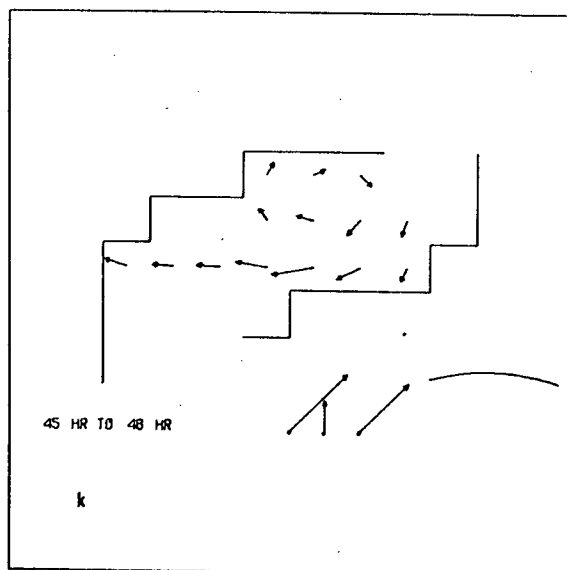
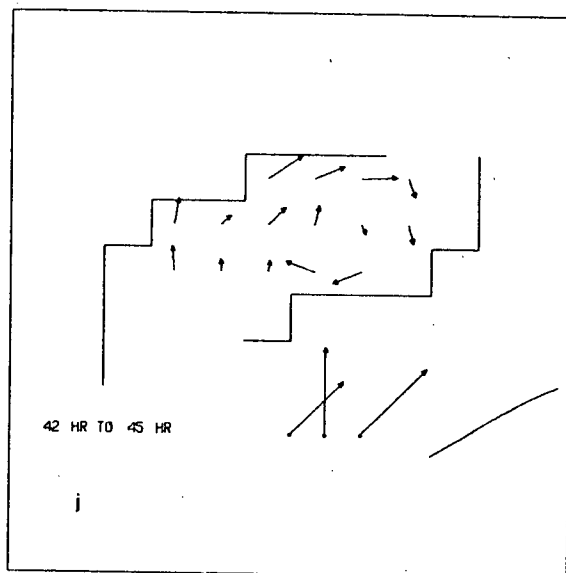
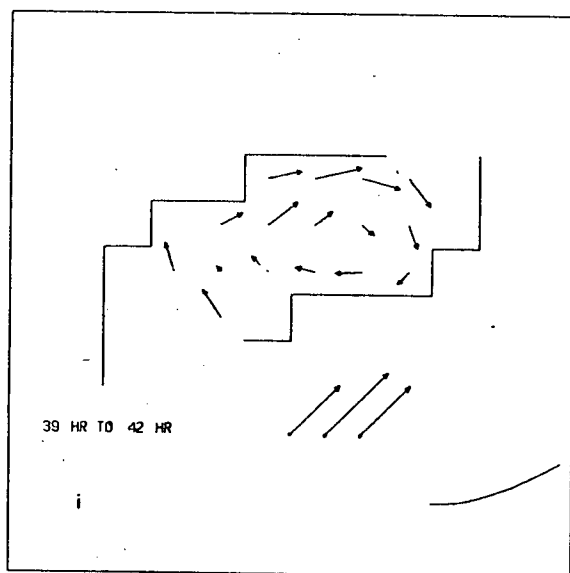
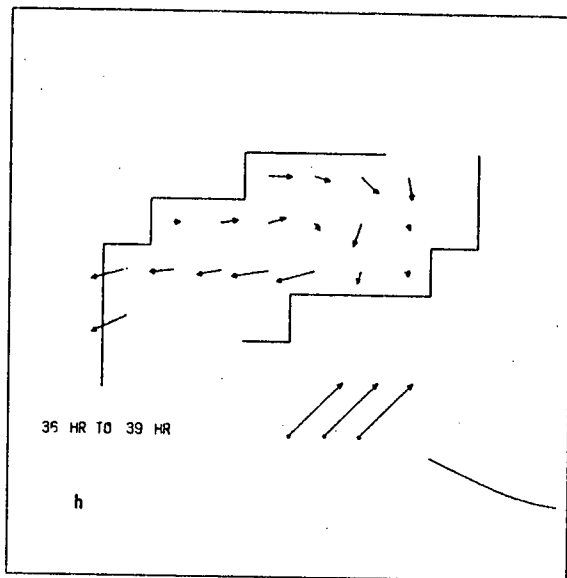
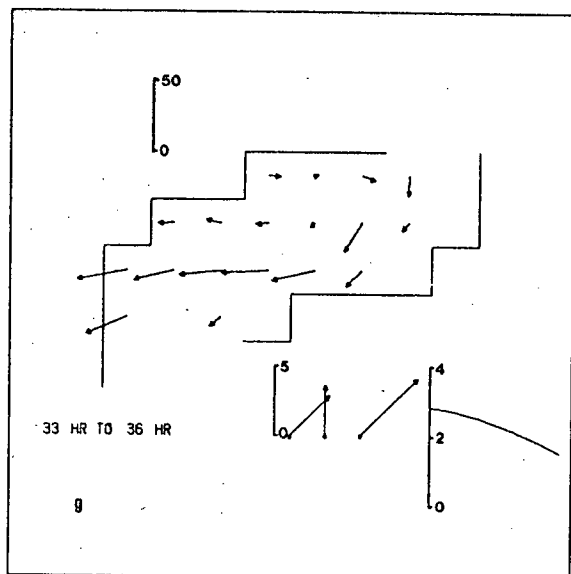


Figure 22 continued.

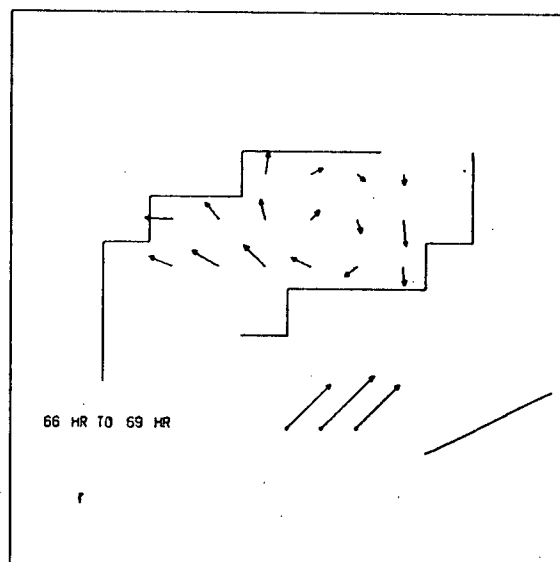
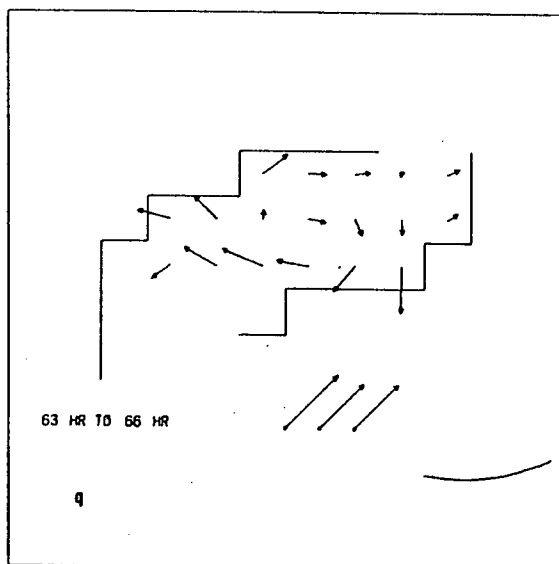
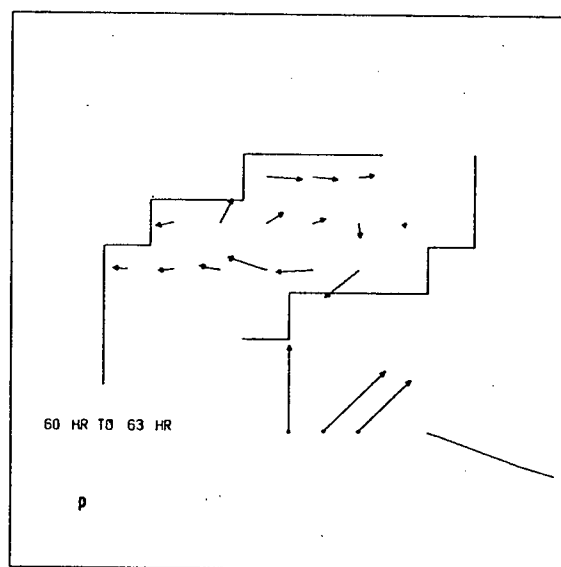
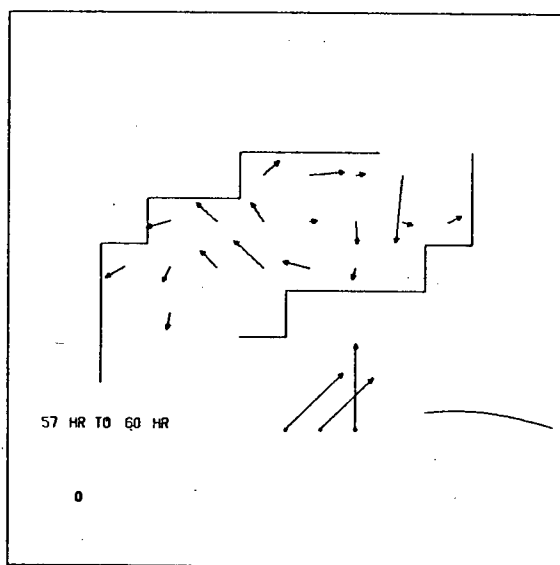
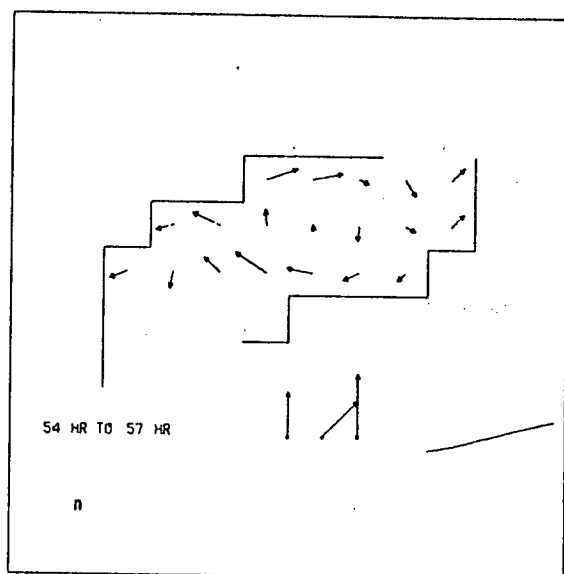
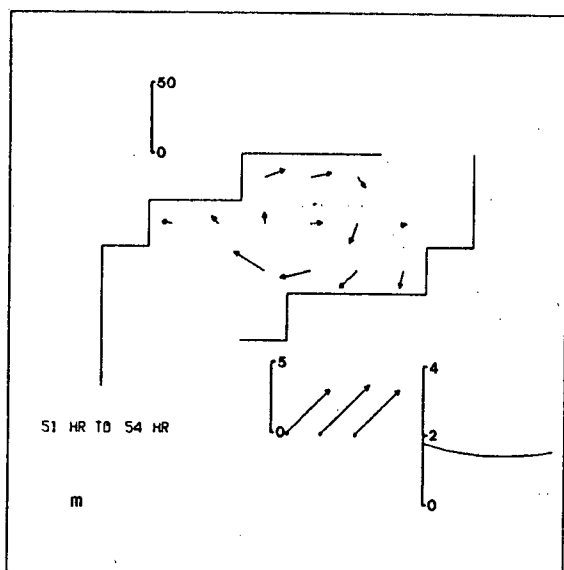


Figure 22 continued.

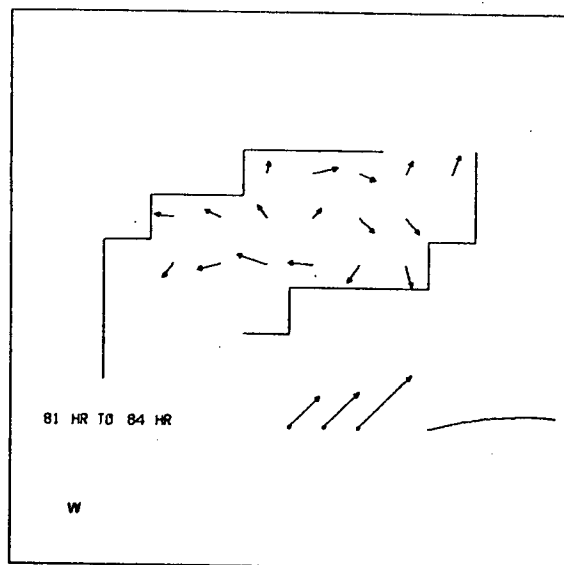
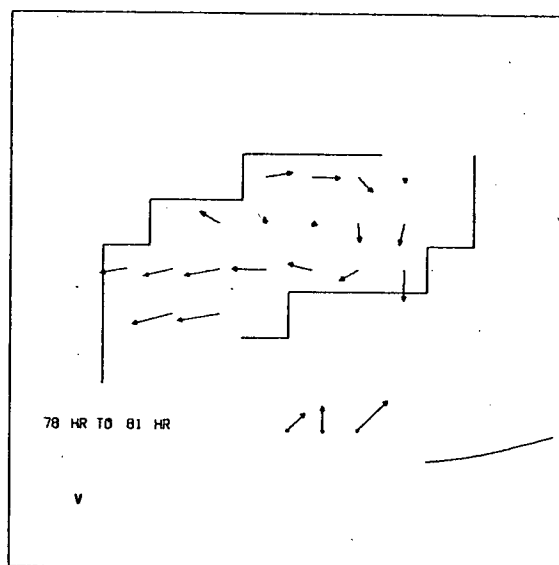
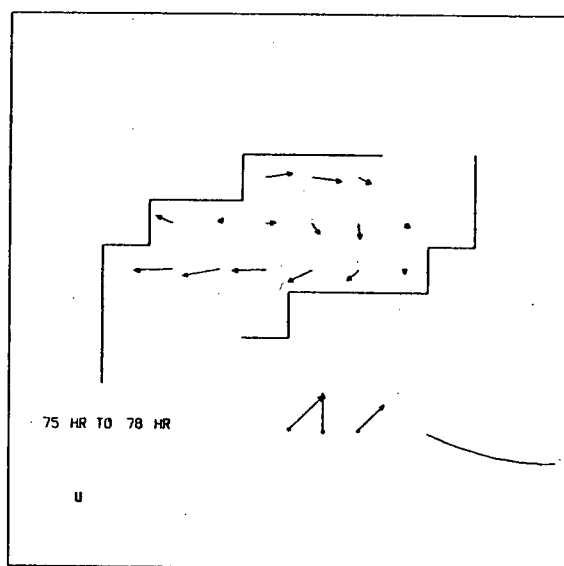
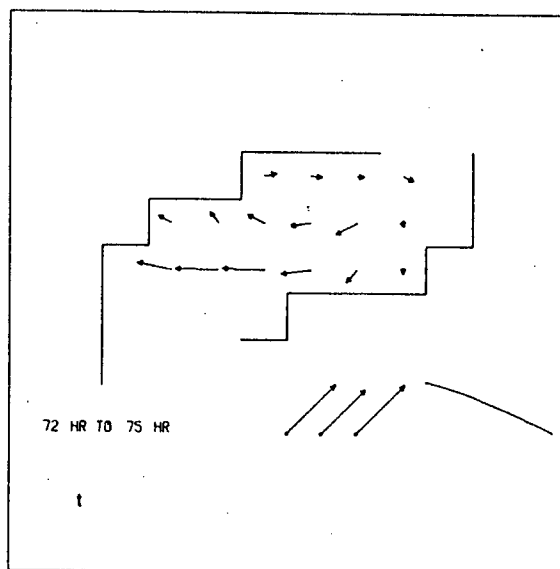
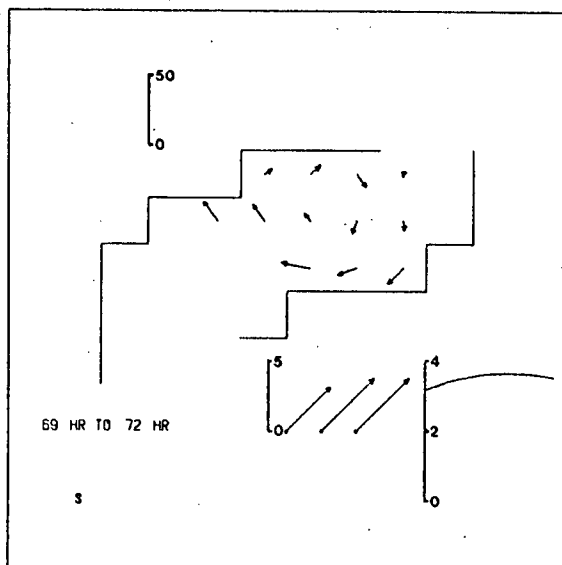


Figure 22 continued.

IV.3.6 Summary Of The Observations

The four weeks of data exhibited two basically different types of behaviour. Wind and tide appeared to have little effect on the current in week 4 and only a small effect in week 2, the weeks closer to the head of the inlet, while the correlation between wind and current appeared to be good in weeks 1 and 3, the areas farther from the head of the inlet.

The effect of the tide cannot yet be ruled out but correlation between tidal height and current did not appear to be as good as the wind - current correlation.

An attempt to verify these hypotheses will be made in the succeeding sections.

IV.4 Temporal And Cross-channel Variations In Surface Layer Flow

Having now had an overview of the general aspects of the data from the surface layer experiment, let us analyse these data in greater detail. A series of five 'bars' were chosen across the inlet at the locations shown in figure 23. Each bar, one mile wide in the long-channel direction, was split into ten equally sized boxes across the channel. The box averages done over one hour time intervals using these boxes are then consistent with the size suggested by the expected scale of variability of the flow as discussed in chapter II.

Figure 24 shows the long-channel component of velocity contoured as a function of cross-inlet position and of time. In a channel of such irregular geometry as Howe Sound, the choice of the long-channel direction at any given point in the inlet is somewhat arbitrary, but has been chosen as the direction of the line that is closest to parallel to both sides of the inlet at that point. This direction is not necessarily the direction of the strongest currents as we shall see. Each of the five frames of this figure represents the data from one of the averaging bars. Also included in each frame are the tidal height curve from Pt. Atkinson and the wind velocity from Squamish. The top of each frame represents the right hand side of the channel (looking upstream). This is the southeast shore in frames a and b, and the east shore in frames c, d, and e. For convenience,

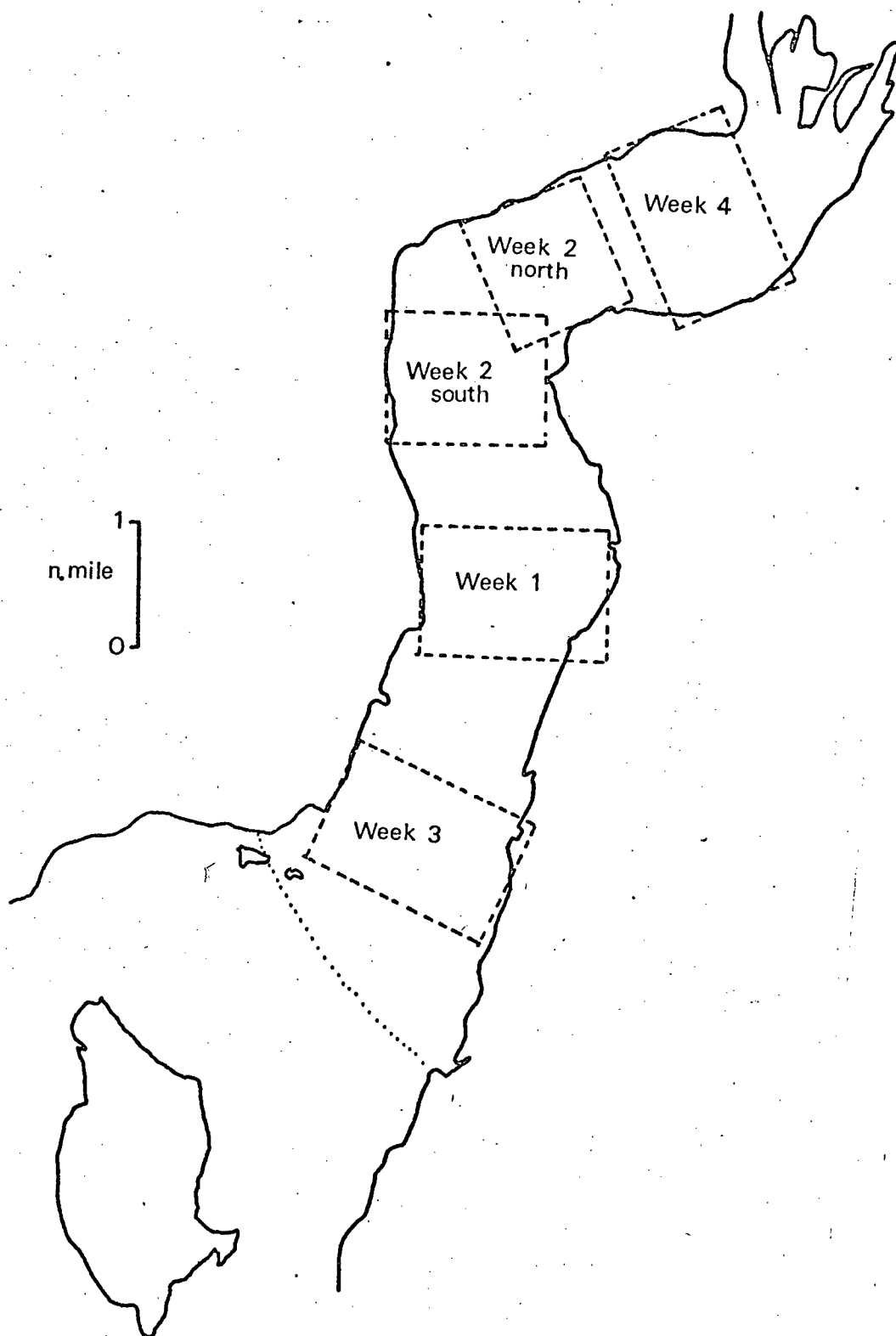


Figure 23 - Location of the five averaging bars.

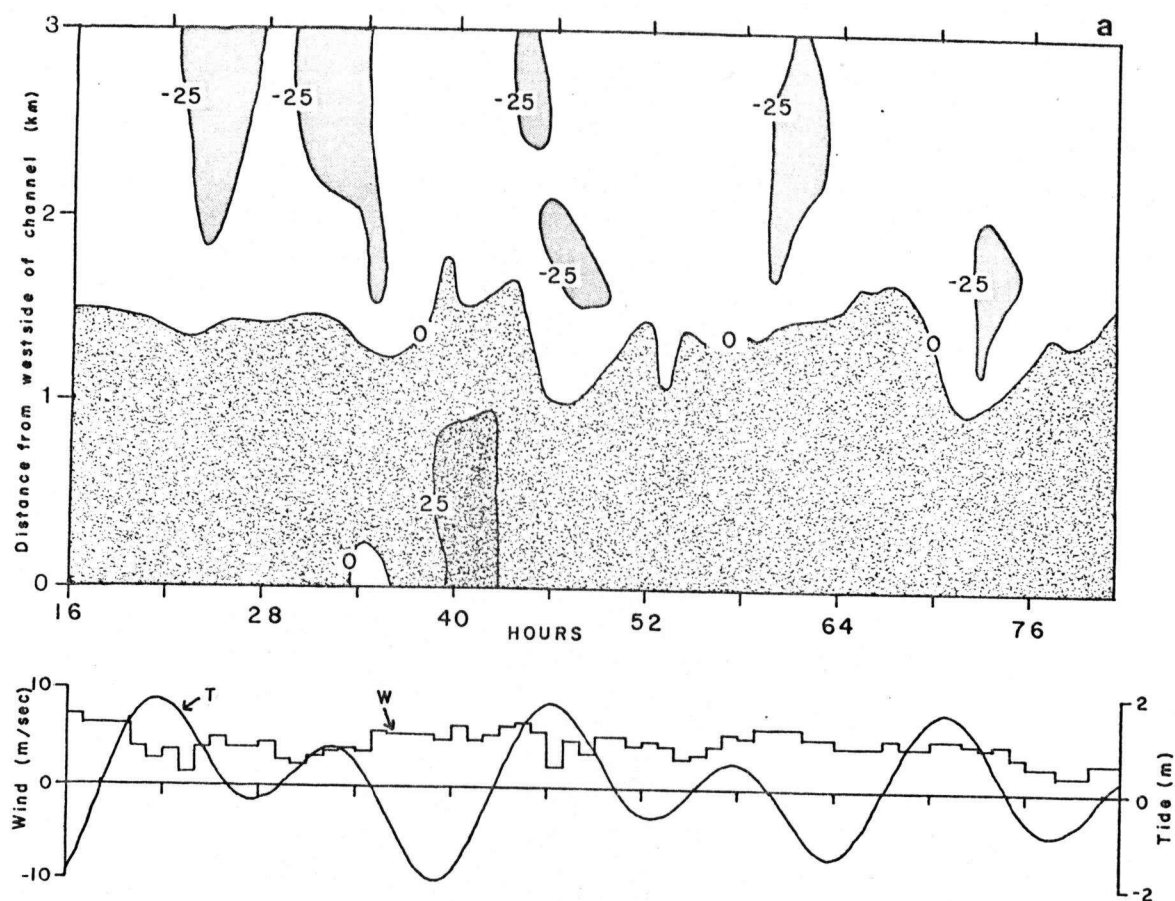


Figure 24 - Contours of long-channel velocity plotted as a function of time (horizontal) and cross-channel position (vertical). Contours are in cm/s. Positive currents are up-inlet. a. week 4. b. week 2(north). c. week 2(south). d. week 1. e. week 3.

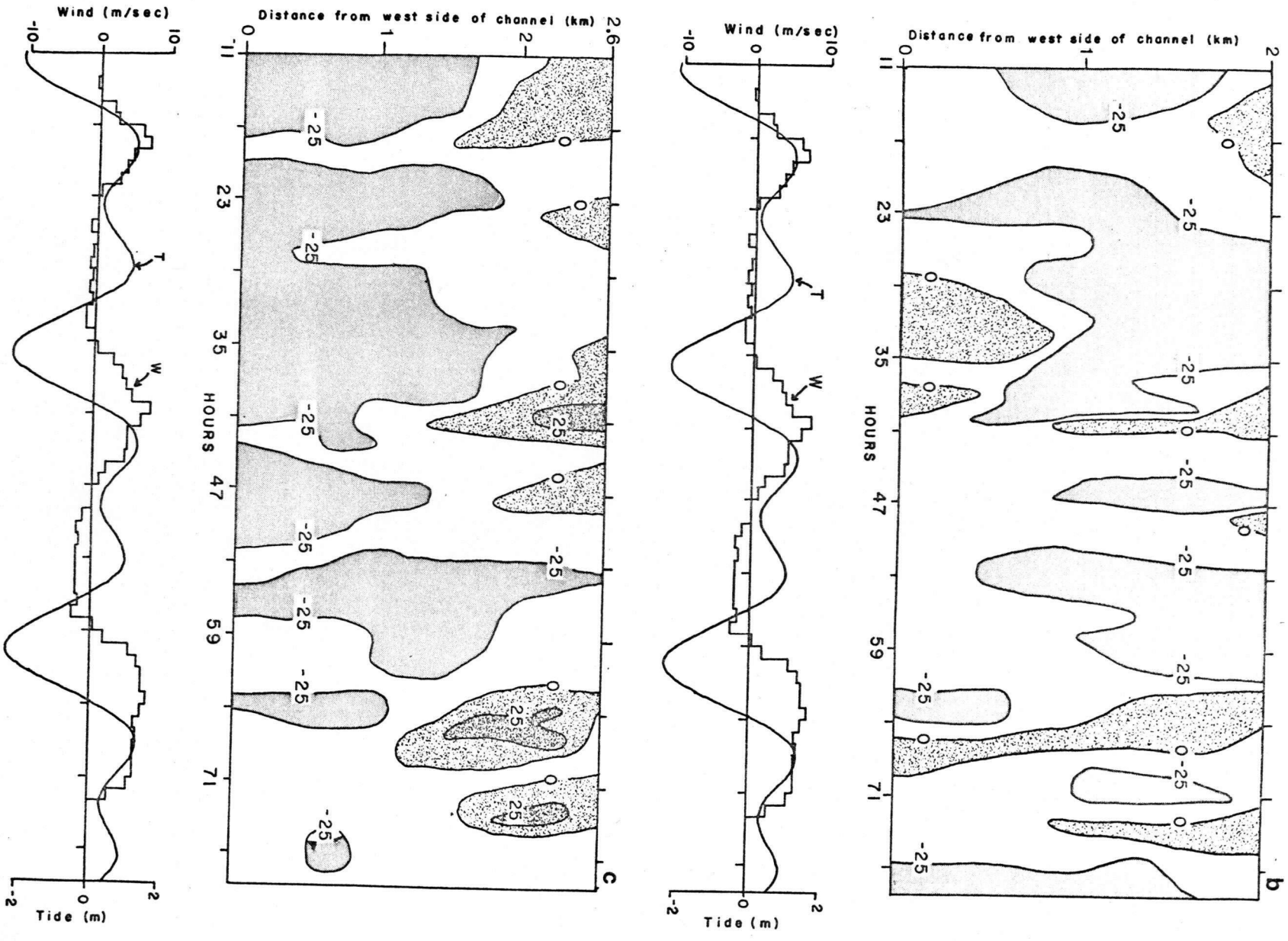


Figure 24 - continued.

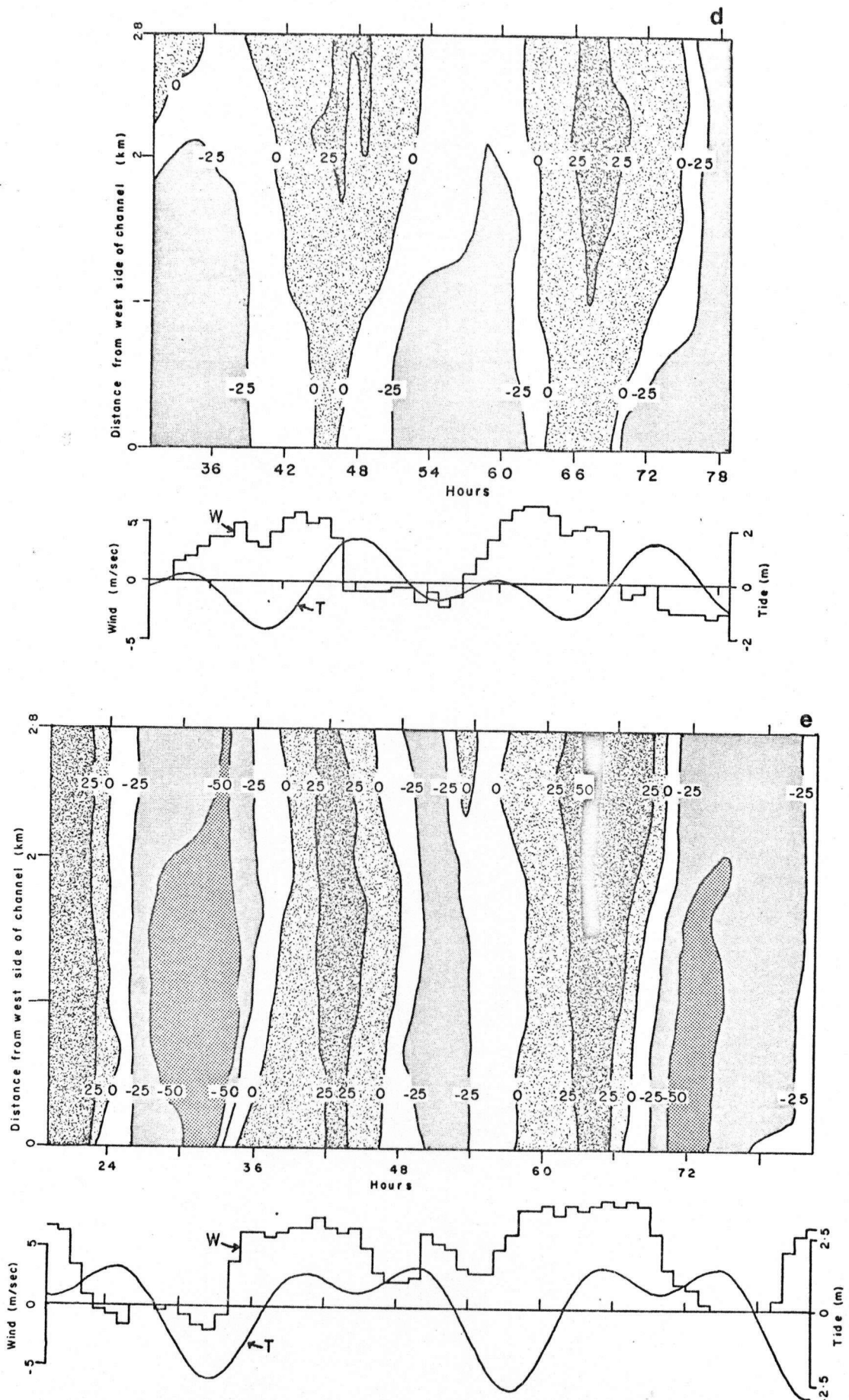


Figure 24 - continued.

this will be referred to from now on as the east shore in all frames. By the same criterion, the bottom of each frame represents the west shore. The frames are arranged in sequence with the band closest to the inlet head first and that closest to the sill last.

In general there is a trend to greater lateral uniformity from frame a to frame e. This trend is evident in that the velocity contours become more closely aligned to the vertical (cross stream) direction proceeding from frame a to e. The region of strongest down-inlet flow is on the east in frames a and b, but shifts to the west in frames c and d. Its location is not obvious in frame e. This presents a picture consistent with the qualitative flow field postulated at the beginning of this chapter.

In frame a there is little variation in wind speed or direction throughout the whole week. Therefore there should be no large variations in the surface current due to wind. The peaks in the down-inlet velocity seem to coincide with peaks in the tidal height. It might be expected that the tidal height and the current would be 90° out of phase, so this apparent in-phase relationship might be indicative of the amplified baroclinic tidal response mentioned in chapter III. This hypothesis will be investigated further in chapter VII.

Frame b has three peaks in the wind curve as well as large tidal variations. Coincident with each up-channel wind peak is an up-inlet current maximum. There is a slight indication of correlation between maximum down-inlet

velocities and peaks in tidal height at about 28, 46, 53, 70 and perhaps 78 hours.

Frame c, made from data taken the same week as frame b, also shows coincidence between up-inlet current maxima and up-channel wind maxima. Tidal height maxima appear to be coincident with maxima in down-inlet velocity, but results seem less certain than in frame b.

In frame d, the variations in current are more regular than in the previous three frames. Maxima in upstream current occur after several hours of up-channel wind. The onset of up-inlet winds seems to be coincident with the time of down-inlet current maxima. The stopping of these winds and the start of down-inlet currents seem coincident. Tidal effects are not obvious. The current maximum at 45 hours occurs just before maximum tidal height; the one at 66 hours, at a minimum of tidal height. Although there are too few cycles to really say for certain, there does not appear to be a consistent relationship between tidal height and current maxima.

In frame e, the current appears to be more laterally uniform. Temporal variations of the current are the strongest of all those observed. As in frame d, maximum up-inlet currents occurred after several hours of up-inlet winds. The down-inlet current maximum at 32 hours was coincident with the increase in wind speed at that time. Strongest down-inlet currents occurred when the wind speed was low. There did not appear to be any tidal correlation.

To summarize this figure we can say that the wind

appeared to play a more dominant role in forcing the surface circulation than did the tide, although near the head of the inlet some tidal effects seem probable. The horizontal shear decreased in strength from the head of the inlet to the sill but the magnitude of temporal variations increased. This last observation may be due of course to differences in the forcing functions from week to week, not to any inherent property of the inlet.

We have looked so far only at the long-channel component of the current. Figure 25 shows the velocity at each cross-channel position for each hour in the averaging bars of week 3 and week 2 (north). In each box, the velocity is represented by a vector, emerging from a small cross marking the centre of the box, pointing in the direction of the average current. The top and bottom of each frame represent east and west in the same sense as the previous figure. A vector pointing to the right therefore represents an average downstream current. In frame a, the currents are basically up and down-channel with no significant cross-channel components. However in frame b, there are two periods when the current appears to be flowing directly across the inlet. It is not clear if this cross-inlet flow is correlated with the wind maxima or with the maxima in tidal amplitude. These occurrences of cross-inlet flow are at times when the river core is forced north of its usual cross-inlet path between Watts Pt. and Woodfibre.

In weeks 1, 3, and 4, the long-channel component of velocity was dominant and in week 2, there were not enough

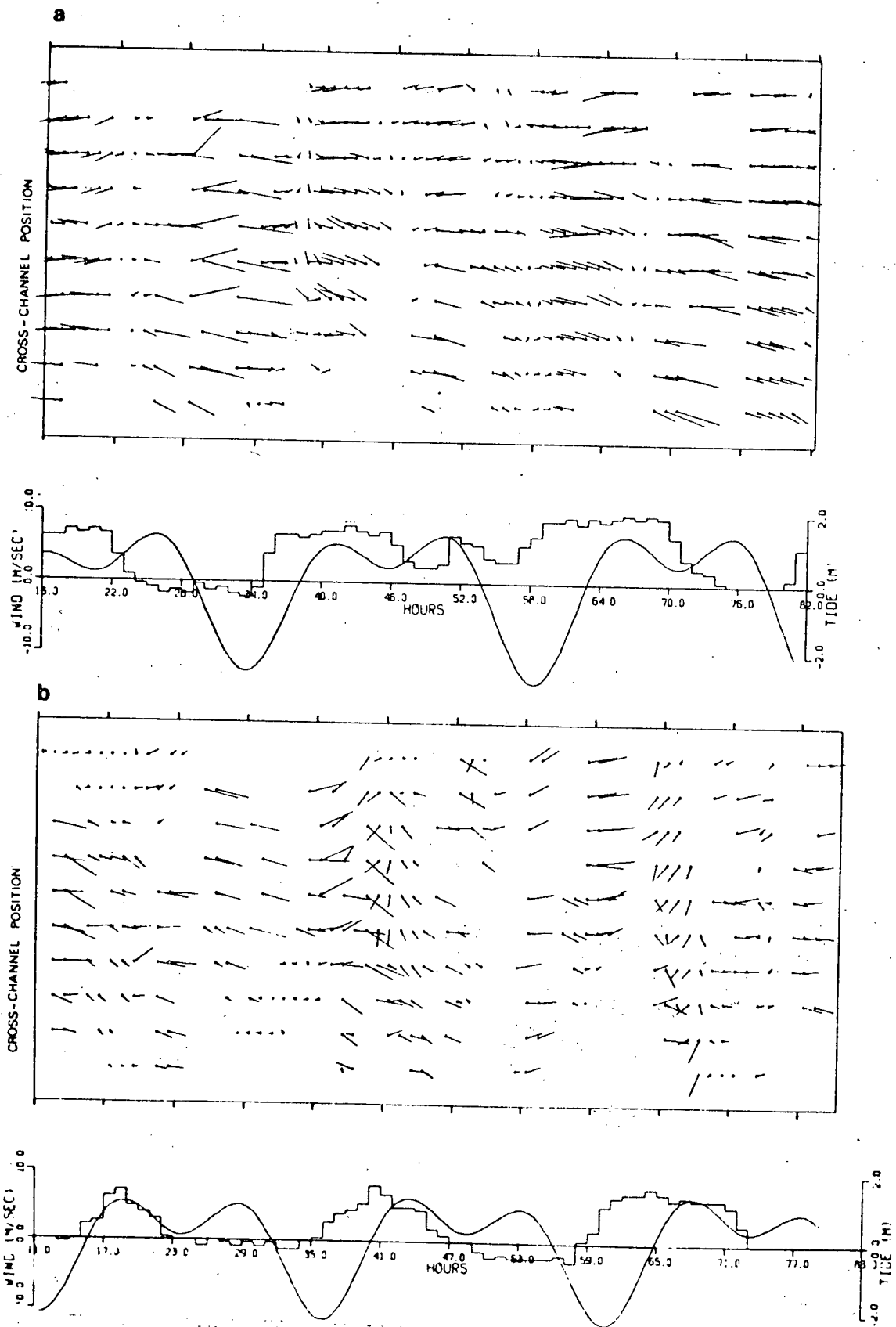


Figure 25 - Relative velocity vs cross-channel position and time for a. week 3 b. week 2N. The arrows represent current vectors. the tails of the vectors are located on small crosses at the centres of the averaging boxes. They point in the direction that the current was flowing to.

measurements made of the movements of the river core to make studies of the cross-stream component possible. Further analyses therefore are of the long-channel component of the quantities of interest only.

IV.5 Lateral Homogeneity Of The Velocity And Acceleration Fields

The contour plots of velocity discussed in the last section showed, in general, a great deal of lateral variation in the flow field. However the velocity extrema occur at about the same time in every cross-channel box. This observation indicates that the time rate of change of velocity may be more uniform than the velocity itself. Acceleration data were calculated as the second derivative of the spline fitted drogue positions. These accelerations may, on average, be taken to be the time rates of change of velocity in the weeks 1 and 3 data sets as is described later in this chapter. Since the curve fit was cubic, these accelerations are linear from point to point of the input data.

Small errors in establishing drogue positions led to much larger errors in the second derivatives of these position estimates. Although the spline fitting routine attempted to minimize changes in second derivatives, the accelerations cannot be expected to be as smooth as the velocities. Thus more accelerations than velocities must be averaged together to produce a smoothly varying function of

time or space. The average number of values in a single box of the size used to generate the contour plots produces smooth velocities but does not produce smooth accelerations. Therefore meaningful contour plots of acceleration cannot be produced.

The accelerations produced from the week 1 data set were the smoothest of all those calculated and are, on average, equivalent to the time rates of change of the velocities. Using them, a rough check on the hypothesis of lateral homogeneity of acceleration may be performed. Figure 26 shows velocity vs. time and acceleration vs. time curves for three separate cross-channel locations in week 1. The data, from the same sort of box averaging done to produce the contour plots of the last section, are for box 2, near the east side of the channel; box 5, in mid-channel; and box 9, near the west side. The three velocity curves can be seen to have essentially the same shape but substantially different mean values. The maximum values, at least in the up-inlet direction, occur within an hour of the same time for all three curves.

Although the acceleration curves at first may appear to be quite different from each other due to the high noise level associated with the small number of data averaged in each box, the general features of each curve are the same. The up-inlet accelerations between 36 and 48 hours and the down-inlet accelerations between 48 and 57 hours and between 72 and 79 hours are common to all three curves. The high noise level tends to obscure the resemblance between the

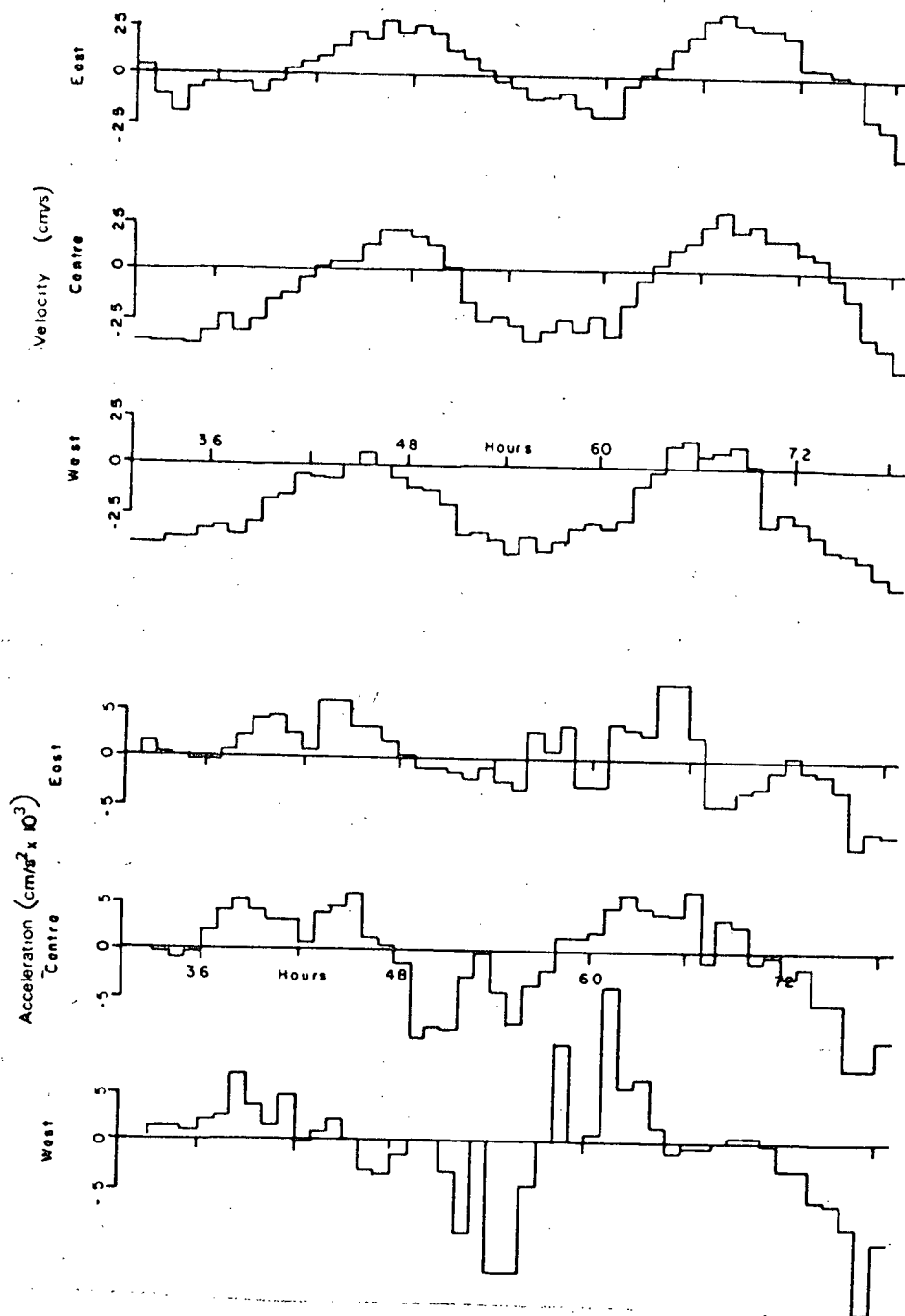


Figure 26 - Velocity and acceleration vs time at 3 cross-channel locations in week 1.

three curves between 48 and 72 hours, but there is a common period of down-inlet acceleration followed by an up-inlet period in all three. The mean values of the three curves appear to be about the same. The high noise level in the acceleration curves may be due partly to local spatial gradients of the velocity field. These gradients may make an important contribution to the acceleration on a small scale, but have a negligible effect when averaged over the entire week 1 data set as is shown in section IV.8.

The velocity curves can be interpreted as showing a mean shear flow overlaid by a laterally homogeneous time varying flow. The acceleration curves show no strong evidence of lateral variation, suggesting that the forces causing temporal variations act homogeneously across the inlet, and that the search for the relationship between the various forces and the temporal variations in the surface flow field may be justifiably performed on lateral averages of velocity and acceleration.

IV.6 Temporal Variations In Laterally Averaged Velocities And Accelerations

The time-varying character of the surface layer flow will be presented in this section using data averaged across the inlet. Data were taken from each of the four weeks and box-averaged according to the scheme described earlier in this chapter. The ten box averages for each hour were averaged to give the data sets presented here. Only one of

the week 2 data sets has been used. Since the variations in wind velocity were very small in week 4, the data from week 2 (north) have been used instead of those from week 2 (south) because they represent the behaviour of the flow north of Watts Pt. The laterally averaged velocity and acceleration data are plotted in figure 27. The four plots on the left hand side of the figure are velocity vs time plots, the four on the right are acceleration vs time plots. The order from top to bottom is from the head of the inlet to the mouth.

Plot a shows the average velocity in week 4. As might be expected from the contour plot, the average velocity is close to zero with a range of only about ± 15 cm/s. The small variations in velocity appear to be almost 180° out of phase with the tidal height. The acceleration, plot b, is negative for almost all the time period. This result is a manifestation of the difference between the total acceleration ($D\bar{u}/Dt = \partial\bar{u}/\partial t + \bar{u} \cdot \nabla\bar{u}$), which the drogues measure, and the Eulerian time rate of change, which a current meter would measure, and indicates that the long-channel rate of change of velocity is a significant part of the total acceleration. Results of calculations of the magnitudes of the temporal and spatial velocity gradients are given in section IV.8. The variations in the acceleration are too small to correlate with either wind or tide.

Plot c shows the velocity vs time information for week 2 north. The velocity stayed at about -25 cm/s for about half the time and made excursions of $+40$ to -25 cm/s from this value. The three peaks in up-channel velocity occur

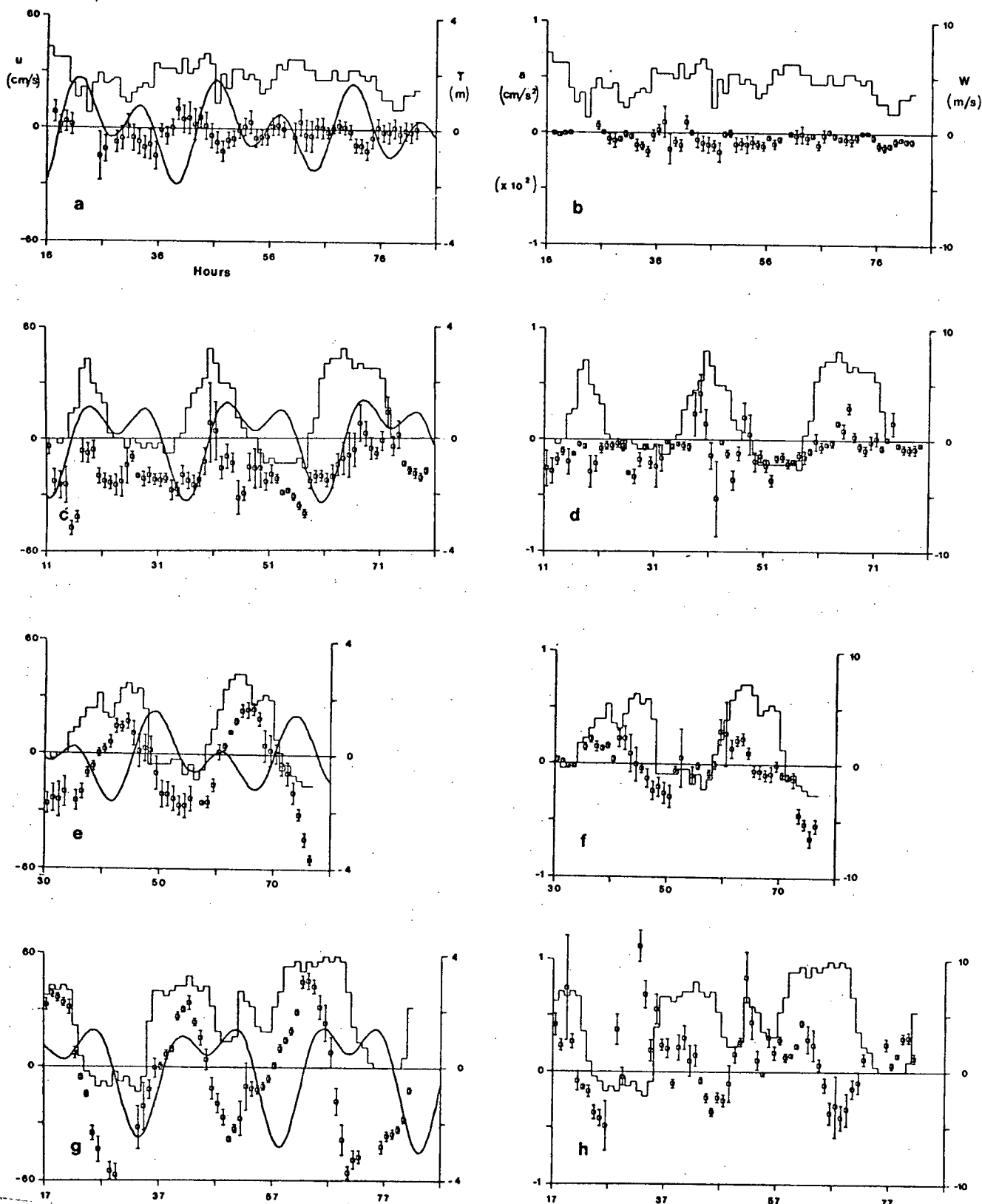


Figure 27 - Laterally averaged velocity and acceleration vs time. Velocity is on the left, acceleration on the right. The curved line on the left plots is the tidal height, the squared line on all plots the long-channel wind component. Progression from top to bottom is from head to sill. The error bars on the velocity and acceleration points are ± 1 SE. a and b. week 4. c and d. week 2N. e and f. week 1. g and h. week 3.

during the three periods of up-channel winds. These peaks could also be associated with the tidal height but then would have the opposite phase relationship with the tide to the week 4 data in plot a. As will be shown in chapter VII, the up-channel velocity is approximately out of phase with the tide and thus the coincidence of the tidal peaks with the wind peaks probably reduces the velocity peaks to below what they would have been if the tidal effects did not occur. In plot d, the week 2 acceleration plot, periods of up-inlet acceleration coincide with two of the up-inlet wind peaks. Although the velocity in c shows no trend, the acceleration in d is, in general, negative, indicating the same sort of relationship between time and space gradients of velocity as in plot b.

Plot e shows the velocity from the week 1 data set. The two velocity maxima are in phase with the wind. A constant phase relationship between the currents and tidal height is not evident. The same observations can be made from plot g, the week 3 data. From these observations it appears that the wind is causing the variations in the surface current. The acceleration plots, (f and h), for weeks 1 and 3 help to confirm this deduction. They both show periods of relatively constant up-inlet acceleration starting at the onset of up-inlet winds. These periods last 6 to 8 hours. Each period is followed by a period of negative acceleration. This sort of behaviour will be shown to be consistent with a model of inlet behaviour that predicts a surface layer acceleration proportional to wind stress until the stress is balanced by

the surface pressure gradient.

IV.7 Cross-channel Structure Of The Velocity Field

It is possible to gain some insight into the lateral structure of the long-channel currents in Howe Sound by looking at a temporal average of the data. Data were averaged in each box in a cross-channel averaging bar for the entire length of each week's observations. These averages were then combined on the plots of figure 28 to show the average cross-channel structure of the currents for each week.

When time averaging periodic data, it is necessary to use an averaging interval that is an integral number of periods long. Otherwise, anomalous values result. It is apparent from figure 27 that the velocity data from this experiment are quasi-periodic, particularly in weeks 1 and 3 when the variations in wind velocity were large. The data are not periodic enough however to choose averaging intervals that started and ended with the same amplitude and phase. Thus the average values may be in error. However, if the time variations are independent of the cross-channel position as hypothesized, then the temporal averages are representative of the cross-channel variations in the flow but the mean flow across the channel may be in error because of the averaging over a small and non-integral number of cycles.

Looking then at figure 28, we see that the down-inlet

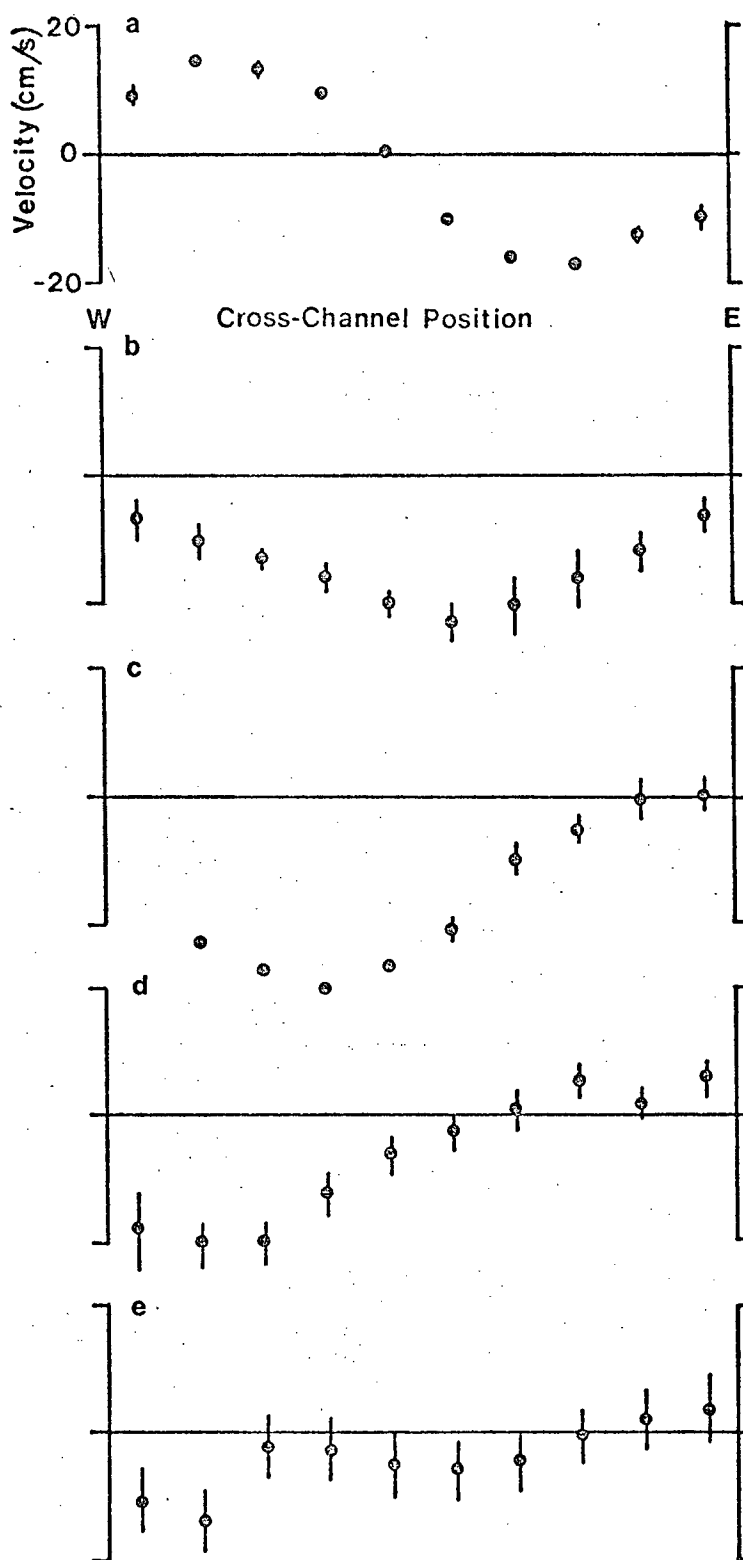


Figure 28 - Time averaged velocity vs cross-channel position. Bars are \pm two standard errors of the mean.
 a. week 4 b. week 2N c. week 2S d. week 1 e. week 3.

flowing river core moves from the east side of the channel in week 4 to the west side in week 1. This core spreads out across the channel as it moves down-inlet. There appears to be somewhat of a decrease in core width from week 2N to 2S. This change is probably due to the geometry of the channel between those two averaging areas. The sharp bend around Watts Pt. forces the flow to the western shore where the forces causing the flow to change direction and hence to converge seem to be larger than those causing it to spread.

The fact that these temporal averages produce a picture of the surface layer current structure consistent with the one formed from all the other forms of data presentation is not particularly significant. What is significant is that this consistency supports the hypothesis that the lateral structure of the surface layer is basically decoupled from the time varying structure. This conclusion is based on the premise that, if the lateral structure were significantly time dependent, then temporal averaging over an arbitrary period would tend to obscure this structure.

IV.8 Ensemble Averaged Velocity Gradients

Calculations of the velocity gradients $\partial u / \partial x$ and $\partial u / \partial y$ in these experiments exhibit large statistical uncertainties. These uncertainties, arising from calculations involving up to fourth differences of the observed values, tend to obscure any significant temporal or spatial variations in the quantities. However, there are enough determinations of these quantities each week to allow statistically significant ensemble averaging of them. These ensemble averages were formed by calculating every value possible of the quantity of interest from the box averaged data each week and averaging these together.

If the cross-channel velocity v is assumed to be small with respect to the long-channel velocity u , then the acceleration as measured by the drogues may be represented by $a_D = a_t + a_x$ where $a_t = \partial u / \partial t$ and $a_x = u \partial u / \partial x$. The term a_t may be approximated from the data set by $a_t(t_i) = (u(t_{i+1}) - u(t_{i-1})) / (t_{i+1} - t_{i-1})$ and hence a_x may be calculated from $a_x(t_i) = a_D(t_i) - a_t(t_i)$. In these equations t_i represents the time of the i 'th cross-channel average, t_{i-1} the time of the previous average and t_{i+1} the time of the next average. Ratios of a_x to a_t are shown in table VI. As seemed apparent from figure 27, the acceleration data from weeks 2 and 4 are influenced by spatial gradients much more greatly on average than are the data from weeks 1 and 3. In figure 27 the acceleration curves for weeks 1 and 3 appear to be the time derivatives of the velocity curves. This result is

Table VI - Ensemble average acceleration ratio and velocity gradients. Acceleration ratio is $u \partial u / \partial x$ divided by $\partial u / \partial t$. The velocity gradients $\partial u / \partial x$ and $\partial u / \partial y$ are in units of $\text{cm s}^{-1} \text{km}^{-1}$. Also shown are the standard deviation and the standard error of the mean value (or r.m.s.) of each quantity. The standard error gives an indication of the accuracy of the value, the standard deviation, of the spread in values.

Data set	wk 4	wk 2N	wk 2S	wk 1	wk 3
ratio					
mean	-0.88	-0.85	-0.41	0.02	-0.09
st. dev.	1.14	1.32	1.30	1.05	0.99
st. err.	0.07	0.14	0.09	0.08	0.07
$\partial u / \partial x$					
mean	1.7	-2.6	2.8	4.3	0.7
st. dev.	15.6	25.0	7.3	10.0	8.8
st. err.	0.9	2.6	0.5	0.7	0.6
$\partial u / \partial y$					
r.m.s.	18.5	17.4	18.0	15.5	11.1
st. dev.	7.9	18.7	18.6	13.8	25.9
st. err.	0.4	1.3	0.7	0.8	1.5

substantiated by the $|a_x/a_t|$ ratios for those weeks of less than 0.1. In weeks 4 and 2(north) the acceleration appeared to have a large component that did not vary as the time derivative of the velocity. This feature is also substantiated by the acceleration ratios. One question arising from table VI is the difference in ratios between week 2N and week 2S. It seems unusual that the acceleration ratio for the southern section should be only half that in northern section, in spite of similar wind and tidal conditions. The section from week 2 (north), alone of the five examined, often had cross-channel currents as strong as the long-channel ones. Therefore it is not correct to assume

that $u \partial u / \partial x \gg v \partial u / \partial y$. Hence the split of the total acceleration into terms containing only gradients of t and of x is probably incorrect. The ratio of the spatial gradient acceleration to the temporal gradient acceleration is likely incorrect for the same reason.

These same calculations of a_x lead to the only direct determination of the long-channel velocity gradient $\partial u / \partial x$. Table VI shows the ensemble average of $\partial u / \partial x$ for each section. These were calculated by ensemble averaging all calculable values of a_x / u . With the exception of the week 2N value, all are positive as is expected from the traditional estuarine salt balance equations. The value for week 2N is probably wrong for the reasons given above. The remaining values may be combined to yield an average value for $\partial u / \partial x$ of $2.4 \pm 0.8 \text{ cm s}^{-1} \text{ km}^{-1}$.

The calculation of $\partial u / \partial y$ was also possible from the box averaged data sets. It was calculated as an ensemble average of the quantity $(u(y_i) - u(y_{i-1})) / \delta y$ where $u(y_i)$ and $u(y_{i-1})$ are spatially adjacent velocity estimates and δy is the separation between the adjacent boxes. Since it is expected that the average measured shear across the inlet at any one time will be nearly zero due to its change in sign across the section, the r.m.s. shear was calculated rather than the mean as an estimate of the amount of shear present in each week of the experiment. The results of these calculations are also shown in table VI. These results show the expected decrease in shear from the head of the inlet to the sill. The average of these values is $16 \pm 3 \text{ cm s}^{-1} \text{ km}^{-1}$.

These average velocity gradients may be used to deduce consistent dimensions for the averaging boxes used in this analysis. The ratio of $\partial u / \partial x$ to $\partial u / \partial y$ is 0.15 ± 0.05 . As was discussed in chapter II, the ratio of width to length (cross-channel dimension to long-channel dimension) of any averaging box should be the same as this ratio to be consistent. The dimensions usually used were 0.2 to 0.3km by 1.8km yielding ratios between 0.11 and 0.16. Thus the box dimensions used were satisfactory by this criterion.

CHAPTER V

INTERLUDE - THE THREE LEVEL DROGUE EXPERIMENT

The surface layer drogue study just described showed remarkable horizontal spatial variability in the observed currents. The comprehensive set of current meter measurements that will be discussed in the next chapter provide a picture of the temporal and vertical spatial variability of the subsurface currents in Howe Sound, but unfortunately provided no clue to the deeper horizontal structure. On September 6, 1973, a short pilot experiment was performed at the week 1 location to gain some insight into the horizontal and vertical structure of the currents in the near surface region.

The basic procedure of the experiment was the same as the surface drogue study. The data were collected and recorded in the manner described in chapter II. The drogues were, however, deployed in a somewhat different manner. The pole and sail assemblies were the same as previously described but the sails were suspended in various ways to cover the depth ranges 0-2m, 2-4m and 4-6m. To cover the 0-2m depth range, the sails were attached to the poles in the standard manner. To cover the 2-4m range, the sails were attached by their top rings to the bottom snap hooks of the poles. To cover the 4-6m range, the sails were suspended by 2m of polypropylene rope from the bottom snap hooks of the

poles. These three types of drogue will be referred to from here on as the shallow, intermediate and deep drogues respectively. Although the shallow drogues closely followed the current from 0-2m, it is possible that the intermediate and deep drogues did not measure the deeper currents as faithfully because of drag on the surface area they had in the shallow zone. The half-submerged flotation sphere had an approximate drag area of 500cm² in the upper 20cm of the water column and the submerged half of the pole had an approximate area of 450cm² in the upper 2m.

The drag on this area caused by the velocity difference between the upper and lower layers changes the velocity estimate of the lower layer made with the drogues according to the following equation:

$$|\vec{U}_{DT} - \vec{U}_{DM}|^2 A_D = A_S |\vec{U}_{ST} - \vec{U}_{DM}|^2 \quad (5.1)$$

assuming that the drag coefficients are about the same in the two layers and that the drag forces are anti-parallel. In this equation \vec{U}_{ST} is the true velocity at depth, \vec{U}_{DM} is the measured velocity at depth and \vec{U}_{ST} is the true shallow velocity. A_S and A_D are the areas of the drogue in the shallow and deep zones respectively. Here the ratio of A_S/A_D is 1/60. The difference $|\vec{U}_{DT} - \vec{U}_{DM}|$ in this experiment had a maximum value of 1 cm/s and was usually smaller. It will be ignored for subsequent analysis.

The drogues were tracked from 1120 when the experiment

started until 1420 when rain obliterated the radar picture. The shallow drogue tracks are shown in figure 29. The flow observed was a typical one. There was a strong southward flow in the western half of the region and a moderately strong northward flow in the eastern half. Drogue S3 moved cross inlet from west to east in agreement with the standard eddy pattern observed in week 1 of the surface experiment.

The tracks of the intermediate drogues are shown in figure 30. The westernmost drogue, I1, moved steadily down-inlet, but the rest moved up-inlet. I2 appeared to start down but was caught by the up-inlet flow and reversed its direction. The strongest flow was roughly mid-channel. The tracks from the deep drogues are shown in figure 31. The westernmost drogue, D1, went nowhere but the other four moved up-inlet with the strongest flow east of the centre of the inlet.

Velocities were calculated for all the drogue tracks and box averaged for each layer in boxes $1/5$ of the inlet width wide by three hours long. The result of this procedure is shown in the velocity contoured section in figure 32. The obvious features of this figure are the wedge of outflowing river water on the western side and the core of return flow just east of centre channel at 3m depth.

Unfortunately, personnel and a vessel were not available to make density measurements at the same time as the drogue measurements, so no comparison can be made between the currents and density structure.

The conclusion from this short experiment is that the

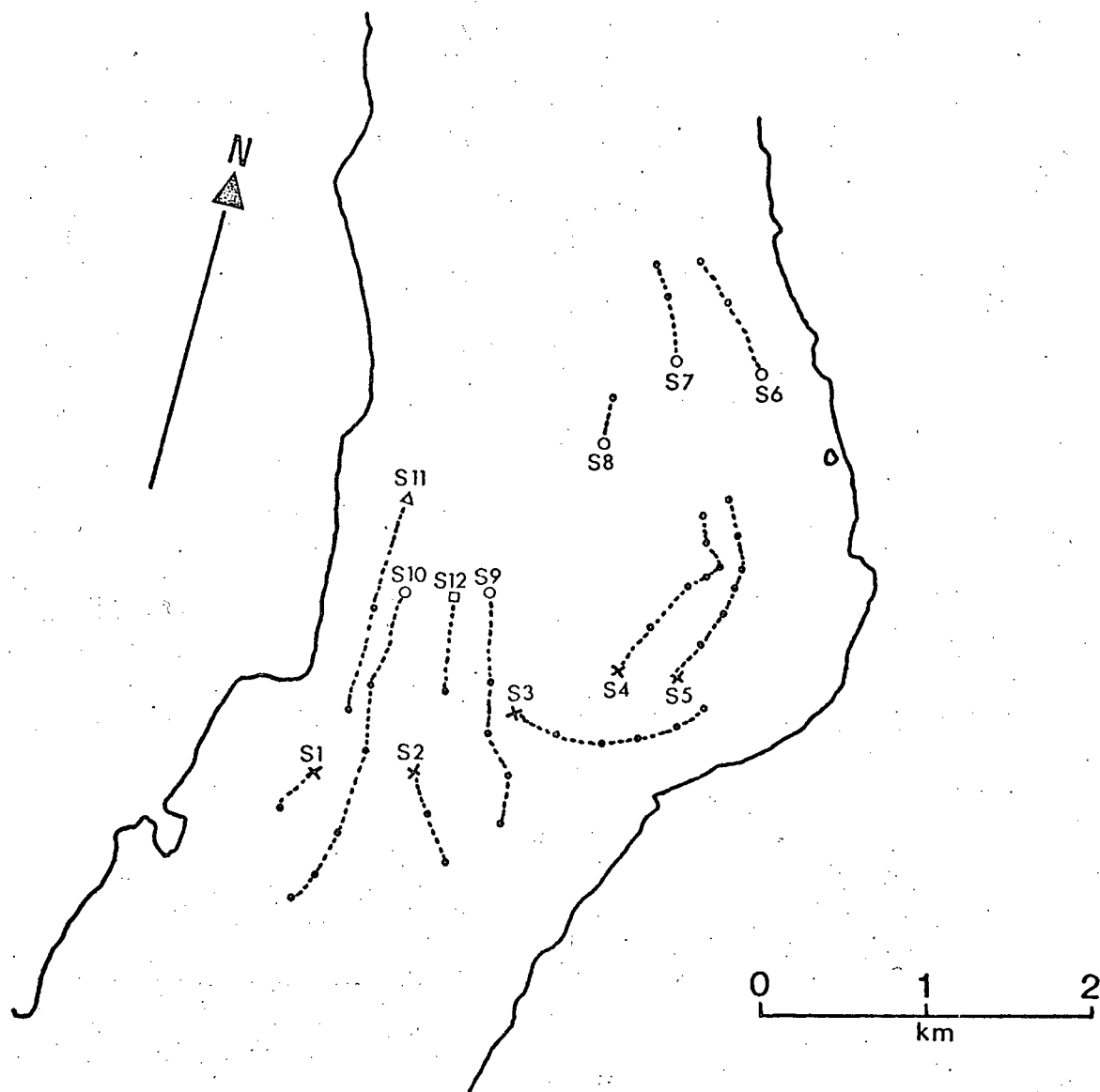


Figure 29 - Shallow drogue tracks. Symbols indicate the time of first observation of each drogue: x 1156, o 1226, Δ 1320, □ 1352. Heavier dots are located approximately every half-hour along the tracks.

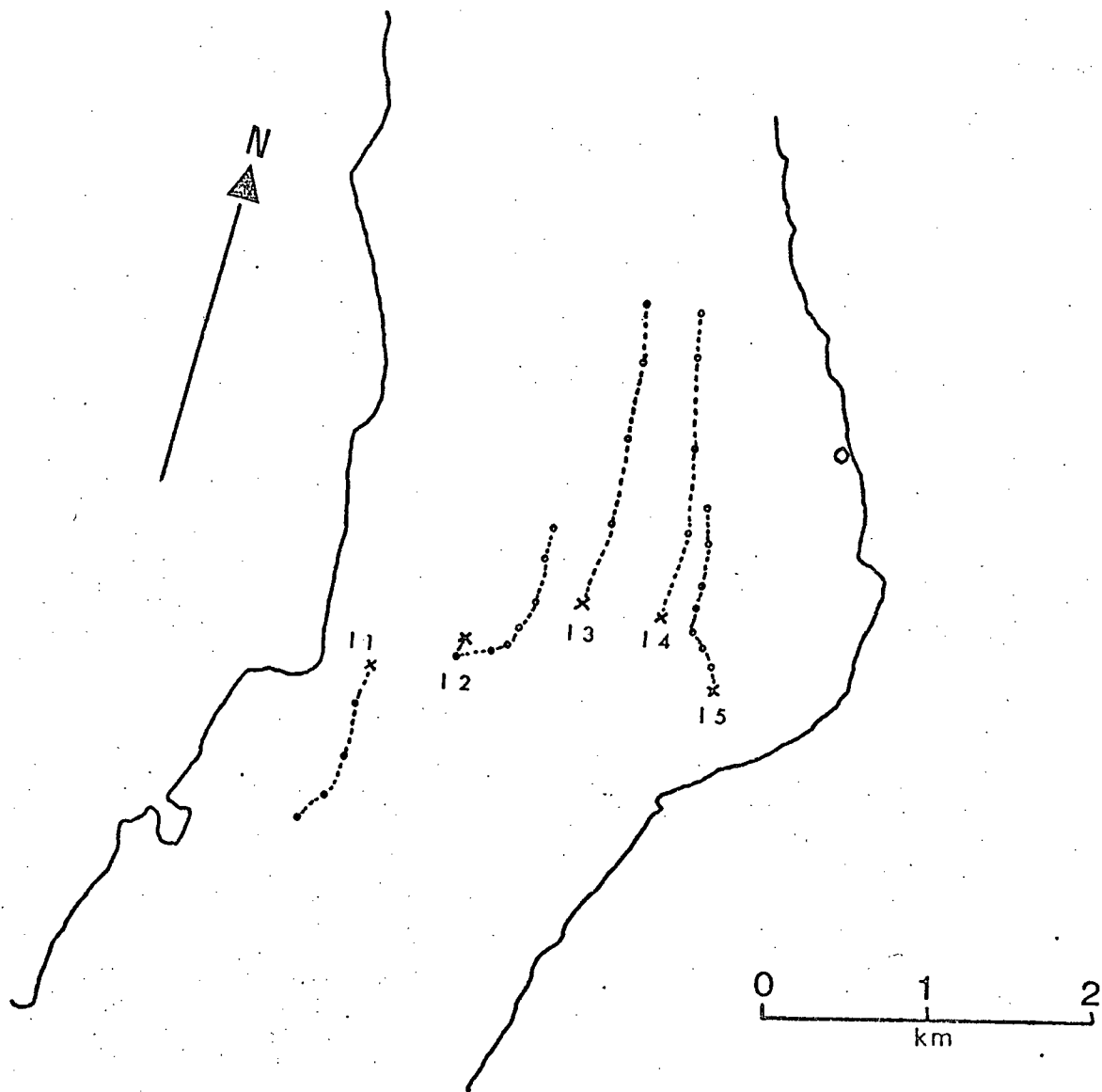


Figure 30 - Intermediate drogue tracks. All drogues were first observed at 1124.

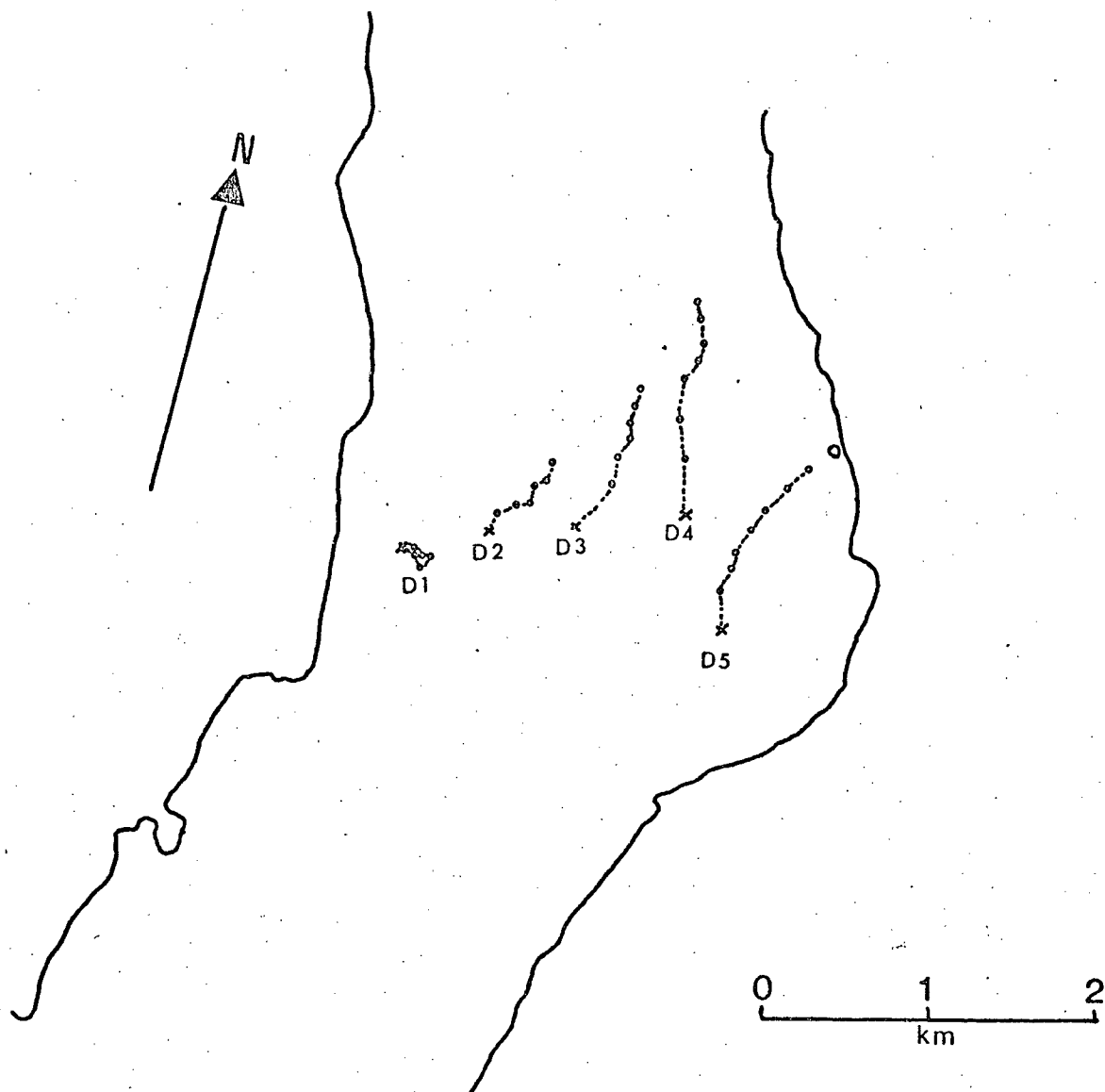


Figure 31 - Deep drogue tracks. All drogues were first observed at 1124.

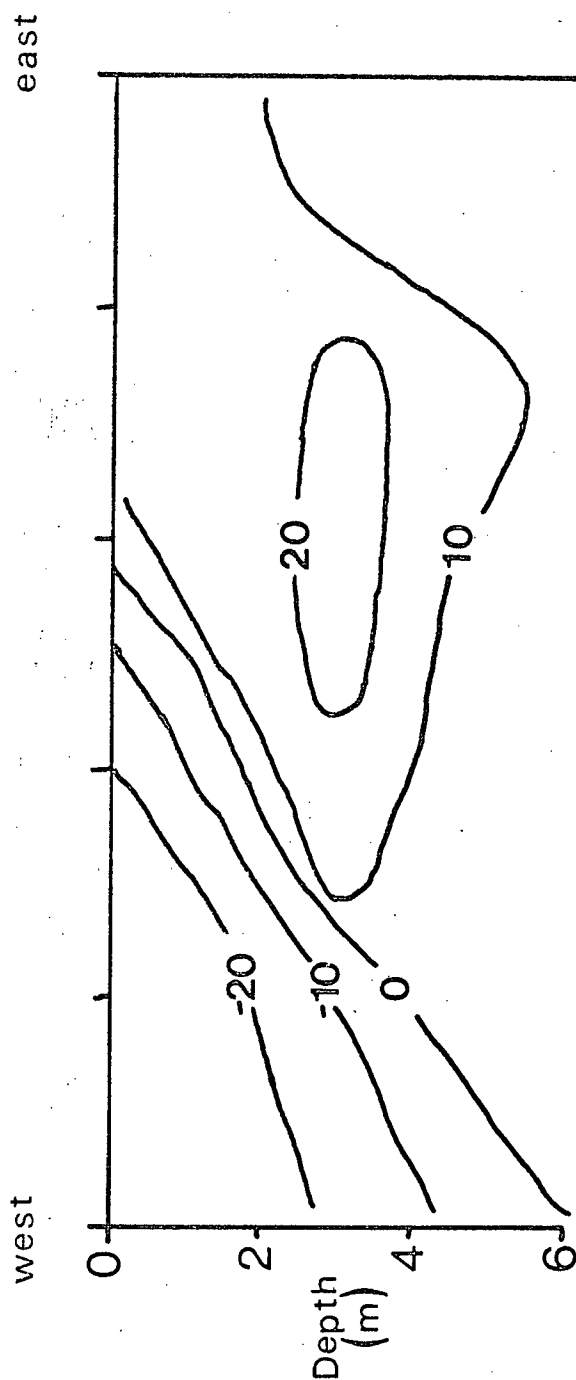


Figure 32 - Contours of up-inlet velocity as deduced from 3 hour box-averages of the three level drogues. Total channel width is 2.8km. Fifteen box averaged values were used to construct this contour plot, one value in each of the three depth ranges in each of five cross-channel boxes.

lateral inhomogeneities, previously described in the surface layer flow, are also present in the subsurface flow. Within the "surface layer" as defined in chapter III, the flow is not vertically uniform. The strongest up-inlet flow occurred, not beneath the seaward flowing surface layer, as assumed in traditional fjord theory, but just below the surface, at the same depth as the deeper parts of the outflow. Flow fields such as this one are known to occur in some shallow estuaries, (Dyer, 1973), but are not usually associated with fjords.

The data records were not long enough to measure reliably the drogue accelerations and to attempt to relate them to changes in the surface winds. If the predictions in previous chapters about surface layer depth and reaction of the surface layer to a wind stress are correct, then the acceleration should be the same for the surface and intermediate drogues, but smaller for the deep drogues which were nominally in the interface between the layers. This hypothesis remains to be confirmed in future studies.

The large lateral velocity gradients found in both the surface layer experiment and this three level experiment force the question of how deep do these lateral velocity gradients persist? Since there is no information available on this question at the present time the analysis of the data from the current meter string that is done in the next chapter will have to proceed keeping in mind the possible existence of these gradients.

CHAPTER VI

SUBSURFACE CURRENTS

VI.1 A Description Of The Subsurface Current Monitoring Programme

A programme of subsurface current monitoring was carried out which complemented the surface current study. Strings of current meters were installed and maintained at three locations in the sound by the Coastal Zone Oceanography Group of the Institute of Ocean Sciences, Patricia Bay, B.C. The data from these installations have been published in the form of progressive vector diagrams (PVD's), histograms of speed, direction, temperature and salinity and three-dimensional histograms of speed and direction by Bell (1975). Although there were three different sites used in Howe Sound, only the one occupied between 24 November, 1972 and 23 February, 1974, whose location is shown in figure 6, will be analysed here because it was the only one located inside the northern basin.

A series of oceanographic cruises was carried out monthly by IOUBC personnel in Howe Sound during the period of current meter installations to monitor water properties to look for possible deep water movements too slow for the current meters to register. The relevant results will be

discussed later in this chapter.

The current meters were installed on taut line moorings with surface floatation. Two separate moorings were used about 250m apart to minimize potential equipment damage or loss due to inadvertent snagging of the installations by the many tug boats in the area. During the operational period, no instruments were lost or obviously damaged in this manner.

Current meters were installed at depths of 3m, 5m, 10m, 15m, 20m, 30m, and 150m. A Geodyne model A-850 meter was used at 3m. It sampled in bursts, recording 15 samples of speed and direction 5 seconds apart four times an hour. The direction vane on this instrument was quite small, allowing it to follow fairly rapid changes in direction such as those caused by mooring motion and by the lower frequencies of wave energy. In the subsequent analysis, these bursts were vector averaged to minimize possible aliasing induced by such higher frequency motions. As a result the meter produced one sample every 15 minutes. The rest of the current meters used were Aanderaa model RCM-4. They were set to sample once every 10 minutes. The data values produced were average current speed over the 10 minute interval and direction as instantaneously measured at the data recording time. The claimed accuracy for the Geodyne meter is $\pm 26\text{mm/s}$ in speed and $\pm 10^\circ$ in direction. Its threshold speed is 26mm/s. The accuracy of the Aanderaa meter is $\pm 4\text{ mm/s}$ in speed (from the calibration formula) and $\pm 5^\circ$ in direction. Its threshold is 15 mm/s.

The data from these meters were transcribed from the meters' internally recorded magnetic tapes to IBM compatible magnetic tape and then calibrated according to the manufacturers specifications by W.H. Bell of Coastal Zone Oceanography. It was from these final calibrated records that the analysis described in this chapter was done.

VI.2 Time Series Records From The Current Meters

The time series records from the current meters were looked at first in order to spot any dominant features and to foresee any possible problems that might be encountered in the subsequent spectral analysis of the data. Figure 33 shows a short section (15 days) of the long-channel component of the current at six depths and of the wind at Squamish. The current data are all one hour vector averages and are plotted on the same scale.

Diurnal oscillations of the currents are a dominant feature of these records. They occur most strongly in the 3m and 5m records but can also be seen even in the 150m record (for example, between 21 and 24 days). The record at 150m also shows evidence of a semi-diurnal oscillation (from 24 to 28 days). The magnitude of the currents at 150m are larger than might be expected deep in a fjord behind a sill.

A study of the phase relationship between the records proves quite interesting. For the most part, the 3m and 5m currents are very nearly in phase, although the 3m seems to be leading by a small variable amount. These currents also

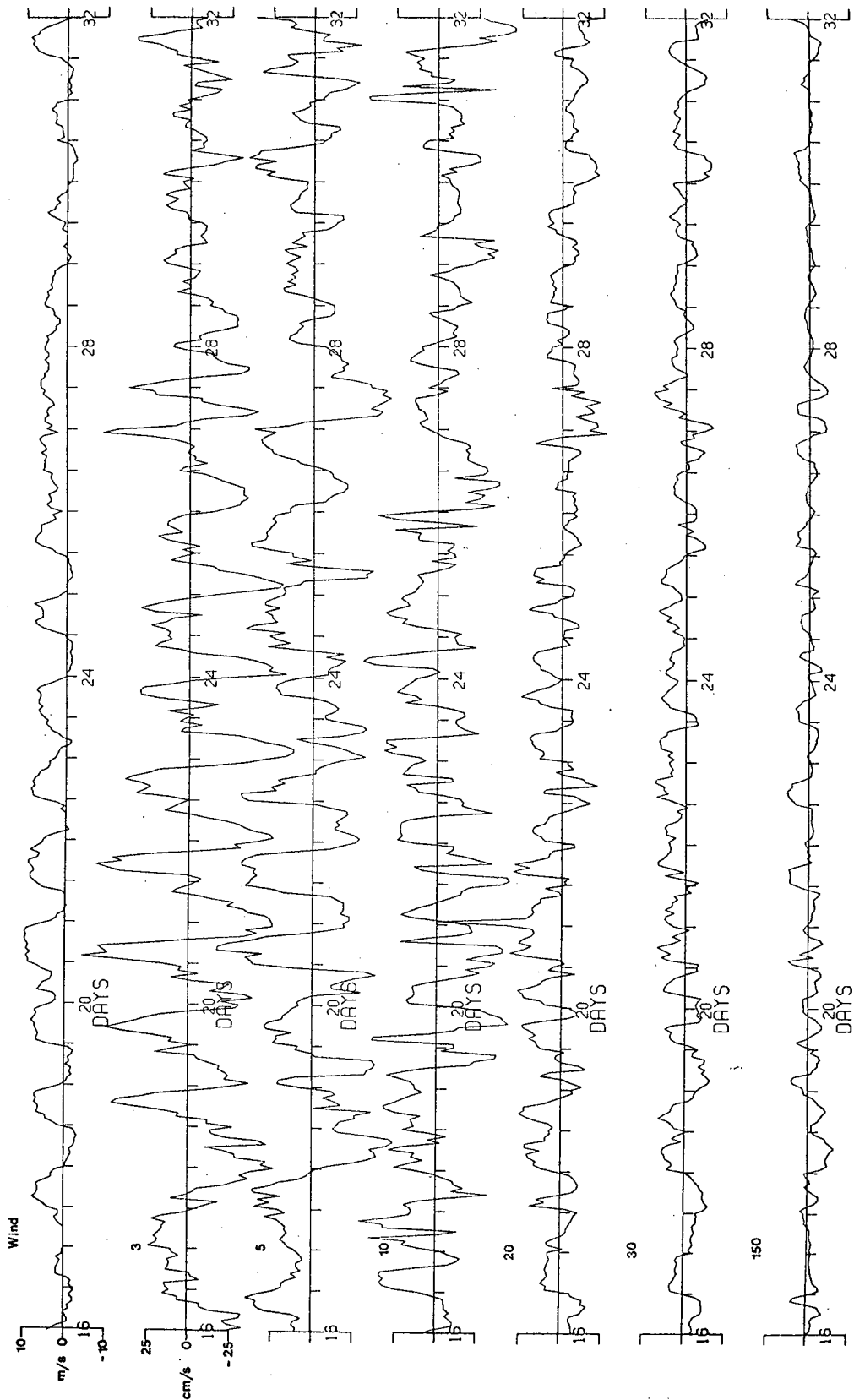


Figure 33 - Long-channel components of wind at Squamish and currents from current meters at the depths indicated. Day 0 is 8 July 1973. All records are hourly averages of the raw data. The scale of all currents is the same. Positive currents flow up-inlet.

appear to be roughly in phase with the wind. Throughout most of the record the 5 and 10m currents appear to be out of phase, but there are times, at 23.5 days, at 25 days and at 26.5 days for example, when the two appear to be in phase. The 10m, 20m and 30m records appear to be approximately in phase. Exceptions occur at 17 days, 26 days and 31.5 days when 10m is out of phase with 20m and 30m, and at 27.5 days when 20m is out of phase with 10m and 30m. The phase relationship between the 150m record and the others is not quite as clear but it does appear to be roughly out of phase with the 30m meter and in phase, at least between 21 and 24 days, with the 3m record.

This section of data appears to indicate a three layer structure in the water column: a surface layer extending to a depth of between 5 and 10m, a middle layer extending to below 30m that oscillates out of phase with the surface layer, and a deep layer encompassing the 150m meter that oscillates in phase with the surface layer. The occasional departures from the standard phase relationship show however that the levels of no horizontal motion separating the layers are not constant in depth in the water column. Levels of no motion are defined here as the depths at which the amplitude of the horizontal current goes to zero as it changes phase from the waters above to the waters below. This definition is used throughout the thesis.

Looking at the relationship between the currents at different depths in this fashion over such a short record cannot conclusively prove anything about the coherence and

relative phases of the currents. Phase analysis done in frequency space via spectral analysis is in general much easier and more convincing. But this look at the temporal record shows a major problem that will arise in coherence and phase calculations. This problem is caused by the shifts in the levels of no motion. Since these shifts cause radical changes in the relative phase of currents recorded by adjacent current meters, they will cause anomalous results in any coherence or phase measurements. Periods of alternate in phase and out of phase currents will tend to cancel and yield low coherence levels when the currents are actually quite coherent but with an unsteady phase relationship.

The current records shown in figure 33 contain a large number of 'spikes', i. e. artificially large changes in magnitude or sign such as the one at 20m, 21 days or 10m, 31.2 days. Most of these spikes are due to mooring motion as will be discussed in the next section, but there are some very rapid changes that are caused by something different. As was shown by the results of chapters IV and V, the river velocity core in the general vicinity of the current meters is not uniformly distributed across the inlet and extends down only 4 or 5 metres. The movement of silt patterns and of the drogues in weeks 1 and 3 shows that this river core can change its position in the channel. If the river core were not flowing across the current meters, the 3m meter would probably register an up-inlet flow or a weak down-inlet flow. If the core then moved over the current meters, the 3m meter would be expected to show a rapid increase in

down inlet current strength and then a rapid decrease as the river core passed by the meters. This type of event is seen at 27 to 27.5 days. Current variations of this sort are uncorrelated with the other current measurements in the fjord and are only indirectly related to the forces causing the currents.

This quick look at the current records provides some insight into what to expect from their spectral analysis. There appears to be a large amount of coherent diurnal energy. The calculated coherence will be less than the real coherence due to phase reversals of the currents caused by shifts in the levels of no motion. Some semi-diurnal energy is also present but coherence between the currents at different depths at this frequency is not obvious. Other strong components at different frequencies are not obviously present but they may be hidden by the spikes in the data. The effects of these spikes must be investigated before proceeding much further into the analysis.

VI.3 Spectral Analysis Of The Currents

The technique of spectral analysis was used on the data records of current and wind. The data records analysed covered the high runoff period in the spring and summer of 1973, spanning a period of 177 days from 20 March to 13 September. The anemometer at Squamish suffered many breakdowns during the period of the current meter installations but was operational continuously for the 177

day period. The current meters at 5m, 20m, 30m and 150m operated for this entire period. The meter at 3m operated for 150 days, from 20 March to 17 August; the one at 10m for 140 days from 26 April to 13 September. The meter at 15m only operated until 6 June, producing only two data records and so will not be considered for further analysis. The data at each depth consisted of four sections of data between 35 and 68 days long with a gap of usually about one day between each section.

VI.4 Techniques And Problems Of Analysis

The techniques of spectral analysis are well known and documented (e.g. Bendat and Piersol, 1971, or Jenkins and Watts, 1968) and will not be described in detail here. Power spectra and coherences were calculated using programmes written by Ian T. Webster and described in Webster and Farmer (1976). The programmes transformed the data using the fast Fourier transform (FFT) algorithm of Singleton (1969).

FFTs were calculated on the first 768 hours (32 days) of each current meter record and the same period of wind record simultaneously. There were no periods of missing data that had to be filled in any of the records. Spectral, cospectral and quad spectral values were calculated from the Fourier transforms of each data record. At each depth these values were averaged over the four or five records to yield 'ensemble' averages of the quantities. Band (frequency) averaging was also done on the spectra. The bandwidth used

was $\Delta(\log_{10} f) = 0.1$. Coherence and phase of the signals were calculated from the band and block averaged spectral data.

A major problem with surface moored current meters is wave induced distortion of the signal which can come either from direct wave action on a shallow current meter or indirectly from wave action moving the surface buoy and hence moving the current meter through the water around it. Either way the effects on the meter are similar. One manifestation of this problem is excessively large recorded speeds ("rotor pumping") caused by short period wave induced currents. These fictitious speeds are a result of the sampling scheme of a Savonius rotor style of current meter that records an integrated current speed over the sample period of the meter but only records an instantaneous direction at the end of the sample period. The problem is reduced in current meters such as the AMF Vector Averaging Current Meter (VACM) whose sample period is dependent on the current speed and is generally less than that of the wave induced currents. There have been several estimates of the magnitude of the discrepancy between actual and recorded currents. Saunders (1976) compared drogue measured velocities with those of a VACM in a manner similar to the comparison done in chapter III and found similarly that the two give comparable results. He then compared the VACM results to an Aanderaa RCM-4 and found a ratio of 2.3:1 between the mean velocities as recorded by the Aanderaa and the VACM over a 12.5 day period. However he found that the

actual rotor speeds of the two meters were almost identical, indicating that the difference lay in the aliasing of the rapidly changing current direction onto the slow sample rate of the Aanderaa's direction sensor. His measurements were made at 12m on a mooring in 2500m of water.

Halpern and Pillsbury (1976) have compared results from surface moored and subsurface moored Aanderaa current meters in shallow (50m) water and found a ratio of mean speeds of 2.1:1 between surface and subsurface moored meters. However the shapes of the spectra were the same at frequencies less than 0.7cph. At greater than 0.7 cycles per hour (cph) there was more energy in the spectrum of the surface moored meter. Similar results were obtained by Halpern et al (1974) in a shallow water instrument intercomparison between a surface moored VACM, a surface moored Geodyne A-850 and a subsurface moored Aanderaa RCM-4. Below a frequency of 0.45cph they found the current spectra to be the same.

It is difficult to understand why the shapes of the wave influenced and the non-wave influenced spectra should be the same. Periodic fluctuations in the strength of the wave field, caused by variations in wind strength, either diurnal as expected in coastal regions like Howe Sound or with the period of weather systems as seen in the oceans, should add energy to the wave influenced spectrum at these periods and hence create a large disparity between the records specifically at these periods. It is possible that the records analysed were too short to examine the behaviour of the spectra at frequencies low enough to get away from

atmospheric periodicity.

These results lead to the conclusion that current meters like the Aanderaa with simple sampling schemes will not reasonably measure the water velocity when either the meter or the top of the mooring is exposed to wave action. All the meters used in this experiment below a depth of 3m were Aanderaas. It is possible therefore that the measured currents will be too large. However the mooring was in relatively shallow, protected waters so the waves were not large and the mooring was relatively stable. Comparison between the drogues and 3m currents and the 3m and 5m currents showed them to be similar in magnitude so that the wave-induced amplification of currents does not appear to be large in this case.

Another symptom of wave action on a subsurface current meter is "vane flop". In surface waters the magnitude of the wave induced currents may be much larger than the mean currents. The magnitude of the wave induced current is:

$$u = a\omega \exp(-\omega^2 z/g) \quad (6.1)$$

so for example in a typical wave field of 0.5m, 4 second waves, the current amplitude at 3m depth is 37cm/s and at 5m is 22cm/s. The buoy follows the waves to some extent and therefore the meters move in the same direction as the water, so the actual wave-induced current seen by the meters is smaller than the above values. An oscillating current,

induced by waves of this four second period, superimposed on an average current may cause a complete reversal of the current direction every two seconds. The direction vane on an Aanderaa meter is too large to respond to this rapidly changing direction, but it will be deflected from its mean position. Because the direction is measured only once per recording cycle, the recorded direction will be a random scatter of values about the mean. When speed and direction are later combined into velocity components, this flop will manifest itself as a series of spikes in the record that decrease the flow along its principal axis and increase it perpendicular to that axis. Behaviour of this sort is seen in figure 34. This figure shows a short section of data from the 5m current meter. Over the entire record the speed trace is quite smooth but the direction trace contains many spikes. The long-channel component of velocity is usually decreased by these spikes and the cross-channel component is usually increased. This behaviour is particularly evident in the vicinity of day 3 in the plot. The smoothed long-channel component of velocity discussed in the next paragraphs is also shown in this figure.

A simple test of the effect of these spikes on the subsequent data analysis was performed. The four 5m records were plotted on an incremental plotter at a scale of 16.67hr/inch. A subjectively smooth curve was then drawn through each trace and digitized on a Gradicon digitizing table at 10 points/inch. Thus the interpolated record had about one point per 1.67 hours. The digitized data were then

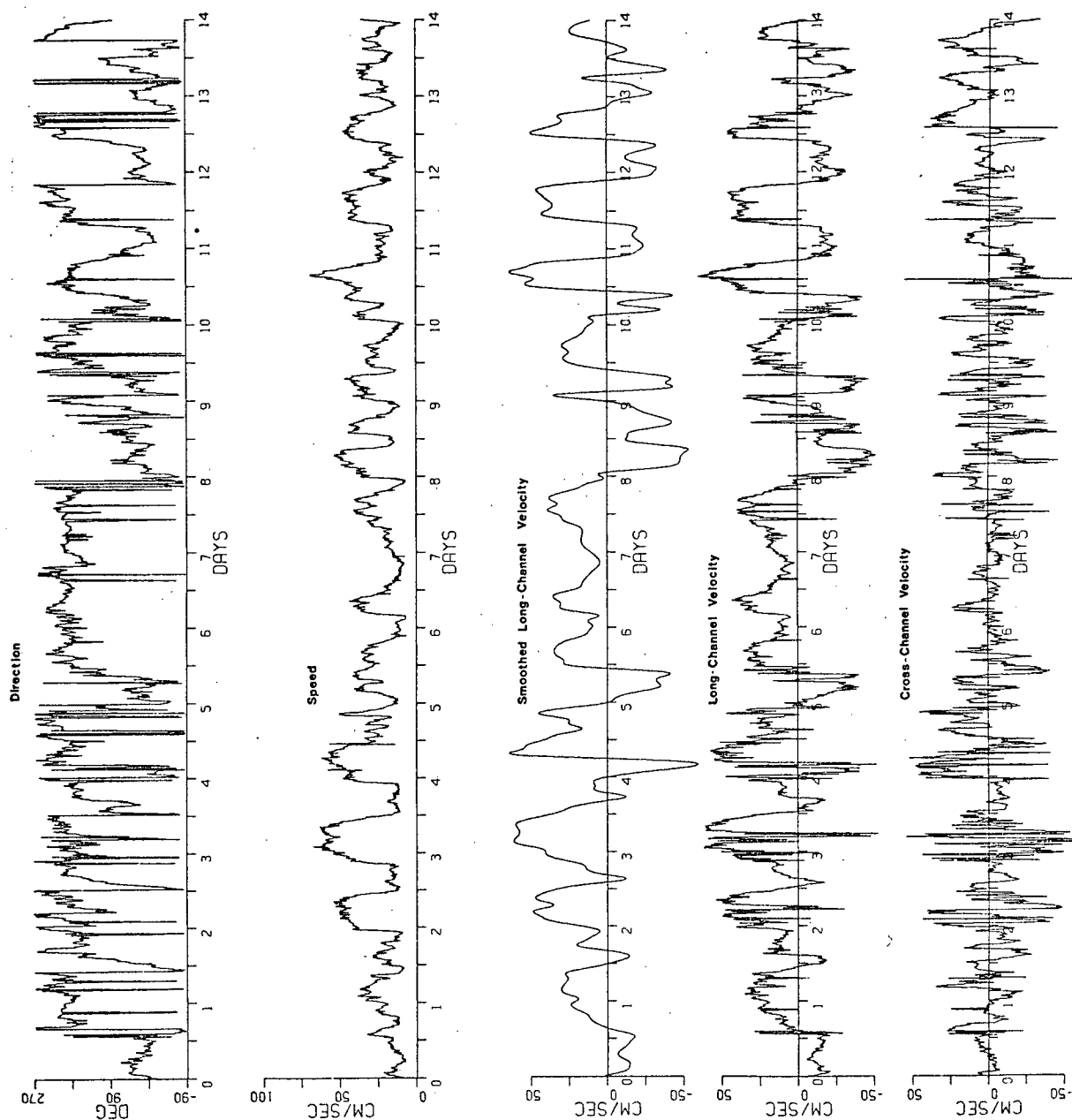


Figure 34 - A section of record from the 5m current meter showing spikes in the component and direction records due to "vane flop". The smoothed and unsmoothed long-channel velocity components were used to calculate the spectra and coherences in fig 35. The time origin is 20 March 1973.

spline-fitted with no extra smoothing allowed and interpolated to regain the six values per hour that the original records had. These two sets of curves, smoothed and unsmoothed, were then Fourier transformed and spectral analysed in the manner described previously. The resulting spectra are shown in figure 35. At frequencies less than 6cpd the spectral levels for the smoothed record were about 1db higher on average than those in the unsmoothed one. This difference is within one standard error on all points. Above this frequency, the spectrum of the noisy record displays a broad peak centred at 20cpd. The spectrum of the smoothed record drops off rapidly above 6cpd as it must. This critical frequency of 6cpd is quite close to the Nyquist frequency, 7.2cpd, of the smoothed data set. The coherence between the two signals is almost unity below frequencies of 2.4cpd. It drops rapidly at higher frequencies and approaches the expected noise coherence level at 9cpd. The phase between the two signals is very close to zero at all frequencies less than 9cpd.

This "brute force" removal of the vane flop spikes from the data record appears not to have affected the phase of the signal in the frequency range of interest and only to have increased the low frequency spectral levels slightly, indicating that there is little leakage of energy from the high frequencies caused by vane flop to the lower frequencies that are of interest in this analysis.

These two potential problems with data from "simple" current meters may lead to problems in the interpretation of

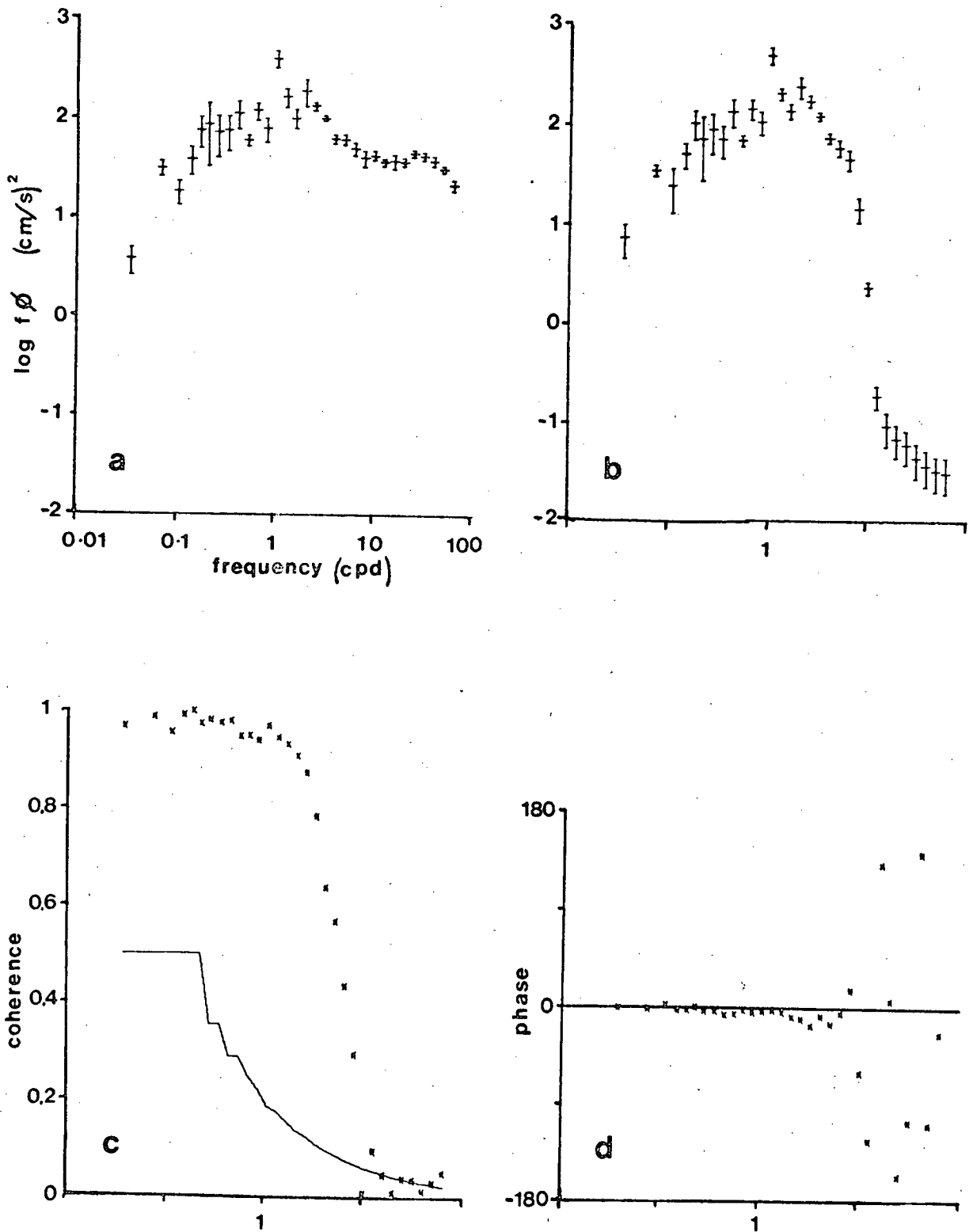


Figure 35 - Spectra, coherence and phase of the "noisy" 5m current meter records and "smoothed" 5m records. The line on the coherence plot is the expected coherence of two random signals with the same number of degrees of freedom as the data, as explained in the text in section 6.5. The error bars on the spectral points are ± 1 SE.

the resulting spectra. However, the shape of the spectra in the frequency range of interest in this experiment appears to be unaffected by vane flop. The spectral levels are probably boosted somewhat by rotor pumping. However, spectral quantities like coherence and phase, in which this increase in spectral level should be nullified by normalization, should be relatively unaffected by problems of surface moorings.

VI.5 Reliability And Stability Of Coherence Estimates

Before we can trust coherence and phase values however, we must have some criterion upon which to judge the stability and reliability of these measurements. A criterion given for reliability in Bendat and Piersol (1971) is the $(1-\alpha)$ confidence interval. They say that a coherence γ has only an α to 1 chance of being outside the limits:

$$\tanh(\tanh^{-1}\gamma - (\nu-2)^{-1} - z_{\alpha/2}(\nu-2)^{-1/2}) < \gamma < \tanh(\tanh^{-1}\gamma - (\nu-2)^{-1} + z_{\alpha/2}(\nu-2)^{-1/2}) \quad (6.2)$$

where ν is the number of degrees of freedom of the estimate and $z_{\alpha/2}$ is abscissa of a standard normal distribution such that the area under the curve between $z_{\alpha/2}$ and ∞ is $\alpha/2$. These limits are valid only for $0.35 < \gamma^2 < 0.95$ and for $\nu > 20$,

but are probably not too wrong outside these limits.

Jenkins and Watts (1968) proposed another approach to the question of coherence reliability. They calculated the expected coherence of two random signals with the same number of degrees of freedom as the coherence estimate under test. This is $\delta_c = \sqrt{2/\nu}$ where ν is the number of degrees of freedom. Since this number represents the level of no real coherence (but with a finite record length so that the calculated coherence is non-zero), presumably any calculated coherence above this value would be greater than zero if an infinite record length were available.

A test was performed on the relationship between the stability of coherence and phase and the number of degrees of freedom by calculating FFT's using the wind signal and the hourly averaged 5m current as inputs. The five resulting blocks of spectral estimates were averaged. Different numbers of these bands were then averaged together and the coherence and phase between wind and current calculated. In table VII the results of this test in the bands containing the 24.00 hour period (high coherence expected) and the 12.42 hour period (no coherence expected) are shown. Also shown are the 95% confidence intervals about the coherences and the expected random coherence.

Let us look first at coherence in the 24 hour band. It is high for 10 degrees of freedom but levels off to a value near 0.5 between 40 and 100 degrees of freedom. Beyond this point the coherence drops slowly. In every case, the lower limit of the 95% confidence limit is well above zero,

Table VII - Coherence and phase estimates between wind and 5m currents for different numbers of degrees of freedom between 10 and 100 in two different bands. Confidence limits are 95% and are shown just above and below each coherence. ν is the number of degrees of freedom. The phase angle is given in degrees.

ν	24.00 hours		12.42 hours		noise coh
	coh	phase	coh	phase	
10	.91		.78		
	.75	-13	.44	-101	.45
	.15		-.33		
20	.84		.67		
	.67	-11	.38	-149	.32
	.29		-.12		
30	.78		.52		
	.61	-7	.24	-131	.26
	.29		-.16		
40	.68		.47		
	.49	-5	.22	-37	.22
	.19		-.12		
50	.71		.43		
	.55	-4	.22	-39	.20
	.30		-.10		
60	.70		.40		
	.55	-3	.18	-40	.18
	.33		-.09		
70	.60		.36		
	.44	0	.15	-114	.17
	.22		-.10		
80	.58		.38		
	.42	-5	.19	-37	.16
	.21		-.04		
90	.58		.31		
	.44	2	.12	-2	.15
	.25		-.10		
100	.62		.23		
	.49	-3	.05	-53	.14
	.32		-.16		

Table VII continued for ν between 120 and 640.

ν	24.00 hours coh	phase	12.42 hours coh	phase	noise coh
120	.53 .39 .22	1	.23 .06 -.13	-55	.13
160	.47 .34 .19	-8	.27 .13 -.03	-45	.11
200	.45 .34 .21	-2	.22 .09 -.05	-45	.10
320	.35 .25 .14	-5	.24 .14 .03	24	.08
480	.32 .24 .15	0	.13 .04 -.05	-70	.06
640	.29 .22 .14	-2	.15 .08 .00	-177	.06

indicating that there is less than a 2.5% chance that any of the calculated coherences are actually zero. A comparison of the coherences with the associated random noise coherences shows that the calculated values are all well above the noise level. By both criteria of reliability then this band has some coherence. The actual value of the coherence appears to be about 0.5. This value is within the 95% confidence interval of all estimates up to 120 degrees of freedom. Above this number, the frequency band is wide enough to include enough noise to mask the one narrow band of coherent signal. The phase of the signals however stays remarkably constant at $-5^{\circ} \pm 7^{\circ}$ over the entire range of the test.

Looking now at the 12.42 hour band, we can see that the coherence drops steadily as the number of degrees of freedom is increased. Its value is always close to the noise coherence for the appropriate number of degrees of freedom. In all cases but one, the lower bound of the 95% confidence interval is equal to or less than zero. Thus both criteria have shown the signals in this band to be incoherent. The phase of the signals is erratic, showing variations of almost $\pm 90^\circ$.

Both criteria for reliability of coherence estimates appear to be workable. From now on only one of the two will be used, the level of random noise coherence. Below about 40 degrees of freedom, coherence estimates do not appear to have reached a stable level. In the band averaged spectra shown in this chapter, the 24.00 hour band has 70 degrees of freedom, the 12.42 hour band has 130. Both of these bands of interest should then produce accurate coherence and phase estimates.

VI.6 Mean Currents

The Fourier transform programme calculated the mean value of each input data block. The mean value for the current at each depth over the 177 days of analysis may therefore be calculated as the average of the mean values from each of the four or five data blocks which comprise the entire record at that depth. A plot of mean current as a function of depth is shown in figure 36. The bars around the points in this figure are two standard errors of the block means about their average and so indicate the range of the mean value of the current calculated approximately monthly over half a year.

The 3m mean current was always down-inlet in this time period. The mean current at 5m was always up-inlet. Those two results verify the existence of the expected gravitationally-driven estuarine circulation pattern of an outflowing surface layer and inflowing compensatory flow, although the return flow is somewhat closer to the surface than was shown in Pickard and Rodgers, 1959, possibly because the Howe Sound measurements were made closer to the head of the inlet than were those in Knight Inlet. The mean currents at 10m, 20m and 30m are all weak and show marked variability in direction over six months. Thus they play no consistent role in the estuarine circulation over that entire period. Of course for any given set of levels of no motion, the currents at these depths probably do form part of the layered estuarine system of inflows and outflows. But

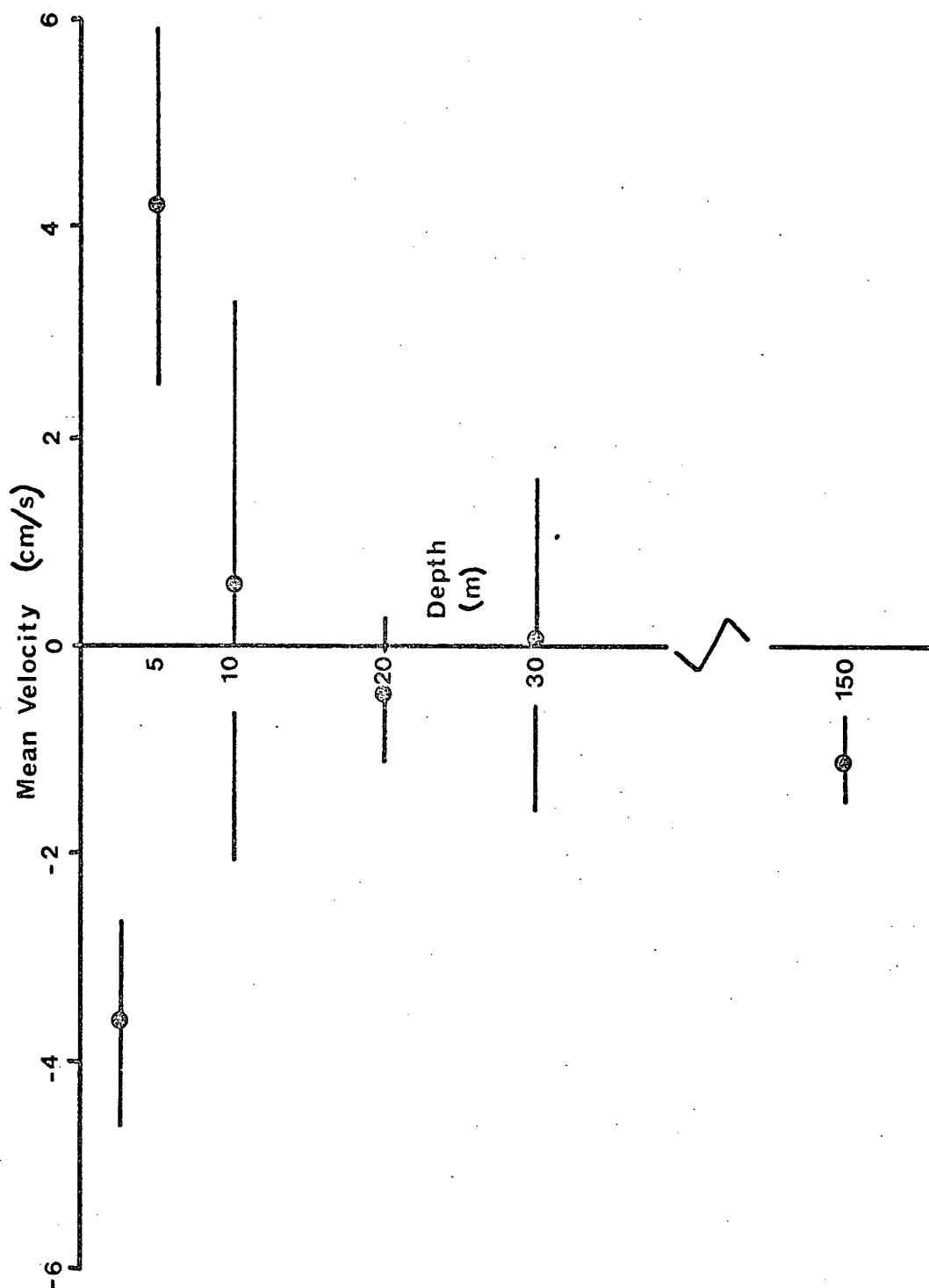


Figure 36 - Mean currents calculated from zeroth harmonics of the Fourier transforms of the current meter records. The bars indicating scatter of the values are ± 2 standard errors of the mean of the zeroth harmonics. Positive current is up-inlet as before.

as we have seen, these levels can change, so that a meter, originally in an inflowing layer, may find itself in an outflowing layer for some period of time or vice versa. For example, the current at 20m flowed up-inlet on average from 20 March to 21 April, down-inlet on average from 26 April to 31 July and up-inlet again from 14 August to 15 September. Analysis of longer term variations of this sort was sacrificed to gain greater statistical significance in the overall mean values.

The current at 150m flowed down-inlet on average for the entire period. It is difficult to explain this result if the current were uniform across the channel. Water moving at 1 cm/s travels almost 1km/day. In a basin only about 20km long a current of this strength cannot persist for longer than 20 days without leaving the basin. The water mass below sill depth in Howe Sound is contained by the sill, the walls of the fjord and by the density gradient above it so that a flow out of the basin is improbable. Hence there must be some other explanation for the mean current at 150m.

The density gradient in the lower 175m of Howe Sound was not measurable by the hydrographic analysis techniques used on the cruises that were made in the Sound. The upper limit on the density change is therefore 0.02 sigma-t units, based on the accuracy of temperature and salinity measurements. The maximum local internal Rossby radius of deformation as defined by:

$$r_R = \sqrt{gh \Delta \rho / \rho} / f \quad (6.3)$$

where h is the depth of the layer of water, $\Delta\rho/\rho$ the fractional density difference across it and f is the Coriolis parameter, is equal to 1.2 km for a layer depth of 175m and a density difference of 2×10^{-5} . Therefore the possibility of Coriolis effects cannot be excluded when attempting to explain the mean current at 150 m. Waves in the deepest parts of the inlet may travel up-inlet on the east side and down-inlet on the west side in an internal Kelvin wave-like fashion. If this were the case then a current meter suspended closer to one side of the inlet than the other would register a net current due to the difference in amplitude at that point between the wave travelling up-inlet and the wave travelling down-inlet.

It is unlikely that the current meter measurement errors previously discussed contributed to this mean current at 150m since this depth is well below the depth of direct surface wave action and wave-induced motion of the surface buoy and mooring line should be effectively damped this far below the surface. In agreement with this statement, the current meter records at 150m showed no evidence of the spikes symptomatic of vane flop caused by wave action.

VI.7 Spectra Of The Wind And Currents

Although the spectral regions of greatest interest in this study are in the vicinity of the diurnal and semi-diurnal periods, a look at the total frequency range of the spectra is also interesting. The spectra of long-channel components of the wind and the currents at six depths are shown in figure 37. On all spectra the diurnal and semi-diurnal frequencies are marked.

The spectra all have the same general shape, rising from low frequency to a maximum value near 1 to 2cpd and then decreasing at higher frequencies. They all have a basic form consisting of a line with slope 1 up to a frequency of about 2cpd and a line with -1 slope for all frequencies above 2cpd. The individual features of each spectrum are then characterized by a series of peaks above this basic shape.

The spectral plots are all of $\log f\phi$ vs $\log f$. A plot of $f\phi$ vs $\log f$ is variance preserving, i.e.

$$2.3 \int f\phi d \log f = \int \phi df = \text{variance.}$$

The log-log plots used are not variance preserving but it is still clear where the dominant contributions to the variance occur. In contrast, a $\log \phi$ vs $\log f$ plot emphasizes the low frequencies. Log-log plots are used because they allow the full dynamic range of the variable to be displayed and they show any power law relationships that exist.

The spectrum of a square wave with period 1 day is zero for $f < 1\text{cpd}$ and then a series of discrete values whose

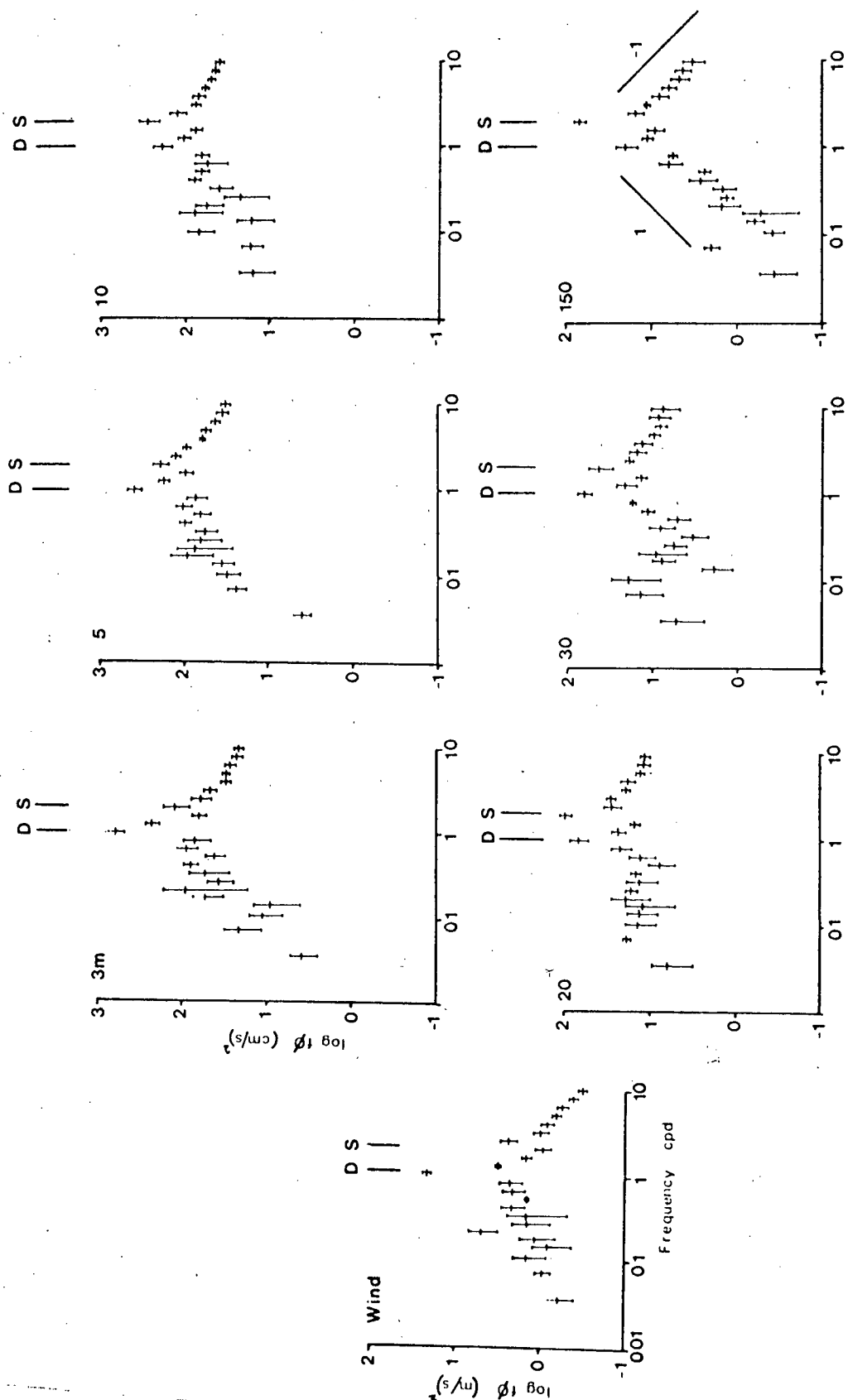


Figure 37 - Spectra of the wind and currents at the depths indicated. D and S indicate the diurnal and semi-diurnal frequencies respectively. Lines of slope 1 and -1 are shown on the 150m spectrum. The error bars on the spectral points are ± 1 SE.

magnitudes decrease as f^{-2} for $f > 1\text{cpd}$. Making the period of the square wave random about 1 day and giving each cycle of the wave a random asymmetry injects essentially random noise at $f < 1\text{cpd}$ causing a constant spectral level at those frequencies and makes the spectrum for $f > 1\text{cpd}$ more continuous but preserves the slope of f^{-2} . When plotted on a $\log f\phi$ vs $\log f$ plot, this spectrum is a line with slope 1 for $f < 1\text{cpd}$ and of slope -1 for $f > 1\text{cpd}$, exactly as postulated for the underlying spectrum of the observed currents.

Another look at figure 33 will show that the wind and currents appear to rise quickly to some particular value and then hold it for some length of time before rapidly changing to another value. Thus there is a reasonable basis for the interpretation of the basic shape of the spectra as being due to a random square wave behaviour of diurnal period with some departures from this base shape.

Looking first at the high frequency end of the spectra, the wind and the 150m spectra show slopes of -1. The other spectra show a high frequency tail whose slope decreases with increasing frequency, indicating more energy at high frequencies than expected from the simple square wave model. This high frequency tail is probably due to the presence of the vane flop spikes and other noise in the data records.

Now let us look at the low frequency end of the spectra. The wind spectrum has a low frequency slope of about $1/2$ indicating that there is more energy at these frequencies than expected from just random lengths of

diurnal wind pulses. There should be energy in the wind at longer periods due to variations on the scale of weather systems. There is a peak in the spectrum at 0.2cpd, a reasonable value for the period of weather systems at this time of year in British Columbia. The spectra of the currents at low frequencies show, for depths other than 150m, slopes less than 1 suggesting some influence of the low frequency wind energy on the currents. At 150m the low frequency slope is almost exactly 1 suggesting that most of the energy is associated with random effects in the diurnal and semi-diurnal constituents. This sort of change in spectral shape with depth can be interpreted as follows. The shallow low frequency currents move in response to the wind. The effect of the wind is also felt deeper in the water column but the effects of the higher frequencies are reduced more at depth than those of the lower frequencies. Thus the wind energy which appears at all frequencies below 1cpd at 3m only seems to appear below 0.2cpd at 30m and may only be present at the lowest frequencies of observation at 150m.

Peaks in the diurnal and semi-diurnal bands are a major feature of the spectra. The band labelled "diurnal" covers the range of periods from 23.63 to 30.12 hours. Thus it contains energy from all of the diurnal tidal constituents and from the diurnal wind. The band labelled "semi-diurnal" covers the range from 15.21 to 12.09 hours. Thus this band contains energy from the major semi-diurnal tidal constituent, M_2 , but not from the S_2 tide or from any wind fluctuations with a 12.00 hour period. In this manner any

wind effects are separated from the semi-diurnal spectral peak. The wind spectrum shows a diurnal peak 9db above the rest of the spectrum but no semi-diurnal peak. The band above the semi-diurnal shows a small peak indicating that there is some energy in the wind at 12.00h. Thus the separation of wind energy from the semi-diurnal band did occur. The current spectra all show both diurnal and semi-diurnal peaks. They do not show any peaks in the band above the semi-diurnal band. With the exception of 30m, the ratio of the diurnal peak to the semi-diurnal peak decreases with increasing depth. This feature is to be expected since the diurnal peak contains both wind and tidal energy but the semi-diurnal peak contains only tidal energy.

An interesting comparison can be made using the amplitudes of these peaks. A measure of the mean square current in any frequency range may be made by multiplying the spectral estimate by its band width. The ratios of such estimates in the diurnal band to estimates in the semi-diurnal band for all the spectra are shown in table VIII.

Also shown is a ratio of mean square tidal currents calculated from the amplitudes of tidal constituents at Squamish. The tidal currents are assumed to be proportional to the time derivatives of the tidal heights and hence have amplitudes proportional to the product of the height and the frequency. Both the diurnal and semi-diurnal bands contained several tidal constituents of slightly different frequency. Although the relative phases of these constituents were not taken explicitly into account in the averaging process, the

Table VIII - Ratios of the mean square currents in the diurnal band to those in the semi-diurnal band for all depths calculated from spectral values. Also shown is the tidal current ratio calculated from the amplitudes of the tidal components as described in the text.

depth	ratio
3m	5.27
5m	2.16
10m	0.74
20m	0.75
30m	1.57
150m	0.30
tidal	0.31

averaging period of the spectra was long enough to allow all possible phases between the constituents. Hence the total tidal current in each band was computed as the sum of the squares of the constituents. The diurnal band contained the O_1 , P_1 and K_1 constituents, the semi-diurnal the N_2 and M_2 . The resulting ratio should be representative if the tidal currents in both bands are primarily barotropic.

The ratios of mean square current shown in table VIII indicate the relative amounts of kinetic energy in the diurnal to the semi-diurnal frequency bands. Only at 150m does the ratio appear to be near to the expected barotropic tidal ratio as calculated from the amplitudes of the tidal constituents. At all other depths there is more diurnal energy than may be explained by the barotropic tide. The ratio generally decreases with increasing depth. This observation is consistent with the hypothesis that the wind driven contribution to the currents decreases with

increasing depth. There is an anomaly in this observation at 30m where the ratio increases to a value between the 5 and 10m values. One possible explanation of this result is that the tidal currents are baroclinic and 30m is near a node in the vertical structure of the semi-diurnal tide.

This look at the spectra of wind and currents has shown several important things about the relationship of the wind, tide and currents. One is that wind effects are prominent in the near surface currents but decrease in importance with increasing depth. The depth of wind influence may be frequency dependent. Tidal currents are present in all current records and there is evidence of baroclinicity in them. It is these aspects of the observations that will be investigated in greater detail in the rest of the chapter.

VI.8 Coherence Of The Wind And Currents

Estimates of coherence and phase between wind and current records were made in an effort to determine the extent of the coupling between them. The results of this study show smaller coherences than might be expected. Figure 38 shows the coherence and phase between the wind and currents at all six depths.

Let us look first at the results from 3m in figure 38, where we might expect the coherence to be high. At periods greater than 10h the coherence is usually well above the noise level and the current leads the wind by about 20°. At periods of 10h and less, the coherence is near the noise

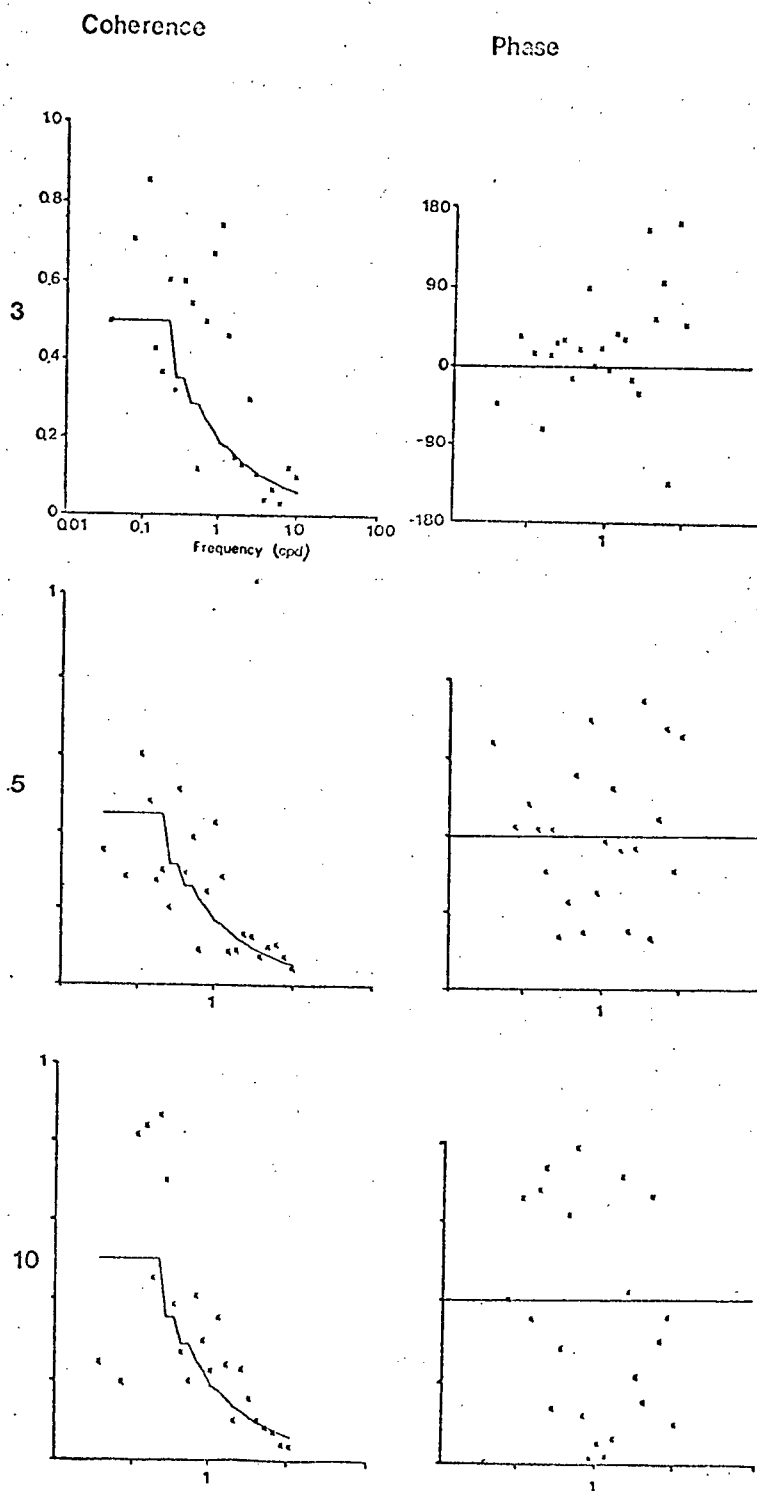
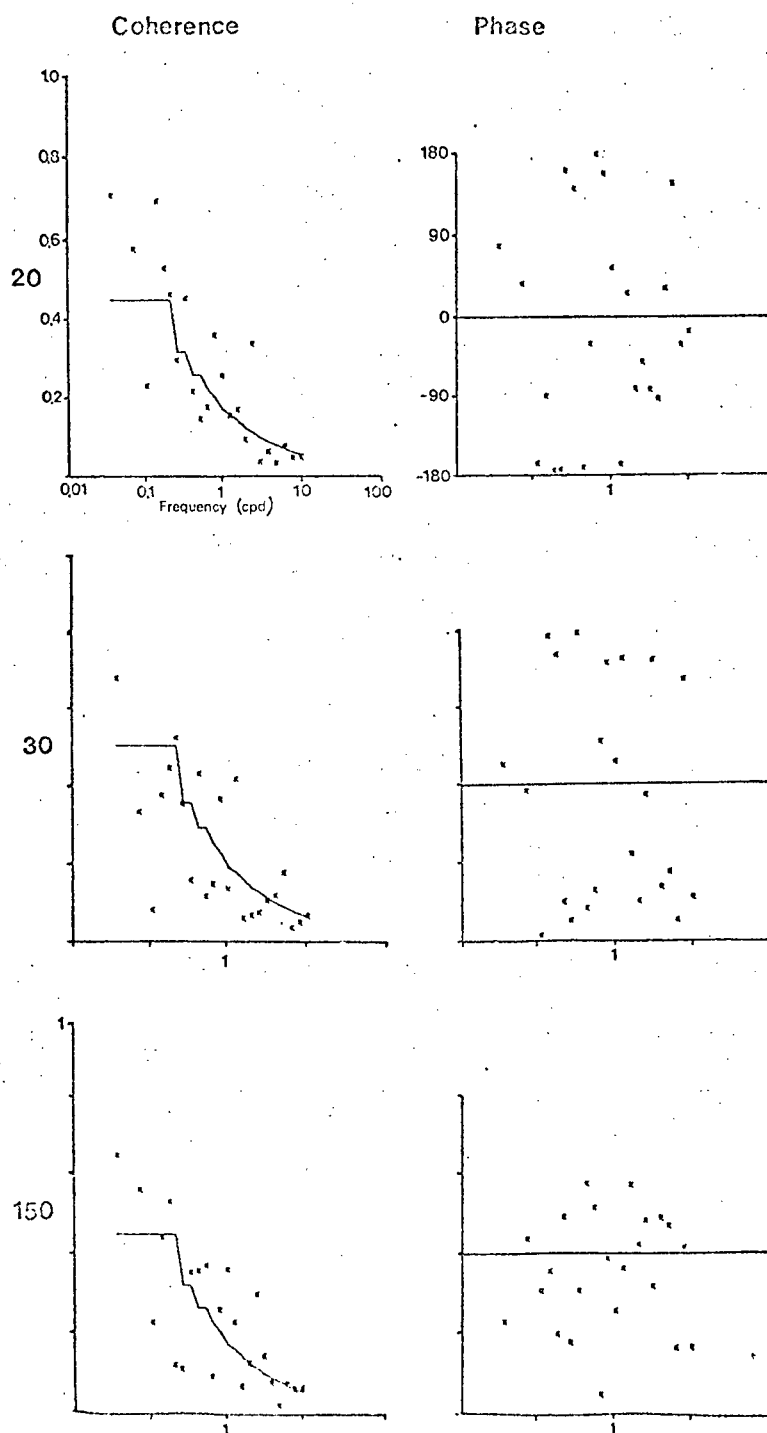


Figure 38 - Coherence and phase between the wind and the current at the metered depths. Positive phase means current leads wind. The solid line on the coherence plots represents the expected random coherence as before.



level. These results are very different from those obtained by Farmer (1972) in Alberni Inlet. He found that the values of coherence-squared between the wind and currents at 2m depth were consistently above 0.8 for frequencies less than 1.2cpd. At higher frequencies it decreased to less than 0.2. The phase varied linearly with the logarithm of frequency from -90° (wind lagging current) at a period of about 500h to 180° at 2h. Farmer attributed this behaviour to the length of time necessary for the wind energy to diffuse through the density gradient from the surface to the depth of the current meter. He postulated a simple diffusion model for this behaviour that related the phase angle between wind and current to the square root of the frequency and the inverse square root of the eddy viscosity. Thus, in effect, he stated that as the frequency of the wind oscillation increased, the period of time for the wind energy to diffuse downwards, as a fraction of the period of oscillation, increased.

The difference in behaviour between Howe Sound and Alberni Inlet probably lies in the difference in the density structure of their surface layers. In Alberni at the time of Farmer's measurements, in the winter of 1971, there was a reasonably constant gradient through the surface few meters whereas in Howe Sound the gradient was very weak to below the depth of the 3m current meter and very strong at some depth below that. Wind energy, which took some time to propagate through the gradient in Alberni, could propagate to the pycnocline in Howe Sound quite rapidly through the

weak gradient, i.e. in Howe Sound, the length of time needed for wind energy to propagate downwards past the 3m current meter was only an insignificant part of the period of oscillation of the driving force. The phase angle between wind and current at 3m in Howe Sound was therefore relatively constant.

The coherence in Howe Sound is probably lower than in Alberni for reasons that also relate to the differing density structure of the surface layer. It was shown in figure 33 that the levels of no motion in Howe Sound could shift, causing relative phase reversals between adjacent current meters consequently lowering the coherence between them. The 3m current meter in Howe Sound is rather close to the level of no motion associated with the pycnocline and therefore might be subject to the occasional phase reversal with respect to the wind. Such behaviour would certainly lower the coherence between the two. The density structure in Alberni was such that an equivalent effect should not be found. Thus the coherence between wind and shallow current should be greater in Alberni than in Howe Sound.

The coherence and phase between the wind and the 5m current meter as shown in figure 38 are quite different from between the wind and the 3m meter. The coherences are in general quite a bit lower and the phase appears to be random. The difference between the response at 3m and that at 5m is due no doubt to the presence of the sharp pycnocline between the two that inhibits direct energy transfer.

The coherence and phase plots at other depths resemble the 5m plots. Phase appears to be basically random in all cases. Coherence values, except for a few instances, lie on or near the random coherence level. No frequency band is consistently above the noise level at all depths. The number of statistically significant coherences decreases from 10m to 30m but then, somewhat surprisingly, rises again at 150m.

Since the dominant peak of the wind spectrum is at 24h let us look at the coherence of the wind and currents in this band. Table IX shows that the coherence drops rapidly as a function of depth. The only significant coherences in

Table IX - Coherence and phase between the wind and currents in the diurnal band. Positive phase is defined as current leading wind. The random coherence level is 0.19.

depth	coh	phase
3m	0.74	-2
5m	0.43	-5
10m	0.22	-156
20m	0.25	55
30m	0.13	26
150m	0.36	-66

this table are at 3m, 5m and 150m. At the shallow depths the wind and currents are essentially in phase. This result substantiates what was seen in figure 33. It is curious that 150m should show a significant correlation with the wind when none is shown at intermediate depths and when table 9 showed that the ratio of energy in the diurnal band to that in the semi-diurnal band was almost exactly what could be attributed to the barotropic tide. The result is probably due to one weakness of coherence analysis. Two different

signals occurring at the same frequency in the Fourier analysis will show a coherence with a third signal if either one of the two is coherent with the third. In this case the diurnal wind and the diurnal tide both act in the same frequency band. The wind is therefore coherent with the tide (although physically related only indirectly of course) and will be coherent with any signal driven by the tide, in this case the 150m current. Higher coherences were not recorded in the mid-depth meters because of the relative phase reversal problems discussed earlier. The 150m meter was presumably in a region of smooth enough density gradient so that relative phase reversals did not occur often.

VI.9 Tidal Influence On The Currents

Since no records of actual tidal height were made during the current meter experiment, the extent of tidal influence on the currents in Howe Sound has to be inferred from the predicted amplitudes of the tidal constituents at Squamish, the spectra of the currents and the coherence and phase measurements between the currents at different depths at tidal frequencies. The amplitudes and periods of the six largest tidal constituents at Squamish are shown in table X. Although the sum of the squares of the amplitudes of the semi-diurnal components is 91% of the sum of the squares of the diurnal components, the kinetic energy associated with purely barotropic tidal currents calculated as the derivatives of sinusoids with the amplitudes and periods

Table X - Amplitude and period of the six major tidal constituents at Squamish. Amplitudes are in cm, periods in hours. The sum of these constituents represents about 80% of the sum of the amplitudes of all the constituents at Squamish.

name	amp	period
O ₁	49.26	25.82
P ₁	27.16	24.07
K ₁	87.45	23.93
N ₂	19.42	12.66
M ₂	94.21	12.42
S ₂	23.23	12.00

given in table X is 3.5 times greater in the semi-diurnal than in the diurnal band. As was shown in table IX, the ratio of mean square currents in the semi-diurnal to diurnal bands as determined from the spectra was found to be close to this value at 150 m. At shallower depths, there was more energy in the diurnal band than could be accounted for by a purely barotropic tide. It seems likely from the results of the previous sections that much of this extra energy comes from the diurnal wind.

Coherence and phase were calculated between the currents at all depths in order to determine the extent that the currents at one depth were related to those at another. Values of coherence between currents presented just as ambiguous a picture in general as did those calculated between the wind and the currents. Problems of relative phase reversal probably are at least partly responsible for the low coherence values as discussed earlier. Measurements of coherence and phase in the two bands of probable tidal excitation however do present an interesting picture. Table XI shows these measurements. The coherence of the 3m

Table XI - Coherence and phase between the currents at different depths at two different periods. In each case, the coherence is listed first followed by the phase in degrees. Positive phase indicates the current at row depth leads the current at column depth. *** indicates that the coherence was at or below the random level. Random coherence level in the diurnal band is 0.19; in the semi-diurnal band it is 0.14.

diurnal band (23.63 to 30.12 hours)

	5	10	20	30	150
3	.69 -24	.35 -88	.35 27	***	.31 -49
5		.53 -11	.40 68	.41 73	.31 -112
10			.40 31	.34 65	.39 179
20				.50 -1	***
30					.66 144

semi-diurnal band (12.09 to 15.21 hours)

	5	10	20	30	150
3	.33 -60	.32 105	.21 21	***	.28 112
5		.53 -24	.46 60	.46 -94	.24 56
10			.79 -39	.72 -55	.61 68
20				.46 -2	.36 89
30					.68 127

currents with those at greater depth is greater in the diurnal band than in the semi-diurnal band. This observation indicates that the surface layer is coupled to a greater extent with the deeper waters at the longer period. In the concluding chapter this difference will be discussed from the point of view of the differences in the basic nature of the forcing functions of wind and tide.

In almost all cases calculated for currents below 3m, the coherence in the semi-diurnal band was greater than the coherence in the diurnal band, suggesting that tidally driven deep currents are more coherent than are those forced partially by the wind, or more likely, that the effects of tidal forcing extend deeper in the water column than do the

effects of wind forcing hence the coherence of tidally forced currents should be higher.

The phase difference between adjacent currents varies more regularly in the semi-diurnal band than in the diurnal band, i.e. the deeper current always lags the shallower in the semi-diurnal band (if the 127° lead of the 150m current over the 30m may be interpreted as a 233° lag) but in the diurnal band the 3m current leads that at 5m, which leads that at 10m, which lags those at 20m and 30m. The difference is best seen in figure 39 which shows phasor diagrams for the currents in each band. The length of each vector represents the r.m.s. current at that depth at that period and the angle represents the phase of the current relative to that at 150m. This phase was actually calculated from the phase difference between adjacent meters.

Several basic differences can be seen on these diagrams between the currents in the semi-diurnal band and in the diurnal band. The currents in the diurnal band are strongest near the surface and decrease continuously as a function of depth while those in the semi-diurnal band have a maximum at 10m and decrease towards the surface. The current strength in the semi-diurnal band also decreases from 10m to 30m but then increases at 150m. The variation in the strength of the currents as a function of depth is greater in the diurnal band, where the minimum is only 18% as strong as the maximum, than in the semi-diurnal band where the minimum is 41% of the maximum.

There are also distinct differences in the relative

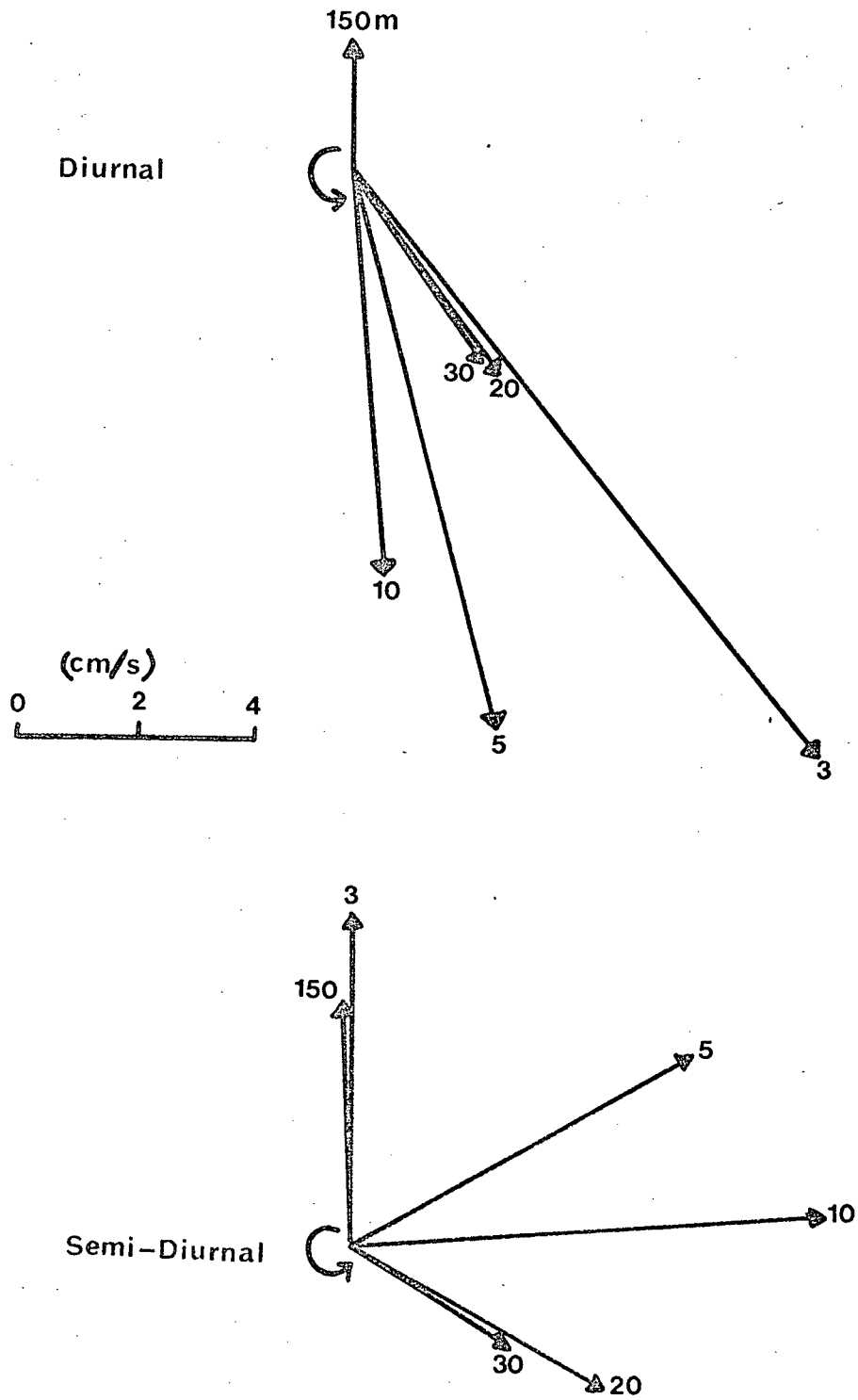


Figure 39 - Current phasors for the diurnal and semi-diurnal frequency bands.

phases of the currents in these two bands. As was mentioned earlier, the deeper currents always lag the shallower ones in the semi-diurnal band but in the diurnal band the 20m and 30m currents appear to lead the 5m and 10m currents. The phasor diagrams show that the 3m and 150m currents are in phase in the semi-diurnal band but in the diurnal band the 150m current is out of phase with the other currents. Thus the diurnal band appears to have a two layered structure with the interface between the two layers between 30 and 150 m. The semi-diurnal band appears to have a more continuous phase distribution, but one that might be typified by a three layer structure with the surface and deep waters in phase. However, the accuracy of the phase determinations has not been calculated so that attempting to draw any conclusions based on the details of the phase relationships is hazardous.

VI.10 Changes In Hydrographic Properties As Indicators Of Currents

The spectral analysis of the currents that was done in this chapter could only examine fluctuating currents at frequencies higher than 0.03cpd (periods less than 768h). Lower frequency currents could only appear as trends in the mean values of successive blocks of the data. Low frequency currents can often be inferred however from changes in the density field and in other properties of the inlet. The hydrographic cruises mentioned in the introduction to this

thesis were carried out to measure such changes. Cruises were made covering two summers and two winters, from July 1972 to March 1974. During the period from March to September, 1973, for which current meter data were analysed, no significant changes were seen in the density below 125m depth. A more sensitive quantity to water changes in Howe Sound is temperature. A contoured time series of temperature vs depth and time at station How 4 is shown in figure 40. Only temperatures at depths of 50m and below have been plotted. In the waters above 100m, the effects of seasonal insolation can be seen, but below this depth there is little change. From March to September there was a change of only -0.08°C at 200m. These measurements indicate that there were no significant events causing slow deep currents.

The dramatic drop of the isotherms between September and November indicates that a deep-basin flushing event took place. Temperature sections of the sound on the 20 September cruise and on the 13 November cruise are shown in figure 41. These two sections show that the deep water in September was displaced to mid-depth near the head of the inlet by water from 75 to 80m outside the sill. Although the isotherms in the November section are tilted the isopycnals are level and roughly the same as in figure 2. There was no detectable density difference between the water at depth inside the sill in September and in November.

The progressive vector diagrams (PVD's) calculated by Bell(1975) from the current meter data at 150m over the period 7 November to 27 November 1973 show a continuous

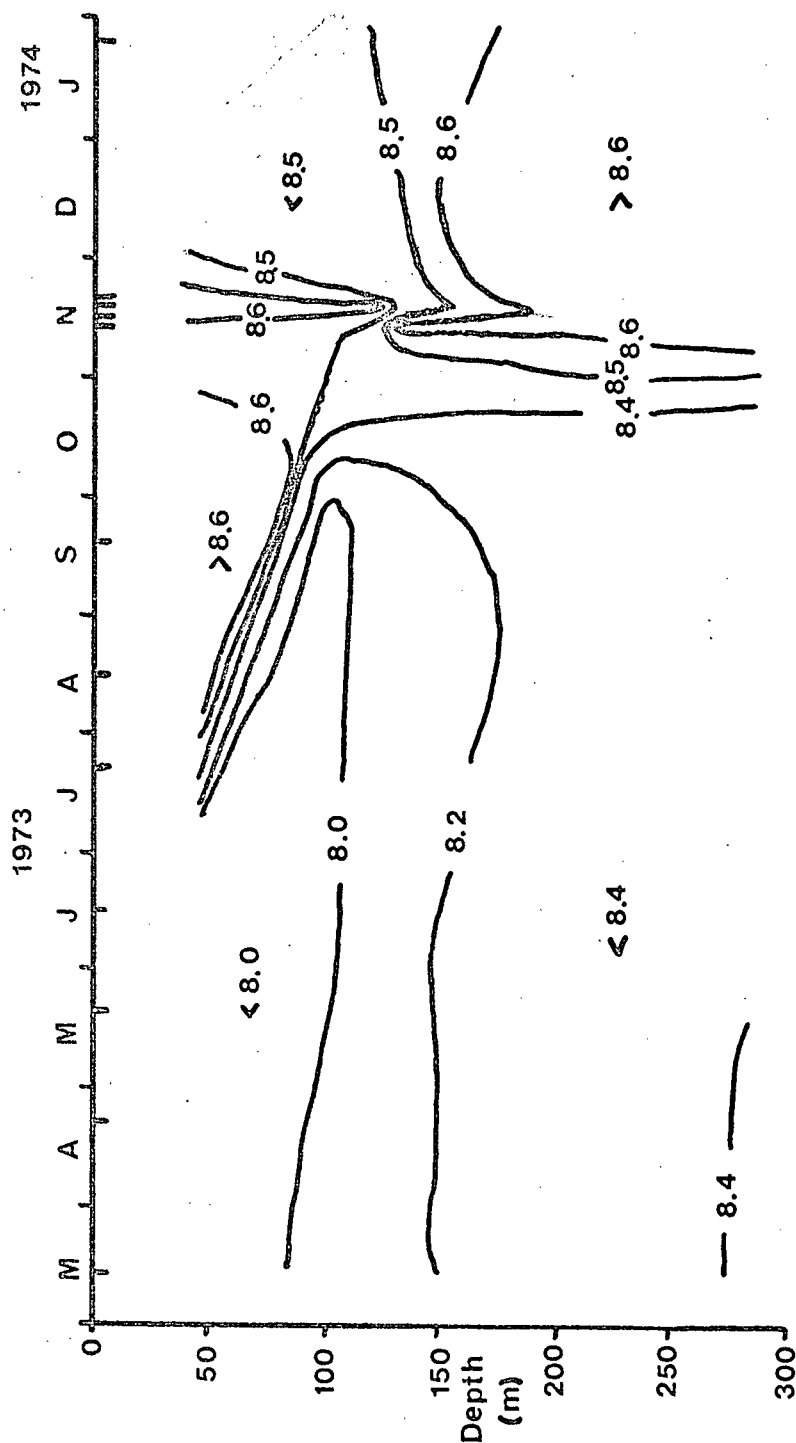


Figure 40 - Isotherms plotted vs time and depth for station 4 (shown in fig 41). Ticks below the time axis indicate sampling dates. No data above 50m were considered.

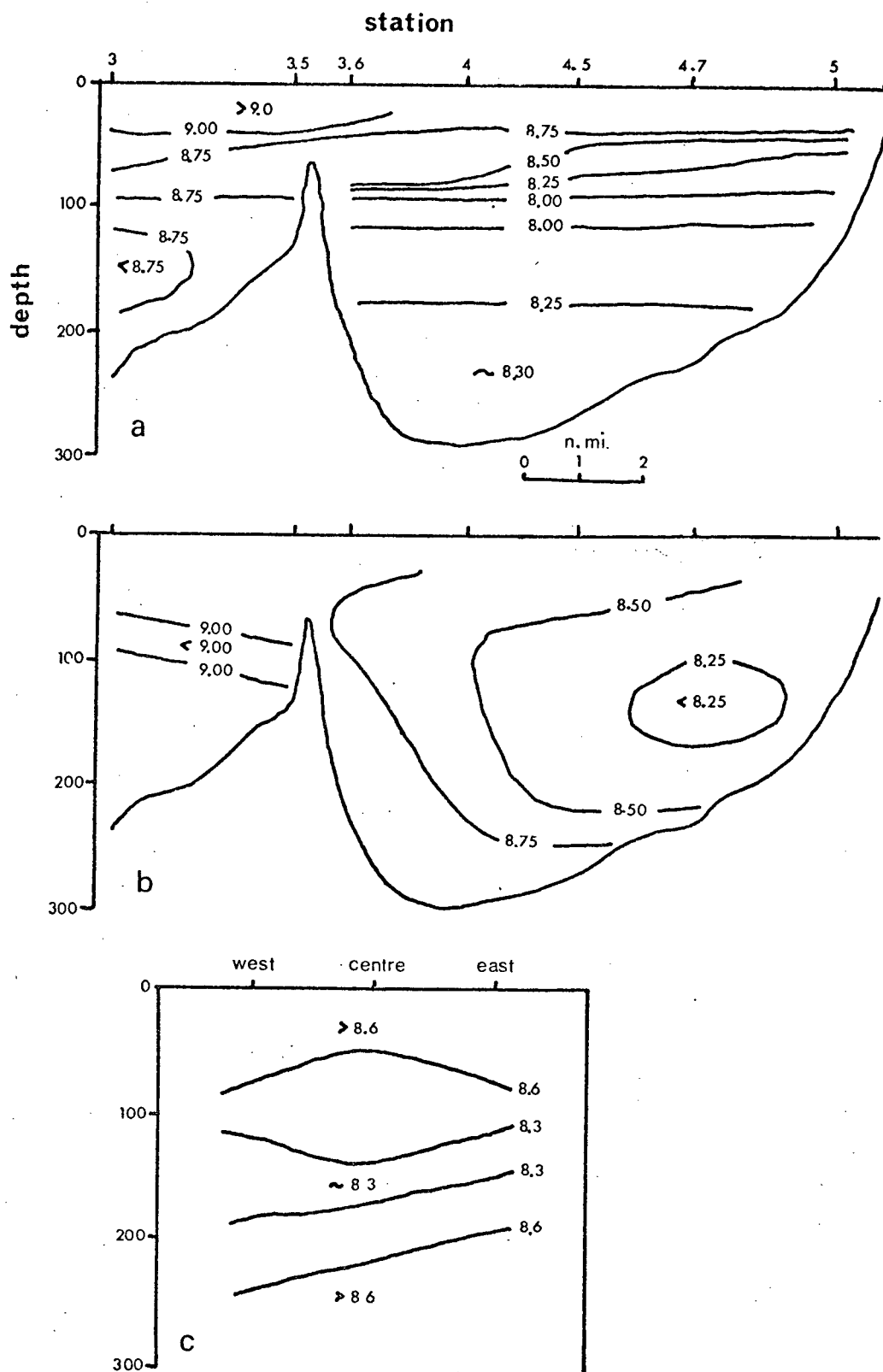


Figure 41 - Isotherm sections of Howe Sound.
 a. Longitudinal section taken 20 September 1973.
 b. Longitudinal section taken 13 November 1973. c. Cross-inlet section taken with STD instead of bottles 21 November 1973. Data above 30m have not been used.

inflow run of about 12.5km from November 9 to 13. This total distance is consistent with the distance that the 8.5° isotherm had to move from sill depth in the 20 September section to 220m depth at How 4.7 in the 13 November section. The PVD shows that the flow is not steady but oscillated with approximately diurnal period. The strongest inflow was on November 10th. On November 9th, strong northerly winds persisted for most of the day. These winds could have caused enough movement of density surfaces in the sound to cause denser water to spill over the sill into the inner basin.

There was only one other period of inflow of more than one day duration in the entire series of PVD's shown by Bell. It occurred under similar circumstances in mid-December 1972 and caused similar changes in the hydrographic structure of the waters in the fjord. The rest of the PVD's showed varying amounts of outflow. The PVD's also showed large net cross-inlet currents usually to the east. These can likely be explained by the same sort of rotationally influenced waves that cause the net down-inlet current at 150m.

Although these data seem to present a consistent picture of this advection of water into the basin, a cautionary note must be made. A series of three STD casts was made in Howe Sound on November 21, 1973 with a Bisset-Berman model 9060 instrument at equally spaced locations across the channel at a long-channel position between How 4 and How 4.5. This temperature section shown in figure 41c indicates that there was a large cross-channel gradient in

temperature in the deeper waters of the same order as the long-channel gradients shown in figure 41b. The new warmer inflowing water is on the right of the channel as it should be in a channel flow affected by the earth's rotation. The volume of water that entered the inlet cannot be calculated on the basis of the difference between the long-channel isotherm sections in figure 41 a and b because of these strong cross channel variations.

This event in Howe Sound has been studied in more detail by Bilodeau and Osborn (1976) who looked at the temperature microstructure in the inner basin of Howe Sound as well as the hydrographic features.

CHAPTER VII

SUMMARY OF RESULTS AND COMPARISON WITH THEORY

This chapter begins with a summary of the results of the surface layer experiment described in chapter IV and of the subsurface current experiment described in chapter VI. Some of these results are then compared with models of estuarine circulation. The adequacy of each model to describe the appropriate features will be assessed.

VII.1 Summary Of The Experimental ResultsVII.1.1 The Surface Layer Experiment

The surface layer experiment provided a great deal of information on the spatial and temporal structure of the surface waters near the head of a fjord.

The surface layer flow was found to be highly variable, both in space and in time. The dominant time scale of the variations was diurnal; the amplitude was about five times the averaged (both temporally and cross-channel) surface flow, including entrainment, expected from the river as was seen in section IV.6. Section IV.7 showed that the spatial scale of variation in the transverse direction of the long-

channel component of velocity was on the order of the inlet width. Near the head of the inlet, the waters usually flowed in opposite directions on opposite sides of the inlet; near the sill, the flow was more spatially uniform. It was shown in section IV.8 that the long-channel velocity gradients were larger near the head than near the sill. There was some indirect evidence, from sections IV.5 and IV.7, that the spatial structure of the velocity field was independent of the time fluctuations of the field.

The measured acceleration field contained similar temporal variations. It appeared in section IV.5 however that the acceleration was much less spatially variable than was the velocity. The contribution to the long-channel component of acceleration from the spatial velocity gradients was much less than that from the temporal gradients except near the head of the inlet. There the contributions were of similar magnitude.

The temporal variations in velocity, discussed in sections IV.4 and IV.6, occurred in synchronization with variations in the wind. After the onset of the wind, the acceleration of the surface layer was constant for several hours. Then it decreased, changed sign, and finally returned to a value near zero even though the wind continued to blow. These effects were more obvious away from the head of the inlet. Near the head of the inlet a coincidence between maximum tidal height and maximum down-inlet velocity was seen. This correlation may have occurred farther down the inlet too but might have been masked by the much stronger

wind effect.

The silt patterns in the surface layer, resembling a river meandering through the waters of the inlet, do correspond in general to the pattern of surface circulation in Howe Sound. However, the non-silty water often moves as fast as the silty water, so caution is necessary when attempting to relate silt patterns to the surface layer current structure.

VII.1.2 The Subsurface Current Experiment

The results of the current meter experiment verified the existence in Howe Sound of the traditional estuarine circulation pattern. The mean velocities, shown in section VI.6 indicated the possible presence of several layers in this pattern. The depths of these levels appear to shift occasionally. Superimposed on the mean flow field were variations several times larger than the mean velocities. Spectra of these variations from section VI.7 showed that they existed predominantly at two frequencies: diurnal and semi-diurnal. The shallow meters also indicated the presence of some energy at lower frequencies.

It was shown in section VI.8 that the currents at 3m had relatively high coherence with the wind. The current led the wind by an essentially constant 20° for periods longer than ten hours. The currents at 5m and deeper were not as coherent with the wind and showed no particular phase relationship with it. Evidence that wind effects penetrated

below 3m came from two sources: the shape of the low-frequency end of the current spectra and the kinetic energy ratios of the diurnal to the semi-diurnal spectral peaks. Both sources indicated that wind forcing of the currents decreased with depth and was not significant at 150m.

Tidal energy, discussed in section VI.9, was present at all depths, as evidenced by the spectral peak at 2 cpd. The root mean square (r.m.s.) currents at this frequency varied in strength only by a factor of two over the entire depth range, with the strongest current occurring close to, but below the surface. In contrast, in the 1 cpd band the r.m.s. current strength varied by a factor of 6 and was greatest at the surface. Examination of the phase relationship between the currents in these two frequency bands also indicated that the currents were baroclinic. The phase structure was markedly different in the two bands.

A surprising feature was the net current flowing down-inlet at 150m. This observation might indicate the existence of Coriolis effects on the motions in the deep waters of the fjord. The only exceptions to this outflow at 150m, discussed in section VI.10, occurred for two periods of inflowing current for a few days in the winters of 1972 and 1973. Hydrographic data taken at the same time showed changes in water properties in the deeper parts of the fjord indicative of a deep-basin water replacement event. The 1973 hydrographic data clearly showed a cross-inlet asymmetry in the in-flow suggestive of the influence of the earth's rotation on the flow.

Cross-channel asymmetry in the flow below the surface was also made evident in a three-level drogue experiment, described in chapter V, in which velocities in the upper 6m of the water column were observed for a few hours.

VII.2 Drag Coefficient Calculations

The pycnocline in Howe Sound is shallow and abrupt at about 4m depth. The currents at 3m and 5m show different behaviour. These facts lend credence to the assumption of a discrete surface layer. As a first approximation, let us assume that the friction between this surface layer and the underlying waters is negligible. This assumption is warranted on the following grounds. The gradient Richardson number

$$Ri = \frac{-g(\partial \rho / \partial z)}{\rho (\partial u / \partial z)^2} \quad (7.1)$$

is about 20 for typical values of density gradient taken from the salinity gradients in figure 13 and velocity gradients taken from figure 32. Because of the crude scale of measurement of the velocity profile and the non-simultaneity of the measurements, this value is only a rough approximation, probably within an order of magnitude. Since $Ri \gg 1/4$, the interface between the layers is quite stable to perturbations and hence there should be no large turbulent drag due to mixing on the interface. Further evidence of stability is given by the measured salinity

change in the surface layer of only 4‰. from the river mouth to the sill at Porteau Cove.

Since the vertical density gradient in the surface layer is small it may also be reasonable to assume that momentum input by the wind through the water surface diffuses rapidly down to the pycnocline. This assumption is consistent with the relatively constant phase between wind and 3m current at periods greater than 10h. Hence a wind stress applied to the water surface should act as a body force on the surface layer to accelerate the water until the stress is balanced by the pressure gradient. We may relate the acceleration of the surface layer to the wind speed using the standard square law wind drag formula:

$$D \rho_w \vec{a} = \rho_a C_D \vec{U} |\vec{U}| \quad (7.2)$$

where \vec{U} is the wind velocity, \vec{a} is the drogue acceleration D the depth of the surface layer, ρ_a and ρ_w the densities of air and water and C_D the drag coefficient. In the experiments we had no measure of the cross-stream components of the wind velocity \vec{U} , but from the geometry of the channel it had to be small with respect to the long-channel component; hence it will be left out of the succeeding calculations. There is some uncertainty in the value of D to be used, as will be discussed shortly. The only unknown in this equation is the drag coefficient C_D . Its value as computed directly from the downward flux of wind momentum

above the sea surface is about 1 to 1.5×10^{-3} (Pond et al (1974), Stewart (1974)). C_D was calculated using equation 7.2 for each hourly average of wind speed and drogue acceleration. The results are plotted (figure 42). Only those values in the range $-4 \times 10^{-3} < C_D < 4 \times 10^{-3}$ are plotted. Values outside this range and negative values in this range obviously contradict the basic assumption that the wind is the dominant cause of the water acceleration. Positive values in this range indicate that, by this criterion, the wind stress is likely the dominant force driving the surface circulation. Such periods should occur at the onset of strong winds. They do in week 1 at 35 hours and 60 hours (fig 42c), and in week 3 at 36 hours and 58 hours (fig 42d). In all these cases the drag coefficients had values of $1-2 \times 10^{-3}$. What is also interesting is that the values of C_D remained approximately constant for several hours after the onset of the winds. After this period they decreased, became negative and in one case returned to zero. This behaviour is indicative of the takeover of some other force as the dominant term in the force balance equation for the surface layer.

The calculated drag coefficients from week 4 (fig 42a) show that there were no significant periods of wind-dominated circulation. Since there were only small variations in a fairly steady up-inlet wind throughout the week, the up-inlet wind stress presumably would have been balanced by a down-inlet pressure gradient throughout the week. There were large variations in wind velocity in the

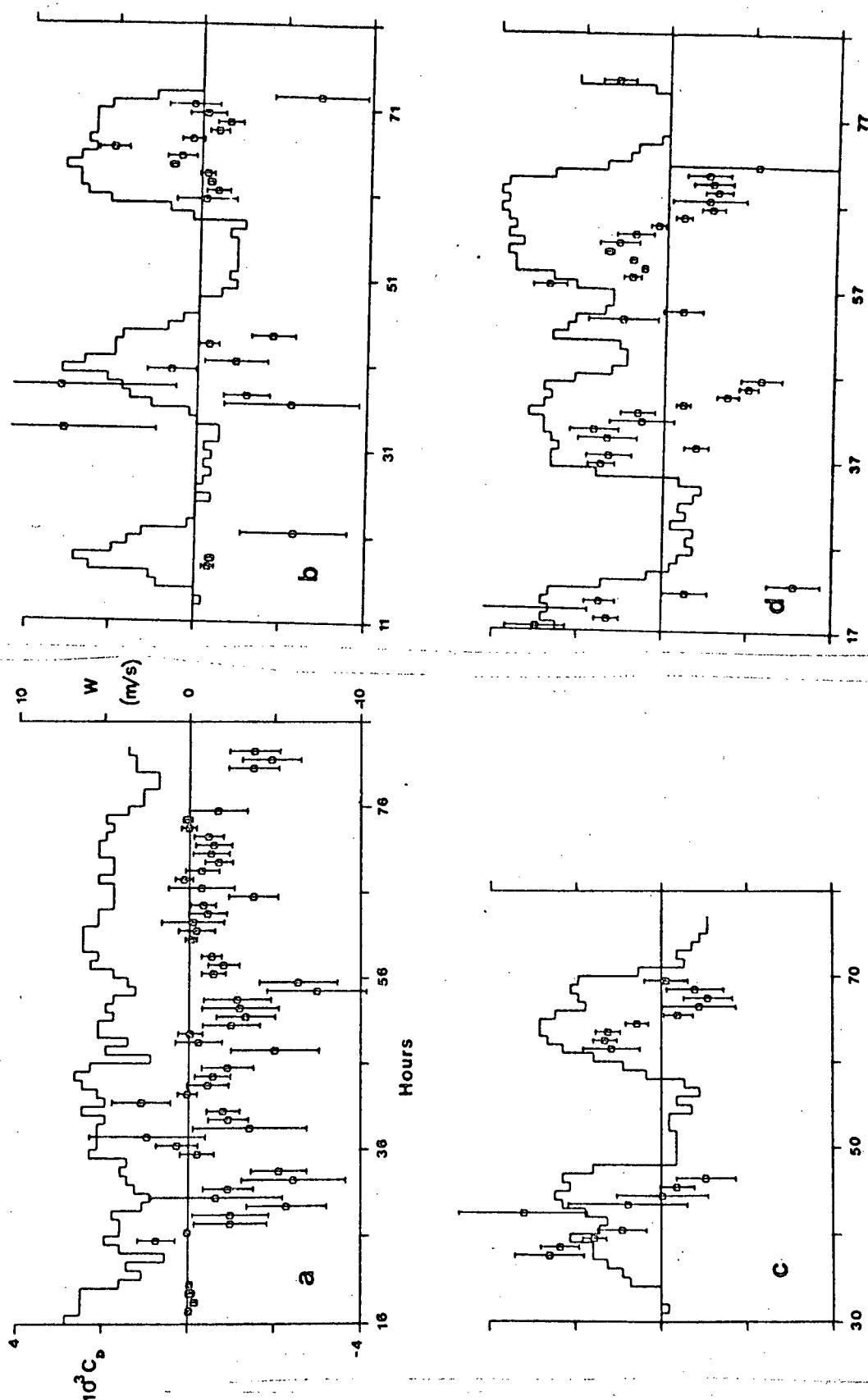


Figure 42 - Drag coefficients calculated from hourly averaged wind velocities and water accelerations. a. week 4. b. week 2N. c. week 1. d. week 3. The solid line is the Squamish wind as has been previously described. The error bars are \pm one standard error of the mean of all values of C_D calculated that hour.

week 2(north) data set (fig 42b) but, as was shown in chapter IV, the currents did not appear to respond to changes in the wind in the same simple way of weeks 1 and 3. The drag coefficient calculations confirm this conclusion. Only in the period of up-inlet winds from 61 to 71 hours are there coefficients of the proper sign and magnitude. There is no period of constant positive drag coefficient in this interval but from 65 to 71 hours there appears to be the same sort of swing from wind stress domination to pressure gradient domination to equilibrium that was seen in the week 1 and week 3 calculations.

Measurements of the surface layer density structure were made only during weeks 3 and 4. From the week 3 salinity profiles shown in figure 13, the middle of the halocline was seen to be about 3.5m. This depth corresponds quite well to the depth of the pycnocline and so was used as the constant layer depth for the drag coefficient calculations. Farmer (1972) showed that wind effects caused a variation in depth of the surface layer. Application of a form of his model to Howe Sound shows that, away from the ends of the fjord, the surface layer depth remains constant for a period of hours after the onset of the wind, so a constant layer depth approximation is adequate. This model will be discussed in more detail in the next section. Since density profiles were not measured in weeks 1 or 2, the layer depth can only be approximated by the week 3 values. This assumption may be partly responsible for the scatter of the drag coefficient values in the week 1 calculations.

Another question that arises is the relationship of the pycnocline depth to the depth of zero current as was discussed in chapter III. If the zero current depth were somewhat smaller than the pycnocline depth or if the pycnocline depth were smaller, then the values of drag coefficient calculated would be smaller and closer to the accepted values of 1 to 1.5×10^{-3} .

These calculations have shown that a two-layer model, with little friction between the layers, may be used to explain some of the wind driven circulation features of the surface layer.

VII.3 Farmer's Model Of A Wind-Driven Surface Layer

As part of his study in Alberni Inlet, Farmer (1972) developed a linear two-layer model to describe the behaviour of the surface waters of a fjord under the influence of a wind stress. The model will not be developed in detail here: only enough of the features will be discussed to present adequately the results and compare them with observations in Howe Sound.

Farmer approximated the inlet by a semi-infinite canal of uniform width and depth containing two homogeneous layers of different density. He described the system with linearized equations of motion and continuity for a two-layer fluid. They were vertically integrated over each layer and converted to a "normal mode" representation. Farmer then proceeded to solve the following equations for U, the upper

layer internal mode (baroclinic) transport and η , the displacement of the interface from the mean layer depth, h .

$$\partial^2 U / \partial t^2 = c^2 \partial^2 U / \partial x^2 + \partial(T - KU) / \partial t \quad (7.3)$$

$$\partial U / \partial t = c^2 \partial \eta / \partial x + T \quad (7.4)$$

In these equations T is the kinematic wind stress, c is the internal wave speed and K is an interfacial friction coefficient for the internal mode. Farmer considered solutions forced by a wind stress applied from $x=0$, the head of the inlet to $x=d$, some point farther down the inlet. Performing a Laplace transform with respect to time of equation 7.3 and applying the appropriate boundary conditions he arrived at the solutions

$$\overline{U} = \frac{\overline{T}}{(s+K)} \left(-\exp(-\gamma x) + \frac{\exp(-\gamma(d+x)) - \exp(-\gamma(d-x))}{2} + 1 \right) \quad (7.5)$$

for $x < d$. Here the overbar indicates the transformed quantity and s is the transform variable. The interface displacement equation then became

$$\overline{\eta} = \frac{\overline{T}}{c^2} \left(\exp(-\gamma x) - \frac{\exp(-\gamma(d+x)) - \exp(-\gamma(d-x))}{2} \right) \quad (7.6)$$

where $\gamma = \sqrt{s(s+K)} / c$. From this point, Farmer inverted the layer depth equation and examined its behaviour for short

periods of wind stress in the region near the inlet head where $x/c < (d-x)/c$.

Let us now diverge from his work and examine the transport and interface displacement for an up-inlet wind stress applied for a long time ($t > (d+x)/c$) in a friction-free situation ($K=0$). The inverse transforms of equations 7.5 and 7.6 are:

$$U = T \left\{ t - (t-x/c) H(t-x/c) + (1/2) (t - (d+x)/c) H(t - (d+x)/c) - (1/2) (t - (d-x)/c) H(t - (d-x)/c) \right\} \quad (7.7)$$

$$\text{and } \eta = (T/c) \left\{ (t-x/c) H(t-x/c) - (1/2) (t - (d-x)/c) H(t - (d-x)/c) - (1/2) (t - (d+x)/c) H(t - (d+x)/c) \right\} \quad (7.8)$$

where $H(t)$ is the Heaviside unit step function. These solutions break naturally into two different sets: those where $x/c < (d-x)/c$ and those where $x/c > (d-x)/c$. In Howe Sound the logical choice for $x=d$ is at the sill, where the up-inlet wind speed increases markedly due to topographic funnelling. Using the "slab" model we can calculate from the transport and layer depth, the mean velocity of the layer as $u = U/(h + \eta)$. For later comparison with measured drogue accelerations, the acceleration of the water in the surface layer may be calculated as $\partial u / \partial t$. Since the model is linear,

the spatial gradient terms in the acceleration may be neglected. The solutions to this system (equations 7.7 and 7.8) for U, η, u , and a are as follows:

$$x/c < (d-x)/c$$

$$(d-x)/c < x/c$$

$0 < t < x/c$	$0 < t < (d-x)/c$
$V = Tt$ $\eta = 0$ $u = Tt/h$ $a = T/h$	
$x/c < t < (d-x)/c$	$(d-x)/c < t < x/c$
$U = Tx/c$ $\eta = (T/c)(t - x/c)$ $u = x/(t - x/c + ch/T)$ $a = -x/(t - x/c + ch/T)^2$	$U = (T/2)(t + (d-x)/c)$ $\eta = -(T/2c)(t - (d-x)/c)$ $u = \frac{ct + d - x}{2ch/T - t + (d-x)/c}$ $a = \frac{2(c^2h/T + d - x)}{(2ch/T + (d-x)/c - t)^2}$
$(d-x)/c < t < (d+x)/c$	$x/c < t < (d+x)/c$
	$U = (T/2)(-t + (d+x)/c)$ $\eta = (T/2c)(t + (d-3x)/c)$ $u = \frac{-ct + d + x}{2ch/T + t + (d-3x)/c}$ $a = \frac{2(-c^2h/T - d + x)}{(2ch/T + (d-3x)/c + t)^2}$

$(d+x) / c < t$
$U=0$
$\eta = (T/c) (d-x)$
$u=0$
$a=0$

This model of a surface layer may be fitted approximately to the north end of Howe Sound by choosing $d=20\text{km}$, $h=5\text{m}$ and $c=1\text{m/s}$. For a steady wind of 10m/s , $T=C_D U|U| (\rho_a/\rho_w)=1.56 \times 10^{-4} (\text{cm/s})^2$ for $C_D=1.25 \times 10^{-3}$. Plots of average layer velocity and acceleration vs time calculated from the above model are shown in figure 43 for $x=6\text{km}$ and $x=15\text{km}$. These values of x correspond roughly to positions of the week 2 (north) and week 3 averaging bands. A direct comparison may be made between the velocity and acceleration curves in figure 43(case 1) and figure 27 c and d and between figure 43(case 2) and figure 27 g and h.

The acceleration and velocity curves in figure 43 can be seen to be composed of three separate sections corresponding to the different forces on the surface layer. The initial forcing arises only from the wind stress which constantly accelerates the surface layer. The other force arises from surface pressure gradients which propagate along the inlet as waves, one of which travels from the head of the inlet and the other of which travels toward the head of the inlet from the point d. Both waves travel at the internal wave speed. The wave that propagates from the head

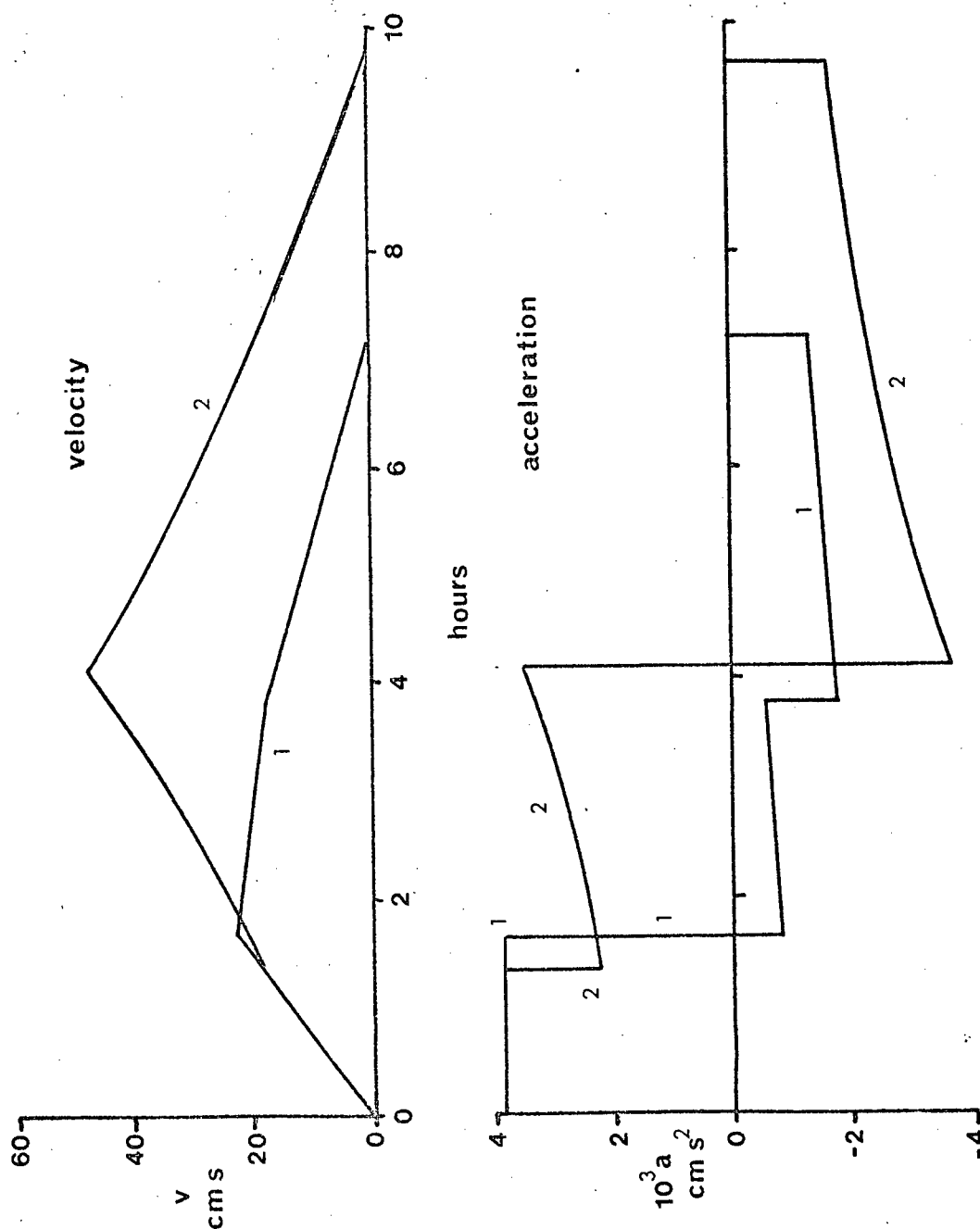


Figure 43 - Velocity and acceleration of the surface layer vs time calculated from Farmer's model for an up-inlet wind of 10m/s applied at $t=0$. Curves labelled 1 are for $x=6\text{km}$, 2 are for $x=15\text{km}$. Model parameters are discussed in the text.

of the inlet, called hereafter the head wave, results from the collecting of water pushed towards the head of the inlet by the up-inlet wind driven transport. This water elevates the surface of the fjord creating a pressure gradient that balances the wind stress. The elevation of the surface causes a simultaneous depression of the interface. The ratio of surface elevation to interface depression is approximately $\Delta\rho/\rho$. The wave propagating from the point d, called the end wave by Farmer, is caused by the necessity of having continuity of transport in the surface layer at that point and hence causing a shallowing of the interface. Before either wave arrives at some point x, the wind causes the constant acceleration of the surface layer that was discussed in the last section. The layer depth does not change. In figure 43, case 1, which is closer to the head of the inlet, the head wave arrives before the end wave. The up-inlet transport then becomes constant and the layer depth increases, hence the velocity decreases and the acceleration becomes negative. When the end wave arrives later the negative acceleration increases in magnitude until the time $(d+x)/c$ when transport, velocity and acceleration become zero. In figure 43, case 2, nearer the point d, the end wave arrives first. Since the layer depth is decreasing and the transport is increasing the acceleration remains positive. However when the head wave arrives, the acceleration drops dramatically and becomes negative. Again, at time $(d+x)/c$ the velocity becomes zero as does the acceleration.

These acceleration curves bear a resemblance to those

shown in figure 27 measured in Howe Sound. The curves in figure 43 of course were frictionless. If friction were added to the solution the sharp corners in the velocity curves would disappear, the sharp changes in acceleration would disappear and the acceleration values would, in general, decrease in magnitude. All these factors should help to bring the theory more in line with the observations. The theoretical acceleration curve remains relatively constant and positive until the time that the head wave arrives, at which time it becomes negative. The observations agree: the period of constant acceleration increases from week 2 to week 1 to week 3. The range of both the theoretical and observed acceleration is $8 \times 10^{-3} \text{ cm/s}^2$. The range of both the observed and theoretical velocities is about 60 cm/s. There are however some major differences between theory and observations. Theory says that the length of time of negative acceleration should be much longer than the time of positive acceleration. The observations show that, although the negative phase is longer than the positive phase, it is only slightly longer. Theory shows a rapid change from positive to negative acceleration and a slow return to zero, while observation shows rates of change from positive to negative and negative to positive that are almost the same. The velocity curves too show some difference between observation and theory. The theoretical velocities are only up-inlet. They must be superimposed on the mean river flow to be comparable to the observed velocities. Even with the -5 cm/s of the mean river flow

added they do not approach the down-inlet strength of the observed currents. Arrival of the waves at a point after a few hours causes the velocity to drop even though the wind continues. Thus the current peak may occur before the wind peak and hence the current may appear to lead the wind as it did in chapter VI.

Farmer's model seems to describe reasonably well many of the observed features of the time variations of the surface layer circulation. It does not agree with the observations when the pressure gradients are interacting with the wind-stress driven flow, i.e. when the interfacial waves reach the point of measurement. The model is linear while the observations have shown that for the important region near the head the flow regime is non-linear. Thus once the pressure gradients that have propagated through this region interact with the purely wind-driven flow, we can expect discrepancies. Heaps and Ramsbottom (1966) have suggested that a circulation exists within a homogeneous surface layer that is in dynamic balance between a wind stress and a surface pressure gradient. Under these circumstances the "slab" representation of the surface layer used in this thesis would not be valid and the theoretical velocity estimates would be wrong as they do appear to be. However Farmer's model and the "slab" representation of the surface layer seem to be in remarkable agreement with the first few hours of the observed interaction between the wind and the surface layer in Howe Sound.

VII.4 Tides And A Normal-Mode Fjord Model

Several sets of observations of the currents in Howe Sound can be explained by the presence of a baroclinic tide. Observed currents at all depths were stronger than 2 cm/s in the semi-diurnal band but a barotropic tidal prism model for Howe Sound mentioned in chapter III predicts only 0.7 cm/s at the current meter location. The phasor diagram in figure 39 for the semi-diurnal currents showed large phase differences between the currents at different depths. The up-inlet surface layer currents near the head of the inlet appeared to be 180° out of phase with the tidal height, not 90° out of phase as would be expected if the current were uniform with depth.

It has been shown (Proudman, 1953) that depth discontinuities in a stratified fluid can cause a baroclinic response to barotropic forcing. Rattray (1960) computed the baroclinic response of the deep ocean to the interaction between a barotropic tidal wave and the continental shelf. A similar study was carried out by Buckley (1974) for barotropic forcing at the mouth of a fjord-like basin. Both studies were of the simplest possible two-layer friction-free type. The formulation and results of both models were very similar but the techniques of solution of the equations differed. The results will be presented in the form given in Rattray.

The model is based on the equations of momentum and continuity in each of two homogeneous layers in a narrow

semi-infinite canal. The solutions to these equations are different in regions of different depth and so are subject to a matching condition for interface height and transport in each layer at the depth discontinuity. Time dependence of the system is assumed to be proportional to $\exp(-i\sigma t)$ so all time derivatives are replaced by $-i\sigma$ and the system of equations is solved for spatial dependence alone. Rattray's model contains no transverse gradients of the variables but does allow for a constant transverse current driven by Coriolis force. Since Howe Sound is too narrow for rotational effects to be significant at the interface, the model has been modified by removing the effects of the earth's rotation. This modification is consistent with the addition of lateral boundaries to Rattray's version of the model. Figure 44 shows the basin geometry used and indicates the variables and parameters in the problem. The equations are solved for the four variables u' , u'' , ζ' and ζ'' where u' is the surface layer transport, u'' the bottom layer transport, ζ' the surface height deviation from the mean and ζ'' the interface height deviation from the mean. The equations can however be separated into a "normal-mode" representation such that each variable is broken into a barotropic part and a baroclinic part i.e. $u' = u'_s + u'_b$ where u'_s is the surface layer transport due to a barotropic wave and u'_b is the surface layer transport due to a baroclinic wave. Solutions are calculated for the regions $0 < x < L$ and $x > L$ representing the regions inside the sill and in the region of the sill. The solutions given by Rattray for $0 < x < L$

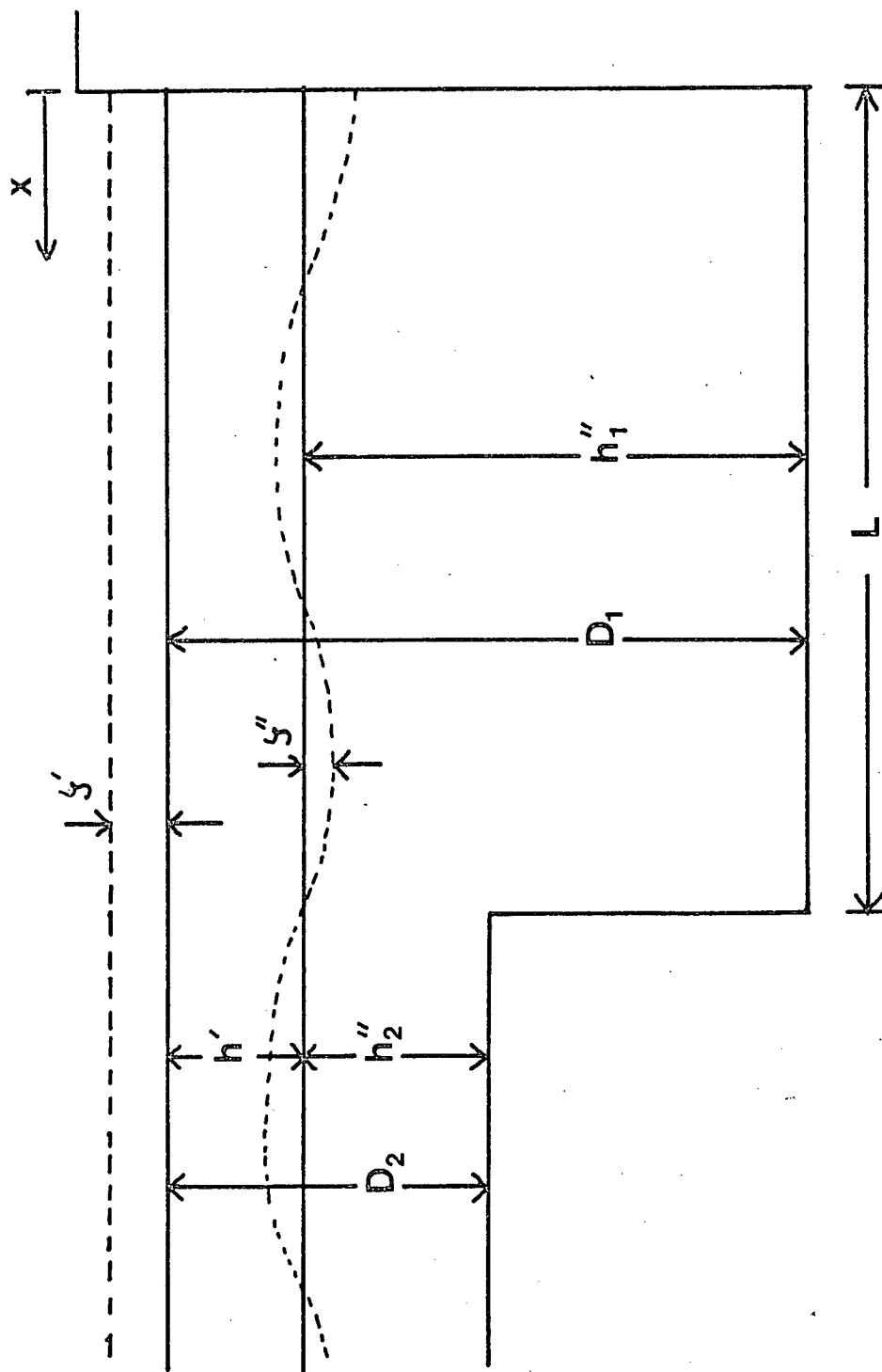


Figure 44 - Basin geometry and parameters used for the two-layer baroclinic tidal model.

neglecting rotational terms are

$$\zeta_s' = \zeta_0' \quad (7.9)$$

$$\zeta_s'' = h' \frac{\zeta_0'}{D_1} \quad (7.10)$$

$$u_s' = u_s'' = -\frac{i\sigma \zeta_0' x}{D_1} \quad (7.11)$$

$$\zeta_i'' = A \cos(k_i x) \quad (7.12)$$

$$h' u_i' = (D_1 - h') u_i'' = (i\sigma/k_i) A \sin(k_i x) \quad (7.13)$$

where

$$k_1^2 = \frac{\sigma^2 D_1}{h' (D_1 - h') g \frac{\Delta \rho}{\rho}} \quad (7.14)$$

$$k_2^2 = \frac{\sigma^2 D_2}{h' (D_2 - h') g \frac{\Delta \rho}{\rho}} \quad (7.15)$$

$$A = \zeta_0' h' (1/D_1 - 1/D_2) \sqrt{1 + k_1^2 L^2} K^{-1} \exp(i(\alpha - \beta)) \quad (7.16)$$

$$K = \sqrt{\cos^2 k_1 L + (k_2^2/k_1^2) \sin^2 k_1 L}$$

$$\alpha = \tan^{-1}(k_2 L)$$

$$\beta = \tan^{-1}((k_2/k_1) \tan(k_1 L))$$

in these equations, L is the basin length, D_1 is the basin depth, D_2 is the sill depth, h' is the surface layer depth and σ is the frequency. A similar set of solutions exists for $x > L$. The system is forced by a barotropic tide imposed as ζ_0' from the region $x > L$. Since the system length L is very small with respect to the wavelength of the barotropic tide, ζ_0' can be assumed to have no spatial variation.

What is of most interest to us now is the phase relationship of the currents to the driving force. The total surface layer current is :

$$u' = u'_s + u'_t \quad (7.17)$$

$$= i \frac{\sigma}{D_1} \zeta_0' x + i \frac{\sigma A}{h' k_1} \sin(k_1 x) \quad (7.18)$$

If A is split into its real and imaginary parts such that

$$A = A' (\cos(\alpha - \beta) + i \sin(\alpha - \beta)) \quad (7.19)$$

then the surface-layer current may be written as

$$u = f + i g \quad (7.20)$$

where

$$f = \frac{A' \sigma}{h' k_1} \sin(\alpha - \beta) \sin(k_1 x) \quad (7.21)$$

and

$$g = \frac{A' \sigma}{h' k_1} \cos(\alpha - \beta) \sin(k_1 x) - \frac{\sigma \zeta_0' x}{D_1} \quad (7.22)$$

The phase of the surface current with respect to the forcing tidal amplitude is therefore:

$$\theta = \tan^{-1} (g/f) \quad (7.23)$$

and the amplitude of the current is

$$|u| = \sqrt{f^2 + g^2} \quad (7.24)$$

In Howe Sound an appropriate choice for the parameters in these equations might be:

$$L = 2 \times 10^6 \text{ cm}$$

$$D = 2 \times 10^4 \text{ cm}$$

$$D = 7 \times 10^3 \text{ cm}$$

$$h' = 500 \text{ cm}$$

$$\frac{\Delta \rho}{\rho} = 2 \times 10^{-2}$$

Using the observed M_2 amplitude gives $\zeta_0' = 94 \text{ cm}$ and $\sigma = 1.41 \times 10^{-4} \text{ rad/s}$. Table XII shows the amplitude and phase of the surface layer current for various values of x . Since

Table XII - Amplitude of the surface layer current and phase relative to the surface elevation as calculated from Rattray's two-layer model parameterized to fit Howe Sound as described in the text. Speed amplitudes are in cm/s, phase in degrees. The distance x is measured in km from the head of the inlet.

x	amp	phase
5	1.79	-14
10	2.74	-17
15	2.47	-27
20	1.53	-63

this model has the long-inlet axis directed down-inlet instead of up-inlet as did the observations, the phase

angles close to zero indicate that down-inlet current and surface elevation are nearly in phase. This is exactly what was observed in the upper regions of Howe Sound as shown in figures 24 and 27. Figure 45 shows the variation along the inlet of the amplitude and phase of the surface-layer currents as predicted by this model for an incoming wave representing the M_2 tide at Squamish. The phase remains essentially constant in the upper half of the inlet but starts changing rapidly near the sill. The amplitude has a maximum value almost halfway between the head and the sill. The amplitude of the current variations shown in figure 27 for weeks 4 and 2N appears to be about 10cm/s, much larger than this model predicts. However, the model was calculated only for a pure M_2 tide of amplitude 92cm, but the actual tidal height change in six hours during those weeks was as much as 4m. The response of the surface layer to this larger tidal change should be proportionately larger. A comparison between the amplitude of the 3m current in the semi-diurnal band and the model-generated amplitude of the surface layer current of the M_2 tide at $x=15\text{km}$ shows that the former is about triple the latter amplitude. Considering the severe distortion of the fjord topography necessary to simplify it enough for the two-layer model, especially in the important region of the sill, the difference between the two is small enough to indicate that the model works well enough to verify that these surface currents could be caused by the suggested tidal mechanism.

Thus this two-layer normal mode model appears to

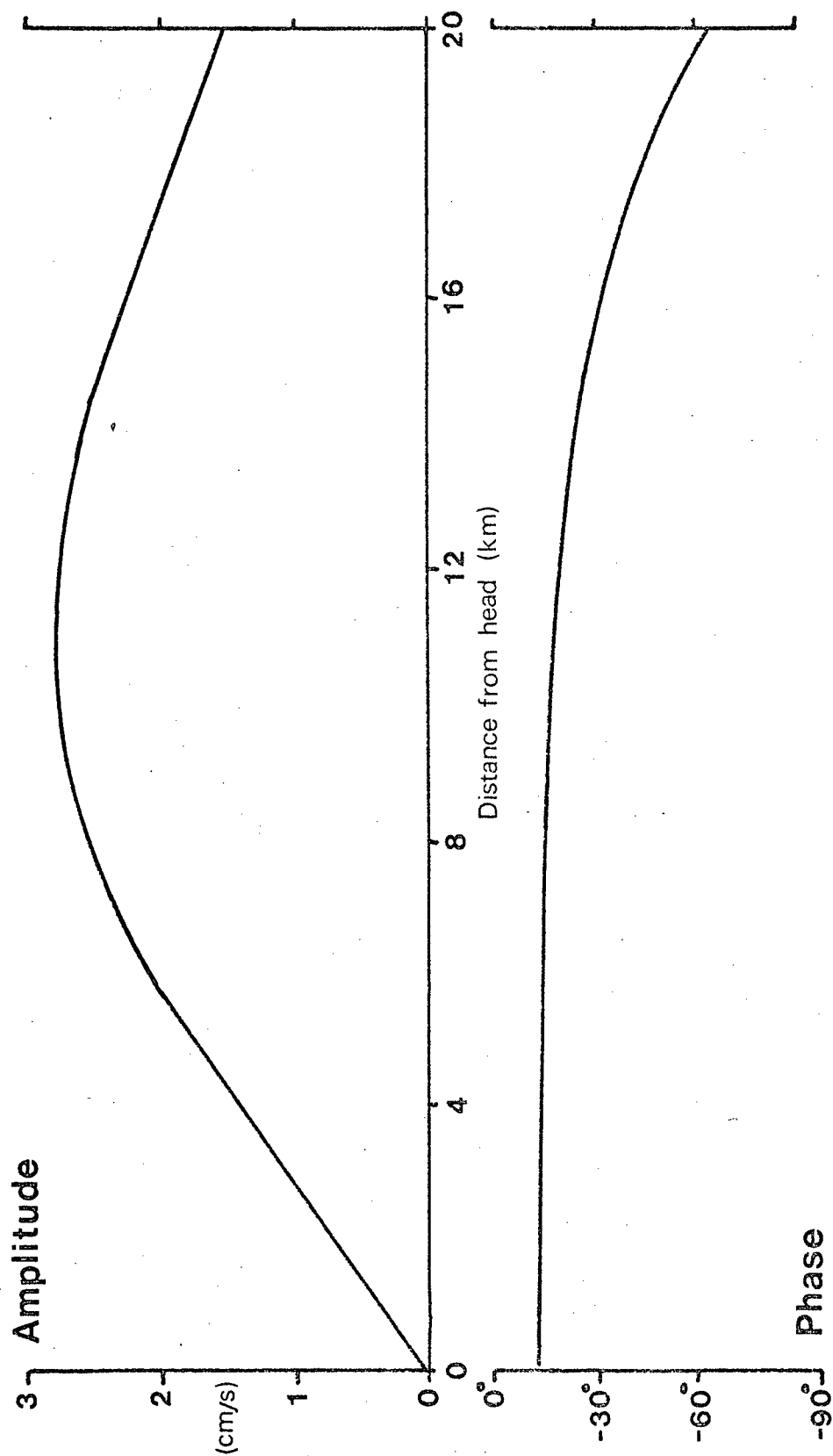


Figure 45 - Amplitude of the surface layer current and phase with respect to the surface tidal amplitude as a function of longitudinal position in the inlet. $x=0$ is the head of the inlet, $x=20\text{km}$ is the sill. Values were calculated from the baroclinic tidal model.

successfully predict the phase response of the surface layer to a barotropic tidal forcing and somewhat less successfully the amplitude response. The model does not however predict successfully the behaviour of the deeper water. The phasor diagram in figure 39 shows that the amplitude of the M_2 current increases below the surface layer, rather than decreasing as this model predicts. The relative phase of the deeper currents is not observed to be constant as a function of depth as is predicted in this model. Therefore a more complex formulation is needed to model the behaviour of the deeper waters.

Rattray et al. (1969) have proposed a continuously stratified model of internal wave generation in the ocean, similar in principle to the two-layer model just discussed. The continuous stratification is modelled, in the same manner as by Lighthill (1969), by an infinite sum of normal modes based on the vertical density structure of the water column. The equations are solved for each mode individually. Since the model is linear, the final solution is the linear superposition of the individual solutions. The modes form a complete set of orthogonal functions, and so forcing functions like an incoming tidal wave or a vertical wind-stress gradient may be represented by sums of these modes. The amplitude of each mode in the sum represents the contribution of the forcing function to that mode. Such a model in a basin of fjord-like geometry has been developed and described by Buckley (1974).

Since the two-layered model worked well to describe the

surface layer behaviour, it is probable that this multi-mode model will describe the behaviour of the deeper waters in a much more realistic fashion.

VII.5 Summary Of The Model Results

The behaviour of the surface layer of a fjord under the influence of wind and tidal forcing was studied with several simple models. The surface layer was first approximated by a slab under the influence of a wind stress gradient as a body force. Calculations of a drag coefficient consistent with those calculated by other techniques showed this to be a valid approximation for the first few hours after the onset of a wind. A version of Farmer's model for a wind-driven surface layer produced satisfactory agreement with the observations in the magnitude of change in velocity and acceleration and in the approximate shape of the velocity and acceleration vs time curves. It did not reproduce adequately the actual observed surface layer velocities or the acceleration many hours after the onset of the wind. A modified form of Rattray's internal tide generation model successfully reproduced the observed phases of the surface layer currents near the head of the fjord. Approximately the right amplitudes were also produced by this model which showed the production of a baroclinic response to a barotropic tidal forcing over the sill.

Based on these two reasonably successful two-layer normal mode models, a stratified normal-mode model was

suggested that might reproduce many of the observed features of the circulation of a fjord like Howe Sound.

BIBLIOGRAPHY

Bell, W.H. 1975. The Howe Sound current metering program. Pac. Mar. Sci. Rept. 75-7, Institute of Ocean Sciences, Patricia Bay, B.C. 3 vols.

Bendat, J.S. and A.G. Piersol. 1971. Random data: analysis and measurement procedures. Wiley-Interscience, J. Wiley and Sons, New York. 407p.

Bilodeau, L.E. and T.R. Osborn. 1976. Deep water renewal in Howe Sound. A paper presented to the 10th annual congress of the Canadian Meteorological Society, Quebec City, Quebec, 26-28 May, 1976. Abstract in Atmosphere 14 (congress edition): p18.

Binder, R.C. 1962. Fluid Mechanics 4th edition. Prentice-Hall Ltd. Englewood Cliffs, N.J. 453p.

Buckley, J.R. 1974. Forced internal oscillations in fjords. Notes on the 1974 summer study program at the Woods Hole Oceanographic Institution, WHOI Ref. 74-63 2:32-44.

Cameron, W.M. 1951. On the dynamics of inlet circulation. Ph.D. Thesis, Univ. Of California, Los Angeles, CA. As reported in Rattray (1966).

Carter, N.M. 1934. Physiography and oceanography of some British Columbia fiords. Proc. 5th Pac. Sci. Congress, 1933 1:721-738.

Dyer, A.J. 1973. Do GHOST balloons measure Eulerian mean velocities? J. Atmos. Sci. 30:510-13.

Dyer, K.R. 1973. Estuaries: a physical introduction. John Wiley and Sons, London, 140p.

Farmer, D.M. 1972. The influence of the wind on the surface waters of Alberni Inlet. Ph.D Thesis, Univ. British Columbia, Vancouver, B.C. 92p.

Gade, H.G. 1970. Hydrographic investigations of Oslofjord - a study of water circulation and exchange processes. Report 24, Geophysical Institute, University of Bergen, Bergen, Norway, 3 vols.

Gade, H.G. 1975. Deep water exchange in a sill fjord: a stochastic process. J. Phys. Oc. 3:213-219.

Halpern, D., R.D. Pillsbury and R.L. Smith. 1974. An intercomparison of three current meters operated in shallow water. Deep-sea Res. 21:489-497.

Halpern, D and R.D. Pillsbury. 1976. Influence of surface waves on subsurface current measurements in shallow water. *Limn. and Oc.* 21(4):611-616.

Heaps, N.S. and A.E. Ramsbottom. 1966. Wind effects on the water in a narrow two-layered lake. *Phil. Trans. R. Soc. London A* 259:391-430.

Hutchinson, A.H. and C.C. Lucas 1931. The epithalassa of the Strait of Georgia. *Can. J. Res.* 5:231-284.

Jenkins, G.M. and D.G. Watts. 1968. Spectral analysis and its applications. Holden-Day, San Francisco. 525p.

Johannessen, O.M. 1968. Some current measurements in the Drobak Sound, the narrow entrance to the Oslofjord. *Hvalradets Skrifter* 50:

Johns, R.E. 1968. A study of the density structure and water flow in the upper 10 m of a selected region of Bute Inlet. M.Sc. Thesis, University of British Columbia, 74p.

Kenney, B.C. 1972. Circulation and diffusion in a small lake. *Proc. Of the 1st Cdn. Symposium on Remote Sensing.* 237-248.

Kirwan, A.D. Jr., G. McNally, M.-S. Chang and R. Molinari. 1975. The effect of wind and surface current on drifters. *J. Phys. Oc.* 5(2):361-368.

Lighthill, M.J. 1969. Dynamic response of the Indian Ocean to the onset of the southwest monsoon. *Phil. Trans. R. Soc. London A* 265:45-92.

Marles, E.W., B.M. Lusk and W.J. Rapatz. 1973. Summary of hydrographic and oceanographic information on some British Columbia estuaries, *Pacific Marine Science Rept.* 73-7.

McAlister, W.B., M. Rattray Jr. and C.A. Barnes 1959. The dynamics of a fjord estuary, Silver Bay, Alaska. University of Washington, Department of Oceanography Tech. Rept. 62-70p.

Munk, W.H. 1975. Vertical motion in the sea. Lecture presented at the XVI General Assembly of the Int. Union of Geodesy and Geophysics, Grenoble, France, 30 Aug. 1975.

Pearson, C.E. and D.F. Winter. 1975. Analysis of stratified inlet flow by the method of weighted residuals. Symposium on modeling of transport mechanisms in oceans and lakes. Canada Centre for Inland Waters, Burlington, Ontario, October 6-8, 1975.

Pickard, G.L. and K. Rodgers. 1959. Current measurements in Knight Inlet, B.C. *J. Fish. Res. Bd. Can.* 16(5):635-678.

Pickard, G.L. 1961. Oceanographic features of inlets in the

B. C. Mainland coast. J. Fish. Res. Bd. Can. 18(6):907-999.

Pickard, G.L. 1975. Annual and longer term variations of deepwater properties in the coastal waters of southern British Columbia. J. Fish. Res. Bd. Can. 32(9):1561-1587.

Pond, S., D.B. Fissel and C.A. Paulsen. 1974. A note on bulk aerodynamic coefficients for sensible heat and moisture fluxes. Boundary Layer Meteorol. 6:333-339.

Proudman, J. 1953. Dynamical Oceanography. Methuen & Co. Ltd. London. 409p.

Rattray, M.Jr. and D.V. Hansen 1962. A similarity solution for circulation in an estuary. J. Mar. Res. 20(2):121-133.

Rattray, M.Jr. 1960. On the coastal generation of internal tides. Tellus XII:54-62.

Rattray, M.Jr. 1967. Some aspects of the dynamics of circulation in fjords. Estuaries (ed.) G. Lauff, American Association for the Advancement of Science, Pub. no. 83:52-63.

Rattray, M.Jr., J.G. Dworski and P.E. Kovalala. 1969. Generation of long internal waves at the continental slope. Deep Sea Res. 16(suppl):179-185.

Reinsch, C.H. 1967. Smoothing by Spline functions. Num. Math. 10:177-183.

Saunders, P.M. 1976. Near-surface current measurements. Deep-sea Res. 23(3):249-257.

Singleton, R.C. 1969. An algorithm for computing the mixed radix Fast Fourier Transform. IEEE Trans. On Audio and Electroacoustics, AU17(2):93-103.

Stern, M.E. 1975. Minimal properties of planetary eddies. J. Mar. Res. 33(1):1-13.

Stewart, R.W. 1974. The air-sea momentum interchange. Boundary Layer Meteorol. 6:151-167.

Stommel, H.M. and H.G. Farmer. 1952. On the nature of estuarine circulation. Ref. Nos. 52-88, 52-51, 52-63 Woods Hole Oceanographic Institution, Woods Hole, MA. As reported in Rattray (1966).

Terhune, L.D.B. 1968. Free floating current followers. Fish. Res. Bd. Can. Tech. Rept. #85, 28p.

Tully, J.P. 1949. Oceanography and prediction of pulp mill pollution in Alberni Inlet. Fish. Res. Bd. Can. Bull. 83.

Vancouver, G. 1798. A voyage of discovery to the North

Pacific Ocean and around the world. G.G. And J. Robinson, London, 3 Vols and Atlas.

Water Survey of Canada, 1974. Historical streamflow summary, British Columbia to 1973, Inland Waters Directorate, Dept. Of the Environment, Ottawa. 694p.

Webster, I.T. and D.M. Farmer. 1976. Analysis of salinity and temperature records taken at three lighthouse stations on the B.C. coast. Pac. Mar. Sci. Rep. 76-11, Institute of Ocean Sciences, Patricia Bay, B.C.

Webster, P.J. and D.G. Curtin. 1974. Interpretations of the EOLE experiment I: temporal variations in Eulerian quantities. J. Atmos. Sci. 31:1860-1875.

Wylie, F.J. 1968. The use of radar at sea. American Elsevier Pub. Co. New York, 280p.

Zeilon, N. 1913. On the seiches of the Gullmar Fjord. Svensk. Hyd-biol. Skr. V, 22p.

APPENDIX I

BEHAVIOUR OF A DROGUE IN A VERTICAL SHEAR

The movement of a drogue is governed by drag and torque forces generated on it by the surrounding air and water. These forces may be estimated by using the standard drag approximation for a flat plate perpendicular to the flow:

$$\vec{F} = (\rho C_D / 2) \vec{U} |\vec{U}| A \quad (\text{A.I.1})$$

where ρ is the density of the fluid, C_D is the drag coefficient for fluid flow perpendicular to a finite rectangular plate, \vec{U} is the velocity of the fluid past the plate and A is the area of the plate.

The effects of wind and surface currents on a deep drogue have been calculated by Kirwan et al. (1975). The

drogues used in this experiment behave differently since their drag elements are rigidly attached to the surface floatation unit. An analysis of their behaviour follows.

The major forces on the drogue are as follows:

- i) F_m . This force, the drogue weight, is directed vertically downward and, since it is concentrated mostly in the reinforcing rod, is taken to act at the centre of the rod.
- ii) F_b . The buoyancy force is exactly equal in magnitude and opposite in sign to the drogue weight. It acts from near to but slightly below the centre of the buoyant sphere.
- iii) F_w . The wind drag on the drogue may be estimated by assuming that the force acts only on the radar reflector. The wind drag on the pole is included in this figure by adding a small amount to the actual area of the reflector. Its magnitude is proportional to the difference between the wind velocity and the drogue velocity. This force acts in a horizontal direction.
- iv) F_d . The water drag on the drogue may be, in most cases, conveniently broken up into two sections; F_{d1} , the force acting in the direction of the drogue velocity caused by the water moving faster than the drogue, and

F_R , the force acting in the direction against the drogue velocity caused by water moving more slowly than the drogue. The former force usually acts on the drogue from the water surface down to the depth at which the drogue velocity equals the water velocity. The latter force acts from this point to the bottom of the drogue.

These forces are shown schematically in figure 46 and are tabulated in table XIII. When the drogue is in equilibrium with these forces, they must balance in the horizontal and in the vertical direction. Thus:

$$F_m + F_g = 0 \quad (A.I.2)$$

and:

$$F_w + F_f + F_R = 0 \quad (A.I.3)$$

The first equation has the solution $F_g = -mg$. The other can only be solved in specific circumstances.

These five forces also exert torques on the drogue which must sum to zero for the drogue to be in equilibrium. Thus:

$$T_m + T_B + T_w + T_f + T_R = 0 \quad (A.I.4)$$

Table XIII - The forces and torques on a drogue. The forces are those shown in figure 46. The torques are about the point z .

Source	force	torque
mass	$F_m = mg$	$T_m = -mg(D - z_0 / \cos \theta) \sin \theta$
buoyancy	$F_b = B$	$T_b = -B(z_0 / \cos \theta) \sin \theta$
wind drag	$F_w = \rho_a C_D / 2 (U_w - u_0) \cdot U_w - u_0 A$	$T_w = \rho_a C_D / 2 (U_w - u_0) \cdot U_w - u_0 A \cdot (D + z_0 / \cos \theta) \cos \theta$
water drag	$F_F = W \rho_w C_D / 2 \cdot \int_0^{z_0} (u - u_0)^2 dz$	$T_F = -W \rho_w C_D / 2 \cdot \int_0^{z_0} (u - u_0)^2 (z - z_0) dz$
water drag	$F_R = -W \rho_w C_D / 2 \cdot \int_{z_0}^{D \cos \theta} (u - u_0)^2 dz$	$T_R = W \rho_w C_D / 2 \cdot \int_{z_0}^{D \cos \theta} (u - u_0)^2 (z - z_0) dz$

ρ_a = density of air

ρ_w = density of water

A = area of drogue in air

W = width of drogue in water

θ = angle of drogue w.r.t. vertical

D = depth of drogue in water, height of reflector above water

z_0 = depth at which drogue velocity = water velocity

\vec{u} = velocity of water

\vec{u}_0 = velocity of drogue

\vec{U}_w = velocity of wind

m = mass of drogue

B = buoyancy force

These two equations must be solved for the three unknowns u_0 , z_0 and θ .

A third equation must be provided for solution. It is usually an equation relating water velocity to depth, $u=u(z)$.

We will now assume several simple forms of the velocity profile and solve the system to examine its behaviour.

In the first case, let us take a constant current of velocity $u(z)=c$. If the wind velocity is in the same direction as the current, $u_0 > c$, all the water moves more slowly than the drogue and hence $z_0=0$. If the wind direction is opposite to that of the current, then $u_0 < c$ and $z_0 = D \cos \theta$. Considering the case where the wind and current are in the same direction and the wind speed is greater than the current speed, the force balance equation becomes:

$$\rho_a A (U_w - u_0)^2 - W \rho_w D \cos \theta (c - u_0)^2 = 0 \quad (\text{A.I.5})$$

The torque balance equation becomes:

$$-mgD \sin \theta + \rho_a C_D / 2 (U_w - u_0)^2 A + \rho_w W C_D / 2 (c - u_0)^2 D^2 \cos^2 \theta / 2 = 0$$

(A.I.6)

To solve these equations the following values are used:

$$\rho_a = 1.25 \times 10^{-3} \text{ gm/cm}^3$$

$$\rho_w = 1 \text{ gm/cm}^3$$

$$C_D = 1.2 \text{ (from Binder, 1962)}$$

$$D = 200 \text{ cm}$$

$$W = 300 \text{ cm}$$

$$g = 980 \text{ cm/sec}^2$$

$$A = 930 \text{ cm}^2$$

$$m = 20000 \text{ gm}$$

For a range of values of U_w and c , the results are given in table XIV.

Table XIV - Drogue speed and tilt angle for various current and wind speeds in a homogeneous current of magnitude c . The wind speed is U_w .

c	0 cm/s		10 cm/s		25 cm/s	
	U_w m/s	u_o cm/s	u_o cm/s	θ deg	u_o cm/s	θ deg
1		0.4	10.4	0.03	25.3	0.02
10		4.1	14.0	2.60	29.0	2.58
20		8.2	18.2	10.35	33.2	10.30

From this table it can be seen that the difference between drogue velocity and water velocity is about 0.4% of the wind velocity and that the drogue tilt is quite small. The tilt, as expected, increases roughly as the square of the wind speed.

The only differences in drogue behaviour when the wind

and the current oppose each other are that the drogue tilt will be in the opposite direction, i. e. the drogue will still tilt downwind, and the sign of $(u_0 - c)$ will change so that the drogue velocity will be decreased rather than increased as is the case when the wind and the current are in the same direction.

Considering now the case of a linear vertical shear $u(z) = s(1 - z/D)$ with the wind in the same direction as the current, the horizontal force balance equation becomes:

$$\rho_a A (U_\infty - u_0)^2 - W \rho_w / 3 (s/D)^2 ((D \cos \theta - z_0)^3 - z_0^3) = 0 \quad (\text{A.I.7})$$

The torque balance equation is:

$$\begin{aligned} -mgD \sin \theta + \rho_a (C_D / 2) (U_\infty - s + sz_0/D)^2 A (D \cos \theta + z_0) \\ + \rho_w W (C_D / 8) (s/D)^2 ((D \cos \theta - z_0)^4 + z_0^4) = 0 \end{aligned} \quad (\text{A.I.8})$$

The solutions to these equations are tabulated in table XV for various values of U_∞ and s .

This table shows that the relatively strong shear of 25 cm/s/m causes by itself only a tilt of 8° . A wind speed of 10 m/s, the maximum allowable for performing the experiment, only increased this by 2° . Comparison with the identical calculations done holding $\theta = 0$ shows that the effect of the

Table XV - Values of drogue speed and tilt in a linear current shear for various wind and current speeds. Wind speeds are in m/s. Current speeds are in cm/s, tilt angles in degrees from the vertical. The values indicated by -- were not calculated because the equations used are not valid for wind-induced drogue motions greater in magnitude than the maximum current speed and because calculation of this special case would not make any difference to the general conclusions.

s	10 cm/s		20 cm/s		50 cm/s	
U_w	u_o	θ	u_o	θ	u_o	θ
0	5.0	0.3	10.0	1.3	25.2	7.9
10	8.0	3.1	11.7	3.9	26.1	10.2
20	--	--	16.3	12.3	28.9	17.1

tilt angle is to increase the drogue speed by a factor of $(1/\cos\theta)$. This difference is not significant for the drogue tilts observed in this experiment, amounting to 2% at 10° and 6% at 20° . These two tables show that the effect of the wind on the drogue's speed and tilt decreases with increasing shear. A 20m/s wind increases the drogue speed by 8.2 cm/s over the average water speed when there is no shear but only by 3.9cm/s in a shear of 25cm/s/m. This result is a consequence of the velocity squared dependence of the drag forces. Since the mean square velocity difference increases as the strength of the shear increases for a constant difference in velocity between the drogue and the water a smaller velocity difference is necessary in the presence of a shear to keep the drogue in equilibrium with the wind drag. When the wind opposes the current direction, the

effect of the wind on the drogue velocity is inhibited even more. The tilt angle of the drogue established by the shear is decreased by the wind and hence the depth of the bottom of the drogue is increased, exposing the drogue to more of the shear. Thus a smaller difference is needed between the drogue velocity and the mean water velocity to create a drag force to balance the wind drag. In the most severe case shown in table 7 with $s=50\text{cm/s}$ and wind and current in the same direction, a wind of 20m/s increases the drogue speed by 3.7cm/s and the drogue tilt by 9.2° over the zero wind values. When the wind and current are opposed, the speed difference is -2.9cm/s and the angle difference is -10.3° . The differences between the two cases are small even in this extreme example and decrease in less extreme ones.

Neglecting now the small effect of tilt on the drogue speeds, it is necessary only to solve the force balance equation with $\theta=0$ to find the effects of various shears and wind velocities on the drogue. Looking at equation A.I.5 with $c=0$ and approximating $U_\omega \gg u_0$

$$u_0 = \sqrt{(\rho_a A / \rho_w W D)} U_\omega \quad (\text{A.I.9})$$

for the parameters relevant to this experiment then

$$u_0 = (4.56 \times 10^{-3}) U_\omega \quad (\text{A.I.10})$$

This result, strictly true only for wind over completely still water, provides a reasonable upper estimate of the difference between drogue speed and water speed as a function of wind speed.

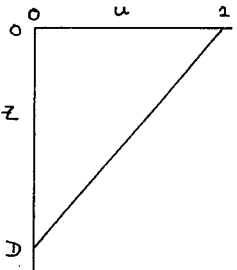
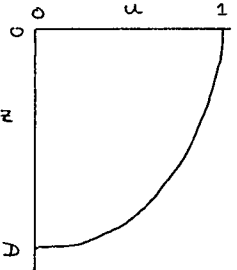
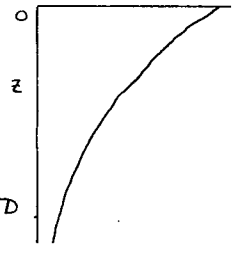
Ignoring now the effects of wind drag as well as those of tilt, let us look at the relationship of u_0 , the drogue velocity, to the mean and r.m.s. velocities of various analytic vertical current shears.

The three to be considered are a linear profile, $u(z)=1-z/D$; a quadratic profile, $u(z)=1-z^2/D^2$, and an exponential profile $u(z)=\exp(-z/D)$. The comparison between these is shown in table XVI. In the quadratic case, where the difference between mean and drogue velocities is the greatest, the shear is much stronger than one would expect to find in Howe Sound. A weaker shear (deeper zero-crossing) would show less discrepancy between the velocity estimates.

From this table it seems apparent that there is no simple universal relation between drogue velocity and mean velocity or r.m.s. velocity for the profiles examined. Therefore such a relation should not be expected for any arbitrary profile.

The results of the three-level experiment described in chapter V showed a maximum shear of 10cm/s/m corresponding to the middle column of table XV if the shear were linear. There were not enough data points in the vertical to determine the shape of the shear profile. If the shear profile is similar to any of those in table XVI then the results in table XIV indicate that the velocities determined

Table XVI - Drogue velocity, mean velocity and r.m.s. velocity for three analytic shears. The mean and r.m.s. velocities are calculated over drogue depth.

Profile		Drogue	Mean	r.m.s.
linear		.5	.5	.58
quadratic		.75	.67	.73
exponential		.645	.632	.658

from the drogues in the experiment should be very close to the mean velocity of the upper layer.

The average wind speed during the experiment was about 5 m/s. This would cause a maximum error in drogue speed of 2 cm/s. Since the r.m.s. drogue speed was greater than ten times this, corrections for wind drag on the drogues have

been neglected and the drogue velocities taken as the water velocity.

APPENDIX II

COMPUTER MOVIE GENERATION

The computer programme MOVIE on the IBM 370/168 , took input data from many sources and combined them to produce a magnetic tape that could be interpreted as a movie by programme MAP6 on the PDP-12 . These input data were:

Drogue positions interpolated at one minute intervals, sorted in temporal order and stored on magtape as the output from *SORT . This is the tape referred to as DATA2 in chapter II.

Wind speeds and directions on a minute by minute basis as interpolated from the winds at Squamish.

Tidal heights on a half-hourly basis as taken from the record at Pt. Atkinson.

A coast outline exactly as prepared for input

to programme MAP5 .

The coastline and tidal height curve were written out at the beginning of the output tape. The remainder of the tape contained a series of records, each one corresponding to the status of the inlet at one particular minute of the experiment. Each record contained the time that the record represented, the position of all the drogues in the water at that time and a series of numbers that corresponded to the positions of dots forming an arrow whose length and direction corresponded to the speed and direction of the wind at that time. The drogue positions and wind vector dot positions were, of course, scaled to PDP-12 screen coordinates.

Programme MAP6 contained basically the same tape handling and display subroutines as did MAP5 . Both programmes could produce "worm" movies on the screen of the PDP-12 as described in chapter II. The difference between the two programmes was that MAP6 had a great deal of flexibility in the display mode and contained an interface routine to control a movie camera. It was possible in MAP6 to select the length of the worm displayed and to control the display speed by varying the number of pictures displayed simultaneously on the screen and the number of minutes between each picture displayed, respectively.

Wind speed and direction was indicated on each frame of the movie by an arrow. Tidal height was indicated on the tidal curve by a cursor whose position was calculated from the relative time of that picture from the beginning of the

experiment.

To transfer the image from the screen of the PDP-12 to film, the programme controlled a relay that triggered a solenoid that triggered a Bolex H16 Reflex movie camera. Using Kodak Tri-X Reversal 16mm film, the CRT screen was dim enough to allow one second exposures at f11. By varying the ratio of camera frames to computer movie frames, the time compression of the final movie could be controlled. For example, if the pictures advanced at 2 minute intervals and the camera took 3 frames of each picture, then there would be 30 pictures displayed of each hour and 90 frames taken of each hour. At a projection rate of 18 frames per second, the time compression is 720:1. This is 1 hour in 5 seconds or 1 day in 2 minutes. A faster rate is obtained by advancing the pictures at 5 minute intervals and taking 2 frames of each. This yields a compression of 2700:1 or 1 day in 32 seconds.

Appendix III is a section of movie that was made in this fashion. It contains two sections of film. The first is the entire week 1 data set shot at the faster rate previously discussed. It is followed by a section of week 1 data at the slower rate showing in detail the effect of the wind event between 56 and 76 hours.